A CAVALCADE OF CLUSTERS: THE INTERPLAY BETWEEN ATOMIC AND ELECTRONIC STRUCTURE IN COMPLEX INTERMETALLICS

A Dissertation

Presented to the Faculty of the Graduate School

of Cornell University

in Partial Fulfillment of the Requirements for the Degree of

Doctor of Philosophy

by

Ryan Henderson

January 2013

A CAVALCADE OF CLUSTERS:

THE INTERPLAY BETWEEN ATOMIC AND ELECTRONIC STRUCTURE IN COMPLEX INTERMETALLICS

Ryan Henderson, Ph.D.

Cornell University 2013

What drives the stability of complex intermetallic compounds? Many, if not most, metals and alloys crystallize in one of the familiar body-centered cubic (bcc), face-centered cubic (fcc), or hexagonal close-packed (hcp) crystal structures. But what of Cu_5Zn_8 with 54 atoms in its unit cell, or Ti_2Ni with its 96? Or larger still $Fe_{11}Zn_{39}$, with 408 atoms in the repeat unit?

Chemically and physically straight-forward semi-empirical calculations can lend us insight, and we review one such technique–the extended Hückel method–with new examples. Along the way, we solve the crystal structures for the new family of ternary compounds $Ir_xRu_{1-x}Zn_{10}$ and see what clues the Ir site preferences can give us about the connection between atomic structure and electronic structure via the Mott-Jones method of constructing electronic wavefunctions from the intensity of Bragg peaks.

Finally, we investigate the connection between intermetallic structures that possess pseudo five-fold diffraction patterns. We find these peaks corresponding to features of several different types of tetrahedral close-packing, which in turn can all be described as three-dimensional projections of a four-dimensional perfect packing of tetrahedra: the 600-cell. We further show that the Bragg peaks comprising the pseudo five-fold diffraction pattern are linked to structural stability, and hence the higher-dimensional geometry.

BIOGRAPHICAL SKETCH

Ryan Henderson was born in Canton, Ohio in 1985. He attended Bowling Green State University, graduating in 2007 receiving a B.Sc. in Physics and Applied Math, Magna Cum Laude. He matriculated to Cornell University the same year to undertake a Ph.D. in Chemistry, graduating in 2012. After graduation (and a short vacation), he will begin work at Intel in Portland, Oregon.

For Mom and Dad, with love

ACKNOWLEDGEMENTS

"...they are fortunate who get a theatre where the audience demands their best."

–George Eliot, *Middlemarch*[1]

Above all I thank my parents for recognizing I had a knack for mathematical and scientific pursuits and pushing me to develop it, even though it was hard and I probably complained. This is of course but one of innumerable debts to them which I can never fully settle. I selfishly hope that my continued happiness, success, and love are repayment enough.

Besides my parents, no one person has helped me expand my personal and professional horizons as much as my Ph.D. advisor, Prof. Stephen Lee. His mentorship and friendship has been simply invaluable. While I am extremely grateful for the chemical knowledge he managed to transfer to me, I am equally appreciative of the non-scientific lessons (like what makes a wine great).

I thank Prof. Roald Hoffmann for his endless patience and inspiration, as well as teaching me how to think with orbitals and how to read between the lines of a scientific paper. I also am thankful to him for forcing me to explain the nearly-inscrutable in as simple terms as possible, something I still struggle with. This has helped my ability to communicate complex ideas immensely, and also sharpened my own thinking. I also must thank him for financial support in the final weeks of the preparation of this dissertation.

Prof. Bernd Harbrecht encouraged me to pursue experimental work in his lab in Marburg, an experience which has been crucial to my development as a scientist. I thank him not only for his energy and expertise, and careful scrutiny of my work, but for giving me the opportunity to work in an environment very different from the one I was used to in a country I was unfamiliar with.

My next career move would not be possible without Prof. Frank DiSalvo, whose professional guidance and connection to industry opened up new opportunities for me. I also thank him for scientific discussion and guidance over the years.

Two people were crucial to my development as a researcher during my undergraduate years: Prof. Lewis Fulcher at BGSU introduced me to scientific research, and served as my *de facto* academic advisor, urging me to pursue graduate studies. Prof. Ben Widom offered me the chance to work for him at Cornell in 2006, and gave me the idea to pursue graduate study in chemistry. I am grateful to both of these men for setting me down the path I'm on today.

I would also like to thank professors Neil Ashcroft and Lou Hand for their careful scrutiny of my work and for their helpful advice.

The sole other graduate student in Prof. Lee's lab whose time overlapped with mine, Dr. Rob Berger, was indispensable in getting me up to speed with research. I also thank the undergraduates I've had the pleasure to work with: Nick Settje, Corey Kaminisky, Zach Nelson, and Jeffers Nguyen. Nick worked closely with me on the work in Chapter D, and Nick, Corey, and Zach are responsible for many of the figures in Chapters 2 and 3. I would also like to thank Dr. Andreas Hermann, a post-doc in Prof. Hoffmann's group, for assistance with VASP calculations. Thanks also to Ada Ng for help with preparation of Figure C.2, and to Katherine Hammes, Chinmayee Subban, and Marie Krysak for help with my job search.

I thank my friend Dr. Partha Jana, at the time a fellow graduate student in Prof. Harbrecht's lab, for teaching me the practical aspects of crystallography. His guidance, along with that of Prof. Klaus Harms and Radostan Riedel, were indispensable in solving the difficult crystal structures in Chapter 1.

I am also indebted to two outstanding high school teachers—Mr. Matt Brown and Mr. Ric Thompson—for acquainting me with the power of mathematics and physics and for truly challenging me for the first time in my academic career.

I thank Pat Hine for her help and assistance with the logistics of teaching, and for helping me to side-step administrative land mines on more than one occasion. I also thank Attilio De Falco and Michael Hint for their computing support even in the face of my terrible system maintenance.

Thank you to the National Science Foundation, the German Academic Exchange Service (DAAD), and Cornell University for financial support.

Finally, I thank my family and friends be they from Ithaca, Marburg, home, or elsewhere. A non-exhaustive list, of the Ithaca crowd: Ada, Angie, Annie, Catherine, Chin, Clare, Claire, Brian, Dan, Eliz, Erika, Erin, Evan, Inish, Janice, Josh, Katherine, Maicol, Margaux, Marie, Mary, Melina, Mike, Pasquale, Paul, Purba, Ry, Srikant, Taz, Val, Wes, and Yev; my good friends from home and college: Andrew, Chris, Evan, James, Jeremy, Krebs, and Mike; and finally, my sisters: Angela and Andrea.

I would not have made it without your support and camaraderie. It's futile to even try to express how much you mean to me or how much I will miss you. I love you all, and hope our paths cross again soon and often.

TABLE OF CONTENTS

Biographical Sketch . . . iii
Dedication . . . iv
Acknowledgements . . . v
Table of Contents . . . viii
List of Tables . . . x
List of Figures . . . xii

1 The $Ir_xRu_{1-x}Zn_{10}$ ($0.1 \leq x \leq 0.4$) System **1**
1.1 Introduction . . . 1
1.2 Experimental Details . . . 4
1.2.1 Synthesis . . . 4
1.2.2 Powder Diffraction . . . 5
1.2.3 Energy-dispersive X-ray spectroscopy (EDX) . . . 5
1.2.4 Single-Crystal structure determination (SCSD) . . . 5
1.3 Results . . . 6
1.4 Origin of the pseudo five-fold diffraction pattern . . . 11
1.5 Electron Counting and Site Preferences . . . 19
1.6 Conclusion . . . 32

2 A Cluster-based approach to pseudo five-fold diffraction in intermetallics **33**
2.1 Introduction . . . 33
2.2 Aufbau of tetrahedral clusters . . . 35
2.3 A unified view for tetrahedral clusters . . . 38
2.4 Crystalline examples of the four types of tetrahedral clusters . . . 49
2.5 Smaller crystalline examples . . . 54
2.6 Larger crystalline examples . . . 62
2.7 Cluster edges and diffraction . . . 64
2.8 Examples of reciprocal-space diffraction clusters . . . 71

3 Connecting Geometric Structure to Electronic Structure **80**
3.1 Introduction to the Jones model . . . 80
3.2 Group 10-12 tetrahedral-cluster structures . . . 88
3.3 Conclusions . . . 110
3.3.1 Symmetry and electrons . . . 110
3.3.2 Mysterious metals . . . 111

4 $Ir_xRu_{1-x}Zn_{10}$ revisited **113**
4.1 Introduction . . . 113
4.2 Reciprocal Space Cluster . . . 113
4.3 Comparing electron-count estimates . . . 117
4.4 Conclusion . . . 119

A The Electronic Structure of $Au_{10}Cr_4Zn_{89}$ **121**
A.1 Introduction . . . 121
A.2 Electronic Structure Calculations . . . 123

B Crystallographic Data **127**
B.1 $Ir_2Ru_8Zn_{100}$ . . . 127
B.2 $Ir_3Ru_7Zn_{100}$ . . . 130
B.3 $Au_{32}Cd_{47}Zn_{21}$ . . . 133
B.4 $Au_{10}Cr_4Zn_{89}$ . . . 136

C Character Table of the 600-cell **139**
C.1 Introduction . . . 139
C.2 Quaternions . . . 139
C.2.1 A Note on 4D rotations . . . 143
C.3 Classes . . . 147
C.4 Representations . . . 152
C.5 The Character Table . . . 157
C.6 Example Projection: the D_{3h} cluster . . . 164

D Additional Dimensions: new crystals from E_8 **168**
D.1 Introduction . . . 168
D.2 Projected Structures . . . 169
D.3 Structure Search . . . 171
D.4 Projected Distance and Electron Transfer . . . 176
D.5 Conclusions . . . 179

LIST OF TABLES

1.1 Crystallographic information and *R*-values for $Ir_2Ru_7Zn_{100}$ and $Ir_3Ru_7Zn_{100}$ . . . 9
1.2 Intensities of Strongest Reflections in $Ir_xRu_{1-x}Zn_{10}$ . . . 21
1.3 Selected properties of Ru, Ir, and Zn . . . 28

2.1 Strongest (*hkl*) in $SiMn_6Pd_{23}Al_{70}$ . . . 70
2.2 Strongest (*hkl*) in Cd_3Cu_4 . . . 73
2.3 Strongest (*hkl*) for $MnAl_4$ . . . 76
2.4 Strongest (*hkl*) in $Mn_{10}Al_{29}$ . . . 77

3.1 Strongest (*hkl*) for $Zn_{11}Au_{15}Cd_{23}$ . . . 93
3.2 Valence electron count for group 10-12 tetrahedral cluster crystal structures . . . 95
3.3 Strongest (*hkl*) for Pt_5Zn_{21} . . . 96
3.4 Strongest (*hkl*) in Pd_3Al_7 . . . 99
3.5 Strongest (*hkl*) for $CdCu_2$ . . . 102
3.6 Strongest (*hkl*) for Cu_5Cd_8 . . . 103
3.7 Strongest (*hkl*) for Cd_3Cu_{10} . . . 104

4.1 Fermi spheres of $RuZn_{10}$ . . . 114
4.2 Strongest (*hkl*) in $RuZn_{10}$ . . . 116
4.3 Intensities of Strongest Reflections in $Ir_xRu_{1-x}Zn_{10}$ . . . 119

A.1 Relative charges of sites in model all-Zn system corresponding to experimental sites. . . . 126

B.1 Atomic coordinates ($\times 10^4$) and equivalent isotropic displacement parameters ($Å^2 \times 10^3$) for $Ir_2Ru_8Zn_{100}$ . . . 128
B.2 Anisotropic displacement parameters ($Å^2 \times 10^3$)for $Ir_2Ru_8Zn_{100}$. 129
B.3 Atomic coordinates ($\times 10^4$) and equivalent isotropic displacement parameters ($Å^2 \times 10^3$) for $Ir_3Ru_7Zn_{100}$ . . . 131
B.4 Anisotropic displacement parameters ($Å^2 \times 10^3$) for $Ir_3Ru_7Zn_{100}$. 132
B.5 Crystallographic information and *R*-values for $Au_{32}Cd_{47}Zn_{21}$ . . 134
B.6 Atomic coordinates ($\times 10^4$) and equivalent isotropic displacement parameters ($Å^2 \times 10^3$) for $Au_{32}Cd_{47}Zn_{21}$ . . . 135
B.7 Anisotropic displacement parameters ($Å^2 \times 10^3$) for $Au_{32}Cd_{47}Zn_{21}$ 135
B.8 Crystallographic information and *R*-values for $Au_{10}Cr_4Zn_{89}$ . . . 137
B.9 Atomic coordinates ($\times 10^4$) and equivalent isotropic displacement parameters ($Å^2 \times 10^3$) for $Au_{10}Cr_4Zn_{89}$ . . . 138
B.10 Anisotropic displacement parameters ($Å^2 \times 10^3$) for $Au_{10}Cr_4Zn_{89}$ 138

C.1 Classes of proper rotations $|\mathbf{R}| = 1$ with at least one fixed axis ($\exists \lambda \in \Re$) . . . 149

C.2 Classes of improper rotations $|\mathbf{R}| = -1$ with at least one fixed axis ($\exists\lambda \in \Re$) . . . 150
C.3 Classes of proper rotations $|\mathbf{R}| = 1$ with no fixed axes ($\neg\exists\lambda \in \Re$) . 151
C.4 Character table for the symmetry group C_{3v} . . . 152
C.5 Multiplication table for C_{3v} . . . 154
C.6 Character table for the symmetry group of the 600-cell, columns 1-12. The top row indicates the order of elements in the corresponding class. . . . 158
C.7 Character table for the symmetry group of the 600-cell, columns 13-20 . . . 159
C.8 Character table for the symmetry group of the 600-cell, columns 21-28 . . . 160
C.9 Character table for the symmetry group of the 600-cell, columns 29-34 . . . 161
C.10 Partial character table for the symmetry group of the 600-cell for classes of improper rotations. Irreducible representations which are character 0 for every class are omitted. . . . 162
C.11 Character Table for the I_h group. . . . 162
C.12 Character Table for the T_d group. . . . 163
C.13 Character Table for the D_{3h} group. . . . 163
C.14 Character Table for the D_{5h} group. . . . 163

D.1 Summary of Experimental Structures Matched. Adapted in Part from Dshemuchadse *et al.*[2] . . . 172
D.2 Fully-ordered structure matches . . . 174
D.3 Structure matches which have mixed or deficient sites . . . 175

LIST OF FIGURES

1.1 Simulated diffraction pattern for $Ir_xRu_{1-x}Zn_{10}$ in the [100] direction from $0 < 2\theta < 80$ for $x = 0$. All peaks are shown on the left, and only the strongest are shown on the right to highlight the pseudo five-fold diffraction pattern. 3

1.2 Powder diffraction patterns for compounds with nominal compositions $Ir_xRu_{10-x}Zn_{100}$. The intensity scale is normalized to the highest peak from each run. 7

1.3 Arrangement of disordered sites around the partially occupied Ru37 site. As in Belin & Belin[3] and Allio's[4] work, we consider the disordered sites as one of three randomly oriented icosahedra (one particular orientation is shown here by the grey lines). During the refinement of the occupation, the following constraints were used: the axial Zn39 and Zn42 groups were constrained to an occupancy of 1. The Zn40 and Zn41 groups were also constrained to a total occupancy of 1. The Zn43 and Zn38 groups were constrained to an occupancy of $\frac{2}{3}$. In this way, an average total occupation of 12 sites coordinating to Ru37 is ensured. 8

1.4 Empirical composition. x = Atomic % Ir / (Atomic % Ir + Atomic % Ru), y = Atomic % Zn. The points are the individual EDX measurements, and the bars are the standard deviations in x and y from those measurements. The "X"s mark the composition determined via single crystal refinement for nominal compositions $Ir_2Ru_8Zn_{100}$ and $Ir_3Ru_7Zn_{100}$. 10

1.5 Simulated diffraction pattern for Al_5Co_2 in the [100] direction from $0 < 2\theta < 80$. All peaks are shown on the left; only the strongest are shown on the right to highlight the pseudo five-fold diffraction pattern. 11

1.6 Construction of the D_{3h} cluster as a set of three mutually penetrating icosahedra. Each icosahedron contains an edge of Co atoms (dark blue) which are the center atoms of the remaining two icosahedra. The dark triangle in the center is the overlapping region, whose vertices form the region of overlap between all three icosahedra. 12

1.7 Top: Perspective view of D_{3h} cluster from Figure 1.6. The overlapping region can be seen in brown in the center. Bottom: Perspective view of D_{3h} cluster with the icosahedra filled. 13

1.8 Structure of the overlapping region. Clockwise from top left: the D_{3h} cluster as shown in 1.7, followed by the D_{3h} cluster made transparent to emphasize the region where the three icosahedra intersect. Next, the overlapping volume by itself and finally, the same region without faces. The overlapping volume is a trigonal bipyramid. 13
1.9 A pseudo five-fold axis of a D_{3h} cluster, shown as the green bar. Note that the pseudo five-fold axis is parallel to a Co-Co edge of the overlapping volume. The bottom pair of illustrations show how two of the three fused icosahedra join to enhance pseudo five-fold symmetry. 14
1.10 The single Co site not contained in the D_{3h} cluster sits in the cluster interstices. The gold lines are chosen to highlight the coordination geometry of the central Co and emphasize newly formed tetrahedra. 15
1.11 View of D_{3h} clusters and interstitial Co atoms down the [001] and [100] directions. 16
1.12 Families of plane waves corresponding to Bragg peaks in the pseudo five-fold diffraction pattern of Al_5Co_2. Only the first quadrant of the [100] diffraction pattern (Figure 1.5) is shown. The parallel colored lines superimposed over the structural pictures correspond to plane waves labeled with the same color in the diffraction pattern. The left picture corresponds to the inner ring of peaks in Figure 1.5, and the right picture corresponds to the outer ring of peaks. Note that every Co atom lies on or near a crest of all six plane waves. 17
1.13 Interaction of the crests of plane waves from the inner ring of the pseudo five-fold diffraction pattern with the atoms of the D_{3h} cluster. 18
1.14 Simulated diffraction pattern for Al_5Co_2 and Al_5Rh_2 in the [100] direction from $0 < 2\theta < 80$. All peaks are shown on the left, and only the strongest are shown on the right to highlight the pseudo five-fold diffraction pattern. 18
1.15 D_{3h} clusters in $Ir_xRu_{1-x}Zn_{10}$. All Ir sites are mixed with Ru or Zn, but all heavy atoms in the D_{3h} clusters are Ru or Ru/Ir. There is some interpenetration among neighboring D_{3h} clusters which can be seen in the [001] view. The center of each of the three fused icosahedra forming each D_{3h} cluster is an Ir/Ru mixed site. One 'vertex' of each D_{3h} cluster icosahedron is actually 4 partially occupied disordered Zn sites, highlighted by the red circle. . . . 19

1.16 Families of plane waves corresponding to Bragg peaks in the pseudo five-fold diffraction pattern of $Ir_xRu_{1-x}Zn_{10}$. Only the first quadrant of the [100] diffraction pattern is shown. Note that each heavy site can be made to lie on or near a crest from all three families of plane waves. 20
1.17 Interaction of the crests of plane waves from the inner ring of the pseudo five-fold diffraction pattern with the atoms of the D_{3h} cluster *and interior atoms.* 20
1.18 Three atomic *p*-orbitals on the left combine to make three π molecular orbitals on the right. Even though all three *p*-orbitals are equivalent, the resulting MO wavefunctions have more electron density on different sites depending on the electron filling. . 22
1.19 Band structure of Zn. The special *k* points are G=(0 0 0), M=(0 1/2 0), K=(1/3 1/3 0), L=(0 1/2 1/2), and H=(1/3 1/3 1/2). LDA-DFT bands are black and eH are red. The flat bands between roughly -8 and -10 eV are the Zn d-bands, which are not included in the eH calculation (in keeping with the Hume-Rothery spirit). The plots were shifted so that their Fermi energies coincide at 0. . 24
1.20 Histogram of interatomic distances in the unit cell of the model all-Zn system, based on $RuZn_{10}$. The interatomic distance in Zn metal is 2.68Å. Taking the true crystallographic sites leads to computational difficulties because the partially occupied sites are unreasonably close to each other. In the *P*1 model, partially occupied disordered sites are replaced by fully ordered sites, as discussed above. Note that the unreasonably short distances between partially occupied sites have vanished. 26
1.21 Plot of site charge from a Mulliken Population Analysis computation as a function of total electron count in a model all-Zn system. Each line represents the relative charge of a symmetry equivalent group of atoms in the original high-symmetry structure. Lower, more negative, charge indicates greater electron concentration. Although all atomic sites in the model structure are Zn, we have highlighted the sites where Ru and Ir are located. Cyan lines are relative charges on the experimental Ru sites, black lines are the relative charges on the experimental Ir/Ru mixed sites, dark grey lines are the relative charges on the mixed Ir/Zn site, and grey lines are the relative charges on the experimental Zn sites. 27

1.22 Box and whisker plot of relative charges for truly crystallographically equivalent sites in the $P1$ model. The T lines denote the minimum and maximum relative charges in the group of crystallographically equivalent sites. The heights of the boxes correspond to the middle 50% of relative charges. The lines in the middle of the boxes are the mean of relative charges of a group of crystallographically equivalent sites. The groups are sorted by mean. The labels on the mixed sites correspond to the compositions in $Ir_{0.2}Ru_{0.8}Zn_{10}$ (top) and $Ir_{0.3}Ru_{0.7}Zn_{10}$ (bottom). The Disordered Icosahedra box includes ten crystallographically inequivalent sites from the true structure, for a total of 48 Zn sites in the $P1$ model (there are 12 Zn sites per disordered icosahedron, and 4 disordered icosahedra per unit cell). 29
1.23 Possible valence s- and p- electron counts for Ir and Ru at different experimentally determined compositions while holding Zn constant at 2 valence s- and p- electrons. We have assumed 1.62 valence s- and p- electrons. The red dot is the point corresponding to Ir taking one electron and Ru taking two. 30
1.24 Possible valence s- and p- electron counts for Ir and Ru at different experimentally determined compositions while holding Zn constant at 2 valence s- and p- electrons, as in Figure 1.23 but with different valence electron counts per atom. 31

2.1 (a) Six equilateral triangles joined together into a regular planar hexagon and either (b) twenty face-sharing regular tetrahedra joined into an icosahedral shape with crevasses or (c) twenty slightly-irregular tetrahedra fused into a regular icosahedron. . . 36
2.2 (a) Five face-sharing regular tetrahedra joined into a five-fold ring with crevasses or (b) five slightly-irregular tetrahedra fused into a D_{5h} face-sharing ring of tetrahedra. 36
2.3 A pair of filled icosahedra fused into a single cluster, the edge-centered tetrahedral cluster. Single vertices from each icosahedron, indicated in red, come together to form an edge, shown in brown in the upper left inset. The cluster is of D_{5h} point group symmetry The shared volume shown in the center of panel (b) is the same fused ring of tetrahedra shown (from another perspective) in Figure 2.2 (b). The full cluster shown here consists of 35 face-sharing tetrahedra. 37
2.4 Three filled icosahedra fused into a single cluster, the polygon-centered tetrahedral cluster. Edges from each icosahedron, indicated by pairs of red-colored vertices, come together to form an equilateral triangle, a polygon, shown in brown in the upper left inset. The cluster is of D_{3h} point group symmetry and consists of 47 face-sharing tetrahedra. 39

2.5 Four filled icosahedra fused into a single cluster, the cell-centered tetrahedral cluster. Faces from each icosahedron, indicated by triangles of red-colored vertices, come together to form a tetrahedron, a cell, shown in brown in the upper left inset. The cluster is of T_d point group symmetry and consists of 57 face-sharing tetrahedra. 40
2.6 2-D (a) single filled-, (c) two edge-centered fused-, and (e) three polygon-centered fused-pentagons forming the projected shapes of a 3-D icosahedron projected down respectively a (b) vertex, (d) edge, and (f) face. 41
2.7 The (a) vertex-, (b) edge-, (c) polygon-, and (d) cell-centered projection of the 4D Platonic solid, the 600-cell. The figures divide the projected 600-cell into inner- and outer-shells shown respectively as polyhedra and ball-and-stick figures. Inner shell colors refer to colors used in Figures 3-6. (a) is the Bergman cluster. (d) is found in γ-brass. 42
2.8 The diffraction pattern of a single (a) 45-atom vertex-, (b) 44-atom edge-, (c) 50-atom polygon-, and (d) 54-atom cell-centered cluster shown down respectively an *II-II*, *CE-CE*, *ITr-ITr*, and *IT-IT* cluster edge. Pseudo-five-fold rotational symmetries are seen in each of these diffraction patterns as 10-fold pseudo-symmetric rosettes. 45
2.9 The diffraction pattern of a single 44-atom edge-centered cluster shown down its *PG-PG* cluster edge. Pseudo-five-fold symmetry is only somewhat recognizable. Interestingly, this diffraction pattern resembles the diffraction pattern of edge-centered cluster structures, shown in Figures 2.12 and 2.22, where pseudo-symmetry is more obviously present. 46
2.10 Site labeling scheme as well as representative edges for the inner shells of the different types of centered tetrahedral packing. First through fourth rows are for respectively vertex-, edge-, polygon-, and cell-centered clusters. First column: color-coded illustrations of the site labeling scheme (full site names given in text); second column: edges which correspond to pseudo-five-fold rotational axes; third column: together with the second column edges, the edges which correspond to the strongest diffraction peaks; and fourth column: the remaining edges whose corresponding diffraction peaks have significant, but not the strongest intensities. 47

2.11 The $Al_6Mg_{11}Zn_{11}$, $Mn_{10}Al_{29}$, $EuSr_2Mg_{13}$, and Pt_5Zn_{21} unit cells. Elements are color-coded. Mixed sites are denoted by the corresponding color mixtures: blue-green and green-red mixtures appear respectively as turquoise and brown. For each structure a single vertex-, edge-, polygon-, and cell-centered cluster is shown. The inner shell is represented as a filled polyhedron. Atoms at the centers of the polyhedra determine the colors of the polyhedral faces. Outer shell is shown in a ball-and-stick format. 50
2.12 Diffraction pattern for the cell-centered Pt_5Zn_{21}, polygon-centered $EuSr_2Mg_{13}$, and edge-centered $Mn_{10}Al_{29}$ crystals along the indicated directions. For $Mn_{10}Al_{29}$, the [0 1 0] and [0 0 1] directions correspond respectively to *CE-CE* and *PG-PG*. The latter pattern shows less-marked pseudo-five-fold symmetry but its relation to the former's pseudo-five-fold symmetry is evident. Cerius^2 Intensity Factors: 0.15 (Pt_5Zn_{21}); 0.04 ($EuSr_2Mg_{13}$); 0.04 ($Mn_{10}Al_{29}$, [0 1 0]); 0.05 ($Mn_{10}Al_{29}$, [0 0 1]) 52
2.13 Diffraction pattern for a cluster-centered 3.0 nm diameter spherical crystallite of the vertex-centered $Al_6Mg_{11}Zn_{11}$ structure shown along the [3 $\bar{5}$ 0] direction. Only peaks whose peak height is $\geq 0.27 \times$ the most intense peaks are shown. 54
2.14 The Mg_2Zn_{11} unit cell. Elements are color-coded and a single vertex-centered cluster is shown. Inner and outer shells are represented respectively in filled-polyhedron and ball-and-stick formats. The polyhedral faces are blue as a Zn atom lies at the cluster center. 56
2.15 The $Cd_2Cs_5Tl_{11}$, Cu_3Cd_{10} and $CdCu_2$ unit cells. Elements are color-coded. For each structure a single edge- or polygon-centered cluster is shown. The inner shell is represented as a filled polyhedron, whose face is colored according to the central site element type. Outer shell is shown in a ball-and-stick format. Cu_3Cd_{10} and $CdCu_2$ outer shells are incomplete: to aid the eye *OTr* or *HG* sites are joined by thin lines. Where necessary for clarity, the unit cell is therefore indicated with dotted lines. $CdCu_2$ has the $MgZn_2$ structure type. 57
2.16 Diffraction pattern for the edge-centered $Cd_2Cs_5Tl_{11}$ and polygon-centered $CdCu_2$ and Cu_3Cd_{10} crystals along the [1 0 0] direction. For the latter two crystals, pseudo-five-fold symmetry is clear, in the former system the pseudo-symmetry is less-marked. Less evident pseudo-symmetry is often found in tetrahedral-packed crystals with small unit cells. Cerius^2 Intensity Factors: 0.10 ($Cd_2Cs_5Tl_{11}$); 0.10 ($CdCu_2$); 0.04 (Cu_3Cd_{10}) . . . 58

2.17 Diffraction pattern for a cluster-centered 1.5 nm diameter spherical crystallite of the vertex-centered Mg_2Zn_{11} structure shown along the [3 $\bar{2}$ 0] direction. The weak intensity of the {2 1 3} reflection in this figure is the result of this reflection's considerable to distance from the plane normal to the [3 $\bar{2}$ 0] direction. Only peaks whose peak height is $\geq 0.10 \times$ the most intense peaks are shown. 59
2.18 The $AuYNi_4$ and Cu_5Cd_8 unit cells. Elements are color-coded. For each structure a single cell-centered cluster is shown. The inner shell is represented as a filled polyhedron, whose face is colored according to the central site element type. While Cu_5Cd_8 has the full outer shell, $AuYNi_4$ has only the *ExT* and *GrTt* outer-shell sites. The $AuYNi_4$ is related to the $MgCu_2$ structure type, where Au and Y lie in the latter's Mg sites. Cu_5Cd_8 has the γ-brass structure. 60
2.19 Diffraction pattern for cell-centered YNi_2, $AuYNi_4$ and $ScNi_2$ crystals along the [1 $\bar{1}$ 0] direction. All three structures are related to the $MgCu_2$ Laves structure. Pseudo-five-fold symmetry is clear in the first two structures but not the third. Cerius^2 Intensity Factors: 0.04 (YNi_2); 0.025 ($AuYNi_4$); 0.04 ($ScNi_2$). 61
2.20 Diffraction pattern for the γ-brass-type Cu_5Cd_8 along the [1 $\bar{1}$ 0] direction. Five-fold rotations applied to either the (330) and (411) peaks would result in a $(2\frac{1}{2}\,2\frac{1}{2}\,2\frac{1}{2})$ peak, a direction not permitted in diffraction. The disallowed $(2\frac{1}{2}\,2\frac{1}{2}\,2\frac{1}{2})$ location is shown as an open circle. Diffraction occurs instead at (222) and (332), the two closest locations where diffraction is symmetry allowed. Cerius^2 Intensity Factor: 0.45. 62
2.21 The vertex-centered $SiMn_6Pd_{23}Al_{70}$, edge-centered Pd_3Al_7, polygon-centered $MnAl_4$, and cell-centered Cd_3Cu_4 unit cells. Elements are color-coded. Mixed sites are denoted by the corresponding color mixtures: green-red mixtures appear as brown. Only a few of the possible tetrahedral clusters are shown. For $SiMn_6Pd_{23}Al_{70}$, the illustrated cluster contains both inner and outer shells; for the remaining cases only the inner shell is illustrated. Due to the large unit cell sizes, chosen here are clusters whose edges correspond to atoms spaced roughly τ further apart than regularly bonded metal atoms. 65

2.22 Diffraction pattern for the cell-centered Cd_3Cu_4, polygon-centered $MnAl_4$, and edge-centered Pd_3Al_7 crystals along the indicated directions. For Pd_3Al_7, the [0 0 1] and [0 1 0] directions correspond respectively to *CE-CE* and *PG-PG*. The latter pattern shows less-marked pseudo-five-fold symmetry but its relation to the former's pseudo-five-fold symmetry is evident. Cerius[2] Intensity Factors: 0.04 (Cd_3Cu_4); 0.06 ($MnAl_4$); 0.06 (Pd_3Al_7 [0 0 1]); 0.08 (Pd_3Al_7 [0 1 0]). 66
2.23 Diffraction pattern for a cluster-centered 3.0 nm diameter spherical crystallite of the vertex-centered $SiMn_6Pd_{23}Al_{70}$ structure shown along the [3 5 0] direction. Only peaks with intensity $\geq$ 0.29 $\times$ the strongest peak are shown. 67
2.24 Top row: 45-atom vertex-centered cluster from the $Al_6Mg_{11}Zn_{11}$ structure together with the planewave corresponding to an *II-II* edge . Bottom row: a 54-atom cell-centered cluster from the Pt_5Zn_{21} structures together with the planewave corresponding to an *IT-IT* edge. Inner and outer shells are color coded. *II* and *IT* sites are shown in red. Both planewaves exhibit strong constructive interference with the projected clusters. 68
2.25 The inner shell of a vertex-centered-projected reciprocal-space 600-cell using $SiMn_6Pd_{23}Al_{70}$ reciprocal space axes as coordinate basis. The strongest diffraction peaks for the $SiMn_6Pd_{23}Al_{70}$ crystal correspond to first and second nearest neighbor vectors derived from this reciprocal space cluster. See Table 1. 69
2.26 The three most central sites (*ITr*, *OTr*, and *OH*) of a cell-centered-projected reciprocal-space 600-cell using Cd_3Cu_4 reciprocal-space axes as coordinate basis. The strongest diffraction peaks for the Cd_3Cu_4 crystal correspond to first and second nearest neighbor vectors derived from this reciprocal-space cluster. See Table 2.2. 72
2.27 The four most central sites (*ITr*, *IL IPr*, and *OPr*) of a polygon-centered-projected reciprocal-space 600-cell using $MnAl_4$ reciprocal space axes as coordinate basis. The strongest diffraction peaks for the $MnAl_4$ crystal correspond to first and second nearest neighbor vectors derived from this reciprocal-space cluster. See Table 2.3. 75
2.28 The three most central sites (*CE*, *PG*, and *PPr*) of an edge-centered-projected reciprocal-space 600-cell using $Mn_{10}Al_{29}$ reciprocal-space axes as coordinate basis. The strongest diffraction peaks for the $Mn_{10}Al_{29}$ crystal correspond to first and second nearest neighbor vectors derived from this reciprocal-space cluster. See Table 2.4. 78

3.1 (a) Linear chain free electron energy as a function of k, the crystal momentum; (b) the "folded" format where k vectors belonging to the same linear chain irreducible representation are placed in the same vertical column; and (c) same energy bands in the presence of s and p orbital atoms. Band gap in (c) at $k = 0.5$ is caused by the difference in energy between the bonding p and the antibonding s orbitals. Note these $k = 0.5$ orbitals both correspond to plane-waves with wavelength $2a$ and are the result of the $k = 1$ Jones-mixing indicated by the red arrow in panel (a). 81
3.2 (a) The two lowest energy square lattice s and p bands from Γ, (0 0); to X, ($\frac{1}{2}$ 0); to M, ($\frac{1}{2}$ $\frac{1}{2}$). (b) The energies of the two lowest bands from M_1, ($\frac{1}{2}$ $\bar{\frac{1}{2}}$); through X; to M_2, ($\frac{1}{2}$ $\frac{1}{2}$). The separation between these two bands is due to Jones mixing. Band energies prior to mixing are shown as a dotted curve. (c) The square lattice first Brillouin zone, shown as a black square. Inscribed inside this square is a blue circle. Both the blue circle in (c) and the horizontal line in (b) denote the same electron count. Optimal electron filling based on Jones mixing is shown in red. Both panels (b) and (c) indicate for this optimal electron count that, from Z_1 to Z_2, a single band is filled, while nearer M_1 and M_2, no orbital is filled. The black square, which is also termed the Jones zone,[5] and the blue circle therefore provide upper and lower bounds for the optimal filling shown in red. 85
3.3 The face-centered-cubic Jones zone. The Jones zone is a truncated octahedron generated by the eight {1 1 1} and six {2 0 0} reflections. 88
3.4 The $Zn_{11}Au_{15}Cd_{23}$ unit cell. Elements are color-coded and a single vertex-centered cluster is shown. Inner and outer shells are represented respectively in filled-polyhedron and ball-and-stick formats. The polyhedral faces are green as a Au atom lies at the cluster center. 91
3.5 Diffraction pattern for a cluster-centered 3.1 nm diameter spherical crystallite of the vertex-centered $Zn_{11}Au_{15}Cd_{23}$ unit cell structure shown along the [3 5 0] direction. 819 atoms, 819/146 about 5.6 unit cells. Ratio: 0.27. 91

3.6 Vertex-centered reciprocal-space cluster and Jones zone for $Zn_{11}Au_{15}Cd_{23}$. The axes shown in the graph indicate relative directions only of the three reciprocal cell axes. $Zn_{11}Au_{15}Cd_{23}$ is a 1/1 quasicrystalline approximant. Its Jones zone differs significantly from the Jones zone presented previously for the 1/1 quasicrystalline approximant $Zn_{20}Al_{40}Mg_{40}$. The previously reported Jones zone is comprised of the {7 1 0}, {5 4 3}, and {5 5 0} reflections, with respective diffraction intensities of 23.0, 26.1, and 0.0%. Interestingly, the strongest intensity reflections for $Zn_{20}Al_{40}Mg_{40}$ are the {5 0 3}, {6 0 0}, and {5 3 2} reflections, with respective intensities of 100.0, 86.2, and 68.9%, the same three sets of reflections found in $Zn_{11}Au_{15}Cd_{23}$. In both structures the latter three reflections are the strongest, the second strongest, and the third strongest of all diffraction peaks up to CuKα_1 of 50°. 92

3.7 Cell-centered reciprocal-space cluster and Jones zone for Pt_5Zn_{21}. Colored cluster based on sites with reflection intensities ≥ 0.30 of the most intense reflection. Reflections are color-coded. The reflections are listed in descending order of intensity and cluster cylinder radii are proportional to intensity. See Table 7. The axes shown in the graph indicate relative directions only of the three reciprocal cell axes. Cluster and Jones zone are not to scale of each other. 97

3.8 Edge-centered reciprocal-space cluster and Jones zone for Pd_3Al_7. Colored cluster based on sites with reflection intensities ≥ 0.30 of the most intense reflection. Reflections are color-coded. The reflections are listed in descending order of intensity and cluster cylinder radii are proportional to intensity. See Table 8. The axes shown in the graph indicate relative directions only of the three reciprocal cell axes. Cluster and Jones zone are not to scale of each other. 100

3.9 The Cu-Cd binary phase diagram adapted from Massalski.[6] The four known stable Cu-Cd phases are color-coded, oxblood: $CdCu_2$; carnelian: Cd_3Cu_4; Spanish-yellow: Cu_5Cd_8; and fluorescent-chartreuse: Cu_3Cd_{10}. See Figure 3.14. 101

3.10 Polygon-centered reciprocal-space cluster and Jones zone for $CdCu_2$. Colored cluster based on sites with reflection intensities ≥ 0.30 of the most intense reflection. Only two of the five reflections which meet this criterion have large enough d_{hkl} values to actually appear in the Jones zone. These two reflections are color-coded. The reflections are listed in descending order of intensity. Cluster cylinder radii are proportional to intensity. Reflections are color-coded. See Table 3.5. The axes shown in the graph indicate relative directions only of the three reciprocal cell axes. Cluster and Jones zone are not to scale of each other. The pictured Jones zone is the same shape as that reported for AgZn elsewhere.[7] 105
3.11 Cell-centered reciprocal-space cluster and Jones zone for Cu_5Cd_8. Colored cluster based on sites with reflection intensities ≥ 0.30 of the most intense reflection. The reflections are listed in descending order of intensity and cluster cylinder radii are proportional to intensity. See Table 3.6. The axes shown in the graph indicate relative directions only of the three reciprocal cell axes. Cluster and Jones zone are not to scale of each other. 106
3.12 Cell-centered reciprocal-space cluster and Jones zone for Cd_3Cu_4. Colored cluster based on sites with reflection intensities ≥ 0.30 of the most intense reflection. Reflections are color-coded. The reflections are listed in descending order of intensity and cluster cylinder radii are proportional to intensity. See Table 2.2. The axes shown in the graph indicate relative directions only of the three reciprocal cell axes. Cluster and Jones zone are not to scale of each other. 107
3.13 Polygon-centered reciprocal-space cluster and Jones zone for Cu_3Cd_{10}. Colored cluster based on sites with reflection intensities ≥ 0.30 of the most intense reflection. Reflections are color-coded. The reflections are listed in descending order of intensity and cluster cylinder radii are proportional to intensity. See Table 3.7. The axes shown in the graph indicate relative directions only of the three reciprocal cell axes. Cluster and Jones zone are not to scale of each other. 108
3.14 The Jones zones of the four binary Cu-Cd phases in order of ascending cadmium content. Phases are color-coded. Oxblood: $CdCu_2$; carnelian: Cd_3Cu_4; Spanish-yellow: Cu_5Cd_8; and fluorescent-chartreuse: Cu_3Cd_{10}. Single Jones zones are plotted at the same e^-/a scale. Neighboring Jones zones show the more cadmium-rich Jones zone enveloping the less cadmium-rich phase. 109

4.1 Polygon-centered reciprocal-space cluster and Jones Zone for $RuZn_{10}$. Colored cluster based on sites with reflection intensities ≥ 0.15 of the most intense reflection. Reflections are color-coded. The reflections are listed in descending order of intensity and cluster cylinder radii are proportional to intensity. See Table 4.2. The axes shown on the graph indicate relative directions only of the three reciprocal axes. Cluster and Jones zone are not to scale of each other. 115
4.2 A reproduction of Figure 1.21. The light blue region represents the upper and lower limits on e^-/a (1.46-1.74 valence e^-/a). The cyan lines correspond to experimental Ru sites, and the grey lines to Zn. The electron counts from Fermi spheres corresponding to the strongest diffraction peaks are also shown (their colors correspond to Figure 4.1.) 118

A.1 The arrangement of clusters in the crystal structure of $Au_{10}Cr_4Zn_{89}$ along the body diagonal, clusters are centered about the high symmetry points of the F-centered cubic unit cell and their identities are specified. The clusters are represented by idealized cuboctahedral shells. Zinc atoms are shown in gray, chromium in lime and gold in orange. 122
A.2 Total density of states of $Au_{10}Cr_4Zn_{89}$. The first two large peaks are due to the Zn and Au d-orbitals respectively. Also note the pseudo-gap formation at the Fermi energy. The vertical axis is given in units of states per valence electron so that the DOS plot is comparable between systems with different sized unit cells. . . 124
A.3 Partial DOS of projected d-states for (from top to bottom) Au, Cr, and Zn respectively. All plots are truncated vertically so that we can see the structure near the Fermi level. The Cr plot (middle) clearly shows the d-states are split at the Fermi level. Note the difference in scale reflecting the relative quantities of Au, Cr, and Zn. 125

C.1 Plaque installed in 1958 to commemorate Hamilton's 1843 discovery of the quaternions. Used under the Creative Commons Attribution-Share Alike 2.0 Generic license.[8] 140
C.2 Rotation in 2D, 3D, and 4D corresponding to Equations C.8, C.9, and C.12, respectively. The axes of rotation are in red. In the 4D rotation, the axes of rotation for each hyperplane lie in the orthogonal hyperplane. 145

C.3 Geometry of the trigonal bipyramid in 4D and 3D. τ is the Golden Ratio: $\tau = (1 + \sqrt{5})/2$. The three gold spheres represent the vertices of the preserved equilateral triangle (ITr), which is regular in 4D and in 3D and lie in the σ mirror plane of the D_{3h} cluster. These three points all lie in the mirror plane. The two green spheres are the axial vertices (IL), and specify the C_3 axis of the D_{3h} cluster. In the 600-cell, these points are positioned such that the two tetrahedra are regular. In 3D this need not be the case: mirror plane symmetry is preserved for any h, thus we are free to choose h in specifying our projection. 165

D.1 Difference in average projected distances 177

D.2 Bader Charge Analysis of electron gain and loss. Results taken from the Supplemental Information of Dshemuchadse *et al*[2] . . . 178

CHAPTER 1

THE $IR_XRU_{1-X}ZN_{10}$ ($0.1 \leq X \leq 0.4$) SYSTEM

1.1 Introduction

Armed with an understanding of the structure of simple molecules such as methane, carbon dioxide, or N_2, why can't we deduce the three-dimensional structure of a protein?* Somewhere along the road from simple to complex, something robs our chemical rationalizations of their predictive power. A look at metallic crystal structures and one sees a similar problem. A "metallic structure" typically brings to mind one of the face-centered cubic (fcc), body-centered cubic (bcc), or hexagonal closest packing (hcp) structure types, and for good reason: all the allotropic structures of the first and second row transition metals–as well as all the alkali and alkaline earth metals–adopt one of these structures under normal conditions.

Start combining elements and more complicated structures emerge: face-centered Laves phases $MgCu_2$ [10,11] and Be_5Au [12] each with 24 atoms in their unit cells; body-centered Cu_5Zn_8 (γ-brass) with 54 atoms;[13–15] and face-centered Ti_2Ni with 96 atoms.[16] These are the carbohydrates of intermetallics: while some parts of their substructures are comprehensible, no one could claim to be able to predict their entire ground state structures from just stoichiometry and thermodynamic conditions; at least not without some computer-assisted guesswork.[17,18]

Intermetallic phases involving Zn are particularly compelling in their struc-

*There has been considerable progress in predicting some features of protein structures computationally.[9]

tural choices: combining each late first-row transition metal with Zn gives a complicated and wildly different structure: hexagonal $FeZn_{10}$ [3] (>500 atoms in the unit cell); cubic $Fe_{11}Zn_{39}$ [19] (408 atoms); incommensurate monoclinic $CoZn_{7.8}$ [20] (60 atoms); orthorhombic $NiZn_3$ [21] (276 atoms); and Cu-Zn phases ranging from the ubiquitous cubic Cu_5Zn_8 to hexagonal/trigonal structures with cell axes up to 160.5 and 2000 Å, respectively[22–24] (each with thousands of atoms in their unit cells). Dozens of twelve, fourteen, fifteen, and sixteen-coordinated sites vie for neighbors in a concerted but frustrated quest for stability. Out of the struggle, puzzling but beautiful structural motifs emerge. In terms of complexity, these phases are the proteins of metallurgy.

What triggers this explosion of complexity? Do we have any hope of gaining a foothold in understanding these complex structures? To understand the structural stability in a complex molecule, we might look for stable shells of electrons corresponding to an energy gap in the electron filling: a larger gap between the LUMO and HUMO indicating more stability. Familiar electron counting rules – from the octet rule[25,26] and 18-electron rule,[27] to the Hückel rules for aromatics[28–30] and the Wade-Mingos rules for polyhedral clusters[31,32]-all follow this principle. In complex intermetallics, one can use a similar viewpoint and look for a pseudogap in the density of states plot. The classic theory to explain pseudogap formation is due to Mott and Jones, who devised a semi-empirical nearly-free electron picture of electronic structure in intermetallics in the 1930s.[5,33] In the Mott and Jones picture, the electrons are in nearly-free electron waves where the crystal potential, and therefore the pseudogap, is determined from the intensity of the Bragg peaks in the single-crystal X-ray diffraction experiment.

We can experimentally control the intensity of the peaks by partial substitu-

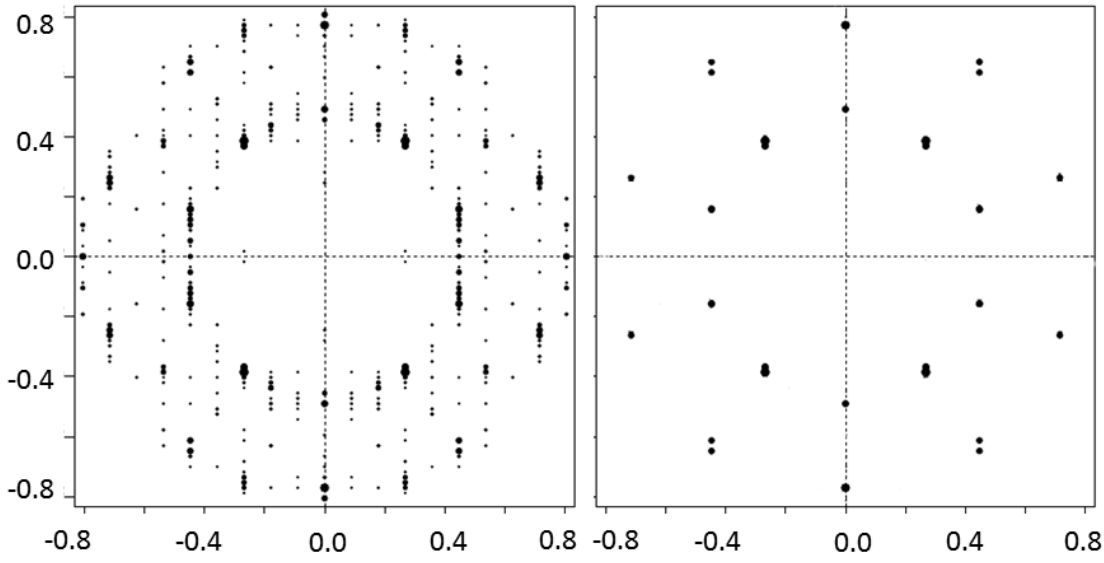

Figure 1.1: Simulated diffraction pattern for $Ir_xRu_{1-x}Zn_{10}$ in the [100] direction from $0 < 2\theta < 80$ for $x = 0$. All peaks are shown on the left, and only the strongest are shown on the right to highlight the pseudo five-fold diffraction pattern.

tion of a heavier atomic species for a lighter one. In the subject of this chapter, the hexagonal $Ir_xRu_{1-x}Zn_{10}$ family of structures, the substitution of Ir for Ru alters the intensity of certain Bragg peaks. We investigate the structure and composition of $Ir_xRu_{1-x}Zn_{10}$ for several x, using single-crystal structure determination (SCSD) and energy-dispersive X-ray spectroscopy (EDX). We will provide a structural description and a rationalization for the site preferences using chemically transparent computational techniques. In later chapters, we will study the link between Bragg peak intensity and structural stability via the Mott and Jones model.

$Ir_xRu_{1-x}Zn_{10}$ also exhibits clear pseudo five-fold diffraction in the [100] direction (Figure 1.1). This characteristic has recently been linked to site preferences and stability of large cubic structures.[34] In particular, past electronic

structure calculations have revealed a link between pseudogap formation and pseudo five-fold diffraction.[35] However, as we will show, the pseudo five-fold diffraction pattern in $Ir_xRu_{1-x}Zn_{10}$ is not related to the tetrahedral atomic clusters found in those cubic structures, nor the icosahedral symmetry of quasicrystals. In later chapters, we will investigate the significance of the pseudo five-fold diffraction pattern and its connection to the overall stability of $Ir_xRu_{1-x}Zn_{10}$ and many other intermetallic compounds.

1.2 Experimental Details

1.2.1 Synthesis

All samples were prepared at nominal composition ($Ir_xRu_{1-x}Zn_{10}$, x = 0.1, 0.2, 0.3, 0.4) from Ir powder (Degussa, 99.99% purity), Ru powder (Degussa, 99.9% purity), and Zn shot (Chempur 99.999% purity). They were sealed in silica tubes under vacuum. Samples were heated from room temperature to 1110° C over 5h and held at 1110° C for 2h before being allowed to cool to 430° C, just below the melting point of Zn. The samples were then allowed to sinter at this temperature for 4 days. The tubes were opened and the product was cracked in a mortar and pestle. Half of each sample was ground up for powder diffraction measurements, and the other half was searched for single crystals suitable for single-crystal diffraction.

1.2.2 Powder Diffraction

Powder diffraction patterns were taken for phase verification. All measurements were done on a Philips X'PERT MPD powder diffractometer [31] using Cu Kα radiation (λ = 1.54Å). For the four nominal compositions $Ir_xRu_{1-x}Zn_{10}$, x = 0.1, 0.2, 0.3, 0.4, the following settings were used: for x = 0.1, 0.2, 0.3, a step size of 0.026° 2θ was used; for x = 0.44, 0.039° 2θ. For x = 0.2 and x = 0.3, a time per step of 49.47s was used; for x = 0.1, 39.27s; for x = 0.4, 97.92s.

1.2.3 Energy-dispersive X-ray spectroscopy (EDX)

A scanning electron microscope (CS-4DV, CAM Scan 20 kV) equipped with a SiLi detector (Thermo Noran Instruments, Pt-L, Zn-L) was used to perform EDX measurements. The Voyager program[36] from Thermo Noran was used for analyzing the spectral peaks and computing the composition. Several crystals from each nominal composition were tested. When possible, the single crystal used for single-crystal structure determination was also analyzed with the microprobe.

1.2.4 Single-Crystal structure determination (SCSD)

Single-crystal data were collected with the Stoe Image Plate Diffraction System (IPDS-II) with monochromated Mo Kα radiation (λ = 0.71 Å) at 100K. The Stoe program suite[37] was used for data collection, finding cell dimensions and integration. Numerical absorption correction was performed using the X-SHAPE

and X-RED programs.[38,39] Structure refinement was performed using SHELX-97[40] starting from the refined structure of $RuZn_{10}$.[4]

1.3 Results

Powder data is shown in Figure 1.2. All compositions have nearly identical powder patterns. A subtle upward shift in 2θ as Ir is added is visible in the largest set of peaks, around $2\theta = 42^\circ$. The powder patterns nevertheless strongly suggest all the studied phases are largely isostructual.

The final, refined atomic coordinates are available in Appendices B.1 and B.2. We supposed that $Ir_xRu_{1-x}Zn_{10}$ is structurally similar to the compounds $FeZn_{10}$[3] and $RuZn_{10}$.[4] Initial isotropic refinement of $Ir_{0.3}Ru_{0.7}Zn_{10}$ against $RuZn_{10}$ coordinates give $R_1 = 9.55\%$. Immediately, there are clues as to the whereabouts of Ir: sites M20 and M21, which are Ru/Zn mixed sites in $RuZn_{10}$, become overoccupied with Ru. Ru09, a fully occupied Ru site in $RuZn_{10}$, refines to a very low thermal parameter ($U_{iso} = 0.006$). Changing these three sites to Ir/Ru mixed sites leads to reasonable occupancies and thermal parameters, and dramatically improves the model ($R_1 = 8.31\%$). The site Zn47′ was removed due to vanishingly small occupancy and thermal parameter. Ru37, a partially occupied (0.69) site in $RuZn_{10}$, is slightly more Ru rich in $Ir_3Ru_7Zn_{100}$, refining to 0.911 occupancy. Refining this site as partially occupied Ir does not improve the R_1 value, so we leave it as partially occupied Ru.

Now we turn to the disordered sites, Zn39-Zn43. The refined occupancies were reasonable but the thermal parameters were not. All the disordered sites coordinate to the partially occupied Ru37 site. As in the works of Belin & Be-

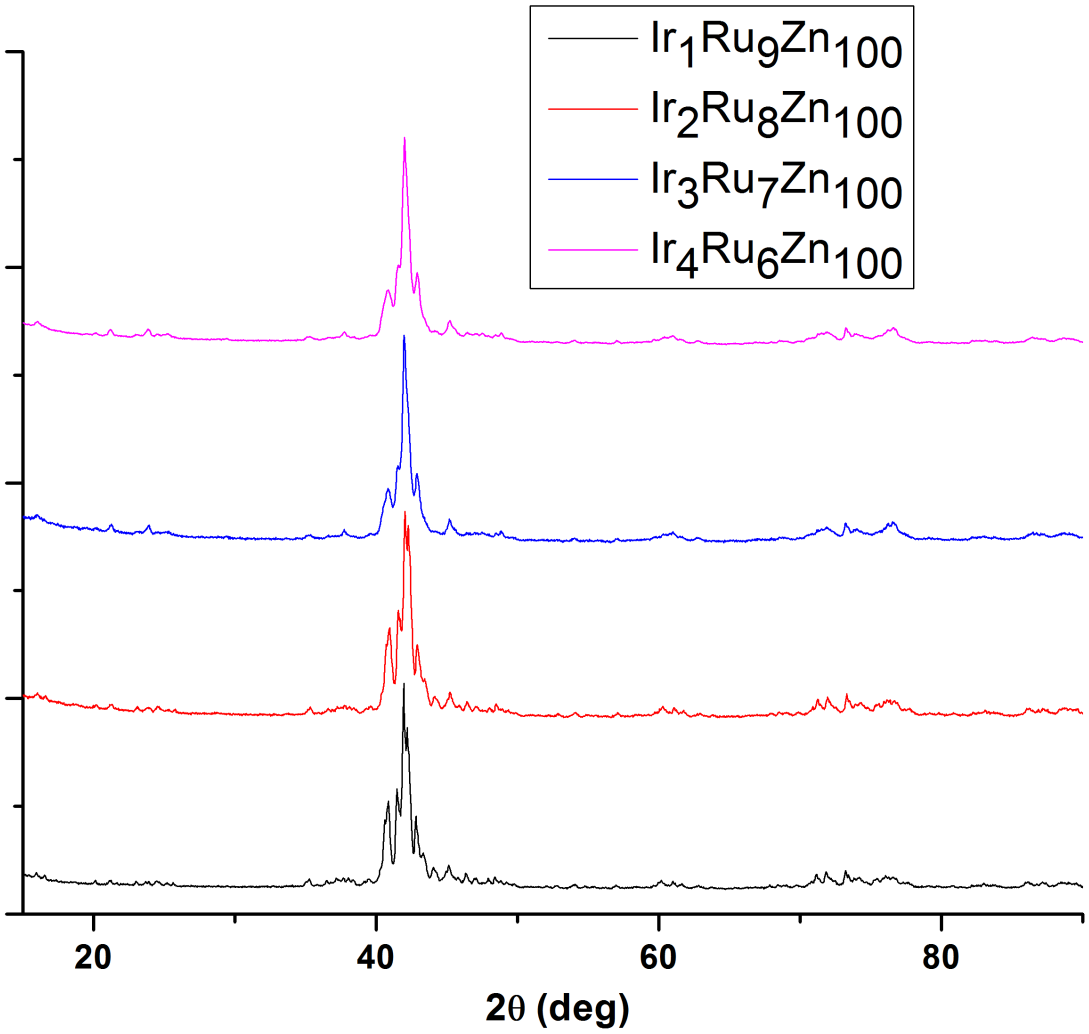

Figure 1.2: Powder diffraction patterns for compounds with nominal compositions $Ir_xRu_{10-x}Zn_{100}$. The intensity scale is normalized to the highest peak from each run.

lin[3] and Allio,[4] the sum of the occupancies is roughly 12, indicating icosahedral coordination. To solve this problem, we first restrained the thermal parameters of a group of disordered sites (for instance, Zn40, Zn40′ and Zn40″) to be the same, and allowed the occupations to refine, subject to the constraint of icosahedral coordination for Ru37 (Figure 1.3). Then, with the refined occupations fixed, the thermal parameters were allowed to refine individually.

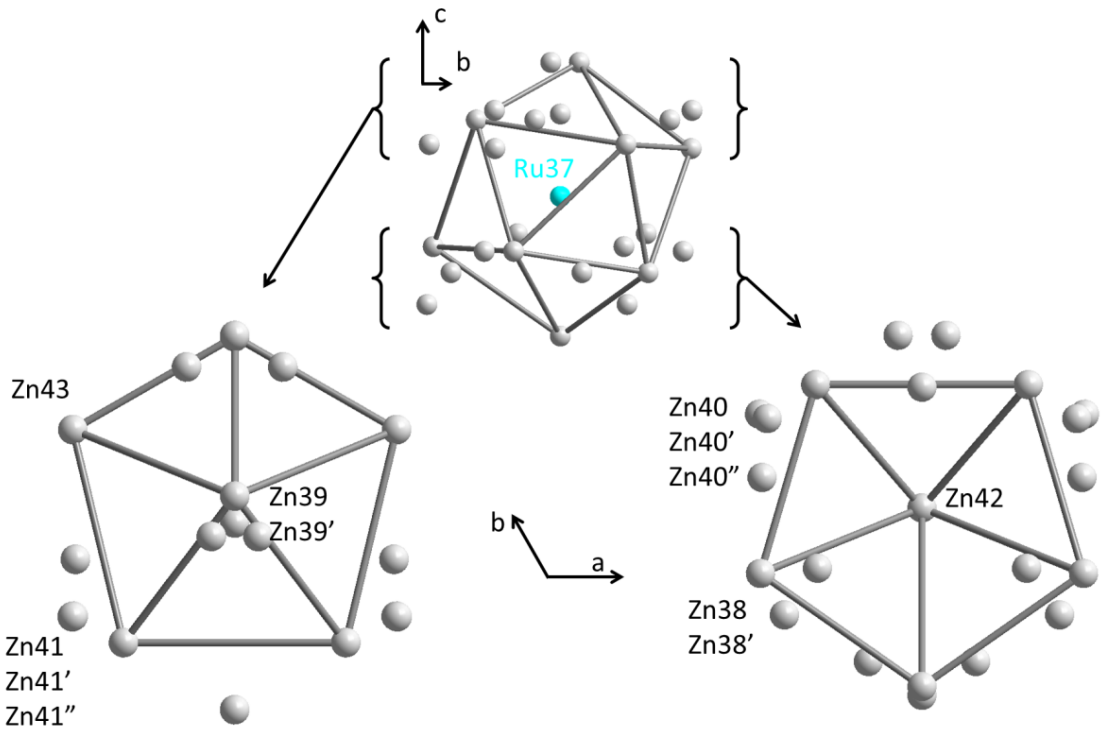

Figure 1.3: Arrangement of disordered sites around the partially occupied Ru37 site. As in Belin & Belin[3] and Allio's[4] work, we consider the disordered sites as one of three randomly oriented icosahedra (one particular orientation is shown here by the grey lines). During the refinement of the occupation, the following constraints were used: the axial Zn39 and Zn42 groups were constrained to an occupancy of 1. The Zn40 and Zn41 groups were also constrained to a total occupancy of 1. The Zn43 and Zn38 groups were constrained to an occupancy of $\frac{2}{3}$. In this way, an average total occupation of 12 sites coordinating to Ru37 is ensured.

Finally, the entire structure was refined anisotropically. For $Ir_{0.2}Ru_{0.8}Zn_{10}$, some disordered sites were kept isotropic in the final structure. The results are shown in Table 1.1. Refinement of cell parameters proved difficult, likely because of closely overlapping peaks due to the long c-axis. Since our aim is primarily to study the substitutional behavior of Ir in the $RuZn_{10}$ crystal structure, very exact determination of the cell parameters is of secondary importance.

Therefore, we gleam the cell parameters from the single crystal results.

Table 1.1: Crystallographic information and R-values for $Ir_2Ru_7Zn_{100}$ and $Ir_3Ru_7Zn_{100}$

Nominal formula	$Ir_2Ru_8Zn_{100}$	$Ir_3Ru_7Zn_{100}$
Empirical formula	$Ir_{1.35}Ru_{9.81}Zn_{100.08}$	$Ir_{2.90}Ru_{8.23}Zn_{100.23}$
Formula weight	7793.47	7941.07
Temperature	293(2) K	293(2) K
Wavelength	0.71073 Å	0.71073 Å
Crystal system	hexagonal	hexagonal
Space group	$P6_3/mmc$	$P6_3/mmc$
Unit cell dimensions	a = 12.8872(18) Å c = 57.437(12) Å	a = 12.900(6) Å c = 57.06(2) Å
Volume	8261(2) $Å^3$	8223(6) $Å^3$
Z	5	5
Density (calculated)	7.833 Mg/m^3	8.018 Mg/m^3
Absorption coefficient	40.362 mm^{-1}	43.376 mm^{-1}
F(000)	17691	17961
Crystal size	0.15 x 0.25 x 0.1 mm^3	0.2 x 0.15 x 0.1 mm^3
θ range for data collection	4.42 to 32.50°	4.42 to 30.00°
Index ranges	$-17 \leq h \leq 13$, $-13 \leq k \leq 18$, $-42 \leq l \leq 81$	$-18 \leq h \leq 17$, $-17 \leq k \leq 15$, $-30 \leq l \leq 74$
Reflections collected	38918	30452
Independent reflections	5547 [R_{int} = 0.1853]	4459 [R_{int} = 0.1130]
Completeness	98.50%	98.00%
Refinement method	Full-matrix least-squares on F^2	Full-matrix least-squares on F^2
Data / restraints / parameters	5547 / 5 / 332	4459 / 5 / 340
Goodness-of-fit on F2	0.774	1.25
Final R indices [$I > 2\sigma(I)$]	R_1 = 0.0634, wR_2 = 0.1418	R_1 = 0.0709, wR_2 = 0.1854
R indices (all data)	R_1 = 0.1582, wR_2 = 0.1971	R_1 = 0.0933, wR_2 = 0.1977
Largest diff. peak and hole	2.779 and -2.138 $e/Å^{-3}$	5.644 and -3.639 $e/Å^{-3}$

By virtue of its crystallographic R-factors, $Ir_{0.3}Ru_{0.7}Zn_{10}$ appears to be a better-refined solution. The refined compositions for $Ir_{0.2}Ru_{0.8}Zn_{10}$ and $Ir_{0.3}Ru_{0.7}Zn_{10}$ are shown along with the microprobe measurements in Figure 1.4.

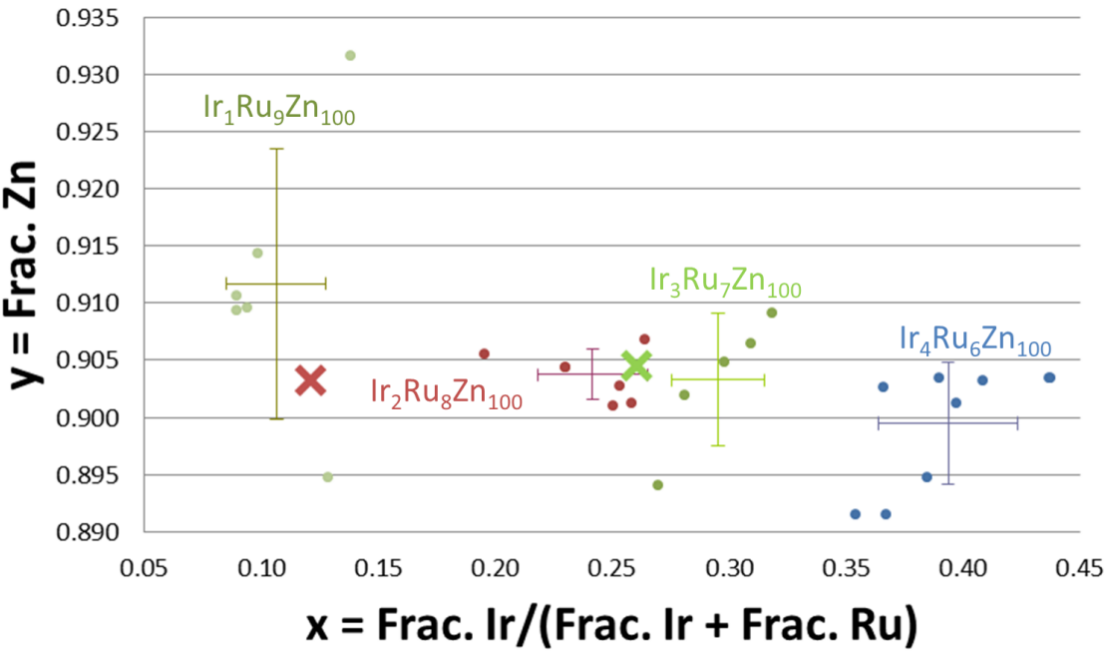

Figure 1.4: Empirical composition. x = Atomic % Ir / (Atomic % Ir + Atomic % Ru), y = Atomic % Zn. The points are the individual EDX measurements, and the bars are the standard deviations in x and y from those measurements. The "X"s mark the composition determined via single crystal refinement for nominal compositions $Ir_2Ru_8Zn_{100}$ and $Ir_3Ru_7Zn_{100}$.

We see that $Ir_{0.3}Ru_{0.7}Zn_{10}$ agrees reasonably well with the composition measured by EDX. However, the refined composition of $Ir_{0.2}Ru_{0.8}Zn_{10}$ is very Ir-poor when compared to the composition determined from microprobe measurements. Figure 1.4 suggests the Zn composition is nearly correct, so one of the fully-occupied Ru sites must be a mixed Ru/Ir sites. Allowing the composition of any of the sites to refine as a mixture, however, invariably tends to >98% Ru. Additionally, as mentioned above, the thermal parameters of all the pure Ru sites are all quite reasonable.

In the proceeding discussion, we will use the atomic coordinates and composition found in the $Ir_{0.3}Ru_{0.7}Zn_{10}$ refinement.

1.4 Origin of the pseudo five-fold diffraction pattern

To explain the structural origin of the pseudo five-fold diffraction pattern of $Ir_xRu_{1-x}Zn_{10}$, we look to the simpler structure of Al_5Co_2.[41,42] Like $Ir_xRu_{1-x}Zn_{10}$, Al_5Co_2 crystallizes in space group no. 194 (Hermann-Mauguin symbol $P6_3/mmc$). Calculations on Al_5Co_2 have shown pseudogap formation at the Fermi level and essentially filled Co 3*d*-states but highly delocalized Al 3*p*-states, as well as charge transfer from Al to Co and evidence of covalent and metallic-type bonding.[43]

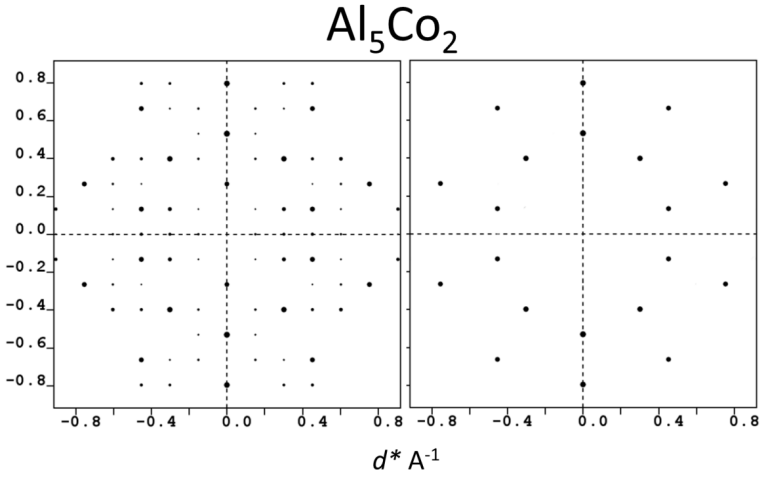

Figure 1.5: Simulated diffraction pattern for Al_5Co_2 in the [100] direction from $0 < 2\theta < 80$. All peaks are shown on the left; only the strongest are shown on the right to highlight the pseudo five-fold diffraction pattern.

Al_5Co_2 exhibits pseudo five-fold diffraction in the [100] direction, seen in Figure 1.5. To understand the geometrical real-space source of the diffraction pattern, we examine the atomic structure of Al_5Co_2. It is comprised almost entirely of one type of cluster of D_{3h} symmetry which we will call simply the D_{3h} cluster. A construction of the 23-atom D_{3h} cluster as interpenetrating icosahedra in the context of Al_5Co_2 is shown in Figure 1.6. A perspective view of the newly

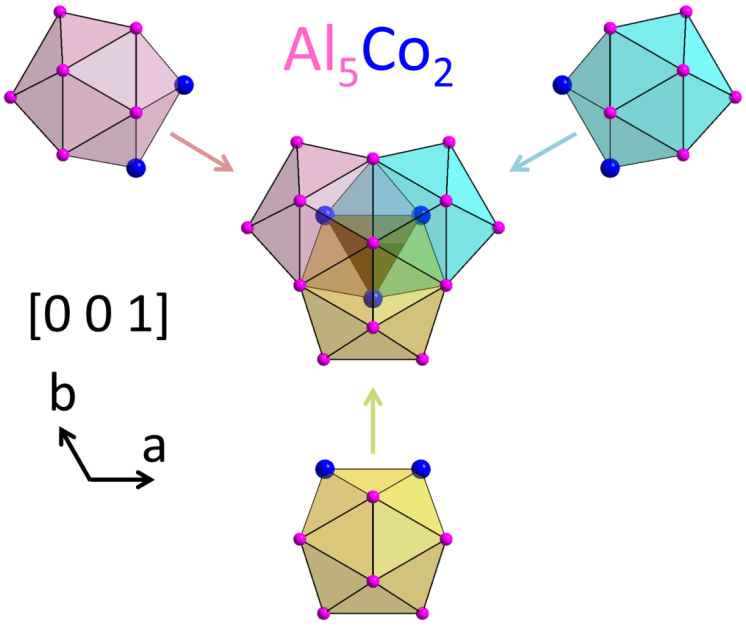

Figure 1.6: Construction of the D_{3h} cluster as a set of three mutually penetrating icosahedra. Each icosahedron contains an edge of Co atoms (dark blue) which are the center atoms of the remaining two icosahedra. The dark triangle in the center is the overlapping region, whose vertices form the region of overlap between all three icosahedra.

assembled D_{3h} cluster from 1.6 is shown in Figure 1.7.

The overlapping region in Figure 1.7 will be of crucial importance in later chapters when we to unite the D_{3h} cluster with atomic clusters of different symmetries. For now, we simply describe its geometry. The atoms which form the vertices of the overlapping region are in a trigonal bipyramidal arrangement, shown in Figure 1.8.

Looking at the completed D_{3h} cluster in the [100] direction (Figure 1.9) the source of pseudo five-fold symmetry is clear: we are looking down the "five-fold" axis of two of the three fused icosahedra (and the two-fold axis of the remaining icosahedra). The D_{3h} cluster accounts for all the atomic positions in

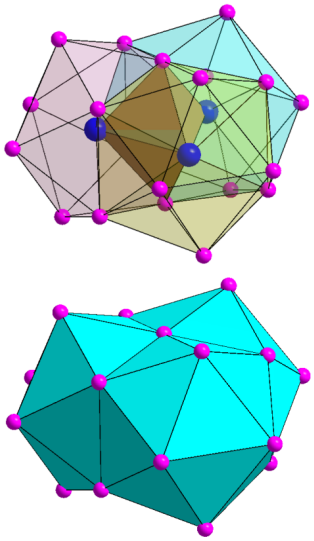

Figure 1.7: Top: Perspective view of D_{3h} cluster from Figure 1.6. The overlapping region can be seen in brown in the center. Bottom: Perspective view of D_{3h} cluster with the icosahedra filled.

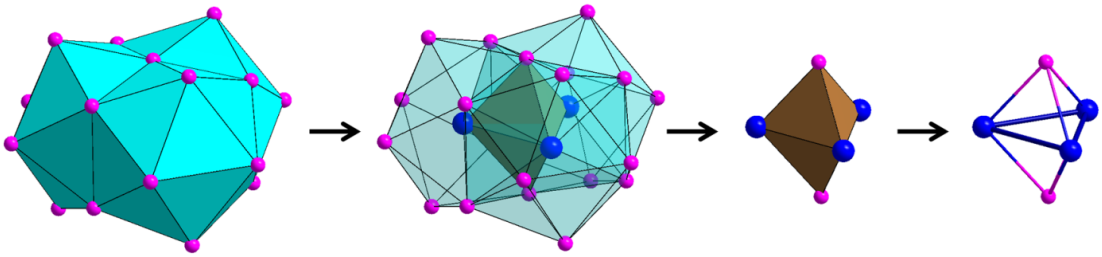

Figure 1.8: Structure of the overlapping region. Clockwise from top left: the D_{3h} cluster as shown in 1.7, followed by the D_{3h} cluster made transparent to emphasize the region where the three icosahedra intersect. Next, the overlapping volume by itself and finally, the same region without faces. The overlapping volume is a trigonal bipyramid.

the unit cell except for one Co site which acts as a geometrical "glue" between the D_{3h} clusters in such a way that it creates more tetrahedra (Figure 1.10). Recent work by Ormeci and Grin[43] demonstrates that the interstitial Co is essentially covalently (two-center) bonded to its six nearest neighbor Al, while the Co

atoms within the clusters are more metallic (many-center) bonded. In this sense, the interstitial Co may be thought of as the chemical as well as geometrical glue holding the D_{3h} clusters together.

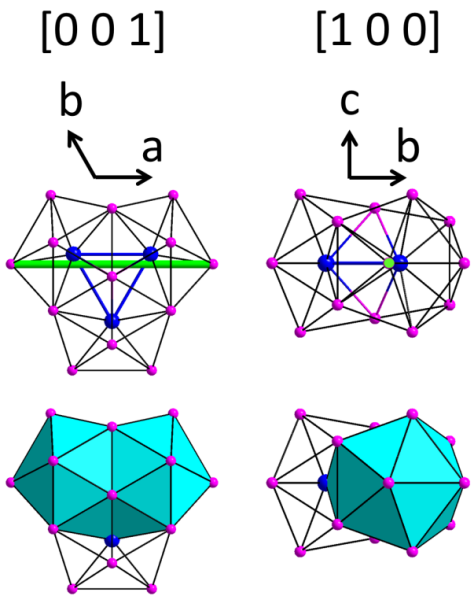

Figure 1.9: A pseudo five-fold axis of a D_{3h} cluster, shown as the green bar. Note that the pseudo five-fold axis is parallel to a Co-Co edge of the overlapping volume. The bottom pair of illustrations show how two of the three fused icosahedra join to enhance pseudo five-fold symmetry.

The stacking of D_{3h} clusters and interstitial Co forming the extended structure of Al_5Co_2 is shown in Figure 1.11. The "five-fold" axes of many distorted icosahedra are plainly visible in the [100] direction. It comes as no surprise that the diffraction pattern in the [100] diffraction plane exhibits pseudo five-fold symmetry (Figure 1.5).

If the intensity of the Bragg peaks in the pseudo five-fold symmetric pattern is linked to pseudogap formation and hence stability, as shown by Berger et al.,[35] it would be useful to know how altering the composition of the structure affects the intensity of those peaks in preparation for our substitutional study of

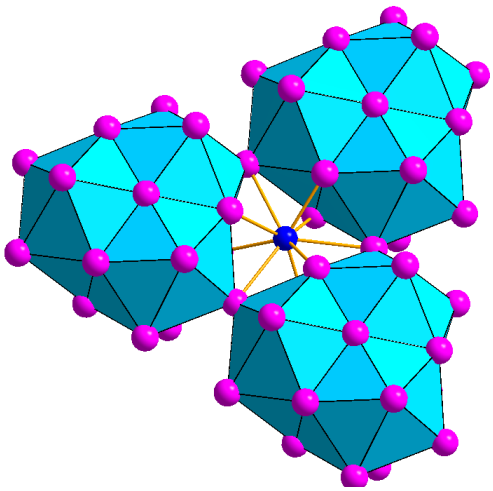

Figure 1.10: The single Co site not contained in the D_{3h} cluster sits in the cluster interstices. The gold lines are chosen to highlight the coordination geometry of the central Co and emphasize newly formed tetrahedra.

$Ir_xRu_{10-x}Zn_{100}$.

The phase of the plane waves corresponding to the Bragg peaks in the pseudo five-fold diffraction pattern can easily be chosen so that all the heavier (more scattering) Co lie near crests 1.12. The origin of the pseudo five-fold diffraction pattern is more obvious when we look at how the plane waves interact with the atoms in the D_{3h} cluster, shown in Figure 1.13.

Replacing Co with more powerful scatterers, then, will undoubtedly enhance the Bragg peaks comprising the pseudo five-fold diffraction pattern. Such a structure, Al_5Rh_2, has been solved.[44] In Al_5Rh_2, Rh directly replaces Co. The diffraction patterns of Al_5Co_2 and Al_5Rh_2 are shown side-by-side in Figure 1.14. While the peaks of the pseudo five-fold diffraction are indeed enhanced, other peaks become at least as prominent, and in some cases more prominent, than peaks in the pseudo five-fold rings.

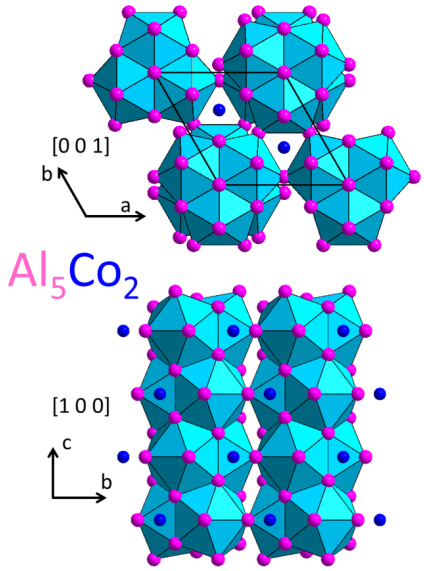

Figure 1.11: View of D_{3h} clusters and interstitial Co atoms down the [001] and [100] directions.

The [100] diffraction pattern of for Al_5Co_2 (Figure 1.5) resembles that of $Ir_xRu_{10-x}Zn_{100}$ (Figure 1.1). To explain these similarities, we first search in $Ir_xRu_{10-x}Zn_{100}$ for D_{3h} clusters, preferably including many of the heavier Ir and Ru sites. Heavier atomic sites on the D_{3h} clusters should increase the strength of the pseudo five-fold diffraction peaks by putting heavier scatterers on their nearly five-fold axes.

Such clusters are shown in Figure 1.15. Note the similarities to the arrangements of D_{3h} clusters in $Ir_xRu_{10-x}Zn_{100}$ (Figure 1.15) to those of Al_5Co_2 (Figure 1.11). In each case, consecutive layers of clusters are rotated 60° with respect to one another. Nearly five-fold axes of the D_{3h} clusters are visible in the [100] direction in both structures. While D_{3h} clusters in Al_5Co_2 neatly interlock in the c-direction, those in $Ir_xRu_{1-x}Zn_{10}$ are well separated and staggered.

The most important difference between the D_{3h} clusters in $Ir_xRu_{1-x}Zn_{10}$, in contrast to those in Al_5Co_2, is size: the fused icosahedra in the Al_5Co_2 D_{3h} clus-

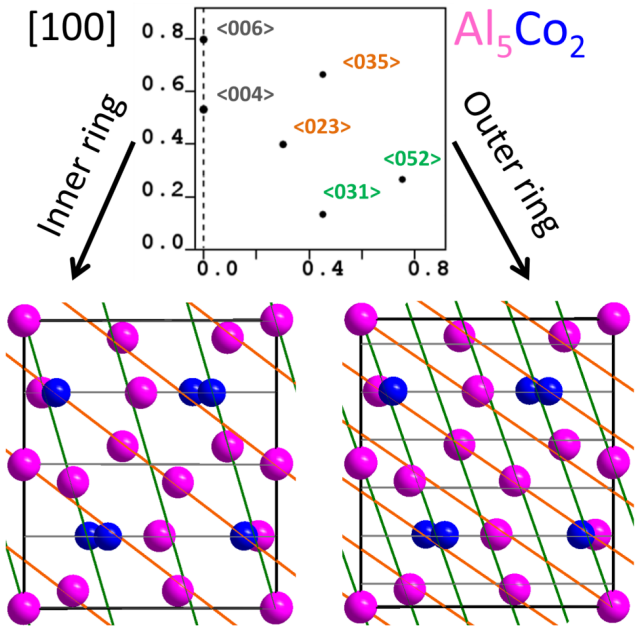

Figure 1.12: Families of plane waves corresponding to Bragg peaks in the pseudo five-fold diffraction pattern of Al_5Co_2. Only the first quadrant of the [100] diffraction pattern (Figure 1.5) is shown. The parallel colored lines superimposed over the structural pictures correspond to plane waves labeled with the same color in the diffraction pattern. The left picture corresponds to the inner ring of peaks in Figure 1.5, and the right picture corresponds to the outer ring of peaks. Note that every Co atom lies on or near a crest of all six plane waves.

ters are essentially the coordination icosahedra of the central Co atoms, and the edges of the icosahedra actually connect nearest-neighbors. In the D_{3h} clusters of $Ir_xRu_{1-x}Zn_{10}$, the vertices of the icosahedra shown are between 5 and 5.6 Å from the central atom; about twice the interatomic bond distance of metallic Zn.[45]

We would like to see if the plane waves corresponding to the peaks in the pseudo five-fold diffraction pattern interact with the D_{3h} clusters in $Ir_xRu_{1-x}Zn_{10}$ in a similar way to the analogous plane waves in Al_5Co_2. This is shown for $Ir_xRu_{1-x}Zn_{10}$ in 1.16. Figure 1.16 should be compared directly to 1.13. The near

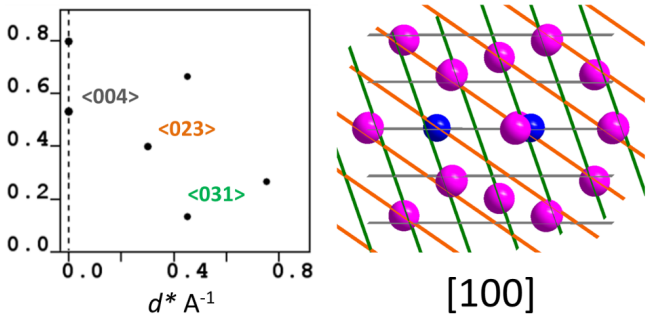

Figure 1.13: Interaction of the crests of plane waves from the inner ring of the pseudo five-fold diffraction pattern with the atoms of the D_{3h} cluster.

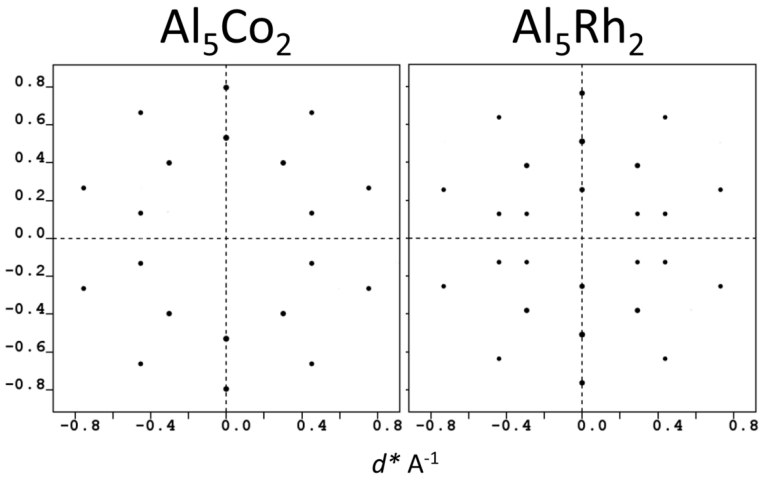

Figure 1.14: Simulated diffraction pattern for Al_5Co_2 and Al_5Rh_2 in the [100] direction from $0 < 2\theta < 80$. All peaks are shown on the left, and only the strongest are shown on the right to highlight the pseudo five-fold diffraction pattern.

five-fold symmetry is even more striking when we add the atoms inside the D_{3h} clusters, shown in Figure 1.17.

The intensities of the most intense peaks in the simulated *powder* pattern for each of the three structures–$RuZn_{10}$ and the two solved ternaries–are shown in Table 1.2. Here, intensities are expressed as a percentage of the most intense peak. First we note two very intense peaks–(3 2 14) and (3 2 15)–which are not

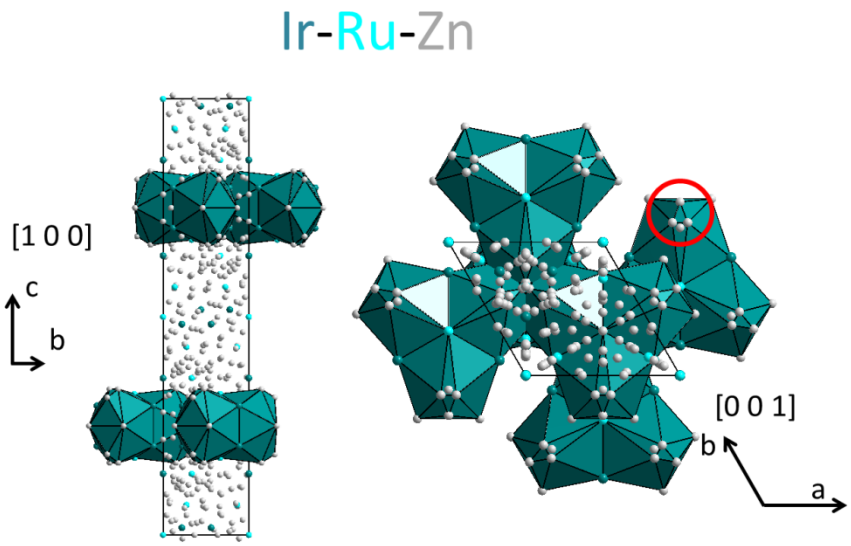

Figure 1.15: D_{3h} clusters in $Ir_xRu_{1-x}Zn_{10}$. All Ir sites are mixed with Ru or Zn, but all heavy atoms in the D_{3h} clusters are Ru or Ru/Ir. There is some interpenetration among neighboring D_{3h} clusters which can be seen in the [001] view. The center of each of the three fused icosahedra forming each D_{3h} cluster is an Ir/Ru mixed site. One 'vertex' of each D_{3h} cluster icosahedron is actually 4 partially occupied disordered Zn sites, highlighted by the red circle.

present in the pseudo five-fold diffraction ring. Second, we notice that only the second most intense peak–(3 0 22)–becomes noticeably more intense. Both of these issues can be understood in terms of the theory developed in forthcoming Chapters 2 and 3. We will revisit $Ir_xRu_{1-x}Zn_{10}$ specifically in Chapter 4.

1.5 Electron Counting and Site Preferences

As early as the 1930s, Hume-Rothery observed that some crystals are isostructural at certain valence electron counts, even when composed from very different elements.[46,47] Under the Hume-Rothery scheme, stability appears to be driven by electron count independent of the identity of the elements. In partic-

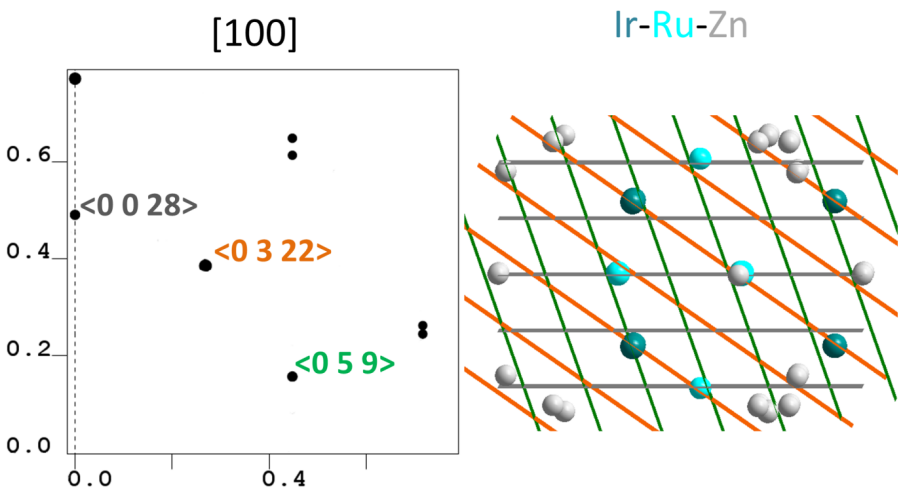

Figure 1.16: Families of plane waves corresponding to Bragg peaks in the pseudo five-fold diffraction pattern of $Ir_xRu_{1-x}Zn_{10}$. Only the first quadrant of the [100] diffraction pattern is shown. Note that each heavy site can be made to lie on or near a crest from all three families of plane waves.

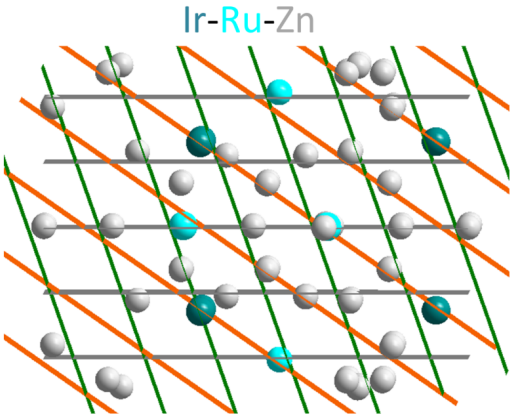

Figure 1.17: Interaction of the crests of plane waves from the inner ring of the pseudo five-fold diffraction pattern with the atoms of the D_{3h} cluster *and interior atoms.*

ular, γ-brass exists only in a narrow region around $\frac{21}{13} = 1.62$ s- and p- valence electrons per atom. Thus Zn, with its two $4s$-electrons, is a not-unexpected recurring participant in Hume-Rothery structures. $Ir_xRu_{10-x}Zn_{100}$, being principally Zn, may behave as a Hume-Rothery metal under a valence electron count-

Table 1.2: Intensities of Strongest Reflections in $Ir_xRu_{1-x}Zn_{10}$

(*h k l*)	$RuZn_{10}$[1]	$Ir_{0.2}Ru_{0.8}Zn_{10}$[1]	$Ir_{0.3}Ru_{0.7}Zn_{10}$[1]
(3 3 0)	100.0	100.0	100.0
(3 0 22)	77.8	87.7	84.9
(3 2 14)	50.2	46.5	48.1
(3 0 21)	43.1	41.4	40.1
(3 2 15)	36.7	37.1	37.9
(5 0 9)	36.5	36.1	35.8

[1] Intensity is given per reflection, with neither atomic Debye-Waller nor Lorentz-polarization factors included.

ing scheme in which Ir and Ru take *s*- and *p*- electrons from Zn to fill their incomplete *d*-shells, either partially or fully. In this way, the number of *s*- and *p*-valence electrons per atom may be drawn down from 2 in pure Zn to something nearer the Hume-Rothery standard count, near 1.62 e/a.

As mentioned in the introduction, some progress has been made in finding a rationale for the empirical Hume-Rothery rules, particularly by Mott and Jones. However, finding a quantitative or qualitative account of the empirical special electron counts in Hume-Rothery metals does not necessarily help us solve the coloring problem. In other words, it may tell us why both Cu_5Zn_8 and isostructural Fe_5Al_8[48] are stable, but not why Fe occupies the same crystallographic sites as Cu.

Relatively simple calculations (inspired by molecular calculations[49]) may be used to get a rough idea of the electronic structure of intermetallic structures.[50,51] The electronic distribution for a homogeneous system (all atoms identical) may give quite differentiated electron distributions at symmetry-nonequivalent sites. That electron distribution then becomes a guide to the preferred substitution, with more electronegative atoms entering the more negative sites.[52–57]

An illustration of this type of reasoning on a simple molecular system can be seen in Figure 1.18. Here we show the π-orbitals of an allyl, a simple organic system. The initial atomic orbitals (AOs) are equivalent, but the molecular orbitals (MOs) of the system create quite differentiated electron distributions in the molecule, depending on electron count. If only the bottom MO is filled, the middle site is the most electron-rich (Figure 1.18: Case A). By the Mulliken reasoning, if a more electronegative atom were substituted for one of the three equivalent sites, it would prefer this middle site. If the system were filled up to the middle MO, a more electronegative atom would prefer an end site (Figure 1.18: Case B).

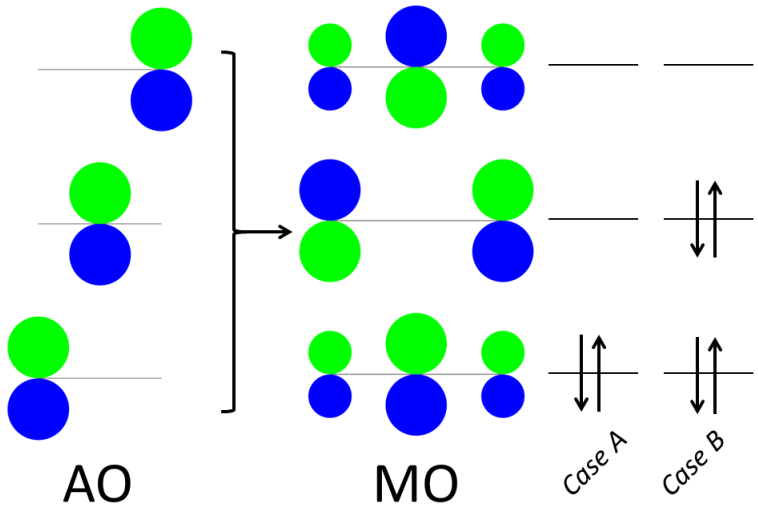

Figure 1.18: Three atomic *p*-orbitals on the left combine to make three π molecular orbitals on the right. Even though all three *p*-orbitals are equivalent, the resulting MO wavefunctions have more electron density on different sites depending on the electron filling.

We use the extended-Hückel (eH) method to determine the electronic structure. The calculations were performed using the YaeHMOP[58] program. The eH

method uses atomic orbitals as basis functions:

$$\phi(\vec{r}) = NR(r)Y_l^m(\theta, \varphi),$$

where N is a normalization constant and Y is the spherical harmonic. $R(r)$ is a Slater function describing the radial component:

$$R(r) = r^{n-1}e^{-\xi r},$$

where n is the principal quantum number, and ξ is a parameter chosen based on the atomic species. The full wave function is a linear combination of atomic orbitals (LCAO):

$$\Phi_j(\vec{r}) = \sum_i C_{ij}\phi_i(\vec{r}),$$

with coefficients C_{ij} coming from the eigenvectors $\mathbf{C}$ of the equation:

$$\mathbf{HC} = \varepsilon\mathbf{SC}.$$

H_{ii} is taken as the valence-state ionization potential. ε is the corresponding energy eigenvalue. S_{ij} is the overlap, computed as $S_{ij} = \int_V \phi_i(\vec{r})\phi_j^*(\vec{r})dV$. The off-diagonal Hamiltonians, H_{ij} are computed by the formula $H_{ij} = K(\frac{H_{ii}+H_{jj}}{2})S_{ij}$. K is usually taken to be 1.75.

In an extended structure, the basis functions are taken as Bloch functions of the atomic orbitals. For a given k-point, the un-normalized wave function is then:

$$\sum_n e^{i\vec{k}\cdot\vec{R}_n}\phi_n(\vec{r}),$$

where n is the index of the orbital and $\vec{R}_n$ is the position of the nth site.

Since eH is a semi-empirical LCAO method, we must provide atomic parameters for Zn in order to generate the crystal orbitals in an extended structure:

the various H_{ii} and ξ. To calibrate our eH calculations, we first compute a band structure for Zn metal using a so-called *ab initio* LDA-DFT method and then adjust the Zn atomic parameters in the eH calculation until there is reasonable qualitative agreement, shown in Figure 1.19.

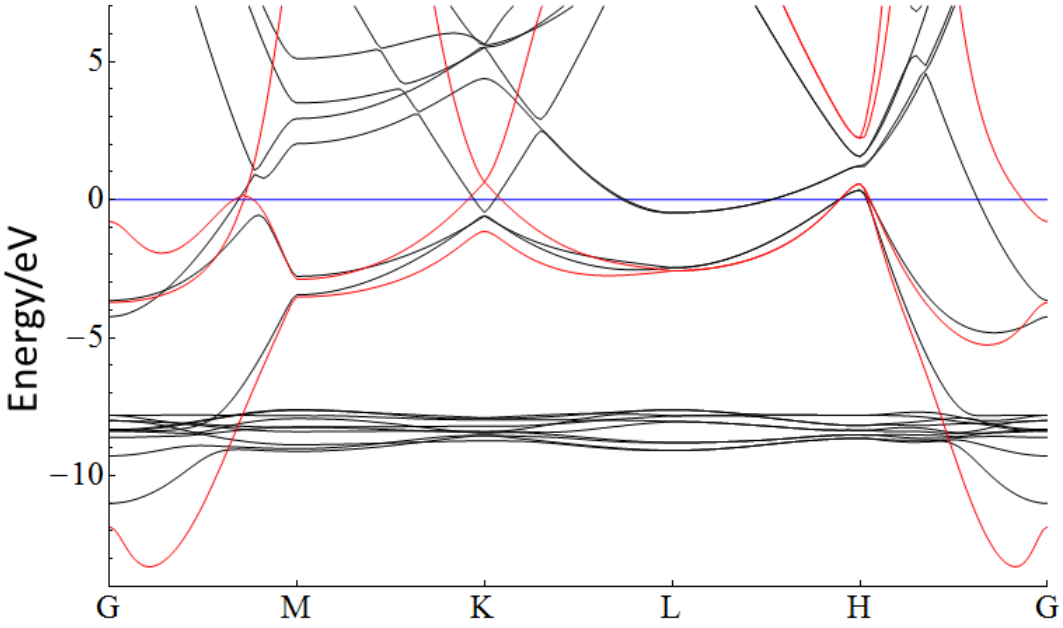

Figure 1.19: Band structure of Zn. The special k points are G=(0 0 0), M=(0 1/2 0), K=(1/3 1/3 0), L=(0 1/2 1/2), and H=(1/3 1/3 1/2). LDA-DFT bands are black and eH are red. The flat bands between roughly -8 and -10 eV are the Zn d-bands, which are not included in the eH calculation (in keeping with the Hume-Rothery spirit). The plots were shifted so that their Fermi energies coincide at 0.

The DFT calculation was carried out with VASP program[59–62] with the Local Density Approximation[63] using ultra-soft pseudopotentials.[64,65] Experimentally determined lattice parameters were used owing to well-known difficulties with optimizing the c/a ratio in elemental Zn.[66] 201 k-points (40 k-points between each special k-point) were used to generate a Zn band structure. The Zn parameters giving the fit shown in Figure 19 are: $H_{ii}(4s) = -8.96$ eV, $H_{ii}(4p) = -4.36$ eV,

$\xi(4s) = 1.35$, and $\xi(4p) = 1.15$.

With Zn parameters in hand, we are ready to investigate the $Ir_xRu_{10-x}Zn_{100}$ electronic structure. We use the coordinates from $RuZn_{10}$ (from 'Kristall 2' on p. 192 of Allio[4]) and treat the disordered Zn icosahedra by simply picking one orientation at random for each occurrence in the unit cell. In other words, we randomly pick one of the three orientations for each of the four disordered icosahedra in the unit cell. This is exactly what Belin and Belin have done in their structural analysis of $FeZn_{10}$.[3]

In this way, reasonable interatomic distances are ensured in our model, shown in Figure 1.20. By "reasonable interatomic distances," we mean ones that do not deviate excessively from the Zn-Zn distance found in bulk Zn, 2.68 Å. The model crystallographic symmetry is reduced to P1, but this does not present a problem in our calculation as YaeHMOP does not use point-group symmetry in calculating properties of extended structures. In our computations, a mesh of 60 k-points is generated using a subroutine included with the YaeHMOP software, based on the method of Ramírez and Böhm.[67]

The inherent difficulty we face is presenting the complex charge distribution in this low symmetry model. The 57 symmetry-inequivalent sites in $RuZn_{10}$ lead to no fewer than 556 distinct Zn sites in the low-symmetry all-Zn model (we remove sites Zn38',Zn39', Zn47', ZN40 since they have low occupancy and are very near to an almost fully-occupied site). The relative charges may shift with the total electron count in the lattice. The results of the Mulliken Population Analysis as a function of valence electron count per atom are shown in Figure 1.21: each line represents the relative charge on a crystallographic site from the original high-symmetry structure. Using this information, we can use

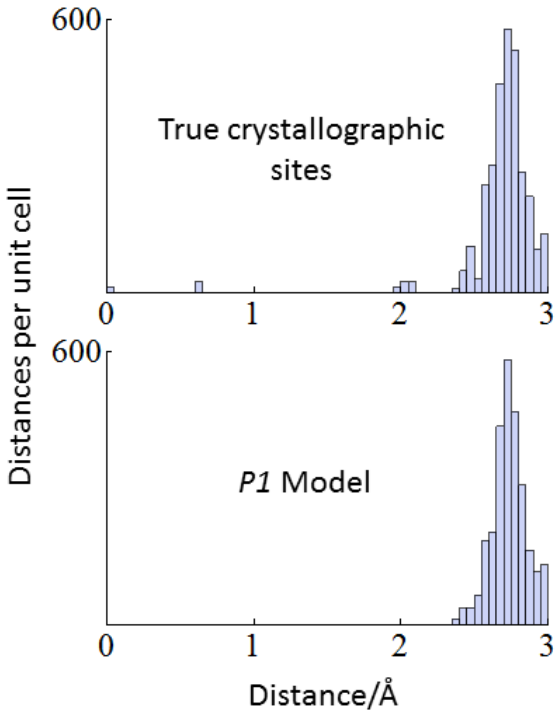

Figure 1.20: Histogram of interatomic distances in the unit cell of the model all-Zn system, based on $RuZn_{10}$. The interatomic distance in Zn metal is 2.68Å. Taking the true crystallographic sites leads to computational difficulties because the partially occupied sites are unreasonably close to each other. In the *P*1 model, partially occupied disordered sites are replaced by fully ordered sites, as discussed above. Note that the unreasonably short distances between partially occupied sites have vanished.

the inherent electron densities to rationalize and predict coloring choices made by the system.

The substitution of Ir and Ru (relative to Zn) should occur at the electron-rich sites, as Ir and Ru are much more electronegative than Zn (Table 1.3). As Figure 1.22 shows, the separation in relative charge between the sites corresponding to experimental Ru sites and sites corresponding to experimental Zn or mixed sites is quite striking, especially between 1.6-1.7 e^-/a. We illustrate this in another way in Figure 1.22 for 1.62 valence e^-/a. Figure 1.22 can be thought

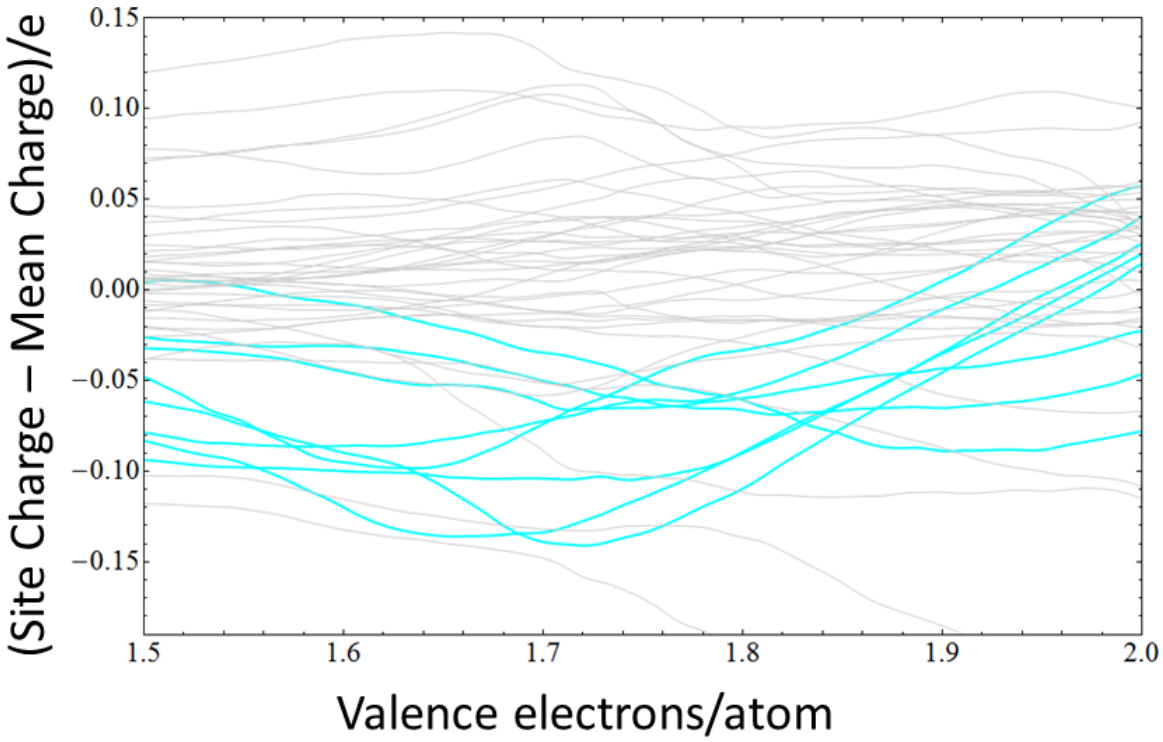

Figure 1.21: Plot of site charge from a Mulliken Population Analysis computation as a function of total electron count in a model all-Zn system. Each line represents the relative charge of a symmetry equivalent group of atoms in the original high-symmetry structure. Lower, more negative, charge indicates greater electron concentration. Although all atomic sites in the model structure are Zn, we have highlighted the sites where Ru and Ir are located. Cyan lines are relative charges on the experimental Ru sites, black lines are the relative charges on the experimental Ir/Ru mixed sites, dark grey lines are the relative charges on the mixed Ir/Zn site, and grey lines are the relative charges on the experimental Zn sites.

of as a "slice" of Figure 1.22 at 1.62 valence e^-/a.

Table 1.3: Selected properties of Ru, Ir, and Zn

Free Atom Properties	**Ru**	**Ir**	**Zn**
Pauling Electronegativity[1]	2.2	2.2	1.65
Metallic Radius (Å)[2]	1.34	1.36	1.34
Electron Configuration	$[Kr]4d^7 5s^1$	$[Xe]\ 4f^{14}5d^7 6s^2$	$[Ar]3d^{10}4s^2$

[1] Electronegativity data taken from.[68]
[2] The metallic radii are taken as half of the distance between neighboring atoms in the bulk metal: taken from.[69]

The distribution of charges as shown in Figure 1.22 is encouraging *vis-á-vis* the applicability of our simple electronic structure calculations, but not conclusive. In particular there are two Zn sites at inexplicably low charge, and the three sites corresponding to Ir/Ru mixed sites are not well separated from the Zn sites. It may be that the coordination environment at these sites favors more d-interation, which is not captured in our model. This would explain why these sites are preferred by Ir, which perhaps has a slightly higher-lying d-orbital energy than Ru.

We would like to know roughly how much electron transfer occurs from the Zn 4s to the Ru and Ir d-shells. According to the Hume-Rothery scheme, the atomic structure should be agnostic to composition for a given valence s- and p- electron count per atom. Since we have altered the electron count by substitution of Ir for Ru without changing the atomic structure, we can use the experimentally determined composition from EDX measurements (from Figure 1.4) to guide our reasoning.

In Figure 1.23, we have plotted Ru valence s- and p- electron counts as a function of Ir valence s- and p-electron count for four fixed compositions and a fixed total s- and p-valence electron count (1.62 e^-/a). In every case, we have

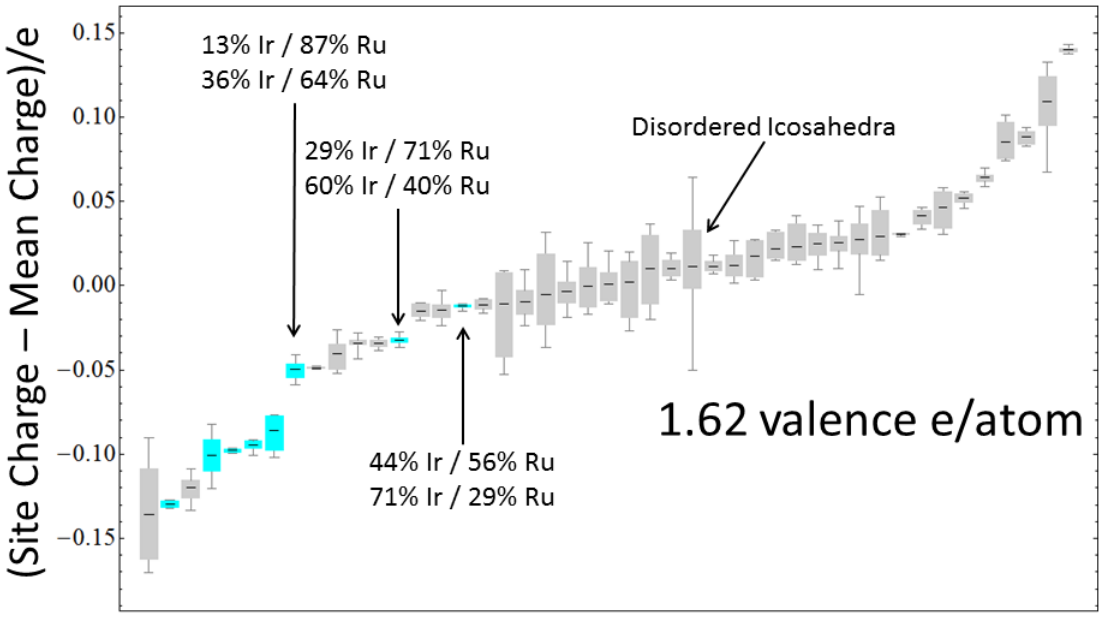

Figure 1.22: Box and whisker plot of relative charges for truly crystallographically equivalent sites in the *P*1 model. The T lines denote the minimum and maximum relative charges in the group of crystallographically equivalent sites. The heights of the boxes correspond to the middle 50% of relative charges. The lines in the middle of the boxes are the mean of relative charges of a group of crystallographically equivalent sites. The groups are sorted by mean. The labels on the mixed sites correspond to the compositions in $Ir_{0.2}Ru_{0.8}Zn_{10}$ (top) and $Ir_{0.3}Ru_{0.7}Zn_{10}$ (bottom). The Disordered Icosahedra box includes ten crystallographically inequivalent sites from the true structure, for a total of 48 Zn sites in the *P*1 model (there are 12 Zn sites per disordered icosahedron, and 4 disordered icosahedra per unit cell).

assumed Zn contributes two valence electrons per atom.

If we assume that all component elements are trying to fill their d- shells, then each Ir will take away one electron, and each Ru will take away 2 electrons. This counting scheme is reflected in Figure 1.23 by the red dot which sits near the intersection of the four lines. That each line has a solution near minus $2e^-$/Ru and minus $1e^-$/Ir supports this electron counting scheme.

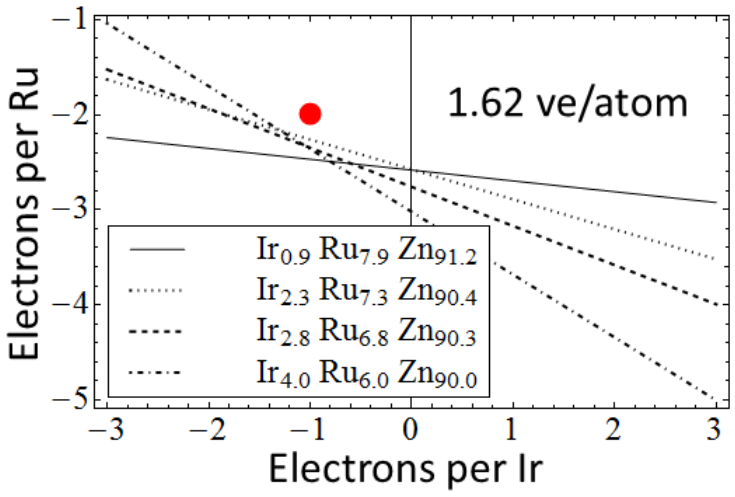

Figure 1.23: Possible valence s- and p- electron counts for Ir and Ru at different experimentally determined compositions while holding Zn constant at 2 valence s- and p- electrons. We have assumed 1.62 valence s- and p- electrons. The red dot is the point corresponding to Ir taking one electron and Ru taking two.

Figure 1.21, however, shows other electron counts which exhibit good separation of charge between the experimental Ir/Ru sites and Zn sites: in particular, for 1.74 and 1.80 valence electrons per atom. Plots of possible Ir and Ru electron contributions for various compositions at these valence electron counts are shown in Figure 1.24.

Using the same reasoning as in Figure 1.23, the plot for compositions at 1.74 ve^-/a in Figure 1.24 suggests a counting rule of 0 electrons per Ir atom, and minus 1 electron per Ru atom. The plot for compositions at 1.80 e^-/a indicates Ru should take just a fraction of an electron per atom, while Ir actually contributes electrons. If either of these schemes more truly captures the electron distribution in this family of structures than in the case of 1.62 e^-/a, it may mean that either electron transfer from Zn to the d-shells of the heavier elements is less complete or that, as mentioned before, the d-orbitals on some Ru and Ir sites

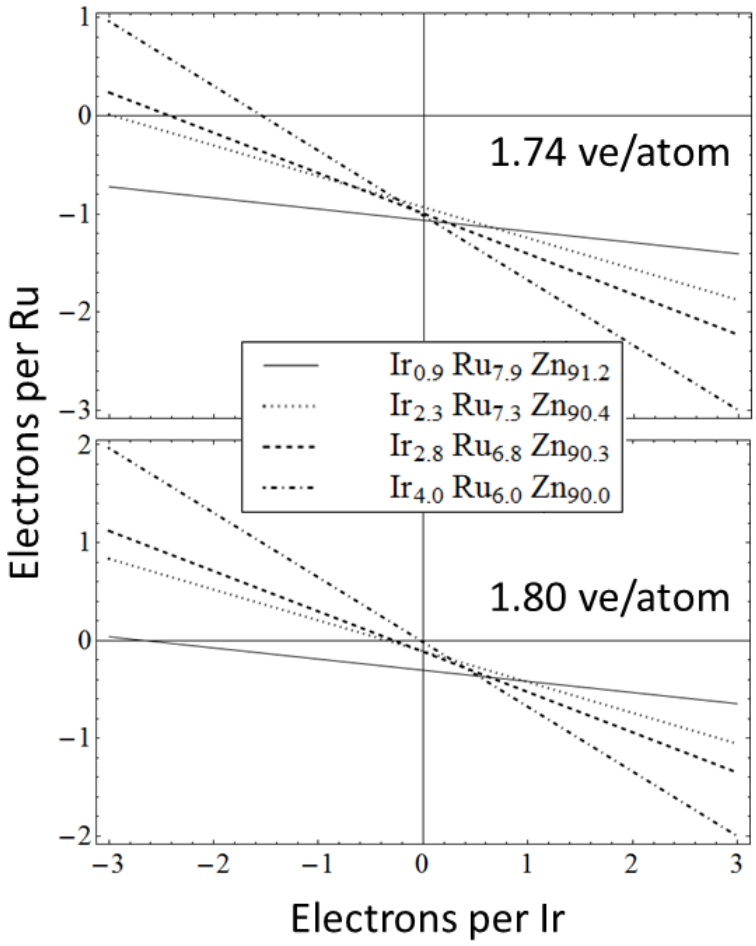

Figure 1.24: Possible valence s- and p- electron counts for Ir and Ru at different experimentally determined compositions while holding Zn constant at 2 valence s- and p- electrons, as in Figure 1.23 but with different valence electron counts per atom.

play a significant role in bonding.[†]

[†]For a parallel electronic structure story, see Appendix A on the electronic structure of the cubic phase $Au_{10}Cr_4Zn_{89}$.

1.6 Conclusion

Our Mulliken population analysis, driven by a calibrated extended-Hückel calculation, can be used to rationalize the site preferences; but only if we are able to guess the valence e^-/a. Here we have, in a somewhat circular way, guessed the electron count *from* the Mulliken population analysis (and our knowledge of Hume-Rothery phases). This approach certainly has value, not the least of which is showing that even a structure so complex as $Ir_xRu_{1-x}Zn_{10}$ can be illuminated with relatively simple orbital calculations.

Ideally, though, we want our electron count on firmer footing. We have, in effect, already drawn the valence orbital diagram: now how shall we fill it with electrons? We will try to answer this question in Chapter 3, using the theories of Mott and Jones translated into orbital language. First, however, we must sharpen our understanding of the atomic structure of intermetallics in general.

CHAPTER 2

A CLUSTER-BASED APPROACH TO PSEUDO FIVE-FOLD DIFFRACTION IN INTERMETALLICS

"The beautiful is hidden from the eyes of those who are not searching for the truth."

–Andrei Tarkovsky

2.1 Introduction

Tetrahedral packing in metal crystals is ubiquitous. It is also complex.[70–73] While tetrahedra combined with octahedra fill space in the well known face-centered-cubic and hexagonal-closest-packed structures, tetrahedral packing leads to the Frank-Kasper phases,[74–77] structures such as the Laves phases,[78,79] $Al_6Mg_{11}Zn_{11}$,[80] and Cd_3Cu_4,[81] with unit cells extending from tens to hundreds or even thousands of atoms.[2,52,82–85]

Worse yet to their understanding, perfect regular tetrahedra do not fill space.* While tetrahedra plus octahedra assemble into clusters of easily discerned octahedral or hexagonal symmetry, symmetries which naturally extend into the crystal symmetry as a whole, twenty tetrahedra come together to make a filled icosahedron, a cluster whose five-fold rotations bear little relation to crystal symmetries.

In this chapter† we will discuss the most regular of tetrahedral cluster pack-

*Although they cannot fill space, tetrahedra pack significantly more efficiently than spheres.[86]

†This chapter and Chapter 3 will appear in a forthcoming paper by S. Lee, R. Henderson, *et*

ing, packing in which tetrahedra come together to make filled icosahedra. We will show how, in these cases, pure tetrahedral packing may not lead to true crystal symmetries, but in general leads to a variety of pseudo five-fold rotational symmetries. We will find that the bonds at the center of these tetrahedral clusters form the pseudo-five-fold rotation axes, rotation axes which can be shown to dominate the single crystal x-ray diffraction patterns.[34,77,81,87] We will see that tetrahedrally-packed icosahedral and decagonal quasicrystals are just two of four limiting cases.

We will further show the symmetries of the strongest diffraction peaks are not only controlled by the central bonds of the tetrahedral clusters, but that viewed as vectors, the directions of these strongest diffraction peaks actually *are* the directions of the central bonds. We will find these strong diffraction peaks viewed as vectors form reciprocal space clusters of unusual shape and pseudo-symmetry.

Examining these diffraction peaks, we can apply the Jones theory of intermetallic stability,[5,33] a quantum theory which connects strong diffraction to optimal numbers of valence electrons. We therefore relate tetrahedral packing to possible atomic stoichiometries and connect the tetrahedral cluster geometry to electronic structure and phase stability. The four known Cu-Cd compounds: $CdCu_2$,[88,89] Cd_3Cu_4,[81] Cu_5Cd_8,[13,90] and Cu_3Cd_{10},[91] will be used to illustrate these relationships.

In this article, we consider four different limiting cases of tetrahedra packed into filled icosahedral clusters. In two of these, the clusters will be of respectively I_h and D_{5h} symmetry, known quasicrystal point groups.[92–96] In the other

al titled *Pseudo-five-fold diffraction symmetries in tetrahedral packing*.

two cases, the clusters will prove to be of T_d and D_{3h} symmetry and will result in respectively cubic and hexagonal crystalline structures. The literature has found common ground for these structures as projections of six-dimensional[97–99] or eight dimensional[100–104] Bravais lattices, curved topology,[87,105,106] and networks of disclinations.[107–109] The current work pares these mathematical approaches to their bare minimum, that is to concepts which describe concrete 3-D crystals: the 3-D pseudosymmetries, the pseudo-equivalences of their 3-D diffraction reflections, and the tetrahedral organization of both their 3-D real and reciprocal space clusters.

2.2 Aufbau of tetrahedral clusters

In the plane, six equilateral triangles pack perfectly around a single atom, Figure 2.1. The analogous three-dimensional question of how many tetrahedra can be placed around a single atom is significantly more difficult. As Figure 2.1 shows, one can place twenty tetrahedra around an atom, but the resultant cluster has deep crevasses, and is not suitable for the packing of atoms. To remove these crevasses, we must make the tetrahedra slightly irregular. If half of the six edges of the tetrahedra are 95% the length of the other half, the twenty slightly irregular tetrahedra coalesce into a single filled and perfect icosahedron, Figure 2.1, with all crevasses between tetrahedra removed.

In exactly the same way, we can pose the question of the best way of placing tetrahedra around a pair of atoms. The answer, as is shown in Figure 2.2, is five, though once again the tetrahedra must be made slightly irregular. If we further fill the empty space at the two ends of this ring of tetrahedra, we end

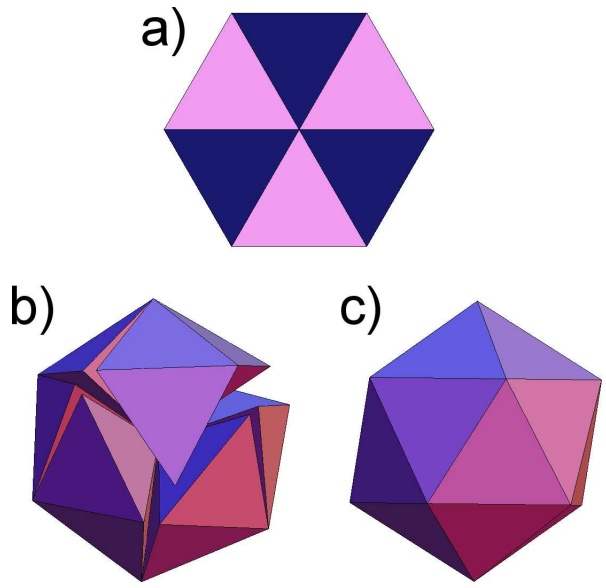

Figure 2.1: (a) Six equilateral triangles joined together into a regular planar hexagon and either (b) twenty face-sharing regular tetrahedra joined into an icosahedral shape with crevasses or (c) twenty slightly-irregular tetrahedra fused into a regular icosahedron.

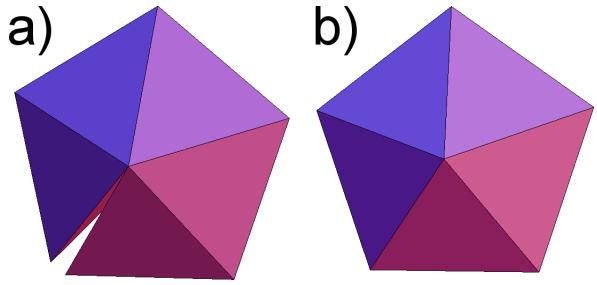

Figure 2.2: (a) Five face-sharing regular tetrahedra joined into a five-fold ring with crevasses or (b) five slightly-irregular tetrahedra fused into a D_{5h} face-sharing ring of tetrahedra.

up with the cluster shown in Figure 2.3. Each of the central atoms now has twenty tetrahedra around it, each of these twenty tetrahedra form imperfect icosahedra. The overall cluster has nineteen atoms to it. As Figure 2.3 shows, this cluster can be viewed as the fusing of two filled icosahedra. The cluster is composed of thirty-five tetrahedra, as the central five tetrahedra are part of both of the filled icosahedra. The cluster has D_{5h} symmetry. As this cluster was built up from a pair of atoms lying along an edge of a tetrahedron, we refer to it as the edge-centered-cluster.

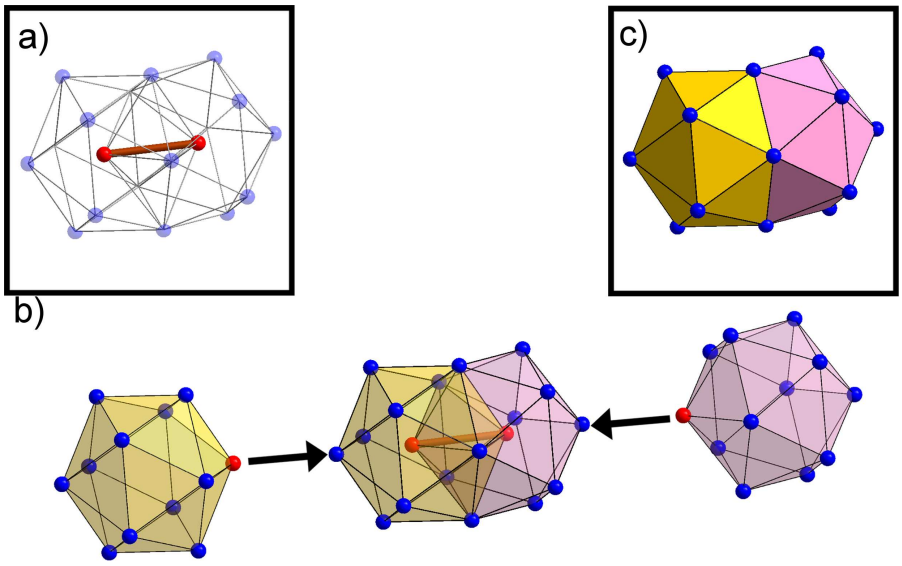

Figure 2.3: A pair of filled icosahedra fused into a single cluster, the edge-centered tetrahedral cluster. Single vertices from each icosahedron, indicated in red, come together to form an edge, shown in brown in the upper left inset. The cluster is of D_{5h} point group symmetry The shared volume shown in the center of panel (b) is the same fused ring of tetrahedra shown (from another perspective) in Figure 2.2 (b). The full cluster shown here consists of 35 face-sharing tetrahedra.

In exactly the same way we can ask the question of placing tetrahedra around a central equilateral triangle of atoms as well as around a central tetrahedron itself. These two clusters are shown in Figure 2.4 and Figure 2.5 respec-

tively. They consist of 47 and 57 tetrahedra derived from respectively three and four fused-icosahedra. The two clusters are of respectively D_{3h} and T_d symmetry. They are referred to in this chapter, respectively, as the polygon-centered-cluster and the cell-centered-cluster. The term cell used here follows the mathematics literature and is used in this case to describe the central tetrahedron of the cluster, the term tetrahedrally-centered-cluster being something of a mental conundrum in the description of a tetrahedrally based structure. Polygon-centered refers to the equilateral triangle, a polygon, at the cluster center.

2.3 A unified view for tetrahedral clusters

In the previous section we have examined four different tetrahedral clusters, clusters whose centers are respectively a vertex, an edge, a triangular polygon, or a tetrahedral cell. All central atoms in all the four clusters lie in the center of icosahedra. We now show an exact connection between these clusters, a connection best understood by the following analogy. In Figure 2.6 we show three different planar arrangements of atoms: the first has a single pentagon with an atom at its center, the second has two such filled pentagons around a central edge, while the third has three filled pentagons built around a common polygon. These three fused pentagonal arrangements can be viewed as two-dimensional analogs of the four tetrahedral clusters discussed in the previous section.

The crux to the analogy is that while as two-dimensional figures, the vertex-, edge-, and polygon-centered arrangements of Figure 2.6 are all distinct from one another, as the lower panel of this Figure shows, they can also be viewed as

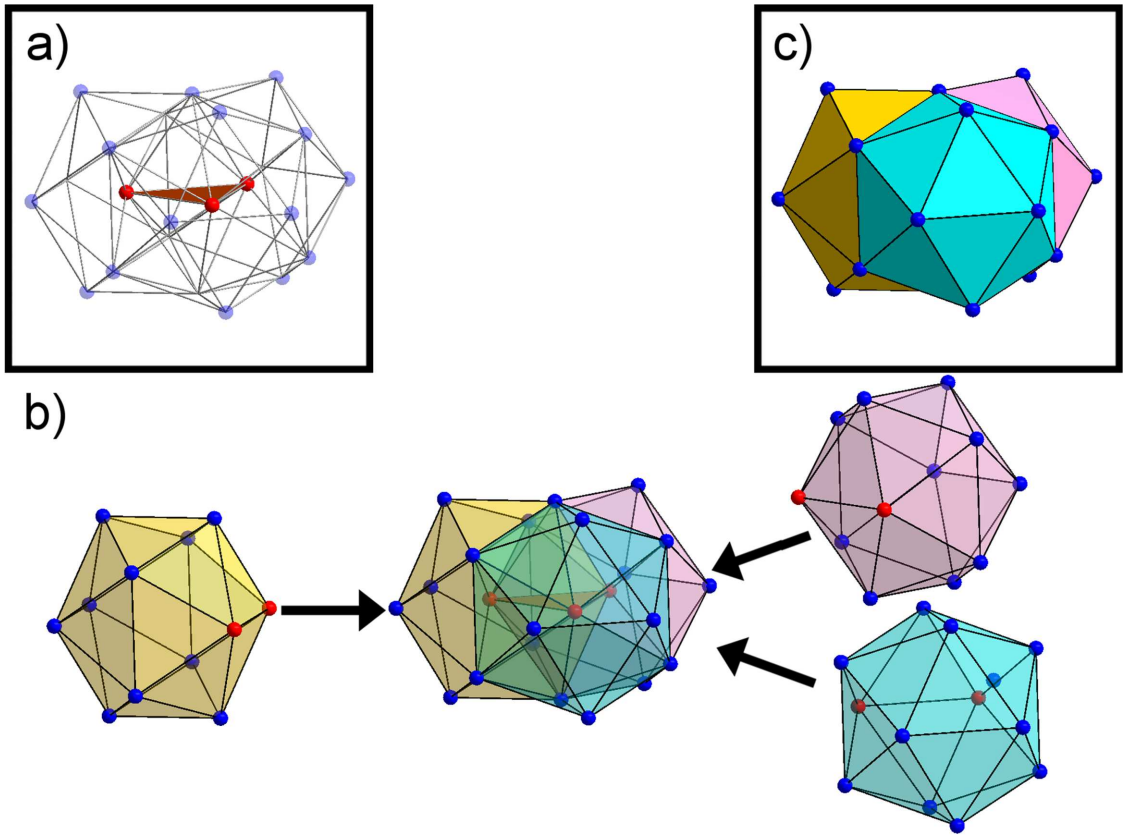

Figure 2.4: Three filled icosahedra fused into a single cluster, the polygon-centered tetrahedral cluster. Edges from each icosahedron, indicated by pairs of red-colored vertices, come together to form an equilateral triangle, a polygon, shown in brown in the upper left inset. The cluster is of D_{3h} point group symmetry and consists of 47 face-sharing tetrahedra.

projections of the same three-dimensional cluster. This 3-D cluster is the icosahedron, one of the most symmetric 3-D Platonic solids.

In exactly the same manner, the vertex-, edge-, polygon-, and cell-centered tetrahedral clusters can be shown to be projections of the same 4D structure, a 4D Platonic solid.[34,102,103] There are six 4D Platonic solids in total. Our interest is with one of the most symmetric 4D Platonic solids, the 600-cell.[110] The 600 cell

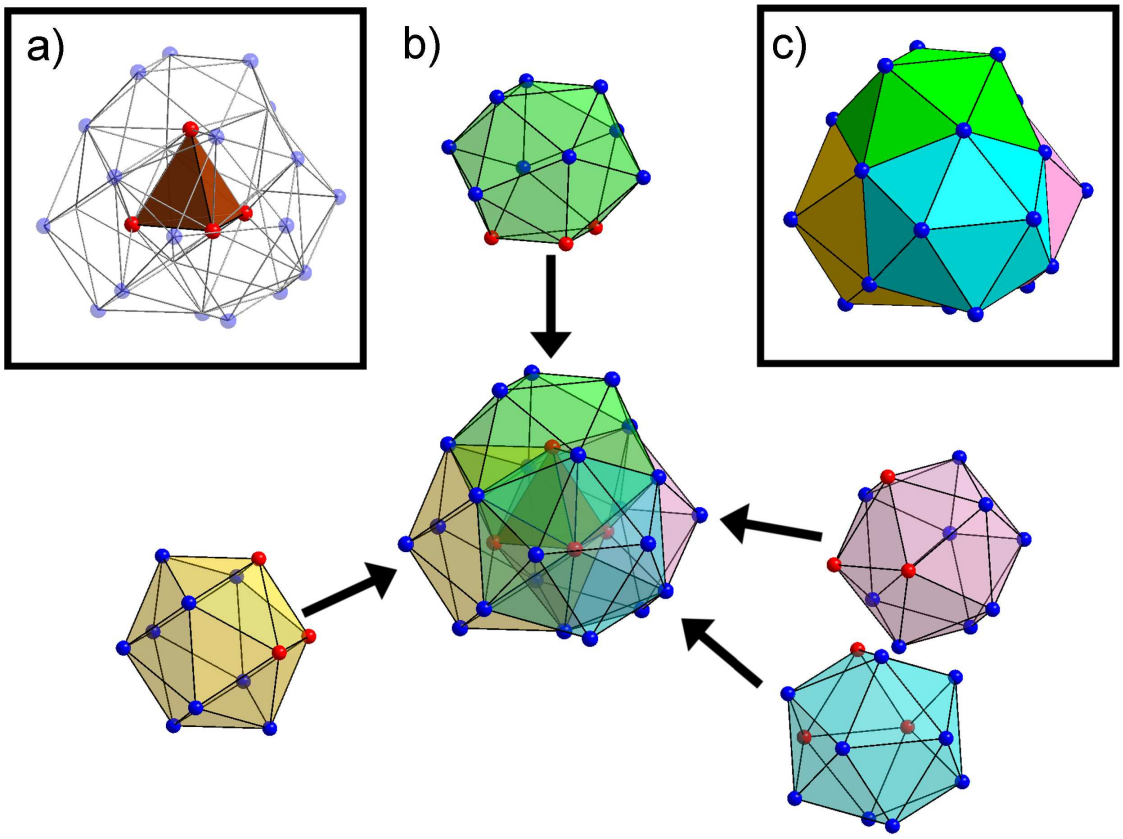

Figure 2.5: Four filled icosahedra fused into a single cluster, the cell-centered tetrahedral cluster. Faces from each icosahedron, indicated by triangles of red-colored vertices, come together to form a tetrahedron, a cell, shown in brown in the upper left inset. The cluster is of T_d point group symmetry and consists of 57 face-sharing tetrahedra.

contains 600 perfect tetrahedra and 120 vertices, all equidistant from the same 4D center. Each of these 120 vertices lies in the center of a perfect icosahedron. With twelve vertices to each icosahedron, the 600-cell contains 720 edges ($720 = (120 \times 12)/2$). Every vertex, edge, face, tetrahedra, and icosahedra are the same as all other vertices, edges, faces, tetrahedra, and icosahedra. The 600-cell is therefore Platonic.

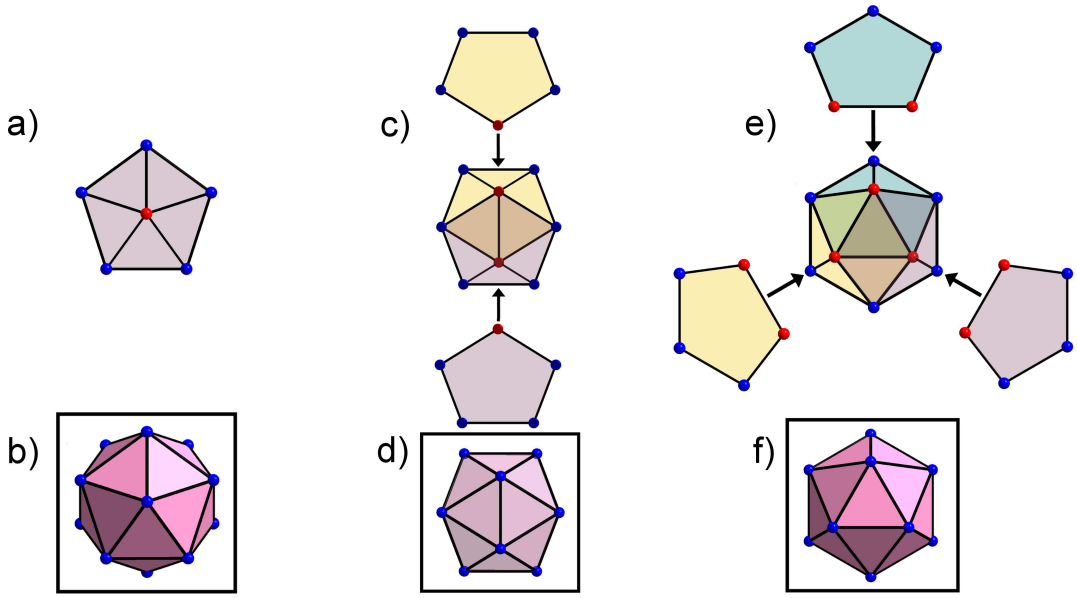

Figure 2.6: 2-D (a) single filled-, (c) two edge-centered fused-, and (e) three polygon-centered fused-pentagons forming the projected shapes of a 3-D icosahedron projected down respectively a (b) vertex, (d) edge, and (f) face.

In Figure 2.7 we show four 3-D views of the 600-cell. As this figure shows, the central portion of the four views correspond to the four different tetrahedral clusters discussed in the previous section. As this figure also shows, however, these four tetrahedral clusters are surrounded by additional atoms. These additional atoms cap the triangular faces, thus generating further tetrahedra.[‡] The vertex- edge-, polygon-, and cell-centered projections have respectively 45, 44, 50, and 54 atoms. Of the four cluster types, the vertex- and cell-centered clusters are best known. The former is termed the Bergman cluster while the latter is best known in γ-brass, Cu_5Zn_8.[13–15,80]

We will call the central portion of the vertex-, edge-, polygon-, and cell-

[‡]For vertex-centered clusters it is traditional to include among the additional atoms those which cap vertices as well as faces.

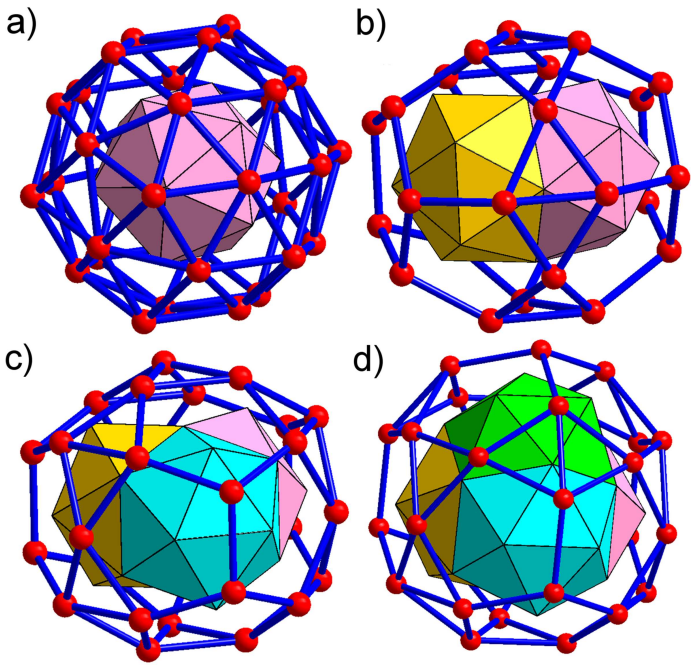

Figure 2.7: The (a) vertex-, (b) edge-, (c) polygon-, and (d) cell-centered projection of the 4D Platonic solid, the 600-cell. The figures divide the projected 600-cell into inner- and outer-shells shown respectively as polyhedra and ball-and-stick figures. Inner shell colors refer to colors used in Figures 3-6. (a) is the Bergman cluster. (d) is found in γ-brass.

centered projections, respectively the single filled, pair of, trio of, and quarto of fused icosahedra the inner shells of the cluster. The atoms capping the triangular faces of this inner shell will be termed the outer shell. For example in the γ-brass structure it is traditional to focus on just the inner shell while for the Bergman cluster inner and outer shells are often viewed together.[§]

[§]It should be noted that the vertex-, edge-, polygon, and cell-centered projections are the only four 4D to 3-D projections which correspond to isolated special points of higher symmetry. In a 3-D globe to a 2-D map projection, specifying the center of the projection, typically in this case a pole, completely specifies the projection itself. The same holds in the 4D to 3-D projection. The symmetry of the "pole" taken in the 4D 600-cell to 3-D projection therefore determines the symmetry of the projected 3-D object. As the 600-cell is a 4D Platonic solid, there are only four high symmetry special points: they are respectively at the center of a vertex, an edge, aface or a cell, ie., they are the four projections shown in Figure 2.7.

While the 600-cell consists of 120 vertices, the four projections contain less than half the original 120 atoms. This reduction is a consequence of the 4D to 3-D projection. We can understand this reduction by the following analogy. When projecting a three-dimensional sphere, the globe, onto a two-dimensional filled circle, a map, we project only half the sphere at a time. Simple projected maps of the Earth typically show just half the surface of the globe, typically either the Northern or Southern hemispheres. In our case, 3-D projections of it show just half of the 4D 600-cell, roughly 60 of the 120 vertices.

There is a further complication caused by the projection. It is in the region near the equator. In 3-D, the equator is defined as the 2-D circle which is projected the farthest away from the central pole. Euclidean features near the equator of a global map are always highly distorted. In 4D, the equator is the 3-D sphere which projects furthest away from the pole.

Just as in the globe-to-map projection, geometrical features near the 4D equator are highly distorted upon projection into 3-D space. Tetrahedra near the equator are unreasonable in shape (they are considerably flattened). Such flattened tetrahedra can not be found in real 3-D crystals and are therefore not included in our projected images. We therefore peel away these outermost tetrahedra from our projected images; projected clusters therefore range from 44 to 54 atoms in size.

The edges of the 600-cell prove to be of significant chemical relevance. They can be the metal-metal bonds. But they serve other functions. First recall that the 600-cell is Platonic. In the original 600-cell the 720 edges are all symmetrically equivalent to one another. These 720 edges prove to define 720 five-fold rotations, all of which belong to the same class of the 600-cell point group. Relevant

to us, these 720 4D edges all project in into 3-D incipient pseudo-five-fold rotational axes. A mathematical treatment of the various symmetry classes of the 600-cell, including irreducible representations and the character table, is available in Appendix C.

In the vertex-, edge-, polygon-, and cell-centered tetrahedral clusters there are respectively 204, 193, 234, and 256 bonds. All of these edges retain, to some extent, symmetry aspects of the original 600-cell. But certain edges retain the symmetries to a much greater degree. An analogy to 2-D projections of the 3-D icosahedron helps illustrate this point. In an icosahedron, the triangular faces of the icosahedron are equilateral triangles. In Figure 2.6 we showed three different projected views of this icosahedron. As this figure shows those triangular faces closest to the center of the projection, retain to the greatest degree their three-fold symmetry: they look most like equilateral triangles.

In a similar manner, those edges which lie closest to the center of the 3-D tetrahedral-cluster projections retain the five-fold rotational symmetry of the original 4D 600-cell. We show this in Figure 2.8. In this figure we show the diffraction image along the most central edge for respectively the vertex-, edge-, polygon- and cell-centered projected 600 cell. As this figure shows, there is discernable pseudo-five fold diffractions along each of these edges. We further show, in Figure 2.9, the diffraction image corresponding to the second-most central edge of the edge-centered cluster. For this cluster this less central edge shows as well, albeit less markedly, pseudo-five-fold rotational symmetry.

Only the most central cluster edges correspond to pseudo-five-fold rotation axes, but less central cluster edges are also significant. Once we turn to real tetrahedral crystal structures, we will find the directions of the central edges

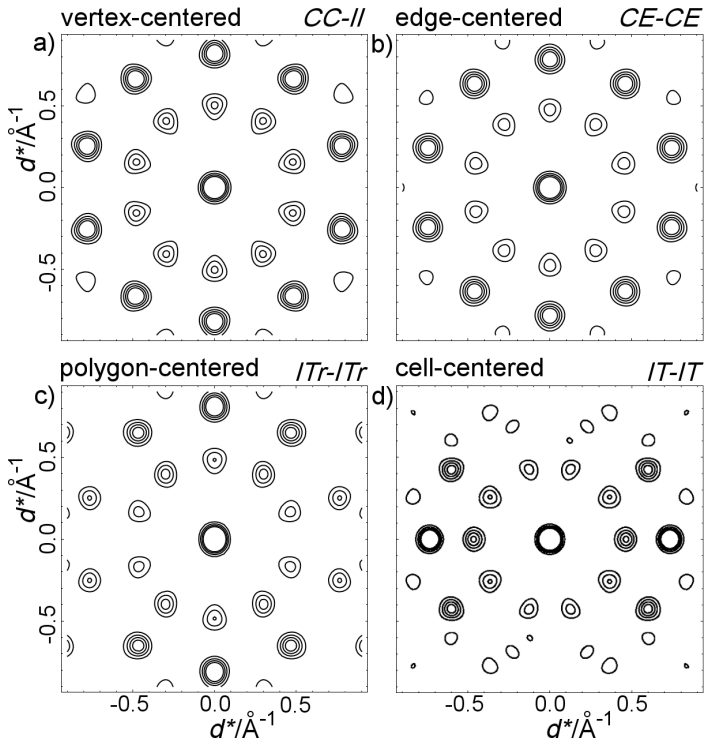

Figure 2.8: The diffraction pattern of a single (a) 45-atom vertex-, (b) 44-atom edge-, (c) 50-atom polygon-, and (d) 54-atom cell-centered cluster shown down respectively an *II-II*, *CE-CE*, *ITr-ITr*, and *IT-IT* cluster edge. Pseudo-five-fold rotational symmetries are seen in each of these diffraction patterns as 10-fold pseudo-symmetric rosettes.

point in the same direction as the principal diffraction peaks. Furthermore the d-spacing of these strongest diffraction peaks are roughly the same as the average bond lengths.

In general, the edges which are shared by more than one of the inner-shell fused icosahedra exhibit the strongest diffraction. But diffraction peaks corresponding to any inner shell edge exhibit significant intensity. We show this hierarchy of edges for each of the four cluster types in Figure 2.10 going from central edges which display pseudo-five-fold diffraction symmetry (second column in the figure), to shared inner-shell edges which correspond to strongly

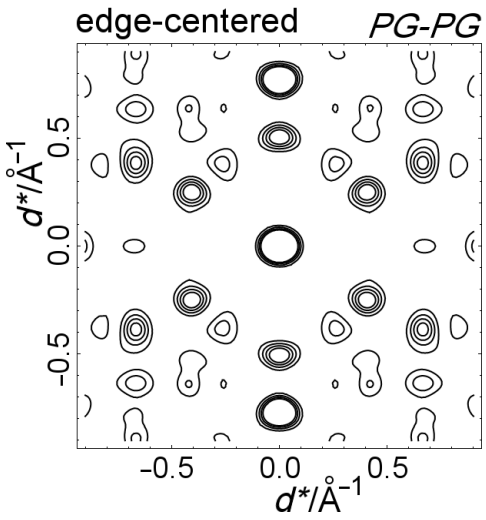

Figure 2.9: The diffraction pattern of a single 44-atom edge-centered cluster shown down its *PG-PG* cluster edge. Pseudo-five-fold symmetry is only somewhat recognizable. Interestingly, this diffraction pattern resembles the diffraction pattern of edge-centered cluster structures, shown in Figures 2.12 and 2.22, where pseudo-symmetry is more obviously present.

diffracting directions (third column), to the remaining inner-shell edges which correspond to less strong but still significant diffraction peaks (fourth column).

In describing these edges, it is useful to introduce a uniform nomenclature. In Figure 2.10, we can see that the cell-centered inner shell has four symmetry inequivalent sites. These sites are traditionally termed *I*nner *T*etrahedron (*IT*), *O*uter *T*etrahedron (*OT*), *O*cta*h*edron (*OH*), and *C*ubo*o*ctahedron (*CO*). Of these four sites, only the *IT*, *OT*, and *OH* sites are shared by more than one of the inner-shell fused icosahedra. Those edges between *IT*, *OT*, and *OH* sites therefore are the most strongly diffracting reflections. And among this set, the edges which correspond to the most discernable pseudo-five fold symmetry are the most central, the six *IT-IT* edges.

We can specify analagous nomenclatures for the vertex-, edge-, and polygon-

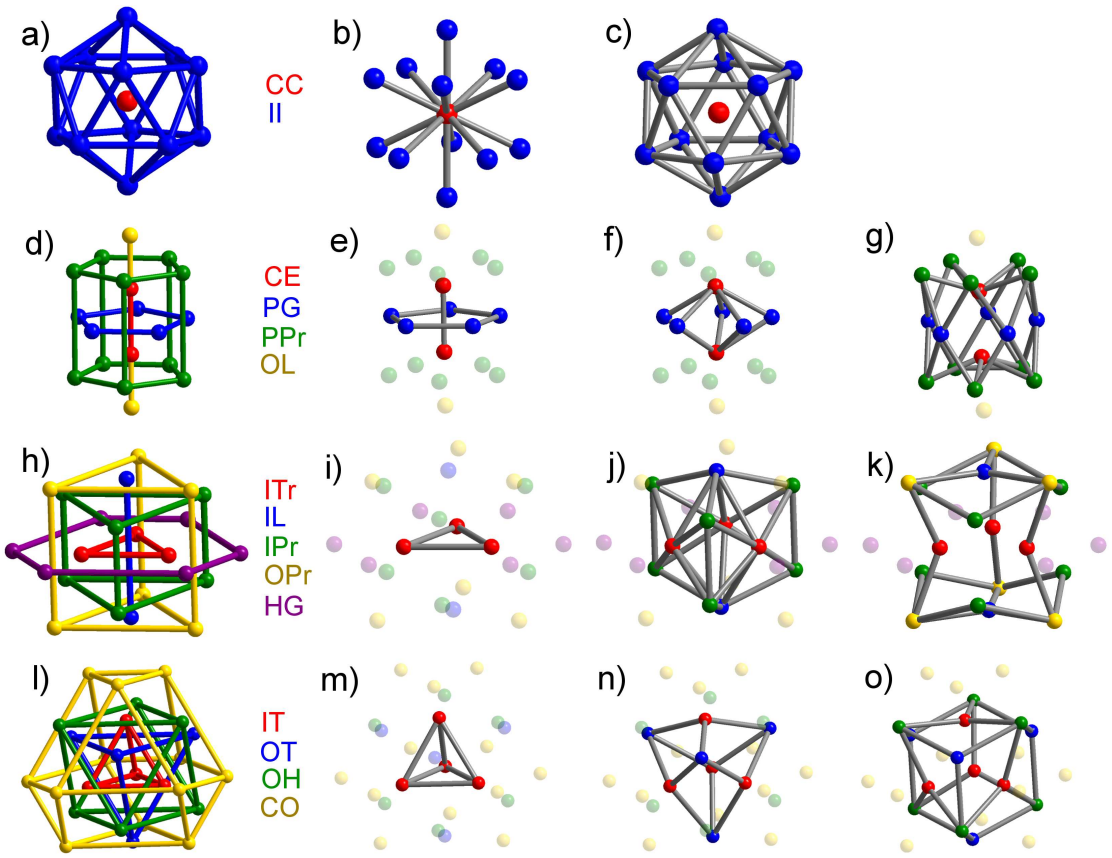

Figure 2.10: Site labeling scheme as well as representative edges for the inner shells of the different types of centered tetrahedral packing. First through fourth rows are for respectively vertex-, edge-, polygon-, and cell-centered clusters. First column: color-coded illustrations of the site labeling scheme (full site names given in text); second column: edges which correspond to pseudo-five-fold rotational axes; third column: together with the second column edges, the edges which correspond to the strongest diffraction peaks; and fourth column: the remaining edges whose corresponding diffraction peaks have significant, but not the strongest intensities.

centered clusters. The vertex-centered inner shell has two central symmetry inequivalent sites, the Cluster Center (*CC*) and the *I*nner *I*cosahedron (*II*) sites. For the edge-centered inner shell there are four symmetry inequivalent sites: Central Edge (*CE*), *P*enta*g*on (*PG*), *P*entagonal *Pr*ism (*PPr*), and *O*uter *L*ine (*OL*). Finally for the polygon-centered cluster, the central symmetry inequivalent sites are *I*nner *L*ine (*IL*), *I*nner *Tr*iangle (*ITr*), *I*nner *Pr*ism (*IPr*), *O*uter *Pr*ism (*OPr*), and *H*exa*g*on (*HG*).

In the case of the vertex-centered cluster, the cluster is so symmetric that the entire projected 600-cell has only four symmetry inequivalent sites. Besides the *CC* and *II* sites, the cluster outer shell contains just two more site types, *OI*, the *O*uter *I*cosahedron and *DH*, the *D*odeca*h*edron.[¶]

In considering atoms which lie on the central molecular axis, we distinguish those which are bonded vs. not-bonded to symmetry equivalent atoms. We term these two cases respectively edge and line sites as in *CE* for *C*entral *E*dge vs. *CL* for *C*entral *L*ine. Where two letter designations are used for simple polyhedra and polygons, the second letter of the designation are respectively *H* for *h*edron and *G* for *g*on. It should be noted that the *HG* label has been applied to a hexagon of D_{3h} rather than D_{6h} symmetry.[‖]

[¶]Less useful but still sometimes in need of consideration are the outer shell sites in the remaining clusters. For edge-centered clusters we have the *O*uter *P*enta*g*on (*OPg*), *El*ongated *P*entagonal *p*rism, (*ElPp*) and *Fl*attened *P*entagonal *p*rism (*FlPp*). For polygon-centered clusters the outer shell has four symmetry inequivalent sites: *H*exa*g*onal *Pr*ism (*HgPr*), *El*ongated *Pr*ism (*ElPr*), *Fl*attened *Pr*ism (*FlPr*), and *O*uter *Tr*iangle (*OTr*). Finally for the cell-centered cluster the three sites are geometrically the *Ex*ternal *T*etrahedron (*ExT*), the *Les*ser *T*runcated *t*etrahedron (*LsTt*), and the *Gr*eater *T*runcated *t*etrahedron (*GrTt*).

[‖]In the case of the outer shell of the cell-centered cluster the terms lesser and greater truncated tetrahedron refer to the degree of truncation present in the specified cluster. Finally where the type of prism is not specified, it is assumed to be a triangular prism.

2.4 Crystalline examples of the four types of tetrahedral clusters

Our interest is in finding crystals which preserve as much as possible of the above symmetries. The vertex-, edge-, polygon- and cell-centered clusters are respectively of I_h, D_{5h}, D_{3h}, and T_d symmetry. These four point groups are maximally compatible with respectively the four space-group-allowed point group symmetries T_h, C_{2v}, D_{3h} and T_d, point groups found respectively in cubic, orthorhombic, hexagonal, and cubic crystals.

Not only should the space group have the above point group symmetries, there need be special sites within the unit cell, Wyckoff positions, which have these exact symmetries. For example for the vertex-centered cluster, the Wyckoff site symmetry T_h or $m\bar{3}$ is required. Possible space groups are therefore $Pm\bar{3}$, $Pn\bar{3}$, $Fm\bar{3}$, $Im\bar{3}$, $Pm\bar{3}n$, and $Fm\bar{3}c$. For cell-centered clusters, we need Wyckoff site symmetry T_d or $\bar{4}3m$. Allowed space groups are $P\bar{4}3m$, $F\bar{4}3m$, $I\bar{4}3m$, $Pn\bar{3}m$, $Fm\bar{3}m$, and $Fd\bar{3}m$.

Crystalline examples of these clusters are found in $Al_6Mg_{11}Zn_{11}$, a 1/1 quasicrystalline approximant and Pt_5Zn_{21},[111,112] a $2 \times 2 \times 2$ superstructure of the γ-brass structure. Their unit cells, along with one example of the corresponding tetrahedral cluster is shown in Figure 2.11. They crystallize in respectively $Im\bar{3}$ and $F\bar{4}3m$ symmetry.

In exactly the same manner we can consider edge- and polygon-centered tetrahedral clusters. The list of space groups with C_{2v} Wyckoff site symmetry is too long to list here. For the polygon-centered cluster with D_{3h}, either of $\bar{6}m2$ or

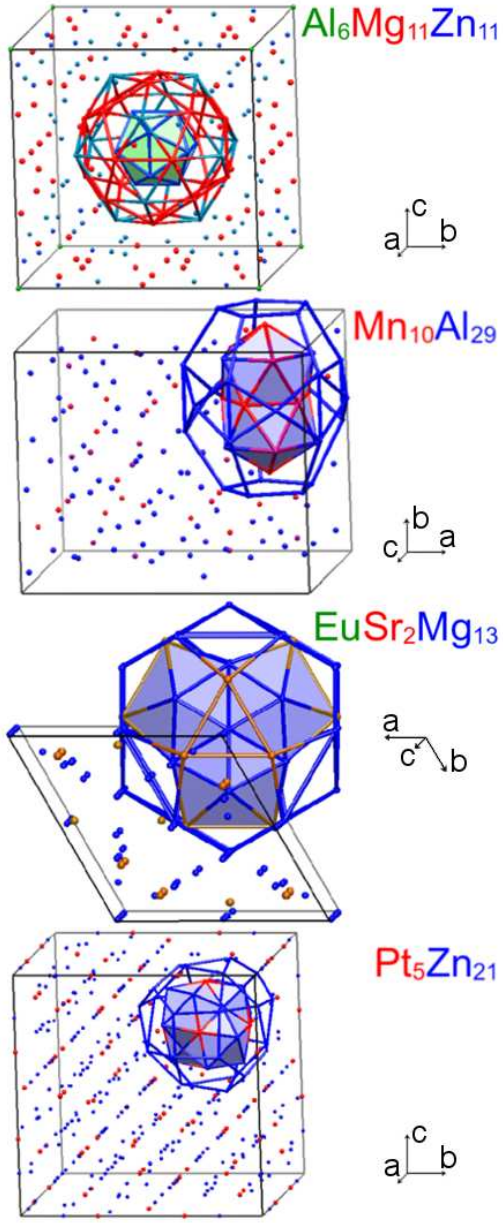

Figure 2.11: The $Al_6Mg_{11}Zn_{11}$, $Mn_{10}Al_{29}$, $EuSr_2Mg_{13}$, and Pt_5Zn_{21} unit cells. Elements are color-coded. Mixed sites are denoted by the corresponding color mixtures: blue-green and green-red mixtures appear respectively as turquoise and brown. For each structure a single vertex-, edge-, polygon-, and cell-centered cluster is shown. The inner shell is represented as a filled polyhedron. Atoms at the centers of the polyhedra determine the colors of the polyhedral faces. Outer shell is shown in a ball-and-stick format.

$\bar{6}2m$ symmetry, the list of possible space groups include $P\bar{6}m2$, $P\bar{6}2m$, $P6/mmm$, $P6_3/mcm$, and $P6_3/mmc$. Neither rhombohedral nor cubic crystal space groups are compatible with Wyckoff site D_{3h} symmetry. Examples of crystal structure with edge- or polygon-centered tetrahedral clusters are the $Mn_{10}Al_{29}$[113] decagonal quasicrystalline approximant and the $EuSr_2Mg_{13}$[114] structure. Their structures with one example each of the corresponding tetrahedral cluster is shown in Figure 2.11. These two crystals crystallize in respectively the *Pnma* and $P6_3/mmc$ space groups.

Not only do these crystal structures show clear examples of the vertex-, edge-, polygon-, and cell-centered tetrahedral packing, they show as well marked pseudo-five-fold diffraction symmetry. The pseudo-five-fold diffraction images are themselves in the directions of the most central edges of the respective clusters. For the cubic Pt_5Zn_{21} and hexagonal $EuSr_2Mg_{13}$ structures, the innermost cluster edges link respectively *IT* to *IT* atoms, the $\langle 110 \rangle$ real lattice directions, and *ITr* to *ITr* atoms, the real space $\langle 100 \rangle$ or equivalently the reciprocal space $\{2\bar{1}0\}$ directions.

In Figure 2.12 we therefore show the diffraction images orthogonal to the cubic $[1\bar{1}0]$ and hexagonal [100] directions. Our interest here is only with the strongest diffraction peaks. Within the Cerius^2 suite of programs,[115] we can filter out weaker peaks by applying an Intensity Factor. With this filter, as Figure 2.12 shows, both crystals show marked rings of ten-fold pseudo-symmetric diffraction in the above specified directions. Such rings correspond to pseudo-five-fold rotational symmetry. The Pt_5Zn_{21} and $EuSr_2Mg_{13}$ show respectively one and two such 10-fold rings. Pt_5Zn_{21} has an inner ring and $EuSr_2Mg_{13}$ has inner and outer rings whose d_{hkl} respectively are approximately 2.1 and 2.7/1.7

.

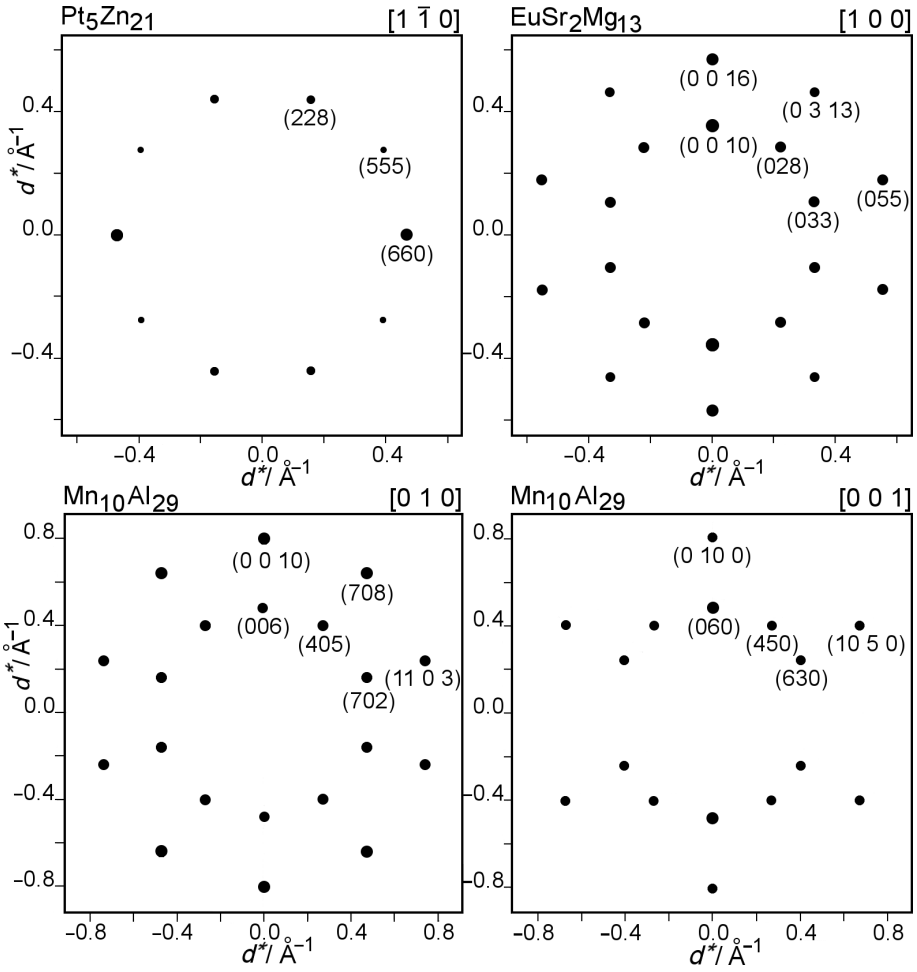

Figure 2.12: Diffraction pattern for the cell-centered Pt_5Zn_{21}, polygon-centered $EuSr_2Mg_{13}$, and edge-centered $Mn_{10}Al_{29}$ crystals along the indicated directions. For $Mn_{10}Al_{29}$, the [0 1 0] and [0 0 1] directions correspond respectively to *CE-CE* and *PG-PG*. The latter pattern shows less-marked pseudo-five-fold symmetry but its relation to the former's pseudo-five-fold symmetry is evident. Cerius[2] Intensity Factors: 0.15 (Pt_5Zn_{21}); 0.04 ($EuSr_2Mg_{13}$); 0.04 ($Mn_{10}Al_{29}$, [010]); 0.05 ($Mn_{10}Al_{29}$, [001])

In the case of the edge-centered-cluster-based structure $Mn_{10}Al_{29}$ the most central edge connects the two *CE* sites to one another. As Figure 2.12 shows this *CE-CE* direction, which in $Mn_{10}Al_{29}$ runs in the [010] real space lattice direction,

has excellent pseudo-five-fold symmetry associated to it.

For edge-centered crystal structures, even the second-most central edge lie sufficiently near the projected-cluster center, a kind of pseudo-five-fold diffraction rings can be observed. These second-most central edges connect *PG* to *PG* sites. There are five different *PG-PG* directions, only one of which is orthognal to a numerically simple real space direction. For $Mn_{10}Al_{29}$ one of the five *PG-PG* edges lies in the [001] real space direction, the other four *PG-PG* directions corresponding to 72 and 144^o rotations of this direction. As Figure 2.12 shows, pseudo-five fold diffraction along this axis is significantly distorted, but its relation to the better *CE-CE* pseudo-five-fold diffraction symmetry, also shown in this figure, is evident.

For diffraction images orthogonal to less simple real-space directions, relatively few diffraction reflections are *exactly* orthogonal to real space lattice directions. Standard diffraction images which show all diffraction reflections orthognal to a given real space lattice direction (this real space direction is called the zone axis) fail therefore to properly capture pseudo-symmetry.

It is easiest in such cases to generate somewhat artificial diffraction images. We do so by choosing a crystallite size, where the crystallite center is chosen to be one of the four types of tetrahedral clusters. We choose crystallites which are 30 in diameter, centered around a high symmetry point of the crystal structure. The small size leads to significant dispersion around each (*hkl*) reflection. Contour maps orthogonal to a given real space direction therefore can capture the intensity of reflections not exactly within the orthogonal plane.

Such crystallite diffraction images can be used to assess the pseudo-five-fold

symmetries. We consider the vertex-cluster based $Al_6Mg_{11}Zn_{11}$ structure. In this structure we choose a zone axis in the ⟨503⟩ real space directions, directions which correspond in real space to *CC-II* edges. Figure 2.13 shows the marked pseudo-five-fold symmetries with respect to these zone axes.

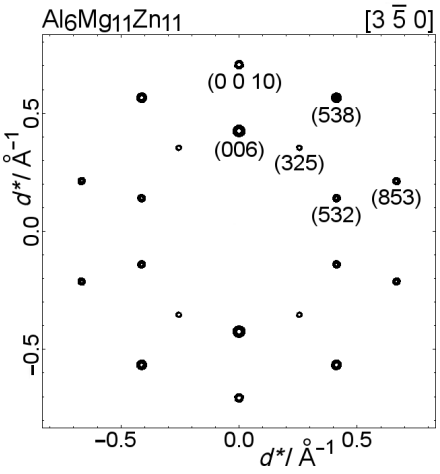

Figure 2.13: Diffraction pattern for a cluster-centered 3.0 nm diameter spherical crystallite of the vertex-centered $Al_6Mg_{11}Zn_{11}$ structure shown along the $[3\,\bar{5}\,0]$ direction. Only peaks whose peak height is $\geq 0.27 \times$ the most intense peaks are shown.

2.5 Smaller crystalline examples

The four crystals considered in the previous section, $Al_6Mg_{11}Zn_{11}$, $Mn_{10}Al_{29}$, $EuSr_2Mg_{13}$, and Pt_5Zn_{21} have Pearson symbols of respectively *cI*162, *oP*156, *hP*96, and *cF*416. Based on the Wyckoff site symmetry of their corresponding space groups these four crystals can have respectively two, four, two, and sixteen tetrahedral clusters all of whose whose cluster edges correspond to chemical bonds. As the vertex-, edge-, polygon-, and cell- centered tetrahedral clusters have respectively 45, 44, 50, and 54 atoms, the tetrahedral clusters can account

for respectively 90, 176, 100, and 864 potential sites.

In the previous examples, the number of atoms in a unit cell are therefore always within a factor of two of the number of atoms in the tetrahedral clusters themselves. In this section we turn to tetrahedral cluster crystals with just tens of atoms in their unit cells, unit cells one-quarter to one-tenth the size of the previous unit cells. These small unit cells nonetheless fashion centered clusters the same size as were found previously. Unit cells with just tens of atoms must lead to clusters forty to fifty atoms in size.

In one case noted below a cubic crystal with a primitive unit cell of just six atoms, generates a full inner-shell cell-centered 26-atom cluster as well as over half the outer shell. In this as well as the other examples , atoms in the inner shell of one cluster belong to outer shells and even the inner shells of neighboring clusters. As may be expected, while some of our examples are able to create full inner and outer shelled tetrahedral clusters, in other examples, the tetrahedral clusters are imperfect: sites in the outer shell are found missing.

Small sized unit cells for the vertex- and edge-centered clusters include Mg_2Zn_{11} [116] (*Pm*$\bar{3}$, *cP39*) and $Cd_2Cs_5Tl_{11}$ [117] (*Amm*2, *oA36*), with respectively one and two clusters per unit cell. The unit cells in both cases are smaller than a single centered cluster. Illustrations of these structures are shown in Figures 2.14 and 2.15. In both these examples both inner and outer shells are fully present. Remarkably, despite their small unit cell sizes, their diffraction images, see Figure 2.16 and 2.17, discernable pseudo-five-fold diffraction symmetry. The pseudo-five-fold symmetry is less marked than that found for the previously discussed crystals.

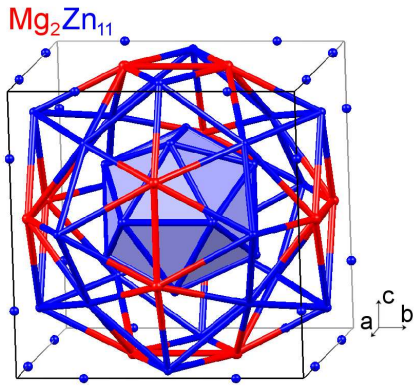

Figure 2.14: The Mg_2Zn_{11} unit cell. Elements are color-coded and a single vertex-centered cluster is shown. Inner and outer shells are represented respectively in filled-polyhedron and ball-and-stick formats. The polyhedral faces are blue as a Zn atom lies at the cluster center.

Small celled examples of the polygon-centered cluster include both the ubiquitous hexagonal Laves phase $MgZn_2$ [118] (*hP12*) and the slightly larger Co_2Al_5 (*hP28*) [42,119] structure. As in the later section of this chapter we will consider the Cu-Cd phase diagram, we illustrate here $CdCu_2$, a $MgZn_2$-type structure and Cu_3Cd_{10}, a Co_2Al_5-type system. Illustrations of their unit cells showing their polygon-centered tetrahedral clusters are given in Figure 2.15.

In $CdCu_2$ the full inner shell of the cluster is present. But with only twelve atoms in the primitive unit cell, it proves impossible to fully recreate the complete outer shell. Of the four outer shell sites, the *ElPr*, *FlPr*, and *HgPr* are present while the *OTr* is not. Similarly in Cu_3Cd_{10}, while the full inner shell is present, only the *ElPr* and *OTr* sites are present in the outer shell. Nonetheless, as Figure 2.16 shows, their diffraction images have excellent pseudo-five-fold symmetry.

The situation for cell-centered clusters is more complicated. The issue is not

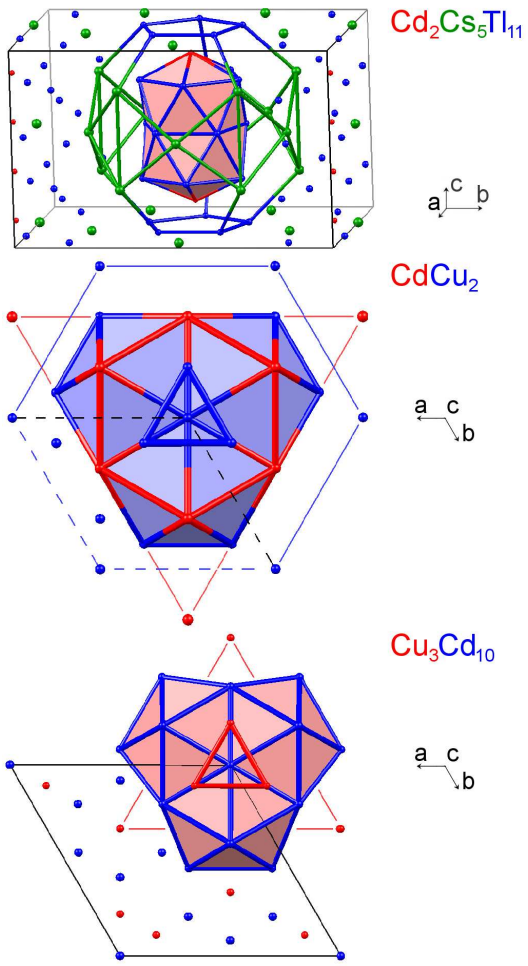

Figure 2.15: The $Cd_2Cs_5Tl_{11}$, Cu_3Cd_{10} and $CdCu_2$ unit cells. Elements are color-coded. For each structure a single edge- or polygon-centered cluster is shown. The inner shell is represented as a filled polyhedron, whose face is colored according to the central site element type. Outer shell is shown in a ball-and-stick format. Cu_3Cd_{10} and $CdCu_2$ outer shells are incomplete: to aid the eye *OTr* or *HG* sites are joined by thin lines. Where necessary for clarity, the unit cell is therefore indicated with dotted lines. $CdCu_2$ has the $MgZn_2$ structure type.

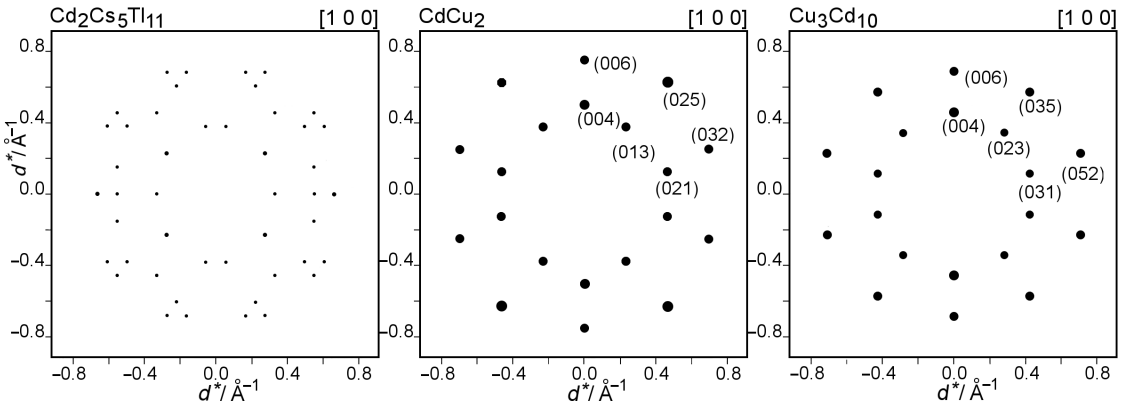

Figure 2.16: Diffraction pattern for the edge-centered $Cd_2Cs_5Tl_{11}$ and polygon-centered $CdCu_2$ and Cu_3Cd_{10} crystals along the [100] direction. For the latter two crystals, pseudo-five-fold symmetry is clear, in the former system the pseudo-symmetry is less-marked. Less evident pseudo-symmetry is often found in tetrahedral-packed crystals with small unit cells. Cerius^2 Intensity Factors: 0.10 ($Cd_2Cs_5Tl_{11}$); 0.10 ($CdCu_2$); 0.04 (Cu_3Cd_{10})

that cell-centered tetrahedral clusters are rare: they are in fact quite common. Both the ubiquitous Laves phase $MgCu_2$ (*cF24*)[10] and the important γ-brass structure (*cF52*), a structure found in Cu_5Cd_8,[120] are based on cell-centered tetrahedral clusters. Figure 2.18 shows both contain the full inner shell cell-centered cluster. γ-brass and $MgCu_2$ contain respectively the full and over half the outer shell of this same cluster. The complication is not in their structures but their diffraction images.

In Figure 2.19 we show diffraction images for three different noble-metal-rich $MgCu_2$-type structures, YNi_2,[121,122] $AuYNi_4$,[123] and $ScNi_2$.[124] (We choose these three as representative examples of noble-metal-rich Laves phases, noble metals being one focus of this chapter.) For the first two, imperfect pseudo-five fold rings composed of members of the {222}, {311}, and {220} sets of reflections

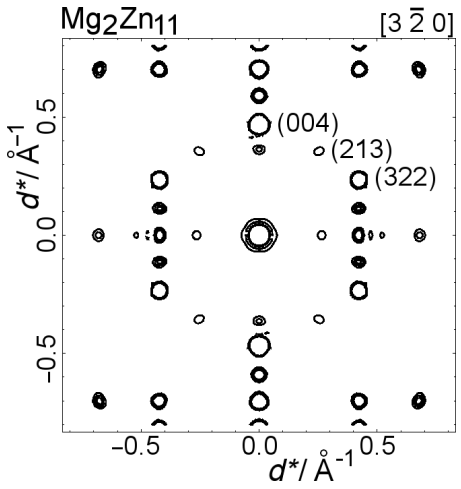

Figure 2.17: Diffraction pattern for a cluster-centered 1.5 nm diameter spherical crystallite of the vertex-centered Mg_2Zn_{11} structure shown along the [3 $\bar{2}$ 0] direction. The weak intensity of the {2 1 3} reflection in this figure is the result of this reflection's considerable to distance from the plane normal to the [3 $\bar{2}$ 0] direction. Only peaks whose peak height is $\geq 0.10 \times$ the most intense peaks are shown.

are evident. In the third, $ScNi_2$, the {220} peak is absent, while {400} is now present and the sense of the pseudo-five-fold symmetry is lost. Chemically it seems evident that scandium and yttrium play similar roles in respectively YNi_2 and $ScNi_2$, but diffraction images depend on total vs. valence electron densities and Y and Sc differ significantly from one another. This result indicates a shortcoming in using diffraction images to elucidate structural stability trends.

The situation with the diffraction pattern of γ-brass structure is even more complex. It can be understood if we refer back to the Pt_5Zn_{21} structure, a $2 \times 2 \times 2$ superstructure of γ-brass. While γ-brass contains two symmetry equivalent polygon-centered tetrahedral clusters in an I-centered cell, the Pt_5Zn_{21} structure has sixteen such clusters based on four crystallographically different polygon-centered clusters in a face-centered cell.

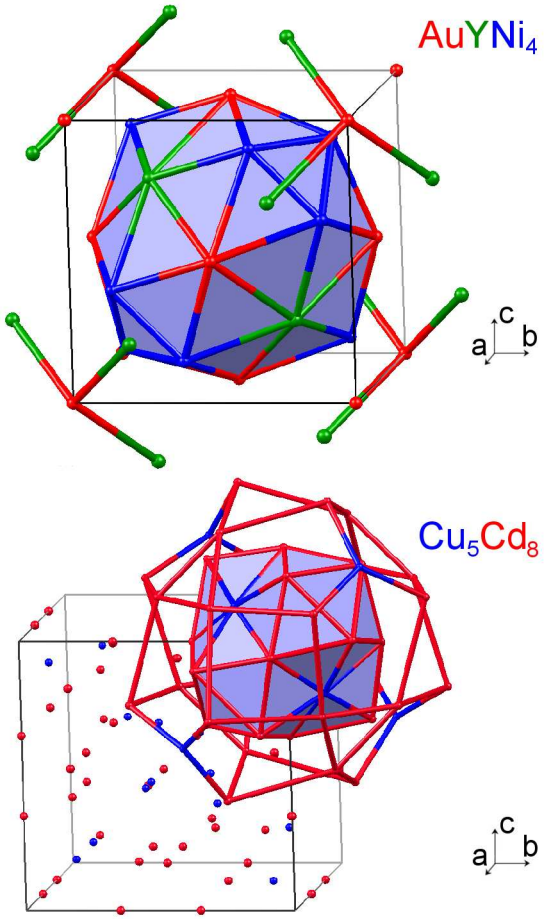

Figure 2.18: The $AuYNi_4$ and Cu_5Cd_8 unit cells. Elements are color-coded. For each structure a single cell-centered cluster is shown. The inner shell is represented as a filled polyhedron, whose face is colored according to the central site element type. While Cu_5Cd_8 has the full outer shell, $AuYNi_4$ has only the *ExT* and *GrTt* outer-shell sites. The $AuYNi_4$ is related to the $MgCu_2$ structure type, where Au and Y lie in the latter's Mg sites. Cu_5Cd_8 has the γ-brass structure.

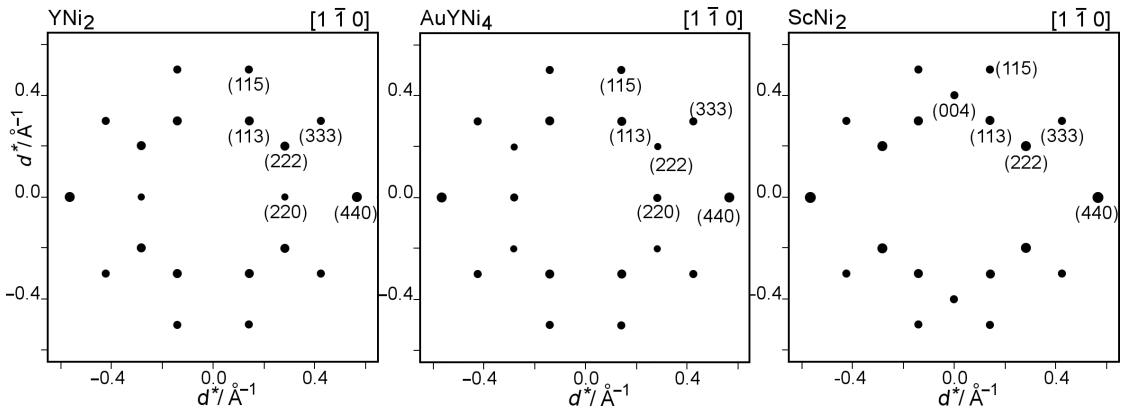

Figure 2.19: Diffraction pattern for cell-centered YNi_2, $AuYNi_4$ and $ScNi_2$ crystals along the [1 $\bar{1}$ 0] direction. All three structures are related to the $MgCu_2$ Laves structure. Pseudo-five-fold symmetry is clear in the first two structures but not the third. Cerius^2 Intensity Factors: 0.04 (YNi_2); 0.025 ($AuYNi_4$); 0.04 ($ScNi_2$).

As shown previously, the Pt_5Zn_{21} has pseudo-five fold symmetry in the $\langle 110 \rangle$ directions. Connected to one another by a pseudo-five-fold rotation along these directions are the (660), (822) , and (555) reflections. In going from the the Pt_5Zn_{21} super-structure to the parent γ-brass type, the real unit cell halves in each axis direction as do the (hkl) indices. The Pt_5Zn_{21} (660), (822) , and (555) reflections therefore correspond to the γ-brass (330), (411) , and ($2\frac{1}{2}$ $2\frac{1}{2}$ $2\frac{1}{2}$) reciprocal space vectors. Of these latter three directions, only the first two are composed of whole number indices and can correspond to γ-brass reflections. Of the four whole-numbered peaks closest to the ($2\frac{1}{2}$ $2\frac{1}{2}$ $2\frac{1}{2}$) direction, ie., the (222), (322), (332), and (333) directions, only the (222) and (332) peaks are observed; (333) and (322), both having $h + k + l = 2n + 1$, are systematically absent in the I-centered γ-brass structure.

In the case of γ-brass ,five-fold pseudo-rotations along the $\langle 110 \rangle$ directions therefore lead to four symmetrically equivalent sets of reciprocal space vectors,

{330}, {411}, {222} and {332}. (A fifth, the {422}, will also prove equally significant in a later section of the chapter.) Figure 2.20 shows the diffraction pattern orthogonal to the ⟨110⟩ direction for Cu_5Cd_8, a γ-brass structured member of the Cu-Cd phase diagram. As anticipated, these four sets of reflections are the four principal sets present in this diffraction pattern. However, although we can understand that this diffraction image as being derived from pseudo-five-fold symmetry, as this figure shows, the pseudo-symmetry itself is not easy to see.

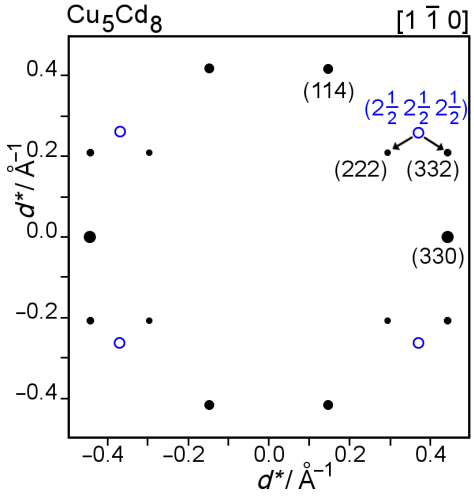

Figure 2.20: Diffraction pattern for the γ-brass-type Cu_5Cd_8 along the $[1\bar{1}0]$ direction. Five-fold rotations applied to either the (3 3 0) and (4 1 1) peaks would result in a $(2\frac{1}{2}\ 2\frac{1}{2}\ 2\frac{1}{2})$ peak, a direction not permitted in diffraction. The disallowed $(2\frac{1}{2}\ 2\frac{1}{2}\ 2\frac{1}{2})$ location is shown as an open circle. Diffraction occurs instead at (2 2 2) and (3 3 2), the two closest locations where diffraction is symmetry allowed. Cerius[2] Intensity Factor: 0.45.

2.6 Larger crystalline examples

We have considered so far crystals whose unit cells are either roughly the same size or are even smaller than the size of individual tetrahedral clusters. We can

however consider unit cells where the Pearson symbol denotes a unit cell significantly greater in size than can be accounted for by potential tetrahedral cluster sites. We could suppose that such larger crystalline structures are projections of four-dimensional objects larger than the 600-cell.

As we and others have shown these larger objects are often 4D quasicrystals,[100,104] but these quasicrystals have the same 4D point group symmetry as the 600-cell itself. In such cases, the five-fold rotational symmetry corresponding to the 720 edges of the 600-cell, retain their character as five-fold pseudo-symmetry axes in their large crystal unit cell 3-D projections. In other words, even in very large 3-D cystal structures, we do not have to delve beyond the 600-cell symmetries in order to understand 3-D pseudo-symmetries. Just as a cube or an octahedron can be used to understand the rotational symmetries of 3-D cubic unit-celled crystals such as rock salt or perovskite, the 600-cell can be used to understand the point group symmetries of 4D quasicrystals.

In looking for examples of such phases, we look for clusters which have the same point group symmetry as the projected 600-cell and whose diffraction images show the same pseudo-five-fold symmetry axes. In this section we consider just the inner-shell of the four centered tetrahedral crystals, this shell being enough to define the overall point group symmetry. We relax the previous restriction that these inner shells have chemical bond edge lengths. Indeed, tetrahedral edge lengths longer than a chemical bond are more in keeping with these crystal's large unit-cells.

Examples of such larger crystal structures are the Al-Pd-Mn,[125] Pd_3Al_7,[126] $AlMn_4$,[127] and Cd_3Cu_4 structures. These unit cells are roughly double the size of the original crystals discussed in this chapter. Their crystal structures and

their respective vertex-, edge-, polygon-, and cell-centered tetrahedral clusters are shown in Figure 2.21. Shown in Figure 2.22 and 2.23 are their corresponding diffraction images along respectively the inner-shell central-edge *CC-II*, *CE-CE*, *ITr-ITr*, and *IT-IT* directions.

Not surprisingly, both the vertex-centered cluster $SiMn_6Pd_{23}Al_{70}$ structure and the cell centered cluster Cd_3Cu_4 structure, with their large unit cells, reveal excellent pseudo-five-fold diffraction. The polygon-centered $AlMn_4$ shows an extra principal spot in its inner-most ring, the {800} set of reflections. In the next two sections we explain the origin of this spot. As we shall see, this extra set of reflections is a direct consequence of pseudo-five-fold symmetry. Finally, in the edge-centered cluster Pd_3Al_7 structure, the *CE-CE* and one of the *PG-PG* edges run in respectively the [001] and [010] directions. While the pseudo-five-fold symmetric nature of the former pattern is the more marked, the relation between the two patterns is evident.

2.7 Cluster edges and diffraction

Central edges in the vertex-, edge-, polygon-, and cell-centered tetrahedral clusters are pseudo-five-fold rotation diffraction symmetry axes. But they play an additional significant role in diffraction. This role can only be understood if we recognize that tetrahedral cluster edges can be used to define planewaves, and not just any planewaves, but in fact the strongest diffracting planewaves.

The planewaves defined by a cluster edge are planewaves whose directions of travel are exactly the same as given cluster edge bond-directions and whose wavelengths can be deduced from the cluster edge bond lengths. For exam-

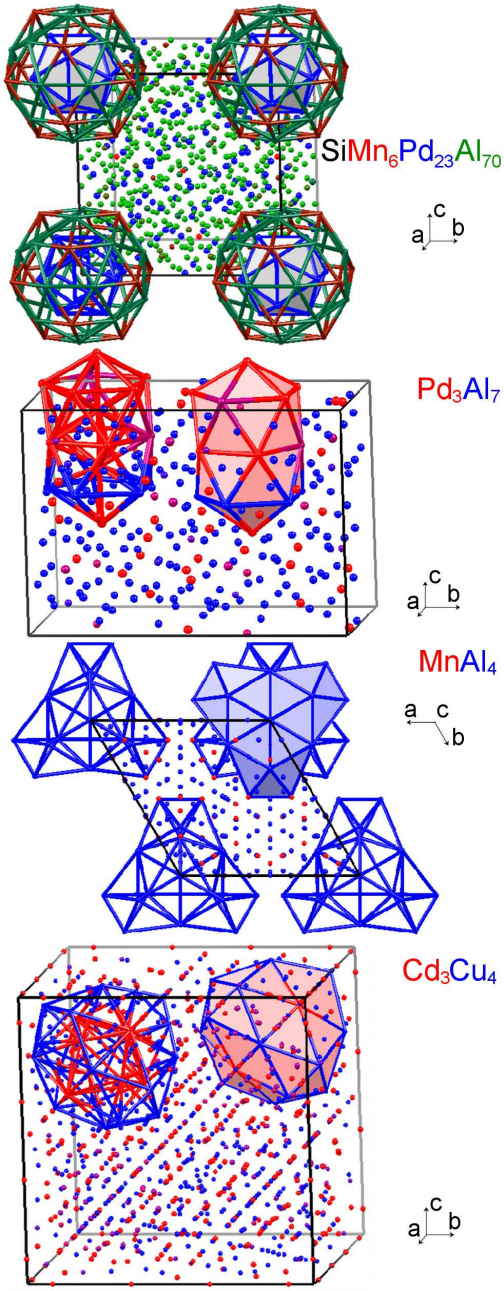

Figure 2.21: The vertex-centered $SiMn_6Pd_{23}Al_{70}$, edge-centered Pd_3Al_7, polygon-centered $MnAl_4$, and cell-centered Cd_3Cu_4 unit cells. Elements are color-coded. Mixed sites are denoted by the corresponding color mixtures: green-red mixtures appear as brown. Only a few of the possible tetrahedral clusters are shown. For $SiMn_6Pd_{23}Al_{70}$, the illustrated cluster contains both inner and outer shells; for the remaining cases only the inner shell is illustrated. Due to the large unit cell sizes, chosen here are clusters whose edges correspond to atoms spaced roughly τ further apart than regularly bonded metal atoms.

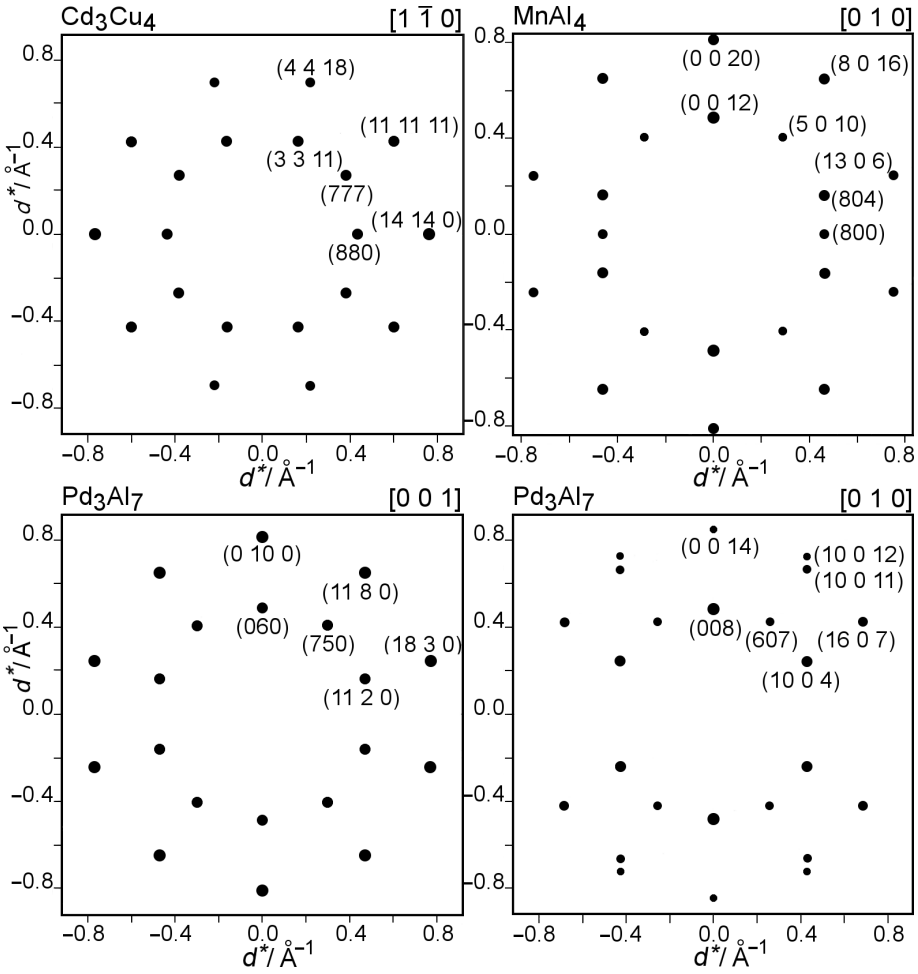

Figure 2.22: Diffraction pattern for the cell-centered Cd_3Cu_4, polygon-centered $MnAl_4$, and edge-centered Pd_3Al_7 crystals along the indicated directions. For Pd_3Al_7, the [0 0 1] and [0 1 0] directions correspond respectively to *CE-CE* and *PG-PG*. The latter pattern shows less-marked pseudo-five-fold symmetry but its relation to the former's pseudo-five-fold symmetry is evident. Cerius[2] Intensity Factors: 0.04 (Cd_3Cu_4); 0.06 ($MnAl_4$); 0.06 (Pd_3Al_7 [0 0 1]); 0.08 (Pd_3Al_7 [0 1 0]).

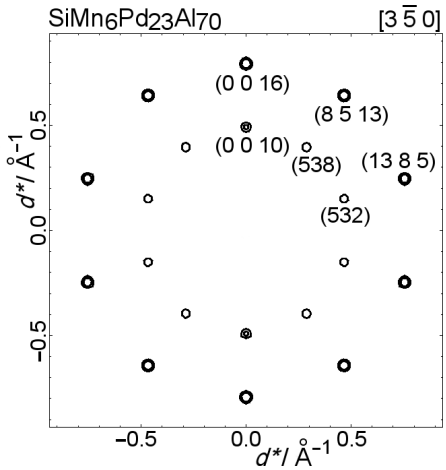

Figure 2.23: Diffraction pattern for a cluster-centered 3.0 nm diameter spherical crystallite of the vertex-centered $SiMn_6Pd_{23}Al_{70}$ structure shown along the [3 5 0] direction. Only peaks with intensity $\geq 0.29 \times$ the strongest peak are shown.

ple, we can consider a central cluster edge of respectively the $Al_6Mg_{11}Zn_{11}$ and Pt_5Zn_{21} structures. The former is a vertex-based and the latter a cell-based cubic structure. Representative central edges are therefore respectively *II-II* and *IT-IT* edges.

In Figure 2.24 we superimpose such a *II-II* and an *IT-IT* central-edge-based plane waves onto respectively the two structure's vertex- and cell-centered clusters. The two planewaves travel in the direction of respectively an *II-II* and *IT-IT* bond. Their wavelength is controlled by the edge bond length and the angles between each individual edge and the direction of travel. (As most bonds lie at an angle to the direction of travel, the optimal wavelength is shorter than the average bond length.) Figure 2.24 shows, both planewaves exhibit excellent constructive interference, and hence both plane waves could lead to strongly diffracting peaks in their respective crystal structures.

But, as we have found previously, all cluster edges are pseudo-symmetric

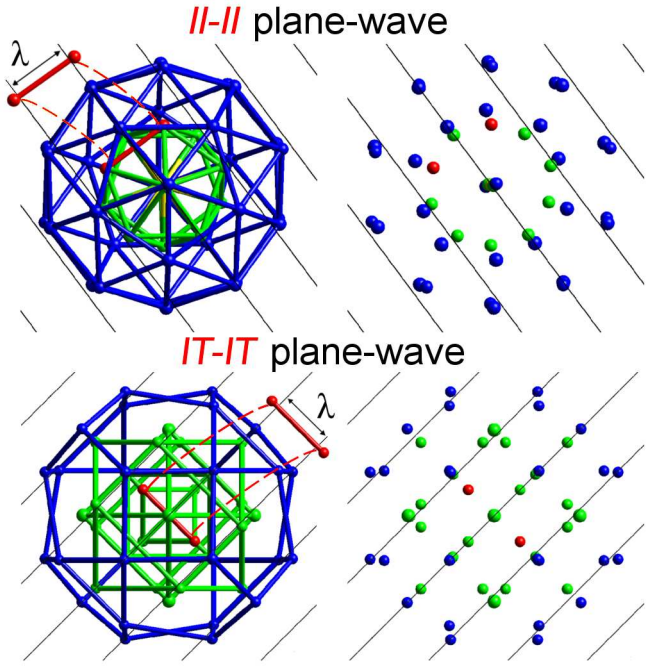

Figure 2.24: Top row: 45-atom vertex-centered cluster from the $Al_6Mg_{11}Zn_{11}$ structure together with the planewave corresponding to an *II-II* edge . Bottom row: a 54-atom cell-centered cluster from the Pt_5Zn_{21} structures together with the planewave corresponding to an *IT-IT* edge. Inner and outer shells are color coded. *II* and *IT* sites are shown in red. Both planewaves exhibit strong constructive interference with the projected clusters.

to one another. If one *CC-II* and one *IT-IT* edge-based planewave have strong constructive interference, then all the other cluster edge-based planewaves will also have similar constructive interference. Edges closest to the cluster center, having the strongest pseudo-symmetry, will naturally follow this principle the best. This fact allows for an unusual but powerful diffraction picture.

In this picture, we take the unusual step of constructing in *reciprocal space* a cluster fully similar to the inner-most shell of the real-space tetrahedral cluster. This inner-most shell contains all the cluster edges which correspond to

the most constructive interference. But as this new cluster is given in reciprocal space, these cluster edges are given in the form of reciprocal space vectors. As such edges correspond to strong constructively interfering planewaves, such a figure gives a pictorial representation of the strongest diffraction peaks.

We form such reciprocal-space clusters using crystalline reciprocal-space unit cell axes. In Figure 2.25 we do so for $SiMn_6Pd_{23}Al_{70}$ the largest unit-celled vertex-centered tetrahedral crystal structure discussed in this chapter. The inner shell of this structure consists of the *CC* site located at the origin and the twelve *II* sites located on all even permutations of $(\pm 8\,0\,\pm 5)$, a total of thirteen positions in all.

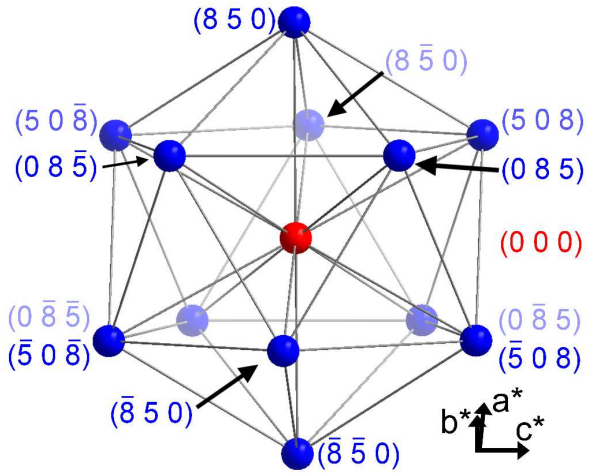

Figure 2.25: The inner shell of a vertex-centered-projected reciprocal-space 600-cell using $SiMn_6Pd_{23}Al_{70}$ reciprocal space axes as coordinate basis. The strongest diffraction peaks for the $SiMn_6Pd_{23}Al_{70}$ crystal correspond to first and second nearest neighbor vectors derived from this reciprocal space cluster. See Table 1.

Between these thirteen vertices are forty-two edges: twelve *II*-*CC*, and thirty *II*-*II* edges. As the figure shows the former edges form the {8 0 5} while the

latter are made up of the twenty-four {8 5 3} and the six {10 0 0}. Also relevant to this discussion will be second nearest neighbor pairs of sites, sites which lie on opposite sides of cluster triangular faces. There are thirty second-nearest-neighbor pairs of sites: the twenty-four {13 8 5} and the six {16 0 0}. These second nearest neighbors may also be deduced from the figure.

In Table 2.1, we show in descending order of intensity all the strongest diffraction peaks for the $SiMn_6Pd_{23}Al_{70}$ structure. This list is based on all diffraction peaks with d_{hkl} up to 1.14 , a value which corresponds to a CuKα_1 2θ value of 85°. Remarkably, the five strongest peaks in this entire structure are exactly the peaks which can be generated from the inner-shell of the reciprocal lattice tetrahedral cluster.

Table 2.1: Strongest (*hkl*) in $SiMn_6Pd_{23}Al_{70}$

(*h k l*)	d_{hkl} [1]	multiplicity	vertex−vertex (*k*-space-coord.)	vertex-vertex (atom sites)	intensity[2]
(8 0 5)	2.14[3]	12	(8 0 5) – (0 0 0)	*II-CC*	100.0
(10 0 0)	2.02	6	(5 8 0) – ($\bar{5}$ 8 0)	*II-II*	69.0
(8 5 3)	2.04	24	(8 0 $\bar{5}$) – (0 $\bar{5}$ $\bar{8}$)	*II-CC*	57.5
(13 8 5)	1.26[4]	24	(8 0 5) – ($\bar{5}$ $\bar{8}$ 0)	*II-II*	56.5
(16 0 0)	1.26	6	(8 0 5) – ($\bar{8}$ 0 5)	*II-II*	53.8
(5 0 3)	3.47	12	(13 0 8) – (8 0 5)	*OI-II*[5]	38.8
(1 0 0)	20.21	6	-	-	21.5
(5 3 2)	3.28	24	-	-	7.0

[1] Table includes d_{hkl} of up to 1.14 , corresponding to CuKα_1 2θ of 85^o.
[2] Intensity is based on powder diffraction data from the Cerius[2] suite of programs but is given per reflection, with neither atomic Debye-Waller nor Lorentz-polarization factors included.
[3] Inner shell edges have d_{hkl} ranging from 2.0 to 2.2 .
[4] Inner shell second nearest neighbors have d_{hkl} ranging from 1.2 to 1.3 .
[5] *OI* is located at {13 0 8} while *DH* is at {8 8 8} and {13 5 0}

In many structures, the most strongly diffracting peaks are (*hkl*) with low numerical indices, reflections like (100) or (110). For tetrahedrally-packed struc-

tures, the strongest peaks correspond to cluster edges. Taking into account reflection multiplicities, they form the two 10-fold rings shown in Figure 2.22; they number 72 reflections in total.

In this table first nearest neighbor edges and second nearest neighbor pairs of capping atoms can be readily distinguished from one another. First and second nearest neighbors have respectively d_{hkl} ranging from 2.0 to 2.2 and 1.2 to 1.3 . As needs be in a tetrahedrally packed icosahedral structure, these d_{hkl} are approximately related to one another by τ, the golden mean, as is expected in all tetrahedrally packed icosahedral structures, $\tau \approx 2.04 \div 1.26$.

2.8 Examples of reciprocal-space diffraction clusters

In exactly the same manner we can consider edge-, polygon-, and cell-centered tetrahedral-structures. We begin with the highest symmetry of the three remaining clusters, the cell-centered type. In Table 2.2 we list the strongest reflections in the Cd_3Cu_4 system, a phase with cell-centered clusters. Just as in the $SiMn_6Pd_{23}Al_{70}$ case, the strongest diffraction peaks are found in two rings at respectively d_{hkl} from 2.1 - 2.3 and 1.3 - 1.4 .

In Figure 2.26 and Table 2.2 we analyze these diffraction peaks using a reciprocal-space tetrahedral cluster, like the one used in the previous section but now cell-centered rather than vertex-centered. Just as in the previous example. we find all strong diffraction peaks correspond to vectors connecting the reciprocal-space cluster first or second nearest neighbors. First nearest neighbor reflections break into four sets, the {8 8 0}, {11 11 3}, {7 7 7}, and {10 4 4} reflections, a total of 68 different reflections ($68 = 12 + 24 + 8 + 24$). Second nearest neighbors

break into another three sets, the {14 14 0}, {11 11 11}, and {18 4 4} reflections, a total of 44 additional directions.

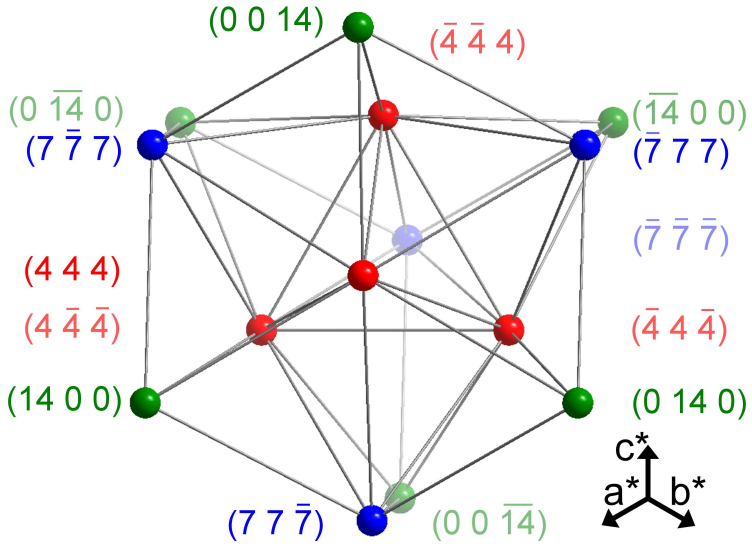

Figure 2.26: The three most central sites (*ITr*, *OTr*, and *OH*) of a cell-centered-projected reciprocal-space 600-cell using Cd_3Cu_4 reciprocal-space axes as coordinate basis. The strongest diffraction peaks for the Cd_3Cu_4 crystal correspond to first and second nearest neighbor vectors derived from this reciprocal-space cluster. See Table 2.2.

The diffraction intensity of the first nearest neighbor reflections, will prove, in the next chapter, significant for phase stability. Their intensities therefore merit close examination. In Table 2.2 we see, in cell-centered clusters, that *IT-IT* reflections are the strongest, closely followed by the *IT-OT* reflections. By contrast both *OT-OH* and *IT-OH* peaks are weaker.

If we recall the concept of the hierarchy of edges presented earlier in this chapter (Figure 2.10) we rationalize the more intense character of the former pair of edges as they are more centrally placed than the latter pair. But that noted, Table 2.2 does present the reader with an additional puzzle. In this table

the *OT-OH* peaks are shown to have an intensity three times stronger than the *IT-OH* peaks. From the point of view of the hierarchy of edges, this is surprising as the *IT-OH* and *OT-OH* edges are both roughly equidistant from the cluster center.

Table 2.2 together with Figure 2.26 accounts for this three-fold variation. Figure 2.26, shows three *OT* vertices nearly eclipsing three *OH* vertices. The three eclipsing pairs of *OH* and *OT* sites are actually related to one another by exactly the same reciprocal lattice vector, {777}, see Table 2.2. Apparently edge reflection intensity is best understood on a per edge basis. *OT-OH* edge reflection intensities therefore need to be divided by three, as they are shared amongst three edges. With this correction factor *IT-OH* and *OT-OH* edges are nearly equal in intensity.

Table 2.2: Strongest (*hkl*) in Cd_3Cu_4

(*h k l*)	d_{hkl} [1]	multiplicity	vertex−vertex (*k*-space-coord.)	vertex-vertex (atom sites)	intensity[2]
(8 8 0)	2.29[3]	12	(4 4 4) – ($\bar{4}$ $\bar{4}$ 4)	*IT-IT*	100.0
(11 3 3)	2.19	24	(4 $\bar{4}$ $\bar{4}$) – ($\bar{7}$ $\bar{7}$ $\bar{7}$)	*IT-OT*	88.8
(14 14 0)	1.31[4]	12	(7 7 $\bar{7}$) – ($\bar{7}$ $\bar{7}$ $\bar{7}$)	*OT-OT*	80.6
(7 7 7)	2.13	8	(7 $\bar{7}$ 7) – (0 $\bar{1}$4 0)	*OT-OH*	75.6
			(7 7 $\bar{7}$) – (0 0 $\bar{1}$4)	*OT-OH*	
			($\bar{7}$ 7 7) – ($\bar{1}$4 0 0)	*OT-OH*	
(11 11 11)	1.36	8	(4 4 4) – ($\bar{7}$ $\bar{7}$ $\bar{7}$)	*IT-OT*	67.5
(18 4 4)	1.37	24	(4 4 4) – ($\bar{1}$4 0 0)	*IT-OH*	34.6
(10 4 4)	2.25	24	(14 0 0) – (4 $\bar{4}$ $\bar{4}$)	*OH-IT*	25.3
(7 7 1)	2.60	24	-	-	11.3
(12 2 2)	2.10	8	-	-	10.2

[1] Table includes d_{hkl} of up to 1.14 , corresponding to CuKα_1 2θ of 85^o.
[2] As in Table 2.1, intensity is given per reflection, with neither atomic Debye-Waller nor Lorentz-polarization factors included.
[3] Inner shell edges have d_{hkl} ranging from 2.1 to 2.3 .
[4] Inner shell second nearest neighbors have d_{hkl} ranging from 1.3 to 1.4 .

Our Cd_3Cu_4 system has reintroduced to us to the concept of the hierarchy of

cluster edges. It has further introduced to us the concept of measuring intensity on a per edge rather than the per reflection basis ordinarily used to report single crystal diffraction data. Inner-most edges are the strongest. On a per edge basis the more central *IT-IT* and *IT-OT* edges are roughly four times as intense as either of the less central *IT-OH* or *OT-OH* edges.

We turn now to $MnAl_4$, a polygon-centered cluster structure. In Table 2.3 and Figure 2.27 we tabulate this structure's strongest diffraction peaks as well as a reciprocal-space polygon-centered cluster which can be used to interpret these intensities. As this table and figure show, the strongest diffraction peaks are found at d_{hkl} of 2.0 - 2.2 and 1.2 - 1.3 , corresponding to the inner shell of first and second nearest neighbors of a reciprocal-space polygon-centered cluster. First nearest neighbors are found in seven symmetry types of reflections, a total of $74 = 2 + 12 + 6 + 6 + 24 + 12 + 12$ directions. Second nearest neighbors comprise five symmetry types composed of $44 = 6 + 12 + 2 + 12 + 12$ directions.

As Table 2.3 shows, polygon-centered clusters contain more equivalent edges than cell-centered ones. For $MnAl_4$, three equivalence relations present themselves: triads of *IPr-IPr* edges point in the same direection as each other; *IL-IPr* edges point in the same direction as pairs of *IPr-OPr* edges; and finally pairs of *IL-OPr* edges point in the same direction.

With this understanding we turn to the first nearest neighbor reflections in Table 2.3, the strong reflections with d_{hkl} ranging from 2.0 to 2.2 . On a per edge basis, edges between *ITr*, *IL*, and *IPr* prove to be the most central; they are uniformly the strongest. Their intensities range from 30-45%. Edges between one of these three more central sites and the more exterior *OPr* site, on a per edge basis are weaker and range from 14-18%, a factor of two to three weaker in

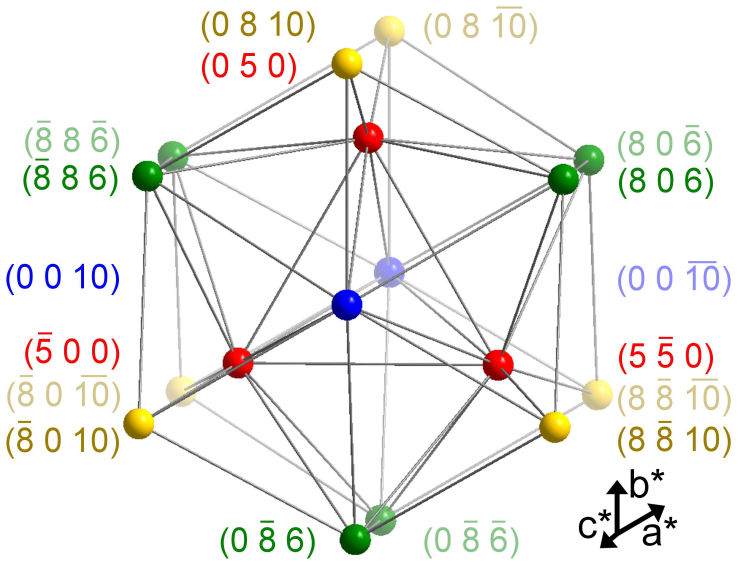

Figure 2.27: The four most central sites (*IT r*, *IL IPr*, and *OPr*) of a polygon-centered-projected reciprocal-space 600-cell using $MnAl_4$ reciprocal space axes as coordinate basis. The strongest diffraction peaks for the $MnAl_4$ crystal correspond to first and second nearest neighbor vectors derived from this reciprocal-space cluster. See Table 2.3.

intensity than the more central edges. We deduce for the {8 0 4} reflection, which is based on one central *IL-IPr* and two less central *IPr-OPr* edges, with a total intensity of 64%, that the *IL-IPr* edge has a weight of 30-45% while the *IPr-OPr* edges have a weight of 10-18%, their sum equaling the requisite total.

Only one type of centered reciprocal space tetrahedral cluster remains to be considered: the edge-centerd one. We consider the $Mn_{10}Al_{29}$ structure here. Its reciprocal space edge centered cluster and this structure's most intense diffraction peaks are presented in Figure 2.28 and Table 2.4. As Table 2.4 shows, the twenty two strongest reflections in this structure are first and second nearest neighbor vectors of the edge-centered reciprocal space cluster. First and second nearest neighbors have respectively d_{hkl} ranging from 2.0 - 2.3 and 1.2 - 1.35 .

Table 2.3: Strongest (*hkl*) for $MnAl_4$

(*h k l*)	d_{hkl} [1]	multiplicity	vertex−vertex (*k*-space-coord.)	vertex-vertex (atom sites)	intensity[2]
(0 0 12)	2.06[3]	2	(8 0 6) – (8 0 $\bar{6}$)	*IPr-IPr*	100.0
			(8 8 6) – (8 8 $\bar{6}$)	*IPr-IPr*	
			(0 $\bar{8}$ 6) – (0 $\bar{8}$ $\bar{6}$)	*IPr-IPr*	
(8 0 4)	2.04	12	(8 0 $\bar{6}$) – (0 0 $\bar{10}$)	*IL-IPr*	63.5
			(8 $\bar{8}$ 10) – (0 $\bar{8}$ 6)	*OPr-IPr*	
			(8 8 $\bar{6}$) – (0 8 $\bar{10}$)	*IPr-OPr*	
(8 8 0)	1.25[4]	6	(0 8 10) – ($\bar{8}$ 0 10)	*OPr-OPr*	55.6
(8 0 16)	1.26	12	(0 0 10) – (8 0 $\bar{6}$)	*IL-IPr*	43.3
(0 0 20)	1.23	2	(0 0 10) – (0 0 $\bar{10}$)	*IL-IL*	38.9
(5 5 0)	2.00	6	(0 5 0) – ($\bar{5}$ 0 0)	*ITr-ITr*	37.3
(8 0 0)	2.16	6	(0 0 10) – ($\bar{8}$ 0 10)	*IL-OPr*	36.1
			(0 0 $\bar{10}$) – ($\bar{8}$ 0 $\bar{10}$)	*IL-OPr*	
(5 3 6)	2.12	24	(5 $\bar{5}$ 0) – (0 $\bar{8}$ 6)	*ITr-IPr*	32.0
(5 0 10)	2.01	12	(0 0 10) – ($\bar{5}$ 0 0)	*IL-ITr*	30.1
(13 0 6)	1.27	12	(8 0 6) – (5 0 0)	*IPr-ITr*	25.8
(0 0 4)	6.17	2	-	-	24.0
(3 0 10)	2.27	12	($\bar{5}$ 0 0) – ($\bar{8}$ 0 10)	*ITr-OPr*	13.8
(8 5 10)	1.30	24	(0 5 0) – ($\bar{8}$ 0 10)	*ITr-OPr*	10.9
(5 0 9)	2.15	12	-	-	8.1

[1] Table includes d_{hkl} of up to 1.14 , corresponding to CuKα_1 2θ of 85^o.
[2] Intensity as in Table 2.1 is given per reflection, with neither atomic Debye-Waller nor Lorentz-polarization factors included.
[3] Inner shell edges have d_{hkl} ranging from 2.0 to 2.2 .
[4] Inner shell second nearest neighbors have d_{hkl} ranging from 1.2 to 1.3 .

Turning just to first nearest neighbors, for edge-centered clusters, the only edge equivalence relations connect *PG-PG* to *PPr-PPr* edges. *PG* sites lie in a pentagon. while the *PPr* sites form a pentagonal prism. As Figure 2.28 illustrates, the two pentagons of the pentagonal prism and the *PG*-pentagon itself all have edges pointing in the same direction as one another. All *PG-PG* edges are therefore equivalent to two *PPr-PPr* edges.

With this understanding, we consider diffraction intensities. The central

Table 2.4: Strongest (hkl) in $Mn_{10}Al_{29}$

(h k l)	d_{hkl} [1]	multi-plicity	vertex−vertex (k-space-coord.)	vertex-vertex (atom sites)	intensity[2]
(0 6 0)	2.07[3]	2	(0 3 0) – (0 $\bar{3}$ 0)	*CE-CE*	100.0
(7 0 2)	2.01	4	(2 0 5) – ($\bar{5}$ 0 3)	*PG-PG*	67.8
			(5 5 $\bar{3}$) – ($\bar{2}$ 5 $\bar{5}$)	*PPr-PPr*	
(4 0 5)	2.07	4	(6 0 0) – (2 0 $\bar{5}$)	*PG-PG*	57.7
			($\bar{2}$ 5 5) – ($\bar{6}$ 5 0)	*PPr-PPr*	
(2 3 5)	2.06	8	(2 0 5) – (0 $\bar{3}$ 0)	*PG-CE*	54.8
(5 3 3)	2.09	8	(0 3 0) – ($\bar{5}$ 0 $\bar{3}$)	*CE-PG*	53.3
(6 3 0)	2.12	4	(6 0 0) – (0 $\bar{3}$ 0)	*PG-CE*	52.1
(0 0 10)	1.25[4]	2	(2 0 5) – (2 0 $\bar{5}$)	*PG-PG*	51.0
(0 0 6)	2.09	2	($\bar{5}$ 0 3) – ($\bar{5}$ 0 $\bar{3}$)	*PG-PG*	48.3
			(5 5 3) – (5 5 $\bar{3}$)	*PPr-PPr*	
(7 0 8)	1.26	4	(2 0 5) – ($\bar{5}$ 0 $\bar{3}$)	*PG-PG*	47.7
(4 5 0)	2.06	4	(2 0 $\bar{5}$) – ($\bar{2}$ 5 $\bar{5}$)	*PG-PPr*	46.8
(3 5 2)	2.09	8	(5 5 $\bar{3}$) – (2 0 $\bar{5}$)	*PPr-PG*	41.5
(11 0 3)	1.28	8	(6 0 0) – ($\bar{5}$ 0 $\bar{3}$)	*PG-PG*	36.2
(1 5 3)	2.11	8	(6 0 0) – (5 $\bar{5}$ $\bar{3}$)	*PG-PPr*	32.7
(2 2 5)	2.22	2	(0 $\bar{3}$ 0) – ($\bar{2}$ $\bar{5}$ $\bar{5}$)	*CE-PPr*	29.7
(10 5 0)	1.27	4	(5 5 $\bar{3}$) – ($\bar{5}$ 0 $\bar{3}$)	*PPr-PG*	29.4
(0 10 0)	1.24	2	($\bar{6}$ 5 0) – ($\bar{6}$ $\bar{5}$ 0)	*PPr-PPr*	29.3
(3 5 8)	1.28	8	(5 5 3) – (2 0 $\bar{5}$)	*PPr-PG*	27.1
(8 5 5)	1.28	8	(6 0 0) – ($\bar{2}$ $\bar{5}$ $\bar{5}$)	*PG-PPr*	25.0
(5 2 3)	2.25	8	(5 5 3) – (0 3 0)	*PPr-CE*	23.2
(6 2 0)	2.30	4	(0 $\bar{3}$ 0) – ($\bar{6}$ $\bar{5}$ 0)	*CE-PPr*	21.3
(2 8 5)	1.30	8	(0 3 0) – ($\bar{2}$ $\bar{5}$ $\bar{5}$)	*CE-PPr*	21.1
(6 8 0)	1.32	4	(0 3 0) – ($\bar{6}$ $\bar{5}$ 0)	*CE-PPr*	12.2
(2 0 6)	2.01	8		-	10.1
(0 2 0)	6.22	8		-	9.8

[1] Table includes d_{hkl} of up to 1.14 , corresponding to CuKα_1 2θ of 85°.
[2] As in Table 2.1 intensity is given per reflection, with neither atomic Debye-Waller nor Lorentz-polarization factors included.
[3] Inner shell edges have d_{hkl} ranging from 2.0 to 2.3 .
[4] Inner shell second nearest neighbors have d_{hkl} ranging from 1.2 to 1.35 .

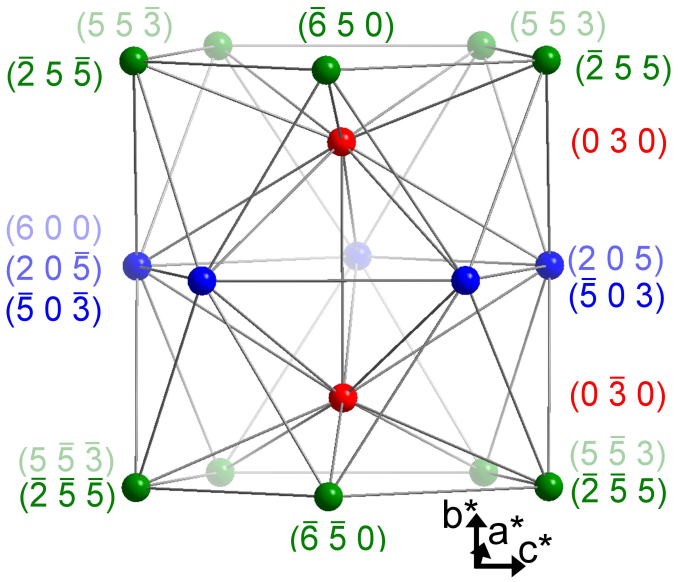

Figure 2.28: The three most central sites (*CE*, *PG*, and *PPr*) of an edge-centered-projected reciprocal-space 600-cell using $Mn_{10}Al_{29}$ reciprocal-space axes as coordinate basis. The strongest diffraction peaks for the $Mn_{10}Al_{29}$ crystal correspond to first and second nearest neighbor vectors derived from this reciprocal-space cluster. See Table 2.4.

most edge in the edge-centered cluster is *CE*, the *CE*-*CE* edge is therefore strongest and in Table 2.4 is set at 100% intensity. Edges involving the *CE* and the somewhat less central *PG* have intensities from 50 - 70%. *PPr* sites are significantly less central than *PG* sites and edges involving a *PPr* site coupled to a *CE* or *PG* edges have intensities range from 21 - 47 %. In summary, the reciprocal-space edge-centered tetrahedral-cluster proves a powerful descriptive tool for $Mn_{10}Al_{29}$ diffraction intensities.

Reciprocal-space clusters composed of projected vertex-, edge-, polygon, and cell-centered 600-cells have a significant advantage over the real-space cluster descriptions more ordinarily used.[57,102,128–132] Real-space clusters have a fundamental ambiguity to them: they can be centered with equal validity around

any of a number of different real space locations.[57] For example, in cell-centered structures, in one real space cluster description a site could be described as a cubo-octahedron, but with another center of equally high symmetry, this same site would be a truncated tetrahedron.

By definition, reciprocal-space clusters can only be centered around one point, the reciprocal-space origin. In describing the strongest diffraction reflections, only a single reciprocal-space cluster is possible. In our real space hunt for metal crystals with projected 600-cell pseudo-symmetries, especially when we turned to large unit cell examples, the real-space clusters could seem almost capriciously chosen. Reciprocal-space clusters remove such uncertainty. The crystals in this chapter have a variety of complex real-space structures, but their reciprocal-space diffraction patterns all belong to one of four types: they are vertex,-, edge-, polygon-, and cell-centered projections of the same 600-cell reciprocal-space cluster.

CHAPTER 3

CONNECTING GEOMETRIC STRUCTURE TO ELECTRONIC STRUCTURE

3.1 Introduction to the Jones model

That in tetrahedral crystals the strongest diffraction reflections are all pseudo-symmetrically equivalent to one another is significant to their crystalline stability. The connection between strong diffraction peaks and metallic stability is probably easiest understood within the context of the venerable Jones model of metallic stability. This section is devoted to a brief introduction of this model couched in the LCAO language most familiar to the chemistry community.

The Jones model is traditionally presented as a nearly-free electron model. Kinetic energy and spherical shells of electrons with similar kinetic energy certainly play a fundamental role in the theory. The Jones model speaks clearest to Hume-Rothery phases,[46,47,133] intermetallic structures with one to two valence electrons per atom, e^-/a. The reason why the Jones model is particularly suited for such compounds, however, is best understood within tight-binding electron theories such as an extended Hückel theory.[35,49,51,134,135]

We consider here three introductory cases: a linear chain, a square lattice, and an fcc structure.[5,51,136] Neither of the first two cases has much to do with actual Hume-Rothery metal structures; they are chosen instead to show us the constructs of Jones theory. In all three cases, we choose lattice constants of a and hypothetical structures composed of a single group 10-12 element. The linear chain will allow us to understand how orbital mixing takes place within the

theory. The square lattice will allow us to understand that the Jones model provides concrete lower and upper theoretical bounds for the numbers of valence electrons per atom, e^-/a. The fcc structure, which is well known in Jones metal theory, will introduce newcomers to the multifaceted Jones zone.

We consider first the 1-D chain. As is traditional, we consider first purely free electrons. For such electrons, potential energy is zero, the total energy is solely the kinetic energy, and, as an electron's reciprocal space k is proportional to the momentum, $E \propto k^2$. The total energy curve therefore has the shape of a parabola, shown in the first panel of Figure 3.1.

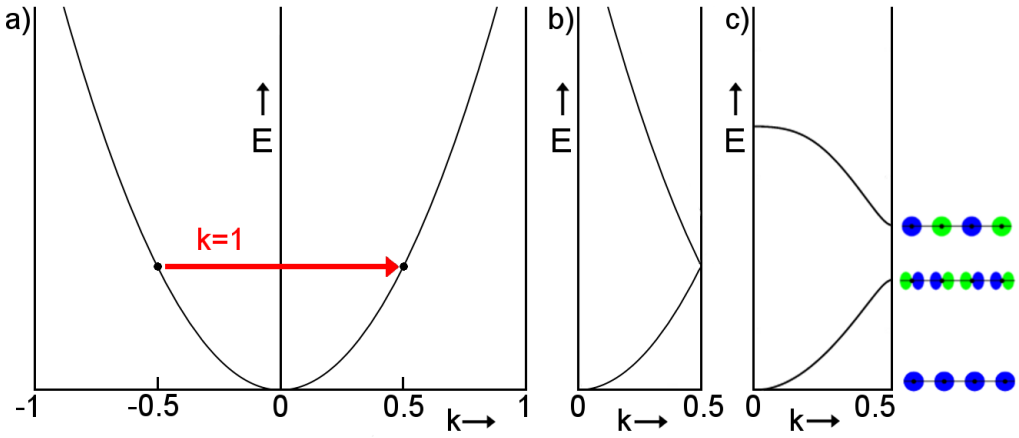

Figure 3.1: (a) Linear chain free electron energy as a function of k, the crystal momentum; (b) the "folded" format where k vectors belonging to the same linear chain irreducible representation are placed in the same vertical column; and (c) same energy bands in the presence of s and p orbital atoms. Band gap in (c) at $k = 0.5$ is caused by the difference in energy between the bonding p and the antibonding s orbitals. Note these $k = 0.5$ orbitals both correspond to plane-waves with wavelength $2a$ and are the result of the $k = 1$ Jones-mixing indicated by the red arrow in panel (a).

This free electron picture is amended by the incorporation of an actual crystal lattice, in this case a linear equally-spaced chain of group 10-12 atoms with

a lattice constant of a. Crystalline orbitals belonging to k values differing from one another by whole integers can, in the presence of a crystal, mix with one another. (We use here the standard crystallographic nomenclature where (hkl) reflections are in whole numbers or as in this case we are dealing with a 1-D system reciprocal lattice k are single whole numbers.) We place those orbitals, which by crystalline symmetry are allowed to mix with one another, vertically atop one another: the parabola takes on the "folded" form shown in the second panel of Figure 3.1.

Orbitals generally perturb most orbitals with the same initial energy. The two states at $k = \frac{1}{2}$, being at the same initial energy, therefore perturb each other significantly. In the final panel of Figure 3.1 we show the perturbed wave functions at this k-value. From the perspective of eH theory, the lower and higher energy orbitals are a bonding p state and an antibonding s state. Preparing for real crystal structures, the bonding p orbital will become $HOMO$-like and will be filled, while the antibonding s orbital will be $LUMO$-like and be unfilled. (In group 10-12 tetrahedral structures, there are pseudo-bandgaps rather than actual bandgaps. Unlike what is found for the 1-D chain, the language of $HOMOs$ and $LUMOs$ is therefore only approximate.)

Equally important are the two orbitals viewed the nearly-free electron standpoint. From this perspective, we note that both the bonding p and antibonding s states resemble planewaves, planewaves with exactly the same wavelength, $\lambda = 2a$, see figure. Such a wavelength corresponds to $k = \pm\frac{1}{2}$. Within the context of free electrons, the bonding p and antibonding s states are linear combinations of the complex planewaves $e^{\frac{2\pi ikx}{a}}$ where $k = \pm\frac{1}{2}$.

Important in the Jones model are these initially free-electron planewave or-

bitals which had to become mixed in order to form the linear chain $k = \pm\frac{1}{2}$ $HOMO$ and $LUMO$ orbitals. In the first panel of Figure 3.1 we indicate which points on the initial parabola correspond to these two planewaves. As this figure shows, these two states differ from one another by $k = 1$, represented in this figure as an arrow.

In Jones theory, electron orbitals are perturbed free-electron orbitals. These perturbations are caused by the atoms in the crystal lattice. The magnitude of these perturbations is measured by the strength of individual diffraction peaks. In the 1-D chain example, we recognize that $k = 1$ is a strong diffraction peak. We therefore consider the bonding p state and an antibonding s states found at $k = \frac{1}{2}$ to be the result of $k = 1$ mixing between the $e^{\frac{2\pi i \frac{1}{2} x}{a}}$ and $e^{\frac{2\pi i \frac{-1}{2} x}{a}}$ planewaves. In Jones theory, the important orbital mixings are always consequences of strongly diffracting reciprocal lattice vectors.

We now consider the 2-D square lattice. In Figure 3.2 we show the "spaghetti" diagram for the two lowest energy orbitals from Γ, $(hk) = (0\ 0)$; to X, $(hk) = (\frac{1}{2}\ 0)$; and finally M, $(hk) = (\frac{1}{2}\ \frac{1}{2})$. (We follow here crystallographic convention and do not place commas between the different vector terms.) As this figure shows, at X the lower and higher energy orbitals are respectively a very bonding p orbital and a net non-bonding s orbital while at M the lower and higher energy orbitals are respectively a net-bonding p orbital and a very antibonding s orbital. All four orbitals are plane-wave-like. At X and M, as can be seen in the figure, their wavelengths are respectively $\lambda = 2a$ and $\lambda = \sqrt{2}a$.

Within the context of Jones theory, the splitting between bonding and non-bonding states at X is due to mixing between $e^{\frac{2\pi i \vec{k}\cdot\vec{x}}{a}}$ with $\vec{k} = (-\frac{1}{2}\ 0)$ and $\vec{k} = (\frac{1}{2}\ 0)$, the two states differing from one another by $\vec{k} = (1\ \ 0)$, a significant diffraction

peak of the structure. In Jones theory, whenever two states are connected to one another by a strong diffraction peak, strong orbital mixing results. Thus the different energies of the bonding and antibonding states at M are the result of mixing between the $e^{\frac{2\pi i\vec{k}\cdot\vec{x}}{a}}$ for $\vec{k} = (-\frac{1}{2}\ -\frac{1}{2})$ and $\vec{k} = (\frac{1}{2}\ \frac{1}{2})$ states, two states differing from one another by $\vec{k}$ = (1 1), another strong diffraction peak.

In Figure 3.2 we show the first Brillouin zone for the 2-D square lattice. This Brillouin zone is in the shape of a square. (1 0), the strong diffraction peak, is shown as an arrow connecting one side of the first Brillouin zone to the opposite side. Two X states are coupled by this arrow. But (1 0) being strong, not only can two X states couple, any state on one square-edge of the Brillouin zone with $(h\,k) = (\frac{1}{2}\,k)$ can couple to another state on the opposite side of the Brillouin zone with $(h\,k) = (-\frac{1}{2}\,k)$

The first panel of Figure 3.2 shows the result of these mixings. Between X and M, the points under discussion here, there is a clear separation between lower and higher energy states. Within the context of Jones theory, this energy separation can be thought of as a splittings due to the intensity of the (1 0) diffraction peak.

We now consider estimates of the most stable electron count. We are interested here in developing bounds for the optimal electron count. The question we pose first is how to represent optimal electron counts on a spaghetti diagram. In the third panel of Figure 3.2 we enlarge the spaghetti diagram for $(h\,k)$ ranging from $M_1 = (-\frac{1}{2}\ \ \frac{1}{2})$, to $X = (\frac{1}{2}\ 0)$, and finally to $M_2 = (\frac{1}{2}\ \frac{1}{2})$. As this figure shows, the two lowest energy bands are both single-minimum curves, one cradled inside the other. Also placed in this figure, shown as a dotted line, is a third curve, the average of the previous two, which can be taken as the energies

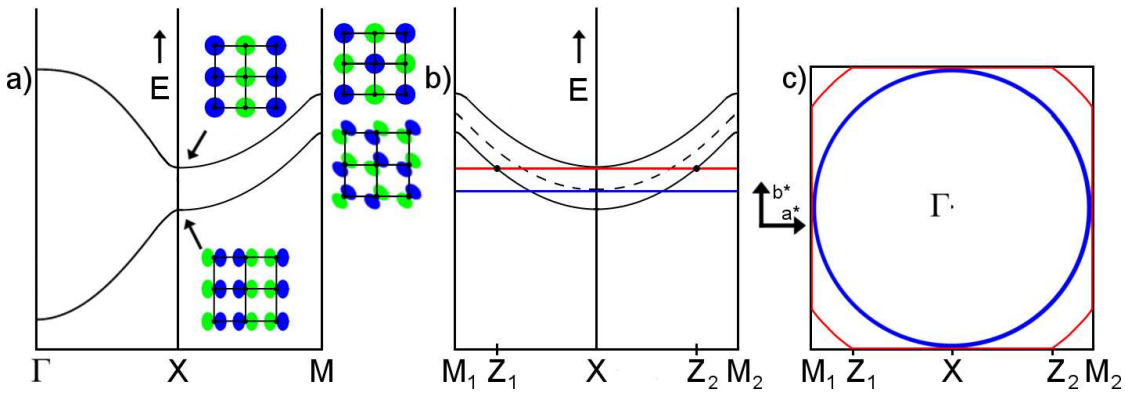

Figure 3.2: (a) The two lowest energy square lattice s and p bands from Γ, (0 0); to X, ($\frac{1}{2}$ 0); to M, ($\frac{1}{2}$ $\frac{1}{2}$). (b) The energies of the two lowest bands from M_1, ($\frac{1}{2}$ $\bar{\frac{1}{2}}$); through X; to M_2, ($\frac{1}{2}$ $\frac{1}{2}$). The separation between these two bands is due to Jones mixing. Band energies prior to mixing are shown as a dotted curve. (c) The square lattice first Brillouin zone, shown as a black square. Inscribed inside this square is a blue circle. Both the blue circle in (c) and the horizontal line in (b) denote the same electron count. Optimal electron filling based on Jones mixing is shown in red. Both panels (b) and (c) indicate for this optimal electron count that, from Z_1 to Z_2, a single band is filled, while nearer M_1 and M_2, no orbital is filled. The black square, which is also termed the Jones zone,[5] and the blue circle therefore provide upper and lower bounds for the optimal filling shown in red.

of these two bands before mixing had set in.

We focus first on this dotted line curve. The energy of this dotted line curve unlike the other two, refers to energies where no Jones mixing has taken place. It describes purely free electrons. Were we to consider the purely free electron model and occupy all states up to the bottom-most point of the dotted line curve (this electron occupation is represented as a blue horizontal line), we would have on hand an electron filling in k-space which corresponds to a circle which just reaches the point X.

We now turn on Jones mixing. The dotted line curve splits into the two single minimum functions. We wish to fill as many as possible of the lower energy function while filling as few as possible of the higher energy function. The optimal electron filling is shown as a red horizontal line, which just touches the nadir of the higher energy curve. Were the electron filling to be any greater in value, we would begin filling the bottom of the upper curve, *s* states which are all slightly antibonding in character. Conversely were we to make the value any lower, we would depopulate states from the lower energy curve, *p* states which are all bonding in character.

As this figure shows, the optimal electron count never intersects the upper energy curve composed solely of antibonding orbitals, and crosses the lower all-bonding curve at points Z_1 and Z_2. From Z_1 to X to Z_2, each point in K-space has a single occupied orbital; from M_1 to Z_1 and M_2 to Z_2 there are no occupied orbital.

We now translate back these results to the Brillouin zone diagram. After Jones mixing has set in, just as in the spaghetti diagram, in the Brillouin zone diagram, all $\vec{k}$ at the edge of the Brillouin zone from Z_1 to X and finally to Z_2 have a single filled orbital. Just as in the spaghetti diagram, those points on the zone edge closer to M_1 and M_2 are entirely devoid of electrons. Importantly, even at X itself, the point where the upper energy function is lowest in energy, only a single one of the two lowest energy bands is filled. We represent this optimal filling by the red curve in the second panel of Figure 3.2. This red curve leaves the edges of the Brillouin zone exactly at the points Z_1 and Z_2. As at no point in the first Brillouin zone is any more than a single orbital filled, no point outside the Brillouin zone is ever filled.

The optimal filling being the one presented, establishing lower and upper bounds within the context of Jones theory becomes straightforward. A lower bound is the area of the largest possible circumscribed circle inside the Brillouin zone, represented as a blue circle (this blue circle corresponds to the blue horizontal line in the adjacent panel). An upper bound is the first Brillouin zone itself. In both these bounds just a single orbital is occupied. These areas may be initially thought of as being in units of orbitals per k-space unit cell. However as we know that a reciprocal space unit cell corresponds to a given real space unit cell, and as we also know the number of atoms per real space unit cell, we can convert these answers from an orbital/reciprocal space unit cell area to an electron/per atom basis.

Let us say that the number of atoms in the real space cell is n and that in units of orbitals per reciprocal space unit cell area, the lower and upper bounds are respectively L and U. The lower and upper bounds in terms of electrons per atom would then be respectively $2L/n$ and $2U/n$, the factor of 2 coming about as there are two electrons to fill every single orbital and the n converting from a reciprocal space unit cell to a real space per atom basis.

We finally, briefly turn to the 3-D fcc structure. In 2-D, the {1 0} diffraction peaks formed the *edges* of the first Brillouin zone. In the 3-D fcc structure, the strong {2 0 0} and {1 1 1} reflections form the *faces* of a polyhedron , termed the Jones zone. This polyhedron is shown in Figure 3.3. Jones zones prove important in the qualitative understanding of noble metal tetrahedral structures.

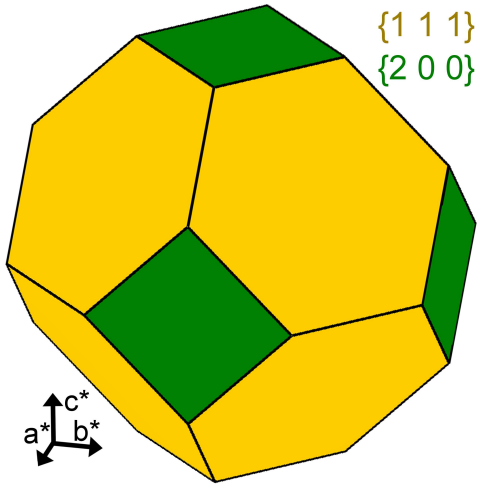

Figure 3.3: The face-centered-cubic Jones zone. The Jones zone is a truncated octahedron generated by the eight {1 1 1} and six {2 0 0} reflections.

3.2 Group 10-12 tetrahedral-cluster structures

The Jones model starts with the observation that free electrons with the same energy lie in *k*-space on a sphere centered at the origin and that crystal structures perturb these free electron states. Through the intermediary of the crystal structure, electronic states couple one another. In the Jones model, electronic states connected to one another by *k*-space vectors, which are themselves strong diffraction vectors, are the electronic states which themselves couple the most strongly.

We therefore consider a *k*-space polyhedron whose faces are always connected to faces on the opposite side by strong diffracting reciprocal lattice vectors. These *k*-space polyhedra are termed Jones zones and represent those points in *k*-space whose electronic states most strongly couple with one another. From the perspective of Jones theory, a metal structure is most stable if its Jones zone

is as similar in possible to the free electron sphere comprised of the metal's valence electrons.

Were the Jones zone and the free electron sphere to be as identical as possible with each other, then orbitals at the the Fermi energy, which in the free electron model are all states which lie on *the surface* of the free electron sphere, would also be points on the Jones zone and therefore would be able to couple with one another. Orbitals at the Fermi energy would therefore split into lower energy, possibly bonding orbitals, and higher energy, possibly antibonding orbitals. In a metal, a pseudogap appears in its band diagram, reminiscent of a HOMO-LUMO gap in a molecule. Like a large HOMO-LUMO gap, a large pseudogap stabilizes the system.[137]

The Jones model presents clear lower and upper limits for the the number of valence electrons. The lower limit is defined by the smallest free electron sphere which just touches a crystal structure's Jones zone.[138] The upper limit is the volume of the Jones zone itself expressed in units of valence electrons per atom, e^-/a.

When looking for an every day analogy of an ideal Jones zone, an excellent object to consider is a soccer-ball-shaped polyhedron, a polyhedron with 32 nearly equidistant faces which looks very much like a sphere. Tetrahedral metal structures can be viewed from this context. As we have seen, tetrahedral cluster structures can have even more than 32 strong diffraction peaks. Some have as many as 72. And these diffraction peaks are all pseudo-symmetric with one another, have roughly the same d_{hkl}, and hence all lead to faces on the Jones zone all roughly equidistant from the center. A tetrahedral structure's Jones zone, could be even more sphere-like than a soccer ball polyhedron, and in one

or two cases, their Jones zones actually are.

Tetrahedral-cluster structures can provide ideal Jones zone candidates. In this section we will consider this connection but only for compounds solely composed of group 10-12 elements (though in order to find an example of an edge-centered tetrahedral cluster we will be forced to relax our criteria to a compound composed of group 10 and 13 elements).

We restrict ourselves to elements from these three columns for mainly three reasons. First the Hume-Rothery electron phases can all be built up from the elements in the same three columns, and Hume-Rothery phases all obey specific electron count rules.[137,139,140] Their connection with the Jones model has been previously established. Second, no transition element with a partially filled *d*-band is included, so that we can assume *a-priori* that the *d*-bands are entirely filled. And third, we include neither groups 1 or 2 elements. Such elements are chemically so dissimilar to group 11 and 12 elements, that assuredly factors other than just electron count must play a role in chemical stability.

We begin with a cubic structure, $Zn_{11}Au_{15}Cd_{23}$, Figure 3.4, an I_h quasicrystalline approximant structure which has the perhaps unique virtue that it is solely based on groups 10-12 elements. Although based on the Mackay real space cluster,[141] as Table 5, Figure 3.5 and Figure 3.6 show, the diffraction in this crystal is well described by a reciprocal-space vertex-centered tetrahedral cluster. In Table 3.1 we list the strongest reflections for $Zn_{11}Au_{15}Cd_{23}$. The strongest diffraction peaks in this structure correspond to the nearest neighbors of a 13-atom reciprocal space cluster. This cluster is comprised of a site at the origin, *CC*, and twelve atoms in an icosahedron, *II*, centered on the origin at {5 0 3}. This cluster is shown in the left panel of Figure 3.6.

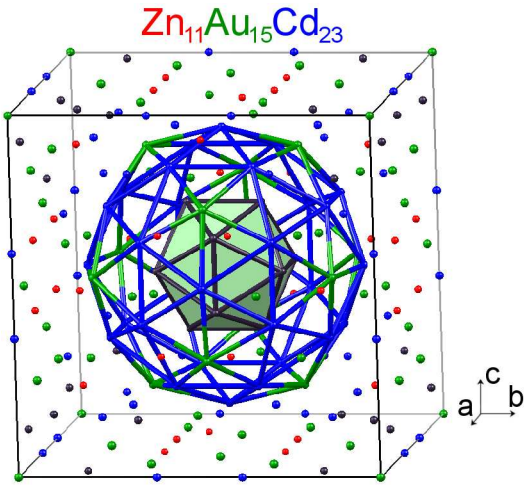

Figure 3.4: The $Zn_{11}Au_{15}Cd_{23}$ unit cell. Elements are color-coded and a single vertex-centered cluster is shown. Inner and outer shells are represented respectively in filled-polyhedron and ball-and-stick formats. The polyhedral faces are green as a Au atom lies at the cluster center.

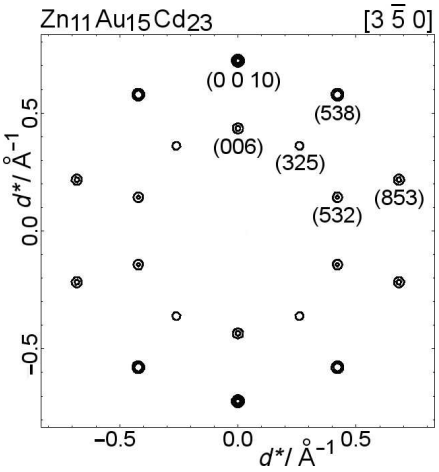

Figure 3.5: Diffraction pattern for a cluster-centered 3.1 nm diameter spherical crystallite of the vertex-centered $Zn_{11}Au_{15}Cd_{23}$ unit cell structure shown along the [3 5 0] direction. 819 atoms, 819/146 about 5.6 unit cells. Ratio: 0.27.

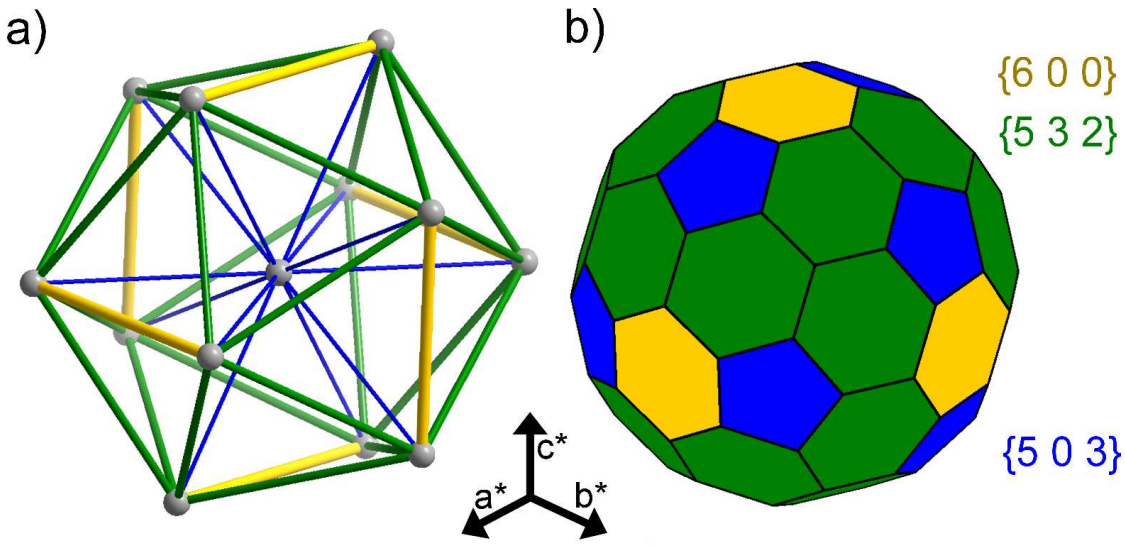

Figure 3.6: Vertex-centered reciprocal-space cluster and Jones zone for $Zn_{11}Au_{15}Cd_{23}$. The axes shown in the graph indicate relative directions only of the three reciprocal cell axes. $Zn_{11}Au_{15}Cd_{23}$ is a 1/1 quasicrystalline approximant. Its Jones zone differs significantly from the Jones zone presented previously for the 1/1 quasicrystalline approximant $Zn_{20}Al_{40}Mg_{40}$. The previously reported Jones zone is comprised of the {7 1 0}, {5 4 3}, and {5 5 0} reflections, with respective diffraction intensities of 23.0, 26.1, and 0.0%. Interestingly, the strongest intensity reflections for $Zn_{20}Al_{40}Mg_{40}$ are the {5 0 3}, {6 0 0}, and {5 3 2} reflections, with respective intensities of 100.0, 86.2, and 68.9%, the same three sets of reflections found in $Zn_{11}Au_{15}Cd_{23}$. In both structures the latter three reflections are the strongest, the second strongest, and the third strongest of all diffraction peaks up to CuKα_1 of 50°.[†]

The reciprocal space tetrahedral cluster provides us with all the information required to make the Jones zone. We need to make a polyhedron where parallel

[†]Previous work has suggested that the Jones mechanism for MacKay-based 1/1 quasicrystalline approximants takes place across {hkl} reflections where $h^2 + k^2 + l^2 = 50$.[142] Planes such as {710}, {543}, and {550} fulfill this requirement. Were we to use these planes for $Zn_{11}Au_{15}Cd_{23}$, we would obtain lower and upper e^- bounds of 2.54 - 2.70 e^-/a, one whole electron/atom higher than the experimentally observed value. As $Zn_{20}Al_{40}Mg_{40}$, contains 40% of the group 2 element magnesium, a modified electron counting approach beyond that done in classic Hume-Rothery theory would appear appropriate.[143]

Table 3.1: Strongest (*hkl*) for $Zn_{11}Au_{15}Cd_{23}$

(*h k l*)	d_{hkl}[1]	multiplicity	vertex−vertex (*k*-space-coord.)	vertex-vertex (atom sites)	intensity[2]
(6 0 0)	2.31	6	(3 5 0) – ($\bar{3}$ 5 0)	*II-II*	100.0
(5 3 2)	2.25	24	(5 0 $\bar{3}$) – (0 $\bar{3}$ $\bar{5}$)	*II-II*	69.0
(5 0 3)	2.37	12	(5 0 3) – (0 0 0)	*II-CC*	36.8
(6 2 0)	2.19	12	-	-	24.1
(4 3 3)	2.37	6	-	-	14.5

[1] Table includes d_{hkl} of up to 1.81 , corresponding to CuKα_1 2θ of 50°.
[2] Intensity as in Table 2.1 is given per reflection, with neither atomic Debye-Waller nor Lorentz-polarization factors included.

faces on opposite sides of the polyhedron are related to one another by one of the edges of the reciprocal space tetrahedral cluster. In the right panel of Figure 3.6 we illustrate this Jones zone. The {6 0 0} edges, which are illustrated in yellow in this figure, generate six faces, shown in yellow in the Jones zone. Only three of these faces can be shown in our single hemisphere picture of the Jones zone. The other three faces are on the exact opposite side of the three shown faces and are thus connected to one another by vectors corresponding to the {6 0 0} edges of the reciprocal space tetrahedral cluster.

The reciprocal lattice cluster contains 42 distinct edges with near I_h symmetry. The corresponding Jones zone is therefore a polyhedron of 42 facets with the same near I_h symmetry. Its near spherical shape is self-evident and corresponds to the shape of the C_{80} buckyball. It is even more spherical in shape than the C_{60} shape, the latter shape being the shape which corresponds to soccer balls.

Of the three sets of reciprocal lattice vectors used in making this Jones zone, that which has the smallest *d*-spacing is the {5 0 3} reflections. They therefore define the Jones model lower bound at an electron count of 1.42 e^-/a. This

lower bound is computed from the volume of the corresponding free-electron sphere. The {5 0 3} peaks lead to a sphere with a radius of $\frac{\pi}{a}\sqrt{5^2+0^2+3^2} = 1.323$ $^{-1}$, where $a = 13.84$, the cell parameter. A sphere with this radius has volume 9.700 $^{-3}$. This number must be contrasted with the volume of a reciprocal space unit cell itself, $\left(\frac{2\pi}{a}\right)^3 = 9.350\times10^{-2}$ $^{-3}$. We conclude that the {5 0 3} sphere contains 103.8 reciprocal space unit cells ($103.8 = 9.700 \div 9.350\times10^{-2}$). In the free electron model reciprocal space unit cells equal orbitals/unit cell. The lower bound is therefore 103.8 orbitals/unit cell.

The upper bound is the volume of the Jones cell. In this case, the Jones cell has three face types ({5 0 3}, {6 0 0}, and {5 3 2}), planes which are at distances of 1.323, 1.362, and 1.399 $^{-1}$ from the origin. Numerical integration results in a volume of 11.548 $^{-3}$, equivalent to 123.5 orbitals/unit cell ($123.5 = 11.548 \div 9.350\times10^{-2}$).

As there are 146 atoms in each unit cell, and assuming two electrons fill each orbital, we deduce that $Zn_{11}Au_{15}Cd_{23}$ has lower and upper bounds of, respectively, 1.42 valence electrons/atom (e^-/a) ($1.42 = (103.8\times2)\div146$) and 1.69 e^-/a ($1.69 = (123.5\times2)\div146$). These numbers are tabulated in Table 6.

Of these two bounds, the upper bound proves more relevant. Within experimental error, it is the same as the experimentally determined electron count, which is calculated to be 1.69 e^-/a, ($1.69 = [(2\times11)+(1\times15)+(2\times23)]\div(11+15+23)$). In the limit of a perfectly spherical shape, or alternatively in the presence of very strong Jones orbital mixing, the upper bound of the Jones model becomes the actual predicted Jones model electron count. It is plausible that up to three significant figures in its electron count, $Zn_{11}Au_{15}Cd_{23}$ has reached this limit.

Table 3.2: Valence electron count for group 10-12 tetrahedral cluster crystal structures

compound	vertices tetrahedral cluster	number faces	cut-off[1]	lower bound e^-/a	range expt. e^-/a	upper bound e^-/a
vertex-centered cluster						
$Zn_{11}Au_{15}Cd_{23}$	*CC + II*	42	0.30	1.42	1.69	1.69
edge-centered cluster						
Pd_3Al_7	*CE + PG*	32	0.30	1.83	2.10	2.38
Pd_3Al_7[2]	*CE + PG + PPr*	72	0.20	1.71	2.10	2.06
polygon-centered cluster						
$CdCu_2$	*ITr + IL + IPr*	18	0.30	0.97	1.33	1.40
Cu_3Cd_{10}	*ITr + IL + IPr*	56	0.30	1.59	1.77[3]	1.85
cell-centered cluster						
Cd_3Cu_4	*IT + OT + OH*	68	0.30 or 0.20	1.35	1.43	1.52
Cu_5Cd_8[4]	*IT + OT*	36	0.30	1.54	1.57-1.66	1.73
Cu_5Cd_8	*IT + OT + OH*	36	0.20	1.54	1.57-1.66	1.73
Pt_5Zn_{21}	*IT + OT*	36	0.30 or 0.20	1.54	1.62	1.73

[1] Only {*hkl*} with intensities higher than stated cut-off × maximum intensity reflection are considered in Jones calculation. If a vertex causes a single (*hkl*) to exceed a given cut-off all reflections due to the vertex type are included.

[2] The Pd_3Al_7 single crystal refinement lists variations in thermal parameters from B=0.02 to 1.97. The upper bound and the experimental e^-/a are therefore only approximately known.

[3] The Cu_3Cd_{10} phase has variable composition. However as there is considerable vacancy disorder, we can calculate the Jones volume only where there is a solved single crystal structure. In this solved structure there are 26.4 atoms/unit cell.

[4] Cu_5Cd_8 is a γ-brass structure. Its range of experimental electron counts resembles that of many other γ-brass structures. In the case of Cu_5Cd_8 there is substitutional but no vacancy disorder. Therefore the upper bound Jones estimate stays at a constant value.

In Table 3.3 we list the strongest reflections for the cell-centered Pt_5Zn_{21} structure. As expected, its strong diffraction peaks can be rationalized based on a reciprocal lattice cell-centered tetrahedral cluster with *IT*, *OT* and *OH* sites at respectively {3 3 3}, {$\bar{5}$ $\bar{5}$ $\bar{5}$} and {10 0 0}. As this table shows, the most central edges, *IT*-*IT* (the {660} reflections) and *IT*-*OT* (the {822} reflections) are the most significant of all diffraction peaks. However the next most central edges, those which include the *OH* site (the {5 5 5} and {7 3 3} reflections) are the third and sixth strongest peaks overall. Their intensities, on a per edge basis, are however

Table 3.3: Strongest (*hkl*) for Pt_5Zn_{21}

(*h k l*)	d_{hkl}[1]	multiplicity	vertex−vertex (*k*-space-coord.)	vertex-vertex (atom sites)	intensity[2]
(6 6 0)	2.13	12	(3 3 3) – ($\bar{3}$ $\bar{3}$ 3)	*IT-IT*	100.0
(8 2 2)	2.13	24	(3 $\bar{3}$ $\bar{3}$) – ($\bar{5}$ $\bar{5}$ $\bar{5}$)	*IT-OT*	33.4
(5 5 5)	2.09	8	(5 5 $\bar{5}$) – (0 0 $\bar{10}$)	*OT-OH*	6.7
			(5 $\bar{5}$ 5) – (0 $\bar{10}$ 0)	*OT-OH*	
			($\bar{5}$ 5 5) – ($\bar{10}$ 0 0)	*OT-OH*	
(4 2 2)	3.69	24	-	-	4.9
(3 3 3)	3.48	8	-	-	4.1
(7 3 3)	2.21	24	(10 0 0) – (3 $\bar{3}$ $\bar{3}$)	*IT-OH*	3.6
(5 1 1)	3.48	24	-	-	3.4

[1] Table includes d_{hkl} of up to 1.81 , CuKα_1 2θ of 50°.
[2] Intensity as in Table 2.1 is given per reflection, with neither atomic Debye-Waller nor Lorentz-polarization factors included.

more than a factor of ten weaker than the *IT-IT* and *IT-OT* reflections.

This table introduces us to a short-coming in the traditional Jones zone model. Once included as a principal diffraction peak, the traditional Jones model does not further take into account relativeintensities. While the {5 5 5} and {7 3 3} undoubtedly play a role in the phase stability of Pt_5Zn_{21}, their role should be lesser than the role played by the {6 6 0} and {8 2 2} reflections.

Within the confines of the traditional Jones model, we therefore only wish to consider the effect of the most significant peaks. Examining the structures reported in Chapter 2 we see that a cut-off of reflections whose intensities are at least 30% provides generally a clean break between inner-most shell and more exterior edges. As Table 3.2 shows, changing this cut-off from 0.30 to 0.20 does not in most cases substantially change the Jones model estimates.

That the Jones model requires an *ad-hoc* cut-off value nevertheless is a poten-

tial liability to the model. Yes, the matching of experimental electron counts to upper and lower Jones bounds can be insensitive to the exact cut-off used. But with any arbitrary cut-off, the possibility that agreement between theory and experiment is being forced rather than being naturally achieved is always an issue.

Using this cut-off value, for Pt_5Zn_{21} we include only the *IT-IT* or *IT-OT* reflections. These two edge types lead to the two Jones zone face types presented in Figure 3.7. The illustrated Jones zone is a well-known one, it is that of γ-brass and consists of 36 faces with O_h symmetry.

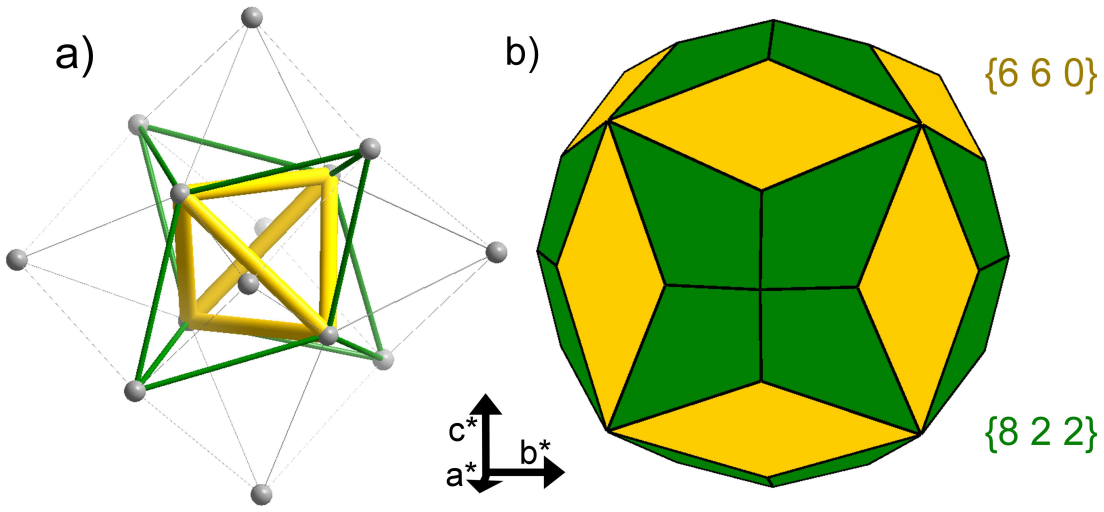

Figure 3.7: Cell-centered reciprocal-space cluster and Jones zone for Pt_5Zn_{21}. Colored cluster based on sites with reflection intensities ≥ 0.30 of the most intense reflection. Reflections are color-coded. The reflections are listed in descending order of intensity and cluster cylinder radii are proportional to intensity. See Table 7. The axes shown in the graph indicate relative directions only of the three reciprocal cell axes. Cluster and Jones zone are not to scale of each other.

The Jones zone approaches a spherical symmetry, though not quite as spherical as the $Zn_{11}Au_{15}Cd_{23}$ Jones zone. Its volume is 360.0 orbitals per unit cell and as there are 416 atoms in each unit cell, we deduce a Jones volume of 1.73 valence electrons/ atom (e^-/a) eg., 1.73 = (360.0×2)÷416. These values can be contrasted with the experimental value of 1.62 e^-/a, $1.62 = [(0 \times 5) + (2 \times 21)] \div (5 + 21)$.and a lower bound of 1.54 e^-/a, see Table 3.2.

The edge-centered Pd_3Al_7 further illustrates the imprecision introduced into the Jones model by the choice of cut-off. As Table 3.4 illustrates, its diffraction pattern can be interpreted with an edge-centered reciprocal space cluster. The *CE* site is at {0 0 4}; *PG* at {8 3 0}, {$\bar{3}$ 5 0}, and {1$\bar{0}$ 0 0}; and *PPr* at {10 0 7}, {3 5 7}, and {$\bar{8}$ 3 7}. As Table 3.4 shows, edges involving solely *CE* and *PG* range in intensity from 50-100% in intensity; edges where one of the two sites is *PPr* range from 10-20% in intensity.

Figure 3.8 graphically illustrates that the inner-most edges are strongest and diffraction reflections become weaker as their corresponding edge becomes less central. It is here where the imprecision of the Jones model becomes apparent. While *CE-PPr* and *PG-PPr* edges are at least a factor of two weaker than the *PG-PG* edges, they are not so weak that they should be entirely ignored. In Table 3.2, we contrast two Jones zones. In the first only reflections based on *CE* and *PG* sites are included; in the second sites involving *PPr* are added to the mix. This corresponds respectively to cut-offs of 0.30 and 0.20.

The Jones model upper bound changes from 2.38 to 2.06 e^-/a. Lower bounds also change significantly from 1.83 to 1.71 e^-/a. Lower and upper bounds differ from one another by as much as 0.55 e^-/a, 0.55 = 2.38 − 2.06; this large spread can be attributed to the less spherical nature of the Jones zone. Given the large

Table 3.4: Strongest (*hkl*) in Pd_3Al_7

(*h k l*)	d_{hkl}[1]	multi-plicity	vertex−vertex (*k*-space-coord.)	vertex-vertex (atom sites)	intensity[2]
(0 0 8)	2.07	2	(0 0 4) – (0 0 $\bar{4}$)	*CE-CE*	100.0
(8 3 4)	2.06	8	(8 3 0) – (0 0 $\bar{4}$)	*PG-CE*	64.1
(3 5 4)	2.04	8	(0 0 4) – ($\bar{3}$ $\bar{5}$ 0)	*CE-PG*	59.2
(10 0 4)	2.04	4	(0 0 4) – ($1\bar{0}$ 0 0)	*CE-PG*	55.7
(11 2 0)	2.01	4	(8 $\bar{3}$ 0) – ($\bar{3}$ $\bar{5}$ 0)	*PG-PG*	53.3
			(3 5 7) – ($\bar{8}$ 3 7)	*PPr-PPr*	
(7 5 0)	1.98	4	($\bar{3}$ 5 0) – ($1\bar{0}$ 0 0)	*PG-PG*	48.9
			(10 0 7) – (3 $\bar{5}$ 7)	*PPr-PPr*	
(0 6 0)	2.05	2	(8 3 0) – (8 $\bar{3}$ 0)	*PG-PG*	49.4
			($\bar{8}$ 3 7) – ($\bar{8}$ $\bar{3}$ 7)	*PPr-PPr*	
(5 2 7)	2.00	8	(8 $\bar{3}$ 0) – (3 $\bar{5}$ $\bar{7}$)	*PG-PPr*	22.6
(2 3 7)	2.02	8	($\bar{8}$ 3 7) – ($1\bar{0}$ 0 0)	*PPr-PG*	22.2
(6 0 7)	2.02	4	(3 $\bar{5}$ 7) – ($\bar{3}$ $\bar{5}$ 0)	*PPr-PG*	21.1
(5 2 1)	3.63	8		-	18.3
(3 1 4)[3]	3.51	8		-	16.6
(3 5 3)	2.16	8	(3 5 7) – (0 0 4)	*PPr-CE*	12.8
(8 3 3)	2.19	8	(0 0 $\bar{4}$) – ($\bar{8}$ $\bar{3}$ $\bar{7}$)	*CE-PPr*	11.5
(10 0 3)	2.15	4	(10 0 7) – (0 0 4)	*PPr-CE*	12.2

[1] Table includes d_{hkl} of up to 1.81 , corresponding to CuKα_1 2θ of 50°.
[2] As in Table 2.1 intensity is given per reflection, with neither atomic Debye-Waller nor Lorentz-polarization factors included.
[3] Nine more reflections with d_{hkl} ranging from 3.1 to 3.8 have intensities between those observed for {3 1 4} and {10 0 3}, ie., have intensities greater or equal to the weakest inner shell reflections *CE-PPr* set of reflections.

spread, it is not surprising that the actual electron count is found between the two bounds: this actual electron count is 2.1 $^-$/a.

To us, the primary issue is not whether the 0.30 or 0.20 cut-off is more accurate (though in this chapter we adopt a cut-off of 0.30), the issue is that a cut-off needs to be chosen at all. All tetrahedral edges are pseudo-symmetric with one another, if one edge stabilizes the structure, they all must stabilize the system.

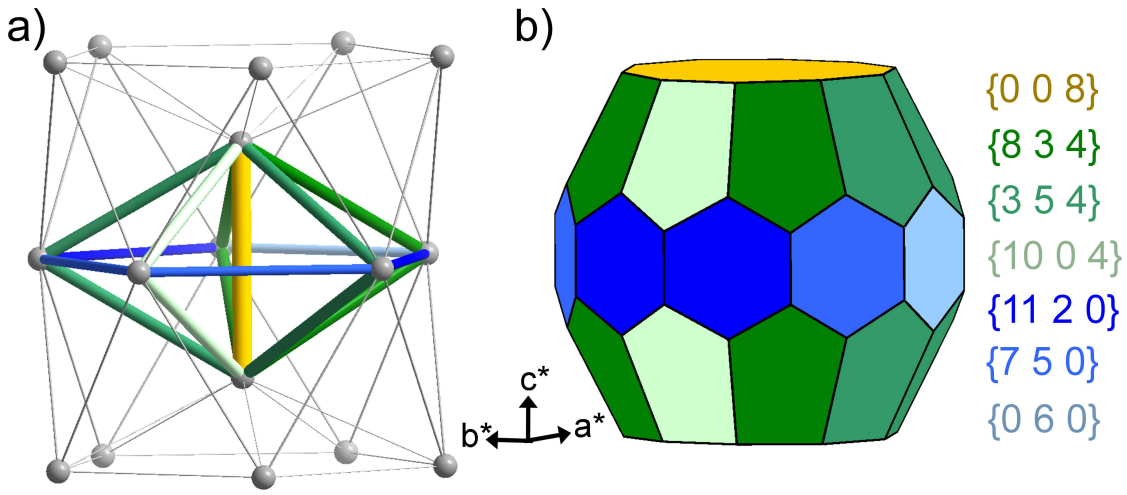

Figure 3.8: Edge-centered reciprocal-space cluster and Jones zone for Pd_3Al_7. Colored cluster based on sites with reflection intensities ≥ 0.30 of the most intense reflection. Reflections are color-coded. The reflections are listed in descending order of intensity and cluster cylinder radii are proportional to intensity. See Table 8. The axes shown in the graph indicate relative directions only of the three reciprocal cell axes. Cluster and Jones zone are not to scale of each other.

Cutting off weaker reflections due to the all-or-nothing nature of the Jones zone results in the loss of significant attributes of the electronic structure.

In all three cases discussed so far there is good agreement between the lower and upper bounds of the Jones model and observed electron counts. This agreement suggests that the Jones model can be used to account for phase stability in group 10-12 tetrahedral cluster structures in general. In this light, compounds based on copper and cadmium prove of genuine interest. The phase diagrams for this pair of elements is shown in Figure 3.9. Four Cu-Cd phases are known, in ascending concentration of cadmium they are $CdCu_2$, Cd_3Cu_4, Cu_5Cd_8, and

Cu_3Cd_{10}.

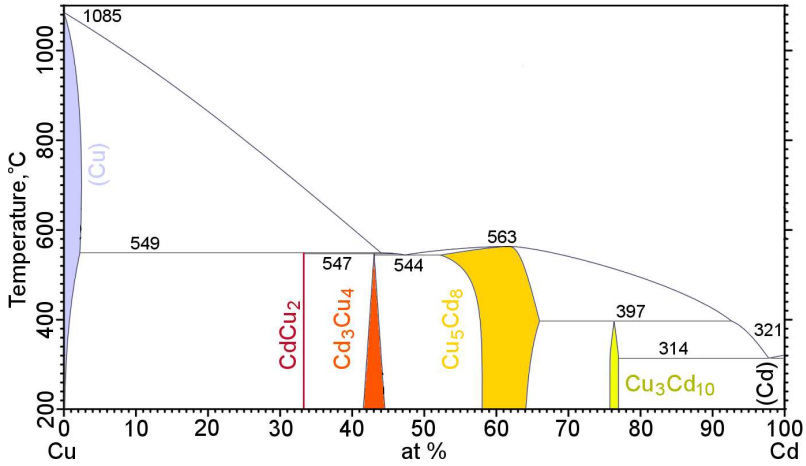

Figure 3.9: The Cu-Cd binary phase diagram adapted from Massalski.[6] The four known stable Cu-Cd phases are color-coded, oxblood: $CdCu_2$; carnelian: Cd_3Cu_4; Spanish-yellow: Cu_5Cd_8; and fluorescent-chartreuse: Cu_3Cd_{10}. See Figure 3.14.

The first and the fourth in this list of structures have polygon-centered tetrahedral cluster structures. The remaining two are cell-centered. Remarkably, for these two elements, and to our knowledge only for these two elements, all known binary phases are different variants of tetrahedral cluster crystal structures. Tables 3.5– 3.7 list the principal reflections for the three structures, $CdCu_2$, Cu_5Cd_8, and Cu_3Cd_{10}, Table 2.2 having previously listed the principal Cd_3Cu_4 reflections.

$CdCu_2$ presents us with the second main limitation inherent in the Jones model. $CdCu_2$, which crystallizes in the hexagonal $MgZn_2$ structure has diffraction spots which can be understood in reference to a polygon-centered cluster with *ITr*, *IL*, *IPr*, and *OPr* sites located at respectively {0 1 0}, {0 0 3}, {2 0 2}, and {2 $\bar{2}$ 3}. The issue here is not the cut-off value. Reflections involving *ITr*, *IL* and *IPr* sites are at least a factor of three stronger than sites involving the *OPr*

Table 3.5: Strongest (*hkl*) for $CdCu_2$

(*h k l*)	d_{hkl} [1]	multiplicity	vertex−vertex (*k*-space-coord.)	vertex-vertex (atom sites)	intensity[2]
(1 1 2)	2.11	12	(1 $\bar{1}$ 0) – (0 $\bar{2}$ $\bar{2}$)	*ITr-IPr*	100.0
			(2 0 2) – (1 $\bar{1}$ 0)	*IPr-ITr*	
(1 1 0)	2.48	6	(0 1 0) – ($\bar{1}$ 0 0)	*ITr-ITr*	77.2
(0 0 4)	2.00	2	(2 0 2) – (2 0 $\bar{2}$)	*IPr-IPr*	75.8
			(0 $\bar{2}$ 2) – (0 $\bar{2}$ $\bar{2}$)	*IPr-IPr*	
			($\bar{2}$ 2 2) – ($\bar{2}$ 2 $\bar{2}$)	*IPr-IPr*	
(1 0 3)	2.26	12	(0 0 3) – ($\bar{1}$ 0 0)	*IL-ITr*	75.2
			($\bar{1}$ 0 0) – ($\bar{2}$ 0 $\bar{3}$)	*ITr-OPr*	
(2 0 1)	2.07	12	(2 0 2) – (0 0 $\bar{3}$)	*IPr-IL*	71.3
(2 0 0)	2.15	6	(0 0 3) – ($\bar{2}$ 0 3)	*IL-OPr*	25.7
			(0 0 $\bar{3}$) – ($\bar{2}$ 0 $\bar{3}$)	*IL-OPr*	
(2 0 2)	1.89	12	-	-	7.7
(1 0 2)	2.93	12	-	-	4.0

[1] Table includes d_{hkl} of up to 1.81 , corresponding to CuKα_1 2θ of 50°.
[2] Intensity as in Table 2.1 is given per reflection, with neither atomic Debye-Waller nor Lorentz-polarization factors included.

site. The cut-off at 0.30 is therefore clean: edges involving *ITr*, *IL*, and *IPr* edges should be included while those involving *OPr* should not. The issue lies in the d_{hkl}.

While the edges in the reciprocal space cluster are all pseudosymmetric with one another and before projection were of equal length, perhaps due to the small size of the $CdCu_2$ structure and the concomitant rounding to whole number diffraction lattice vectors, their final observed d_{hkl} vary from 2.00 to 2.48 . As Table 3.5 and Figure 3.10 shows although there are five intense reflections: {112}, {110}, {004}, {103}, and {201} corresponding respectively to *ITr-IPr*, *ITr-ITr*, *IPr-IPr*, *ITr-IL*, and *IL-IPr*, only two of these five reflections have a large enough d_{hkl} to actually form faces in the Jones zone. The Jones zone does not incorporate the

Table 3.6: Strongest (*hkl*) for Cu_5Cd_8

(*h k l*)	d_{hkl}[1]	multiplicity	vertex−vertex (*k*-space-coord.)	vertex-vertex (atom sites)	intensity[2]
(3 3 0)	2.26[3]	12	$(\frac{3}{2}\ \frac{3}{2}\ \frac{3}{2}) - (\frac{\bar{3}}{2}\ \frac{\bar{3}}{2}\ \frac{3}{2})$	*IT-IT*	100.0
(4 1 1)	2.26	24	$(\frac{3}{2}\ \frac{\bar{3}}{2}\ \frac{\bar{3}}{2}) - (\frac{\bar{5}}{2}\ \frac{\bar{5}}{2}\ \frac{\bar{5}}{2})$	*IT-OT*	65.0
(3 3 2)	2.04	8	$(\frac{5}{2}\ \frac{5}{2}\ \frac{\bar{5}}{2}) - (0\ 0\ \bar{5})$	*OT-OH*	22.8
			$(\frac{5}{2}\ \frac{\bar{5}}{2}\ \frac{5}{2}) - (0\ \bar{5}\ 0)$	*OT-OH*	
			$(\frac{\bar{5}}{2}\ \frac{5}{2}\ \frac{5}{2}) - (\bar{5}\ 0\ 0)$	*OT-OH*	
(4 2 2)	1.96	24	$(5\ 0\ 0) - (\frac{3}{2}\ \frac{\bar{3}}{2}\ \frac{\bar{3}}{2})$	*IT-OH*	17.1
(1 1 0)	6.78	24	-	-	16.1
(5 1 0)	3.48	24	-	-	12.5

[1] Table includes d_{hkl} of up to 1.81 , CuKα_1 of 50°.
[2] Intensity as in Table 2.1 is given per reflection, with neither atomic Debye-Waller nor Lorentz-polarization factors included.
[3] Inner shell edges have d_{hkl} ranging from 2.1 to 2.2 .

effect of three of the five principal reflections responsible for the $CdCu_2$ phase stability. Nonetheless, as Table 3.2 shows, the actual $CdCu_2$ electron count lies comfortably between the lower and upper Jones zone bounds.

The next two phases in the Cu-Cd phase diagram are both based on cell-centered clusters. Cu_5Cd_8 is a γ-brass structure and our previous discussions on this structure and on the Pt_5Zn_{21} γ-brass superstructure examine almost all the relevant issues. Its principal diffraction peaks, reciprocal lattice cluster, and Jones zone is shown in Table 3.6 and Figure 3.11. One important distinction between Cu_5Cd_8 and Pt_5Zn_{21}, is that, due to rounding, both the *IT-OH* and *OT-*

Table 3.7: Strongest (*hkl*) for Cd_3Cu_{10}

(*h k l*)	d_{hkl} [1]	multiplicity	vertex−vertex (*k*-space-coord.)	vertex-vertex (atom sites)	intensity[2]
(0 0 4)	2.19	2	(3 0 2) – (3 0 $\bar{2}$)	*IPr-IPr*	100.0
			($\bar{3}$ 3 2) – ($\bar{3}$ 3 $\bar{2}$)	*IPr-IPr*	
			(0 $\bar{3}$ 2) – (0 $\bar{3}$ $\bar{2}$)	*IPr-IPr*	
(3 0 1)	2.26	12	(3 0 2) – (0 0 $\bar{3}$)	*IL-IPr*	52.1
			(3 $\bar{3}$ 3) – (0 $\bar{3}$ 2)	*OPr-IPr*	
			(0 3 3) – ($\bar{3}$ 3 2)	*OPr-IPr*	
(2 1 2)	2.27	24	(2 $\bar{2}$ 0) – (0 $\bar{3}$ $\bar{2}$)	*ITr-IPr*	50.4
(2 0 3)	2.24	12	(0 0 3) – ($\bar{2}$ 0 0)	*IL-ITr*	36.8
(2 2 0)	2.03	6	(0 2 0) – ($\bar{2}$ 0 0)	*ITr-ITr*	36.1
(3 0 0)	2.34	6	(0 0 3) – ($\bar{3}$ 0 3)	*IL-OPr*	22.1
			(0 0 $\bar{3}$) – ($\bar{3}$ 0 $\bar{3}$)	*IL-OPr*	
(1 0 3)	2.69	12	($\bar{2}$ 0 0) – ($\bar{3}$ 0 $\bar{3}$)	*ITr-OPr*	20.6
(2 1 0)	2.66	12		-	16.3
(2 0 2)	2.74	12		-	16.2

[1] Table includes d_{hkl} of up to 1.81 , corresponding to CuKα_1 2θ of 50°.
[2] Intensity as in Table 2.1 is given per reflection, with neither atomic Debye-Waller nor Lorentz-polarization factors included.

OH reflections have significantly shorter d_{hkl} than the *IT-IT* and *IT-OT* peaks. It therefore proves irrelevant to the Jones zone, whether edges involving *OH* sites are included. A change in cut-off from 0.30 to 0.20 does lead to inclusion of edges involving *OH* sites, but no change in either Jones lower or upper bounds ensues from this change.

The Cd_3Cu_4 structure presents us with one last issue in our Jones model treatment. This structure, being comprised of cell-centered tetrahedral clusters, has as principal edges in descending order of importance *IT-IT*, *IT-OT*, and *IT-OH* and *OT-OH*, these last two reflections being roughly equal in importance, see Table 2.2. The issue is whether in evaluating the importance of a given Jones face intensities on a per reflection or a per edge basis should be considered. If

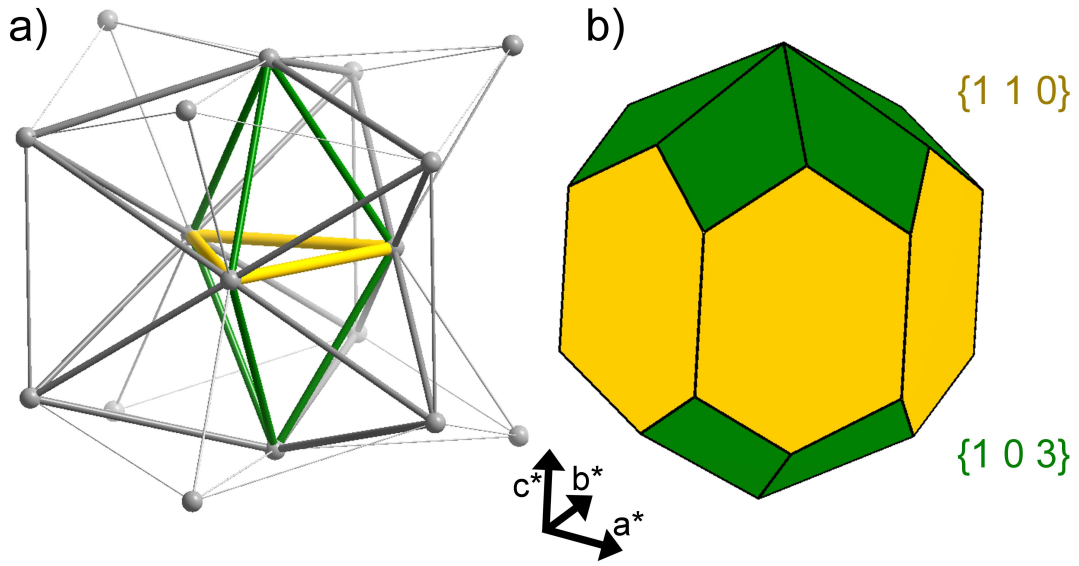

Figure 3.10: Polygon-centered reciprocal-space cluster and Jones zone for $CdCu_2$. Colored cluster based on sites with reflection intensities ≥ 0.30 of the most intense reflection. Only two of the five reflections which meet this criterion have large enough d_{hkl} values to actually appear in the Jones zone. These two reflections are color-coded. The reflections are listed in descending order of intensity. Cluster cylinder radii are proportional to intensity. Reflections are color-coded. See Table 3.5. The axes shown in the graph indicate relative directions only of the three reciprocal cell axes. Cluster and Jones zone are not to scale of each other. The pictured Jones zone is the same shape as that reported for AgZn elsewhere.[7]

a reflection has a strong intensity, then in the Jones model this should result in a strong mixing of states. From the perspective of the Jones model, it does not matter if a multitude of equivalent edges are responsible for the reflection intensity.

We therefore assume that in the choosing of Jones zone cut-off values, intensity on a per reflection basis should be used. For Cd_3Cu_4, the *OT-OH* reflection is only slightly weaker than the *IT-IT* and *IT-OT* reflections. With this

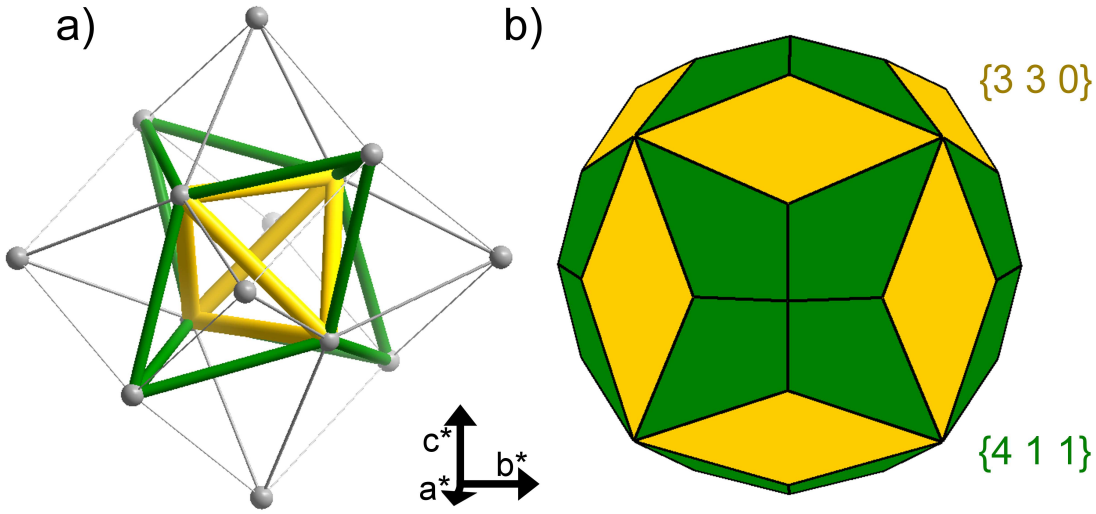

Figure 3.11: Cell-centered reciprocal-space cluster and Jones zone for Cu_5Cd_8. Colored cluster based on sites with reflection intensities ≥ 0.30 of the most intense reflection. The reflections are listed in descending order of intensity and cluster cylinder radii are proportional to intensity. See Table 3.6. The axes shown in the graph indicate relative directions only of the three reciprocal cell axes. Cluster and Jones zone are not to scale of each other.

understanding, edges involving the *OH* site are well above the 0.30 threshold and certainly require inclusion. In Figure 3.12, we therefore construct our Jones zone using all edges involving *IT*, *OT*, and *OH* sites. The inclusion of the *OH* sites leads to four rather than two faces in the Jones zone. The zone is reasonably spherical. Lower and upper bounds are 1.35 and 1.52 e^-/a compared to an experimental value of 1.43 e^-/a.

The final Cu-Cd phase is Cu_3Cd_{10}, a polygon-centered cluster structure. In this structure *ITr*, *IL*, *IPr*, and *OPr* sites are located at respectively {0 2 0}, {0 0 3}, {3 0 2}, and {3 $\bar{3}$ 3}. Its diffraction data is shown in Table 3.7. As this table shows,

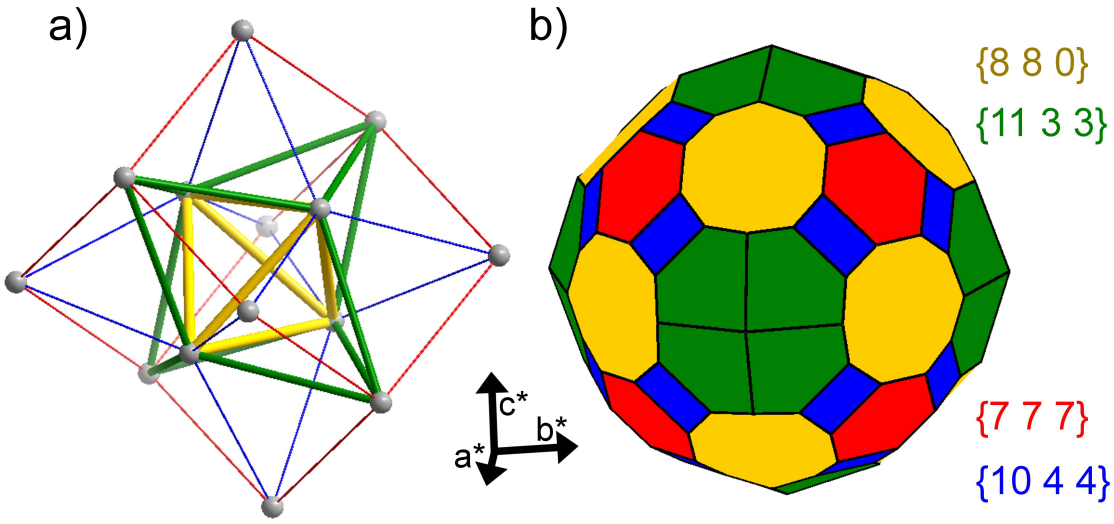

Figure 3.12: Cell-centered reciprocal-space cluster and Jones zone for Cd_3Cu_4. Colored cluster based on sites with reflection intensities ≥ 0.30 of the most intense reflection. Reflections are color-coded. The reflections are listed in descending order of intensity and cluster cylinder radii are proportional to intensity. See Table 2.2. The axes shown in the graph indicate relative directions only of the three reciprocal cell axes. Cluster and Jones zone are not to scale of each other.

reflections based solely on *ITr*, *IL*, and *OPr* edges are two to four times stronger than those involving *OPr* sites. Using a cut-off of 0.30, only the former edges are included. The reciprocal space cluster and Jones zone is illustrated in Figure 3.13. The Jones zone is somewhat spherical with lower and upper bounds of 1.59 and 1.83 e^-/a, values which comfortably straddle the experimental electron count of 1.77 e^-/a.

In all seven cases considered in this section, see Table 3.2, the Jones zone model provides reasonable lower and upper bounds for phase stability, this despite the inherent liabilities of the method. We leave this section with a graphical

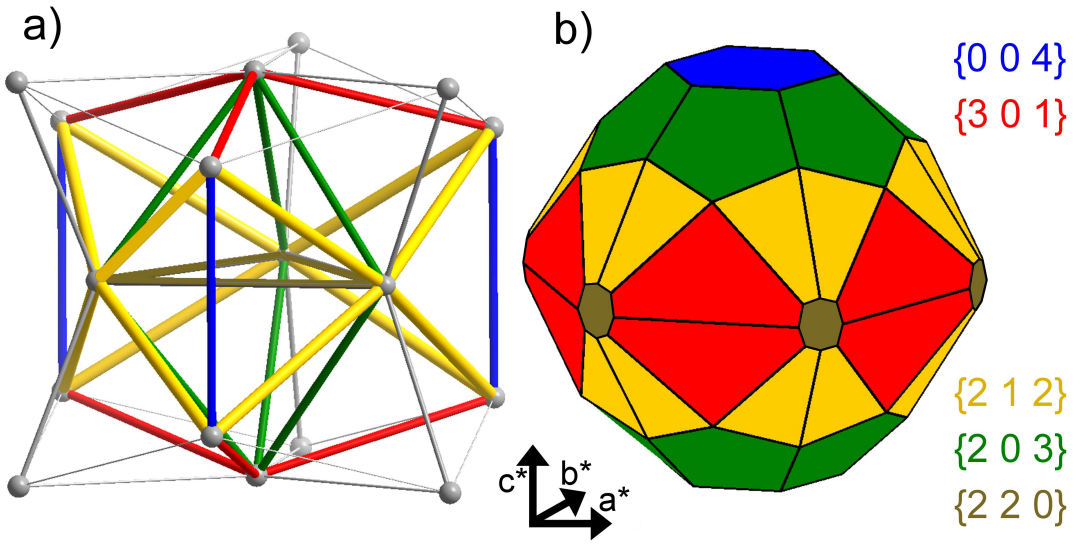

Figure 3.13: Polygon-centered reciprocal-space cluster and Jones zone for Cu_3Cd_{10}. Colored cluster based on sites with reflection intensities ≥ 0.30 of the most intense reflection. Reflections are color-coded. The reflections are listed in descending order of intensity and cluster cylinder radii are proportional to intensity. See Table 3.7. The axes shown in the graph indicate relative directions only of the three reciprocal cell axes. Cluster and Jones zone are not to scale of each other.

representation of the overall Jones model. In Figure 3.14 we illustrate the Jones zones for all four known Cu-Cd phases, using in all four of the zones identical e^-/a scales. They range in Cd content from 33 - 77%. In going from the most Cd-poor to the most-Cd rich phase, ie., in progressing from $CdCu_2$, to Cd_3Cu_4, to Cu_5Cd_8, and finally to Cu_3Cd_{10} their experimental e^-/a progress from 1.33 to 1.43 to 1.62 to 1.77 just as their Jones zone volumes travel from 1.40, to 1.52, to 1.73, and finally to 1.85 e^-/a.

Each Jones zone volume is only slightly bigger than the next volume, but the four volumes track the actual number of valence electrons in these structures.

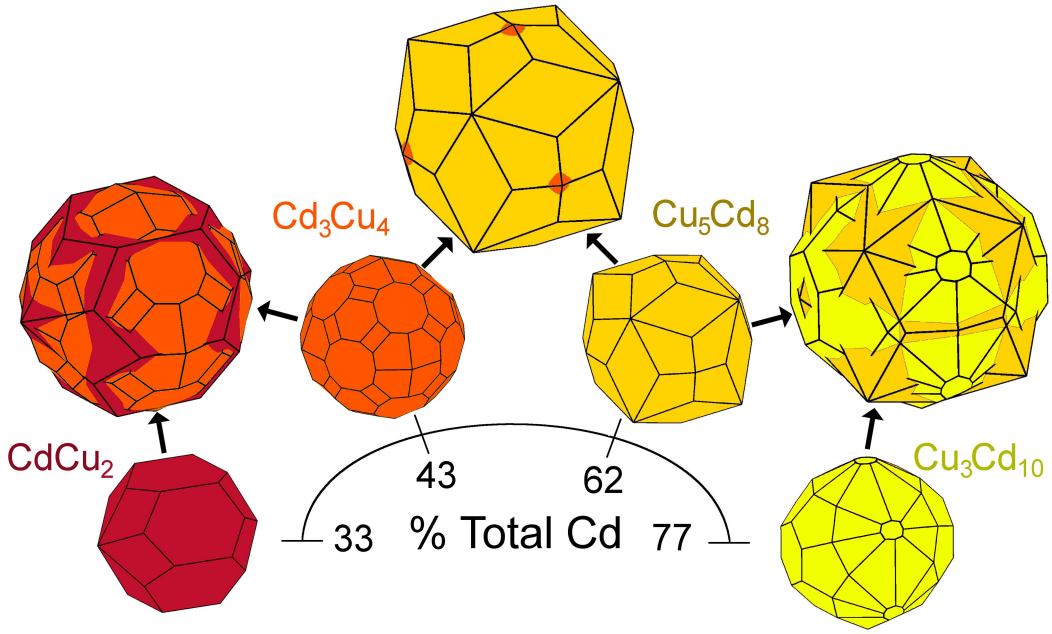

Figure 3.14: The Jones zones of the four binary Cu-Cd phases in order of ascending cadmium content. Phases are color-coded. Oxblood: $CdCu_2$; carnelian: Cd_3Cu_4; Spanish-yellow: Cu_5Cd_8; and fluorescent-chartreuse: Cu_3Cd_{10}. Single Jones zones are plotted at the same e^-/a scale. Neighboring Jones zones show the more cadmium-rich Jones zone enveloping the less cadmium-rich phase.

In Figure 3.14 we directly compare each Jones zone with the preceding zone following the progression of the phases. Each zone partially swallows up the preceding zone. As the cadmium content increases, so does the number of valence electrons. Within the constraints of possible crystal structures, Jones zones recapitulate free electron spheres.

3.3 Conclusions

3.3.1 Symmetry and electrons

The basic story of this chapter has been told before. Electronic states mix and stabilize the structure. Symmetry organizes the way this mixing occurs. The twist here is that the symmetry comes from two different sources. On the one hand there is the crystal, on the other hand there are the electrons. The crystal symmetry is described by a space group; the electron symmetry, at first, is that of a free electron sphere. We can couch both symmetries in terms of reciprocal space. Orbital mixing proves best when the crystal symmetry, best thought of in terms of the Jones zone, mimics the second.

The crux of this chapter, and Chapter 2, is that were it possible for the crystal to go beyond the most symmetrical 3-D point groups, O_h and I_h, and thus have even greater numbers of faces in their Jones zone, it would be possible to have even more mixing on the Fermi surface free electron sphere. Amazingly, crystals find a way to do so. They can not find more 3-D symmetries, there are none; they find 3-D pseudo-symmetries instead. Knowing best the language of perfect symmetry, we invoke a 4D Platonic solid to describe them.

Tetrahedrally packed quasi-crystalline approximants and Frank-Kasper phases crystals whose highest symmetry sites are T_d, T_h, D_{3h}, or C_{2v}, adopt a collection of true and pseudo-symmetry axes which are all projections of objects with the same 4D point-group. And this point group organizes the faces of their nearly sphere-like Jones polyhedra into pseudo-symmetrically equivalent faces. Mixing, pseudogaps and stability ensue. It's a bit of a mouthful, but

it is just symmetry controlling the fate of electronic states and electronic states controlling the stability of molecules.

3.3.2 Mysterious metals

Molecules make sense. Hydrogen and oxygen form H_2O, the stoichiometry and the number of bonds corresponds to the hydrogen and oxygen valencies. Metals do not work the same way. Their stoichiometry, the number of their bonds, and their atomic valencies seem to cascade to more and more complex formulations. It seems hopeless to explain in any language as straightforward as that used for hydrogen and oxygen, why copper and cadmium make four compounds with the stoichiometries $CdCu_2$, Cd_3Cu_4, Cu_5Cd_8, and Cu_3Cd_{10}, let alone their forbidding crystal structures with 12, 1124, 52 and 28 atomic sites per unit cell.

The Hume-Rothery rules and the Jones model tell us a lot about the factors controlling their stability. For example, for the γ-brass structure, Cu_5Cd_8, the Hume-Rothery rules tell us that it should be found at 21/13 e^-/a, which it does, and Jones theory tells us that this electron count is controlled by the {3 3 0} and {4 1 1} and other reflections, a result confirmed by pseudo-gap measurements[137,144–146] , high quality band structures,[147–151] and even Hückel and extended Hückel theory.[35] These models certainly tell us a lot about why γ-brass exists. But even with these results, can we see the γ-brass structure as something simple, in the same way that we can think of the structure of one water molecule as simple?

We can't. But perhaps there is hint that some day we will. All the diffraction patterns of all the crystals discussed in 2 are all projections of the same 4D Pla-

tonic solid. This 4D solid, like all 3-D Platonic solids, is in some sense simple. Our Platonic view though is in reciprocal space, not real space. Today, to project the real space structure of γ-brass from an object with just a few sites in its asymmetric unit, we need to to project from the 6D D_6 or 8D E_8 Bravais lattices. (Of these two, the 8D Bravais lattice can capture the full 600-cell point group symmetry while the D_6 can not; the point group of D_6 being $6! \times 2^5$ element, it can not be a supergroup of the 600-cell point group, H_4, with $5!^2$ group elements.[152]) Perhaps real space geometrical constructions remain to be found, simpler than the known 6D or 8D Bravais projections, whose higher dimensional geometry is solely based on 4D Platonic solids, or their point groups. If so, they would bring us be one step closer to thinking of this one class of metal structures as simple and transparent.

CHAPTER 4

$\mathbf{IR_XRU_{1-X}ZN_{10}}$ REVISITED

4.1 Introduction

With the electron counting rules delineated in the previous chapter, we can attempt to further constrain our electron counts of the ternary family of compounds $Ir_xRu_{1-x}Zn_{10}$ discussed in Chapter 1. The challenge presented by these structures that they contain at least some sites with transition metals (Ru and Ir) which have open d-shells. In Chapter 2, we deliberately confined our analysis of compounds containing only group 10-12 metals so that we could be absolutely sure of the true s- and p-orbital electron counts. Adding transition metals muddy the waters: as we have seen with $Ir_xRu_{1-x}Zn_{10}$, the degree to which partially filled d-bands absorb or donate electrons to the s- and p-bands affects the Hume-Rothery electron count in a non-negligible way.

However, precisely because $Ir_xRu_{1-x}Zn_{10}$ appears to be Hume-Rothery structures–possessing roughly the right electron count–and exhibits pseudo five-fold diffraction patterns due to atomic clusters which are symmetric projections of the 600-cell, we can apply the methodology of the previous chapter in order to sharpen our understanding of the electronic structure of these phases.

4.2 Reciprocal Space Cluster

The diffraction pattern of $Ir_xRu_{1-x}Zn_{10}$ (Figure 1.1) was discussed extensively in Section 1.4. We first encountered the D_{3h} atomic cluster in this section, which

Table 4.1: Fermi spheres of $RuZn_{10}$

($h\ k\ l$)	radius (Å^{-1})	multiplicity	volume (e$^-$/a)	intensity
(3 3 0)	1.458	6	1.57	100.00
(3 0 22)	1.487	12	1.66	77.84
(3 2 14)	1.443	24	1.52	50.23
(3 0 21)	1.468	12	1.60	43.13
(3 2 15)	1.473	24	1.61	36.67
(5 0 9)	1.424	12	1.46	36.48

we later saw was the driver behind the pseudo five-fold diffraction pattern in $Ir_xRu_{1-x}Zn_{10}$. In this section, we will build the Jones zone corresponding to the strongest diffraction peaks in $Ir_xRu_{1-x}Zn_{10}$. In doing so, we can put bounds on possible electron counts and provide a useful benchmark against which to check our predictions of valence e$^-$/a counts from the extended-Hückel analysis of $RuZn_{10}$ (see Section 1.5).

The free-electron (Fermi) spheres corresponding to each peak are shown in Table 4.1. As before, we only consider peaks with intensity $\geq 30\%$ the intensity of the most intense peak. We can immediately read off our lower boundary on valence e$^-$/a count: the (5 0 9) peak, which is the least intense, dictates the lower boundary: 1.46 e$^-$/a. The upper bound is dictated by the volume of the Jones zone, which is shown in Figure 4.1 along with the attendant reciprocal space cluster.

On an intensity per reflection basis, other peaks become relevant (Table 4.2). The Jones Zone for $RuZn_{10}$ is encouragingly sphere-like. Its volume is 1.74 e$^-$/a. The geometry of the reciprocal space cluster, and the intensities of the peaks corresponding to its edges, are given in Table 4.2. As is clearly illustrated in Figure 4.1, the edges nearest the center of the reciprocal-space cluster ($ITr - ITr$ and $IL - ITr$) correspond the strongest diffraction peaks.

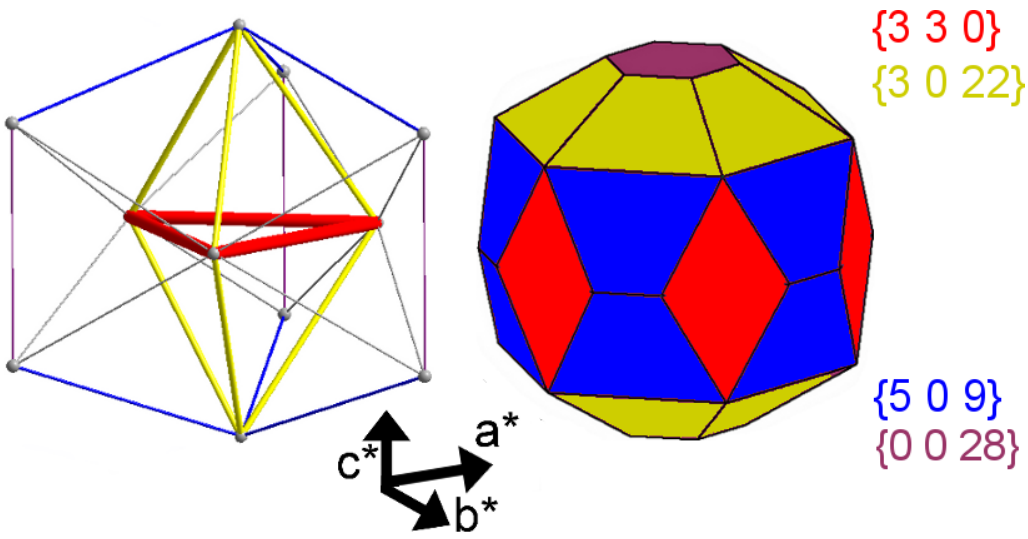

Figure 4.1: Polygon-centered reciprocal-space cluster and Jones Zone for $RuZn_{10}$. Colored cluster based on sites with reflection intensities ≥ 0.15 of the most intense reflection. Reflections are color-coded. The reflections are listed in descending order of intensity and cluster cylinder radii are proportional to intensity. See Table 4.2. The axes shown on the graph indicate relative directions only of the three reciprocal axes. Cluster and Jones zone are not to scale of each other.

Table 4.2: Strongest (*hkl*) in $RuZn_{10}$

(*h k l*)	d_{hkl} [1]	multiplicity	vertex−vertex (*k*-space-coord.)	vertex-vertex (atom sites)	intensity[2]
(3 3 0)	2.15	6	(0 3 0) – ($\bar{3}$ 0 0)	*ITr-ITr*	100.0
(3 0 22)	2.14	12	(0 0 22) – ($\bar{3}$ 0 0)[3]	*IL-ITr*	38.9
(3 0 21)	2.21	12	(0 0 22) – ($\bar{3}$ 0 0)[3]	*IL-ITr*	21.6
(5 0 9)	2.11	12	(5 0 $\bar{1}$3) – (0 0 $\bar{2}$2)	*IPr-IL*	18.2
(0 0 28)	2.05	2	(5 0 13) – (5 0 $\bar{1}$3)	*IPr-IPr*	17.3
(3 2 14)	2.18	24	(3 $\bar{3}$ 0) – (0 $\bar{5}$ $\bar{1}$3)[4]	*ITr-IPr*	12.5

[1] Table includes d_{hkl} of up to 2.0 , corresponding to CuKα_1 2θ of 45°.

[2] Intensity is based on powder diffraction data from the Cerius[2] suite of programs but is given per reflection.

[3] The reflections (3 0 22) and (3 0 21) correspond to nearly the same boundary planes when constructing the Jones zone. For the purposes of Figure 4.1, only (3022) is used. Both sets of planes are used in the calculation of the zone volume.

[4] The reflections (3 2 14), (3 2 15) and (3 2 13) correspond to nearly the same boundary planes when constructing the Jones zone. For the purposes of Figure 4.1, only (3 2 14) is used, although (3 2 13) is the only plane which fits the reciprocal space cluster *exactly*. Only (3 2 14) and (3 2 15) are used in the calculation of the zone volume.

4.3 Comparing electron-count estimates

Our Jones zone analysis in the previous section gave us a range of electron counts: 1.46-1.74 valence e^-/a. In group 10-12 intermetallic structures, we found the upper bound more closely tracks experimental electron counts (see Table 3.2) for most structure types.

In Section 1.5, we used Mulliken population analysis to argue for certain valence e^-/a counts based on which counts most definitively separated the more electronegative element, Ru, from the less electronegative element, Zn. On this basis, we found the valence e^-/a counts of around 1.62 or 1.74 e^-/a to be most plausible. The electron count is contingent on the electron count per Ru: does each Ru take two valence electrons into its d-shell, or zero? Our previous analysis could not answer that question. Our current analysis of the volume of the Jones zone supports the latter count (implying a Ru e^-/a count of 0) without necessarily discounting the former.

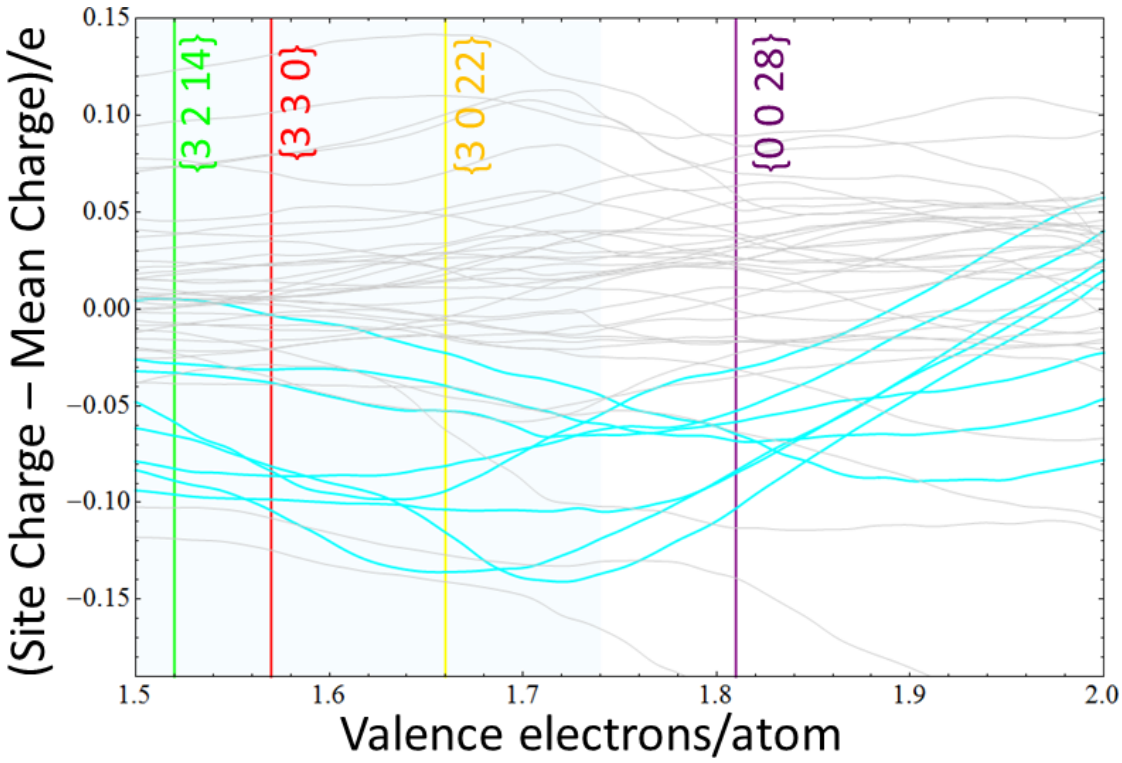

Figure 4.2: A reproduction of Figure 1.21. The light blue region represents the upper and lower limits on e^-/a (1.46-1.74 valence e^-/a). The cyan lines correspond to experimental Ru sites, and the grey lines to Zn. The electron counts from Fermi spheres corresponding to the strongest diffraction peaks are also shown (their colors correspond to Figure 4.1.)

In Figure 4.2, we show again the relative charges of symmetry-equivalent sites in $RuZn_{10}$ derived from Mulliken population analysis based on all-Zn model structure (see Figure 1.21). We can see that the upper limit–the volume of the Jones zone–sits in a region where most of the sites corresponding to Ru are well-separated from those corresponding to Zn.

Finally, we want to remark on the intensities of the strongest reflections across the $Ir_xRu_{1-x}Zn_{10}$. In Chapter 1, we asked whether substituting Ir for Ru would increase the intensity of the peaks in the *psuedo* five-fold diffraction ring.

Table 4.3: Intensities of Strongest Reflections in $Ir_xRu_{1-x}Zn_{10}$

$(h\ k\ l)$	$RuZn_{10}$	$Ir_{0.2}Ru_{0.8}Zn_{10}$	$Ir_{0.3}Ru_{0.7}Zn_{10}$
(3 3 0)	100.0	100.0	100.0
(3 0 22)	77.8	87.7	84.9
(3 2 14)	50.2	46.5	48.1
(3 0 21)	43.1	41.4	40.1
(3 2 15)	36.7	37.1	37.9
(5 0 9)	36.5	36.1	35.8

We now know the more correct question to ask is "Does substituting Ir for Ru would increase the intensity of the peaks in the corresponding to *psuedo*-symmetric edges in the reciprocal-space cluster?"

We don't have a definitive answer to this question, as shown in Table 4.3 (reproduced from Table 1.2). The relative intensity of the strongest peaks remain largely constant as Ir is added. We note that the (3 0 22) peak, which corresponds to the second most central edge in the reciprocal space cluster (*IL-ITr*), is significantly more intense in the two more Ir-rich structures.

4.4 Conclusion

$Ir_xRu_{1-x}Zn_{10}$ is a tetrahedrally closest-packed structure, and is mostly Zn: a metal which makes an unambiguous valence e^-/a contribution in intermetallics. On the one hand, then, we are not surprised that the Jones zone machinery developed in Chapters 2 and 3 gives us bounds on the valence e^-/a consistent with our estimates from other methods.

Unlike the group 10-12 metal structures of the previous chapters, however, we do not have an experimental valence e^-/a count to guide us. Since many

structures having pseudo five-fold diffraction contain transition metals or are even isostructural to existing group 10-12 structures, future development of the theory will have to contend with less well-defined electron counts. Our analysis of $Ir_xRu_{1-x}Zn_{10}$ is a step in that direction.

Substituting a heavier atomic species for a lighter one—for example, Ir for Ru—when such a substitution does not alter the structure provides relatively straightforward experimental test our reciprocal space cluster model and the Jones model in general. Will the substitution tend to occur in a way which strengthens the intensity of the innermost edges of the reciprocal space cluster, or are the relative intensities of the strongest peaks largely irrelevant as long as the Jones zone volume is correct?

To decide, not only will existing and new experimental data have to be examined, but band structure calculations will have to be used to investigate the existence and magnitude of band gaps and pseudogaps—and hence, orbital mixing—corresponding to the strong diffraction peaks.

APPENDIX A

THE ELECTRONIC STRUCTURE OF $AU_{10}CR_4ZN_{89}$

A.1 Introduction

Like $Ir_xRu_{1-x}Zn_{10}$, $Au_{10}Cr_4Zn_{89}$ is a principally group 10-12 metal (Au and Zn) compound with some transition metal (Cr) mixed in.* However, $Au_{10}Cr_4Zn_{89}$ is cubic (space group $F\bar{4}3m$), fully-ordered, and considerably less complex than $Ir_xRu_{10-x}Zn_{100}$, containing just 103 atoms in its primitive cell as opposed to over 500 for $Ir_xRu_{10-x}Zn_{100}$.

The crystallographic data and atomic coordinates for $Au_{10}Cr_4Zn_{89}$ are given in Appendix B.3. We attempt to provide a simplified description of the atomic structure according to the cluster concept. In this view, the structure is described as four non-intersecting clusters (of $\bar{4}3m$ or equivalently T_d symmetry) on the high symmetry points of the unit cell: (0 0 0), ($\frac{1}{4}$ $\frac{1}{4}$ $\frac{1}{4}$), ($\frac{1}{2}$ $\frac{1}{2}$ $\frac{1}{2}$), and ($\frac{3}{4}$ $\frac{3}{4}$ $\frac{3}{4}$), and their symmetry equivalents. Thus, $Au_{10}Cr_4Zn_{89}$ is composed of 16 clusters of four types.

As shown in Figure A.1, we designate each cluster type by a capital letter indicating the central position of each cluster:[34] Z for 0, Q for $\frac{1}{4}$, H for $\frac{1}{2}$, and T for $\frac{3}{4}$. The clusters are differentiated by a set of three or four atomic shells from which they are composed. The shells have the geometry of one of the various Platonic and Archimedean solids. Each shell corresponds to a distinct crystallographic site and is distinguished by two capital letters in congruence with the

*The experimental and computational results will appear in a forthcoming paper by P. Jana and R. Henderson *et al* titled *Spatially correlated structural disorder phenomena in a γ-brass related complex zinc-rich alloy (Au,Cr)Zn_n; n = 10.2 − 6.4.*

standard used for γ-brass clusters. CC designates the center of a cluster, IT is the inner tetrahedron, OT is the outer tetrahedron, TT is a truncated tetrahedron (also called Friauf polyhedron), and CO for cuboctahedron.

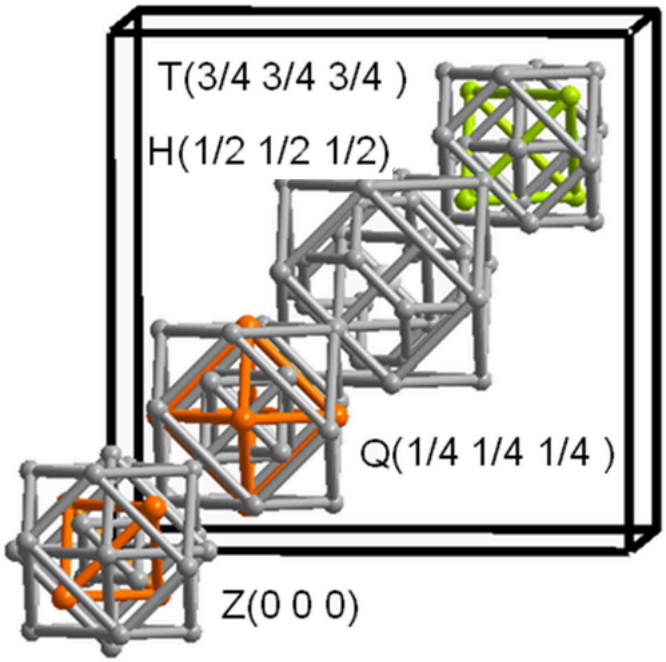

Figure A.1: The arrangement of clusters in the crystal structure of $Au_{10}Cr_4Zn_{89}$ along the body diagonal, clusters are centered about the high symmetry points of the *F*-centered cubic unit cell and their identities are specified. The clusters are represented by idealized cuboctahedral shells. Zinc atoms are shown in gray, chromium in lime and gold in orange.

The Z and Q-clusters are typical of the geometry of γ-brass. The H cluster is found in α-Mn while the T cluster is of the Ti_2Ni type.

The site preferences shown in Figure A.1 are puzzling. In particular, why should two neighboring γ-brass clusters color different sites with Au: one on the IT site, and the next on the OH site? We'll use a mix of *ab initio* and semi-empirical methods to attempt to find out. But to get a handle on the problem, we begin with the Hume-Rothery rules.

A.2 Electronic Structure Calculations

As discussed in Chapter 1, the Hume-Rothery rules are heuristic guidelines for rationalizing the structure of intermetallic compounds at particular electron counts. To recap, an extended structure is a Hume-Rothery structure if 1) its electronic structure depends primarily on s- and p- orbital interactions and 2) the s- and p- electron count is near that of Cu_5Zn_8 (21/13≈1.62 e^-/atom). This means that d-orbitals of the constituent atomic sites are filled and for the most part not involved in bonding.

A straightforward approach is simply to fill the d-orbitals of $Au_{10}Cr_4Zn_{89}$ completely. The valence d-shells of Au and Zn are already full: $5d^{10}6s^1$ and $3d^{10}4s^2$ respectively. Hence, Au contributes 1 electron, and Zn contributes 2. Cr has a half-filled d-shell, $3d^54s^1$. Therefore, in order to fill its d-shell, Cr contributes -4 electrons. This counting scheme gives 1.67 e^-/a, which is very close to the Hume-Rothery standard for γ-brass.

Is that a reasonable assumption for $Au_{10}Cr_4Zn_{89}$? To find out, we used DFT-LDA[†]. The total DOS is shown in Figure A.2. Some signatures of the Hume-Rothery structures are present: there appears to be localized, filled d-orbitals well below the Fermi energy, as well as good pseudo-gap formation.

To test whether the d-orbital states are filled, we investigate the projected d-DOS for each atom type: Au, Cr, and Zn. Since VASP uses a plane-wave basis set rather than atomic orbital basis set, the projections are not perfect. In particular, adding together several projected DOS will typically not give the total DOS.

[†]DOS plots for $Au_{10}Cr_4Zn_{89}$ were generated with VASP using the Local Density Approximation (LDA)and ultra-soft pseudopotentials. There are 103 ions in the primitive cell, and we used 35 k-points in the irreducible wedge of the Brillouin zone. The energy cutoff was 250 eV.

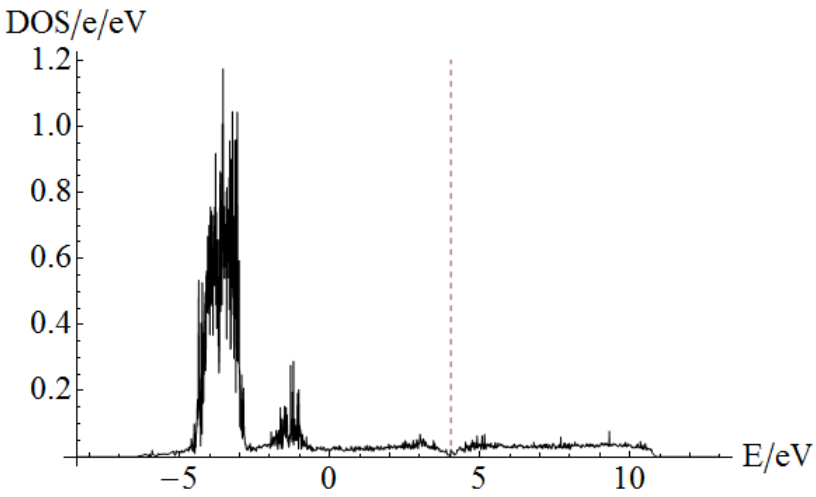

Figure A.2: Total density of states of $Au_{10}Cr_4Zn_{89}$. The first two large peaks are due to the Zn and Au d-orbitals respectively. Also note the pseudo-gap formation at the Fermi energy. The vertical axis is given in units of states per valence electron so that the DOS plot is comparable between systems with different sized unit cells.

We can see in Figure A.3 that for Au and Zn, the d-orbital density lies mostly below the Fermi level. Perfectly filled d-orbitals would result in 10 d-electrons per atom. Numerical integration over partial Au-d and Zn-d states up to the Fermi level gives 8.7 and 10.0 electrons in d-states per atom, respectively.

Contrast Au and Zn to the Cr case. The projected Cr d-states are clearly split at the Fermi level and appear to be about half-filled. In fact, integration gives 4.5 d-electrons per Cr. The half-filling suggests we take the Cr valence electron configuration as in the free atom: $3d^5 4s^1$. Then Cr contributes +1 e instead of -4 e, and the s- and p-electron count becomes 1.86 e^-/a: a significant deviation from the Hume-Rothery standard but comparable to some hcp compounds of noble metals.[140]

With a feasible electron-counting scheme in hand, we can focus on the ques-

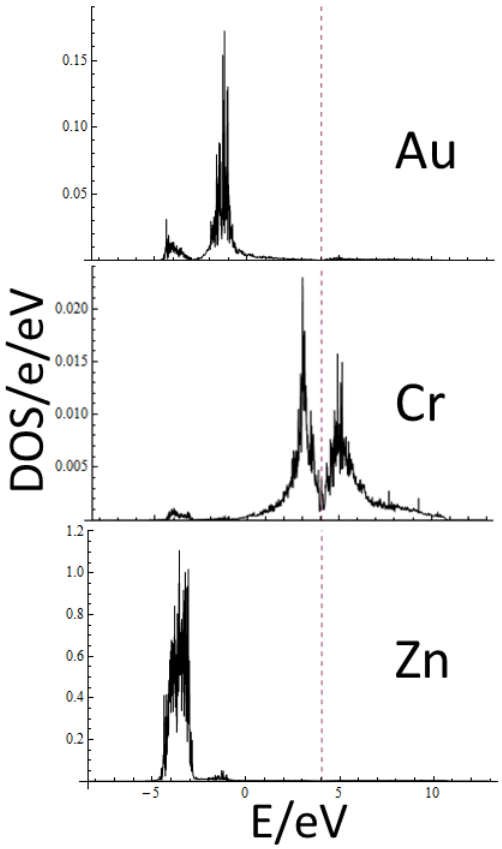

Figure A.3: Partial DOS of projected d-states for (from top to bottom) Au, Cr, and Zn respectively. All plots are truncated vertically so that we can see the structure near the Fermi level. The Cr plot (middle) clearly shows the d-states are split at the Fermi level. Note the difference in scale reflecting the relative quantities of Au, Cr, and Zn.

tion of site preferences. Here we turn once again to the extended Hückel (eH) method. In particular, we will use Mulliken population analysis to tell us the electron population on different sites, just as in Section 1.5. If there is a chemical rationale behind the site coloring, eH should capture it. Our strategy is to model all sites as the majority element, Zn, and see which sites accumulate the most electrons. The most electron-rich sites should correspond to the most electronegative element, Au (Pauling electronegativity 2.54 versus 1.66 for Cr and 1.65 for Zn[69]).

Table A.1: Relative charges of sites in model all-Zn system corresponding to experimental sites.

Site	Charge
Au23 (QOH)	-0.14
Au12 (ZOT)	-0.13
Zn32 (HOT)	-0.06
Zn21 (QIT)	-0.03
Zn22 (QOT)	-0.02
Zn25 (QCO)	-0.01
Cr42 (TOT)	0.00
Zn15 (ZCO)	0.00
Zn34 (HTT)	0.02
Zn13 (ZOH)	0.03
Zn45 (TCO)	0.03
Zn35 (HCO)	0.05
Zn11 (ZIT)	0.06
Zn30 (HCC)	0.06
Zn43 (TOH)	0.06

Our analysis agrees very well with the experimentally found sites, shown in Table A.1, particularly in distinguishing the Au sites from the remaining Zn and Cr sites. That we were unable to distinguish the Cr site from the Zn sites is not surprising given that Cr and Zn are similar in electronegativity and the extent to which the Cr d-orbitals play a role in bonding is not taken into account.

APPENDIX B

CRYSTALLOGRAPHIC DATA

B.1 $Ir_2Ru_8Zn_{100}$

Table B.1: Atomic coordinates ($\times 10^4$) and equivalent isotropic displacement parameters ($Å^2 \times 10^3$) for $Ir_2Ru_8Zn_{100}$

Site	Occ.	x	y	z	U_{eq}[1]
M21[2]	0.44	0	0	1404(1)	25(1)
Ru37	0.96	6667	3333	1403(1)	22(1)
M20[2]	0.29	1135(1)	2270(1)	2039(1)	25(1)
Ru08		1367(1)	2734(1)	689(1)	25(1)
Ru31		3333	6667	1768(1)	23(1)
Ru32		4676(1)	5323(1)	2500	23(1)
Ru01		0	0	0	22(1)
Zn50		3333	6667	490(1)	28(1)
M09[2]	0.13	4404(1)	2202(1)	166(1)	24(1)
Zn46		5390(1)	4610(1)	784(1)	29(1)
Zn45		4531(3)	2266(1)	2068(1)	33(1)
Zn47	0.96	6667	3333	2281(1)	25(1)
Zn44		3335(2)	3572(2)	1378(1)	32(1)
Zn26		934(2)	1868(3)	2500	26(1)
Zn24		3238(2)	2966(2)	1828(1)	31(1)
Zn07		3648(2)	3648(2)	0	28(1)
Zn22		1149(1)	2299(2)	1561(1)	29(1)
Zn49		3333	6667	960(1)	31(1)
Zn04		1508(2)	754(1)	725(1)	29(1)
Zn48		4498(1)	5502(1)	1110(1)	28(1)
Zn34		5321(1)	4679(1)	2091(1)	28(1)
Zn14		5481(1)	4519(1)	317(1)	28(1)
Zn19		0	0	2192(1)	28(1)
Zn16		2021(1)	4043(2)	1055(1)	33(1)
Zn27		3001(1)	3588(2)	2263(1)	28(1)
Zn02		709(1)	1418(2)	346(1)	28(1)
Zn33		4519(1)	5481(1)	1673(1)	31(1)
Zn18		1397(2)	699(1)	1794(1)	29(1)
Zn05		3172(1)	2740(2)	454(1)	29(1)
Zn30		4073(1)	5927(1)	2114(1)	28(1)
Zn06		1969(1)	3938(2)	279(1)	28(1)
Zn35		2630(1)	5260(2)	1409(1)	32(1)
Zn17		6667	3333	265(1)	27(1)
Zn03		2261(2)	1131(1)	84(1)	28(1)
Zn36		4606(2)	3256(2)	2500	29(1)
Zn11		3404(2)	4712(2)	656(1)	31(1)
Zn10		813(1)	1626(2)	1093(1)	32(1)
Zn23		2315(2)	1157(1)	2233(1)	32(1)
Zn29		2601(2)	5202(3)	2500	28(1)
Zn12		3203(2)	2808(2)	930(1)	32(1)
Zn28		2171(1)	4341(2)	1847(1)	30(1)
Zn25		2374(2)	1187(1)	1345(1)	33(1)
Zn13		4987(2)	2494(1)	625(1)	31(1)
Zn15		4072(1)	5928(1)	124(1)	29(1)
Zn42		6667	3333	941(1)	45(1)
Zn43	0.66	4464(4)	2232(2)	1580(1)	45(1)
Zn39	0.3	6986(5)	3493(3)	1846(1)	22(2)
Zn38	0.26	5361(6)	4114(6)	1219(1)	29(1)
Zn41	0.08	5536(15)	4464(15)	1678(6)	29(6)
Zn40	0.05	4640(80)	2320(40)	1045(16)	60(20)
Zn38′	0.2	5670(30)	4330(30)	1244(9)	123(17)
Zn39′	0.09	6667	3333	1590(30)	120(40)
Zn40′	0.31	4514(8)	2257(4)	1239(2)	32(2)
Zn40″	0.32	4810(5)	2968(5)	1152(1)	31(1)
Zn41′	0.31	5240(5)	3769(5)	1657(1)	31(1)
Zn41″	0.3	5552(4)	4448(4)	1563(2)	33(2)

[1] U_{eq} is defined as one third of the trace of the orthogonalized U_{ij} tensor.

[2] For M sites, the listed occupation x is the Ir content. The Ru content is given by $1 - x$.

Table B.2: Anisotropic displacement parameters ($Å^2 \times 10^3$)for $Ir_2Ru_8Zn_{100}$

Site	U_{11} [1]	U_{22}	U_{33}	U_{23}	U_{13}	U_{12}
M21	23(1)	23(1)	29(1)	0	0	11(1)
Ru37	23(1)	23(1)	20(1)	0	0	11(1)
M20	24(1)	22(1)	30(1)	0(1)	0(1)	11(1)
Ru08	23(1)	21(1)	29(1)	-2(1)	-1(1)	11(1)
Ru31	23(1)	23(1)	24(1)	0	0	11(1)
Ru32	22(1)	22(1)	26(1)	0	0	13(1)
Ru01	20(1)	20(1)	24(2)	0	0	10(1)
Zn50	26(1)	26(1)	30(2)	0	0	13(1)
M09	21(1)	23(1)	27(1)	0(1)	0(1)	10(1)
Zn46	27(1)	27(1)	36(1)	-2(1)	2(1)	14(1)
Zn45	34(1)	29(1)	38(1)	-3(1)	-6(1)	17(1)
Zn47	26(1)	26(1)	22(2)	0	0	13(1)
Zn44	37(1)	27(1)	33(1)	0(1)	0(1)	17(1)
Zn26	24(1)	26(2)	28(2)	0	0	13(1)
Zn24	29(1)	33(1)	34(1)	0(1)	-1(1)	18(1)
Zn07	27(1)	27(1)	33(1)	0(1)	0(1)	14(1)
Zn22	27(1)	27(1)	32(1)	-1(1)	0(1)	14(1)
Zn49	29(1)	29(1)	35(2)	0	0	14(1)
Zn04	28(1)	26(1)	34(1)	-1(1)	-2(1)	14(1)
Zn48	25(1)	25(1)	33(1)	0(1)	0(1)	13(1)
Zn34	26(1)	26(1)	31(1)	0(1)	0(1)	12(1)
Zn14	23(1)	23(1)	37(1)	0(1)	0(1)	9(1)
Zn19	25(1)	25(1)	34(2)	0	0	12(1)
Zn16	30(1)	30(1)	38(1)	-8(1)	-4(1)	15(1)
Zn27	24(1)	28(1)	29(1)	-1(1)	-3(1)	10(1)
Zn02	25(1)	24(1)	35(1)	0(1)	0(1)	12(1)
Zn33	28(1)	28(1)	36(1)	-1(1)	1(1)	12(1)
Zn18	32(1)	26(1)	31(1)	0(1)	-1(1)	16(1)
Zn05	26(1)	28(1)	34(1)	1(1)	2(1)	15(1)
Zn30	27(1)	27(1)	33(1)	1(1)	-1(1)	15(1)
Zn06	25(1)	28(1)	33(1)	1(1)	1(1)	14(1)
Zn35	31(1)	30(1)	34(1)	-8(1)	-4(1)	15(1)
Zn17	24(1)	24(1)	34(2)	0	0	12(1)
Zn03	23(1)	29(1)	29(1)	0(1)	0(1)	11(1)
Zn36	34(1)	25(1)	34(1)	0	0	17(1)
Zn11	25(1)	25(1)	40(1)	0(1)	-4(1)	11(1)
Zn10	30(1)	32(1)	33(1)	3(1)	2(1)	16(1)
Zn23	29(1)	29(1)	39(1)	0(1)	-1(1)	14(1)
Zn29	24(1)	29(2)	33(2)	0	0	14(1)
Zn12	31(1)	29(1)	32(1)	-1(1)	1(1)	11(1)
Zn28	26(1)	24(1)	39(1)	0(1)	0(1)	12(1)
Zn25	27(1)	27(1)	43(1)	-1(1)	-3(1)	13(1)
Zn13	30(1)	27(1)	36(1)	-1(1)	-1(1)	15(1)
Zn15	26(1)	26(1)	35(1)	-2(1)	2(1)	12(1)
Zn42	53(2)	53(2)	29(2)	0	0	27(1)
Zn43	23(2)	66(3)	32(2)	2(1)	4(2)	11(1)
Zn39	22(4)	22(2)	22(3)	-2(1)	-4(2)	11(2)
Zn38	32(2)	37(3)	27(3)	7(2)	6(2)	23(2)
Zn40′	32(4)	24(2)	42(5)	-2(2)	-5(3)	16(2)
Zn40″	30(2)	37(2)	31(3)	4(2)	2(2)	21(2)
Zn41′	30(2)	32(2)	33(3)	5(2)	5(2)	18(2)
Zn41″	31(2)	31(2)	35(5)	-3(2)	3(2)	14(3)

[1] The anisotropic displacement factor exponent takes the form: $-2\pi^2[h^2a^{*2}U^{11} + \ldots + 2hka^*b^*U^{12}]$

B.2 $Ir_3Ru_7Zn_{100}$

Table B.3: Atomic coordinates ($\times 10^4$) and equivalent isotropic displacement parameters ($Å^2 \times 10^3$) for $Ir_3Ru_7Zn_{100}$

Site	Occ.	x	y	z	U_{eq}[1]
M21[2]	0.71	0	0	1403(1)	18(1)
Ru37	0.91	6667	3333	1403(1)	14(1)
M20[2]	0.60	1139(1)	2277(1)	2038(1)	18(1)
Ru08		1365(1)	2730(1)	688(1)	17(1)
Ru31		3333	6667	1768(1)	12(1)
Ru32		4680(1)	5320(1)	2500	12(1)
Ru01		0	0	0	14(1)
Zn50		3333	6667	492(1)	18(1)
M09[2]	0.36	4396(1)	2198(1)	166(1)	17(1)
Zn46		5392(1)	4608(1)	788(1)	24(1)
Zn45		4544(2)	2272(1)	2067(1)	28(1)
Zn47	0.95	6667	3333	2283(1)	17(1)
Zn44		3349(2)	3578(1)	1378(1)	27(1)
Zn26		924(1)	1849(3)	2500	20(1)
Zn24		3240(1)	2963(1)	1827(1)	24(1)
Zn07		3650(2)	3650(2)	0	20(1)
Zn22		1150(1)	2300(2)	1559(1)	22(1)
Zn49		3333	6667	962(1)	23(1)
Zn04		1509(2)	755(1)	725(1)	22(1)
Zn48		4497(1)	5503(1)	1110(1)	18(1)
Zn34		5319(1)	4681(1)	2093(1)	20(1)
Zn14		5485(1)	4515(1)	316(1)	20(1)
Zn19		0	0	2190(1)	20(1)
Zn16		2018(1)	4037(2)	1056(1)	26(1)
Zn27		3001(1)	3586(1)	2263(1)	21(1)
Zn02		708(1)	1417(2)	346(1)	21(1)
Zn33		4517(1)	5483(1)	1673(1)	23(1)
Zn18		1391(2)	695(1)	1793(1)	22(1)
Zn05		3174(1)	2740(1)	455(1)	21(1)
Zn30		4074(1)	5926(1)	2114(1)	21(1)
Zn06		1966(1)	3932(2)	278(1)	21(1)
Zn35		2630(1)	5260(2)	1408(1)	23(1)
Zn17		6667	3333	261(1)	22(1)
Zn03		2256(2)	1128(1)	83(1)	20(1)
Zn36		4606(2)	3254(2)	2500	20(1)
Zn11		3408(1)	4710(1)	656(1)	24(1)
Zn10		811(1)	1622(2)	1092(1)	24(1)
Zn23		2317(2)	1159(1)	2229(1)	26(1)
Zn29		2602(1)	5203(3)	2500	23(1)
Zn12		3194(1)	2806(1)	931(1)	27(1)
Zn28		2173(1)	4347(2)	1846(1)	20(1)
Zn25		2369(2)	1185(1)	1345(1)	25(1)
Zn13		5004(2)	2502(1)	621(1)	24(1)
Zn15		4073(1)	5927(1)	124(1)	23(1)
Zn42		6667	3333	941(1)	30(1)
Zn43	0.67	4434(3)	2217(2)	1576(1)	35(1)
Zn39	0.3	6989(5)	3494(3)	1848(1)	23(2)
Zn38	0.34	5370(4)	4128(4)	1221(1)	34(1)
Zn41	0.23	5546(4)	4454(4)	1689(2)	15(2)
Zn40	0.11	4395(19)	2198(9)	1045(4)	28(5)
Zn38′	0.15	5935(12)	4065(12)	1280(3)	42(5)
Zn39′	0.09	6667	3333	1676(12)	38(14)
Zn40′	0.32	4502(7)	2251(3)	1237(1)	26(2)
Zn40″	0.26	4805(5)	2965(5)	1151(1)	22(1)
Zn41′	0.26	5237(4)	3768(5)	1657(1)	17(1)
Zn41″	0.26	5553(3)	4447(3)	1562(2)	19(2)

[1] U_{eq} is defined as one third of the trace of the orthogonalized U_{ij} tensor.

[2] For M sites, the listed occupation x is the Ir content. The Ru content is given by $1 - x$.

Table B.4: Anisotropic displacement parameters ($Å^2 \times 10^3$) for $Ir_3Ru_7Zn_{100}$

Site	U_{11} [1]	U_{22}	U_{33}	U_{23}	U_{13}	U_{12}
M21	17(1)	17(1)	20(1)	0	0	8(1)
Ru37	15(1)	15(1)	12(1)	0	0	8(1)
M20	18(1)	17(1)	20(1)	-1(1)	0(1)	8(1)
Ru08	17(1)	15(1)	18(1)	-2(1)	-1(1)	7(1)
Ru31	12(1)	12(1)	12(1)	0	0	6(1)
Ru32	13(1)	13(1)	12(1)	0	0	6(1)
Ru01	13(1)	13(1)	17(1)	0	0	7(1)
Zn50	18(1)	18(1)	20(2)	0	0	9(1)
M09	17(1)	17(1)	17(1)	0(1)	-1(1)	8(1)
Zn46	21(1)	21(1)	31(1)	-1(1)	1(1)	10(1)
Zn45	34(1)	25(1)	29(1)	-5(1)	-10(1)	17(1)
Zn47	15(1)	15(1)	20(2)	0	0	7(1)
Zn44	38(1)	23(1)	21(1)	2(1)	3(1)	16(1)
Zn26	20(1)	22(1)	19(1)	0	0	11(1)
Zn24	22(1)	30(1)	21(1)	1(1)	-1(1)	15(1)
Zn07	20(1)	20(1)	21(1)	1(1)	-1(1)	11(1)
Zn22	23(1)	23(1)	20(1)	1(1)	0(1)	12(1)
Zn49	24(1)	24(1)	21(2)	0	0	12(1)
Zn04	24(1)	21(1)	23(1)	0(1)	0(1)	12(1)
Zn48	17(1)	17(1)	17(1)	0(1)	0(1)	8(1)
Zn34	20(1)	20(1)	19(1)	0(1)	0(1)	10(1)
Zn14	20(1)	20(1)	19(1)	0(1)	0(1)	10(1)
Zn19	19(1)	19(1)	23(2)	0	0 9	(1)
Zn16	24(1)	26(1)	29(1)	-10(1)	-5(1)	13(1)
Zn27	20(1)	20(1)	20(1)	0(1)	-3(1)	8(1)
Zn02	20(1)	20(1)	22(1)	-2(1)	-1(1)	10(1)
Zn33	20(1)	20(1)	25(1)	-1(1)	1(1)	7(1)
Zn18	25(1)	19(1)	24(1)	-1(1)	-3(1)	13(1)
Zn05	21(1)	23(1)	20(1)	-1(1)	2(1)	11(1)
Zn30	21(1)	21(1)	21(1)	1(1)	-1(1)	10(1)
Zn06	21(1)	26(1)	18(1)	1(1)	1(1)	13(1)
Zn35	23(1)	25(1)	21(1)	-4(1)	-2(1)	12(1)
Zn17	19(1)	19(1)	29(2)	0	0	9(1)
Zn03	18(1)	20(1)	22(1)	-2(1)	-3(1)	9(1)
Zn36	25(1)	19(1)	21(1)	0	0	14(1)
Zn11	21(1)	20(1)	30(1)	0(1)	-3(1)	9(1)
Zn10	23(1)	30(1)	22(1)	4(1)	2(1)	15(1)
Zn23	22(1)	22(1)	35(1)	-1(1)	-2(1)	11(1)
Zn29	20(1)	21(1)	29(2)	0	0	10(1)
Zn12	26(1)	26(1)	22(1)	0(1)	-1(1)	7(1)
Zn28	19(1)	17(1)	24(1)	0(1)	0(1)	8(1)
Zn25	19(1)	20(1)	35(1)	-2(1)	-4(1)	9(1)
Zn13	25(1)	22(1)	25(1)	-2(1)	-3(1)	12(1)
Zn15	20(1)	20(1)	27(1)	-2(1)	2(1)	10(1)
Zn42	38(1)	38(1)	13(2)	0	0	19(1)
Zn43	18(2)	51(2)	24(2)	2(1)	4(1)	9(1)
Zn39	29(4)	25(3)	17(3)	-3(1)	-5(2)	14(2)
Zn38	30(2)	39(2)	37(2)	9(2)	-1(2)	22(2)
Zn41	18(2)	18(2)	11(4)	2(2)	-2(2)	11(2)
Zn40	25(10)	35(8)	22(10)	3(4)	6(8)	13(5)
Zn38′	40(6)	40(6)	22(8)	0(5)	0(5)	0(8)
Zn39′	10(10)	10(10)	90(50)	0	0	5(5)
Zn40′	33(4)	28(2)	20(3)	-3(1)	-6(3)	17(2)
Zn40″	20(2)	33(3)	17(2)	7(2)	0(2)	15(2)
Zn41′	15(2)	21(2)	15(2)	3(2)	2(2)	9(2)
Zn41″	24(2)	24(2)	17(4)	-5(2)	5(2)	17(2)

[1] The anisotropic displacement factor exponent takes the form: $-2\pi^2[h^2a^{*2}U^{11} + \ldots + 2hka^*b^*U^{12}]$

B.3 $Au_{32}Cd_{47}Zn_{21}$

The structure of $Au_{32}Cd_{47}Zn_{21}$ was solved by Joshua Schmidt and Ji Feng, and will appear in a forthcoming paper by S. Lee, R. Henderson, *et al* titled *Pseudo-five-fold diffraction symmetries in tetrahedral packing*. Samples of $Au_{32}Cd_{47}Zn_{21}$ were prepared by mixing a one gram sample of Au (shaved metal), Cd (powder), and Zn(powder) with nominal 99.9 % metal purity and sealing the mixture in an evacuated silica tube. The mixture was heated from room temperature to 650°C over 5 hours, held at that temperature for another 5 hours, and then cooled to 250°C gradually over a 2 week period, after which the furnace was turned off. Microprobe measurements of crystals extracted from the bulk sample yielded a composition of $Zn_{11.0(1)}Au_{15.0(1)}Cd_{23.2(1)}$.

A crystal was then selected for single crystal refinement. Initial refinement with 100 % occupation of all sites led to a crystal similar to the one reported, but where the Cd4 site had a thermal factor substantially larger than that of the other sites. We therefore allowed mixed occupation of this site permitting Au, Cd, and Zn to occupy this position, now renamed site M4, while constraining that overall site M4 remained fully occupied. With the inclusion of only these two new parameters wR_2 for all reflections lowered from 12.80% to 12.24%, a statistically significant decrease. The final refined crystal stoichiometry was $Zn_{11.0}Au_{15.0}Cd_{23.0}$, in good agreement with the microprobe measurements, see above.

Table B.5: Crystallographic information and R-values for $Au_{32}Cd_{47}Zn_{21}$

Empirical formula	$Au_{44.62}Cd_{68.54}Zn_{32.83}$
Formula weight	12958.50
Temperature	293(2) K
Wavelength	0.71073 Å
Crystal system	cubic
Space group	$I\bar{m}3$
Unit cell dimensions	a = 13.8432(19) Å
Volume	2652.8(6) $Å^3$
Z	1
Density (calculated)	8.111 Mg/m^3
Absorption coefficient	57.845 mm^{-1}
F(000)	5414
2θ range for data collection	2.94 to 37.56°
Index ranges	$-23 \leq h \leq 12$, $-5 \leq k \leq 23$, $-21 \leq l \leq 10$
Reflections collected	5781
Independent reflections	1282 [R_{int} = 0.0761]
Completeness	99.6%
Refinement method	Full-matrix least-squares on F^2
Data / restraints / parameters	1282 / 0 / 38
Goodness-of-fit on F2	0.775
Final R indices [$I > 2\sigma(I)$]	R_1 = 0.0353, wR_2 = 0.1048
R indices (all data)	R_1 = 0.0533, wR_2 = 0.1224
Largest diff. peak and hole	2.950 and -4.013 $e/Å^{-3}$

Table B.6: Atomic coordinates ($\times 10^4$) and equivalent isotropic displacement parameters ($Å^2 \times 10^3$) for $Au_{32}Cd_{47}Zn_{21}$

Site	Occ.	x	y	z	U_{eq} [1]
Au1		0	0	0	18(1)
Au2		3306(1)	0	2096(1)	9(1)
Au3		5000	0	3290(1)	8(1)
M4 [2]	0.27/0.37/0.36	1740(1)	0	1027(1)	29(1)
Cd7		5000	-1178(1)	5000	9(1)
Cd8		3031(1)	1815(1)	1134(1)	12(1)
Zn9		3331(1)	0	4035(1)	9(1)

[1] U_{eq} is defined as one third of the trace of the orthogonalized U_{ij} tensor.

[2] The occupation shown for site M4 is the fraction Au/Cd/Zn. Refining the M4 site as a mixture (shown here) rather than pure Cd lowers the R_1 value from 3.71% to 3.53% (for $I > 2\sigma(I)$).

Table B.7: Anisotropic displacement parameters ($Å^2 \times 10^3$) for $Au_{32}Cd_{47}Zn_{21}$

Site	U_{11} [1]	U_{22}	U_{33}	U_{23}	U_{13}	U_{12}
Au1	18(1)	18(1)	18(1)	0	0	0
Au2	9(1)	9(1)	8(1)	0	1(1)	0
Au3	7(1)	12(1)	6(1)	0	0	0
M4	20(1)	29(1)	38(1)	0	-19(1)	0
Cd7	8(1)	11(1)	9(1)	0	0	0
Cd8	14(1)	10(1)	12(1)	2(1)	0(1)	2(1)
Zn9	7(1)	11(1)	8(1)	0	2(1)	0

[1] The anisotropic displacement factor exponent takes the form: $-2\pi^2[h^2a^{*2}U^{11} + \ldots + 2hka^*b^*U^{12}]$

B.4 $Au_{10}Cr_4Zn_{89}$

$Au_{10}Cr_4Zn_{89}$ was solved by Partha Jana, and the experimental and computational results will appear in a forthcoming paper by P. Jana and R. Henderson *et al* titled *Spatially correlated structural disorder phenomena in a γ-brass related complex zinc-rich alloy (Au,Cr)Zn_n; $n = 10.2 - 6.4$.*

Table B.8: Crystallographic information and R-values for $Au_{10}Cr_4Zn_{89}$

Empirical formula	$Au_{10}Cr_4Zn_{89}$
Formula weight	7995.60
Temperature	293(2) K
Wavelength	0.71073 Å
Crystal system	cubic
Space group	$F\bar{4}3m$
Unit cell dimensions	a = 18.4299(7) Å
Volume	6259.9(4) $Å^3$
Z	4
Density (calculated)	8.484 Mg/m^3
Absorption coefficient	57.308 mm^{-1}
F(000)	14224
2θ range for data collection	3.13 to 32.49°
Index ranges	$-24 \leq h \leq 27$,
	$-27 \leq k \leq 27$,
	$-24 \leq l \leq 25$
Reflections collected	20193
Independent reflections	1170 [R_{int} = 0.2019]
Completeness	99.7%
Refinement method	Full-matrix least-squares on F^2
Data / restraints / parameters	1170 / 0 / 63
Goodness-of-fit on F2	1.188
Final R indices [$I > 2\sigma(I)$]	R_1 = 0.0517, wR_2 = 0.0819
R indices (all data)	R_1 = 0.0573, wR_2 = 0.0834
Largest diff. peak and hole	2.262 and -3.220 $e/Å^{-3}$

Table B.9: Atomic coordinates ($\times 10^4$) and equivalent isotropic displacement parameters ($Å^2 \times 10^3$) for $Au_{10}Cr_4Zn_{89}$

Site	x	y	z	U_{eq} [1]
Zn11	534(1)	534(1)	534(1)	11(1)
Au12	9135(1)	9135(1)	9135(1)	7(1)
Zn13	1845(2)	0	0	18(1)
Zn15	1549(1)	1549(1)	241(1)	17(1)
Cr42	6489(1)	6489(1)	6489(1)	5(1)
Zn43	6452(2)	2500	2500	11(1)
Zn45	1083(1)	1083(1)	7758(1)	15(1)
Zn30	5000	5000	5000	19(2)
Zn32	4148(1)	4148(1)	4148(1)	13(1)
Zn34	480(1)	480(1)	6534(1)	15(1)
Zn35	1890(1)	1890(1)	5245(1)	17(1)
Zn2B	3177(2)	3177(2)	3177(2)	25(1)
Zn22	1693(2)	1693(2)	1693(2)	16(1)
Au23	796(1)	2500	2500	14(1)
Zn25	839(1)	839(1)	2710(1)	19(1)

[1] U_{eq} is defined as one third of the trace of the orthogonalized U_{ij} tensor.

Table B.10: Anisotropic displacement parameters ($Å^2 \times 10^3$) for $Au_{10}Cr_4Zn_{89}$

Site	U_{11} [1]	U_{22}	U_{33}	U_{23}	U_{13}	U_{12}
Zn11	11(1)	11(1)	11(1)	2(1)	2(1)	2(1)
Au12	7(1)	7(1)	7(1)	-1(1)	-1(1)	-1(1)
Zn13	18(2)	17(1)	17(1)	3(1)	0	0
Zn15	17(1)	17(1)	15(1)	-5(1)	-5(1)	-3(1)
Cr42	5(1)	5(1)	5(1)	-1(1)	-1(1)	-1(1)
Zn43	12(1)	11(1)	11(1)	-4(1)	0	0
Zn45	18(1)	18(1)	9(1)	1(1)	1(1)	-1(1)
Zn30	19(2)	19(2)	19(2)	0	0	0
Zn32	13(1)	13(1)	13(1)	1(1)	1(1)	1(1)
Zn34	12(1)	12(1)	21(1)	-1(1)	-1(1)	-5(1)
Zn35	19(1)	19(1)	12(1)	3(1)	3(1)	-2(1)
Zn2B	25(1)	25(1)	25(1)	13(1)	13(1)	13(1)
Zn22	16(1)	16(1)	16(1)	2(1)	2(1)	2(1)
Au23	9(1)	17(1)	17(1)	-2(1)	0	0
Zn25	21(1)	21(1)	15(1)	2(1)	2(1)	0(1)

[1] The anisotropic displacement factor exponent takes the form: $-2\pi^2[h^2a^{*2}U^{11} + \ldots + 2hka^*b^*U^{12}]$.

APPENDIX C

CHARACTER TABLE OF THE 600-CELL

C.1 Introduction

In this section, we construct the character table for the symmetry group of the 4D regular polytope, the 600-cell.* The symmetry group of the 600-cell is alternatively known as the H_4 group and has been widely studied in the mathematics community.[110,153]

The symmetry group of the 600-cell is of order 14400, meaning there are 14400 symmetry operations. Intuitively this makes sense–each of the 120 symmetry-equivalent points in the 600-cell is coordinated to an icosahedron of neighbors with a local symmetry of the more familiar 3Dimensional I_h group, which is of order 120: $120 \times 120 = 14400$. A analogous argument can be made for the icosahedron–the icosahedron consists of 12 equivalent vertices each coordinated to a pentagon of neighbors, with local symmetry C_{5v}. The C_{5v} group is of order 10: hence, $10 \times 12 = 120$, the order of the I_h group. A rigorous and general explanation can be found in Coxeter's book.[110]

C.2 Quaternions

First we wish to enumerate all 14400 symmetry elements in systematic way. Eventually we will want to express the rotations and reflections as matrices, but

*We had finished this construction by summer 2008. Unknown to us, Lundeen had already solved the character table in 2007.[153] We include our derivation here for completeness and to emphasize chemical applications.

there is a more elegant construct suited to the task of finding them: quaternions. Quaternions were discovered by Hamilton[154] as an extension of the complex numbers. A general quaternion takes the form

$$q = q_1 + q_2 i + q_3 j + q_4 k \tag{C.1}$$

where q_n are real numbers and

$$i^2 = j^2 = k^2 = ijk = -1 \tag{C.2}$$

As a historical aside, Hamilton is said to have discovered Equation C.2 in a "flash of genius" while walking over the Broom (Brougham) Bridge with his wife in Dublin, Ireland on October 16, 1843.[155] In 1958, a plaque commemorating the discovery was fixed to the bridge featuring Equation C.2, shown in Figure C.1.

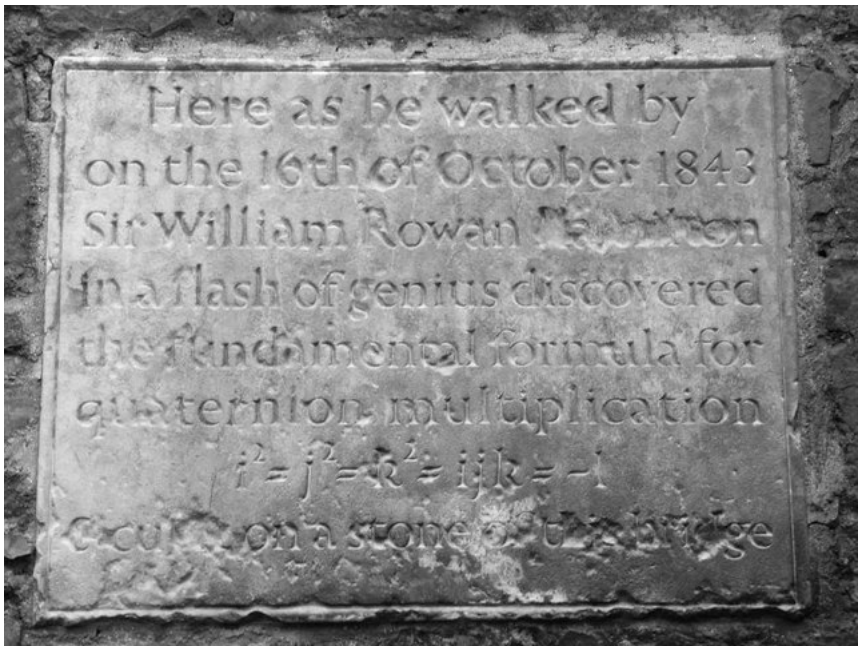

Figure C.1: Plaque installed in 1958 to commemorate Hamilton's 1843 discovery of the quaternions. Used under the Creative Commons Attribution-Share Alike 2.0 Generic license.[8]

Quaternion multiplication is straightforward if one keeps in mind that multiplication of the complex parts of the quaternion do not commute: for example $ij = k$ but $ji = -k$. These rules are implicit in Equation C.2. In general, then, quaternion multiplication of quaternions l and r is as follows:

$$\begin{aligned}(l_1 + l_2 i + l_3 j + l_4 k)\,(r_1 + r_2 i + r_3 j + r_4 k) = \\ l_1 r_1 - l_2 r_2 - l_3 r_3 - l_4 r_4 \\ + (l_1 r_2 + l_2 r_1 + l_3 r_4 - l_4 r_3)\, i \\ + (l_1 r_3 - l_2 r_4 + l_3 r_1 + l_4 r_2)\, j \\ + (l_1 r_4 + l_2 r_3 - l_3 r_2 + l_4 r_1)\, k \end{aligned} \tag{C.3}$$

The conjugate of a quaternion is defined in the expected way: the quaternion in Equation C.1 has the conjugate $\tilde{q} = q_1 - q_2 i - q_3 j - q_4 k$. The conjugate, together with the multiplication rules in Equation C.3, defines a norm: $\|q\| = \sqrt{q\tilde{q}}$. Crucially, the conjugate and norm together give a recipe for a reciprocal quaternion:

$$q^{-1} = \frac{\tilde{q}}{\|q\|} \tag{C.4}$$

Notably, if the quaternion is of unit norm ($\|q\| = 1$) then by Equation C.4 $q^{-1} = \tilde{q}$. If we take as quaternions the 120 vertices of the *unit* 600-cell, we can form a symmetry group under a quaternionic multiplication operation.[156,157] This means that each coordinate vector $\vec{q} = (a\,b\,c\,d)$ becomes a quaternion $q = a + bi + cj + dk$. Recall that the 120 vertices of the unit 600-cell are as follows: 8 permutations of (±1 0 0 0), 16 permutations of $(\pm\frac{1}{2}, \pm\frac{1}{2}, \pm\frac{1}{2}, \pm\frac{1}{2})$, and 96 even permutations of $\frac{1}{2}(\pm\tau, \pm 1, \pm\frac{1}{\tau}, 0)$, where $\tau = \frac{1+\sqrt{5}}{2}$ is the Golden Ratio.

The symmetry operation R is defined as quaternion multiplication:

$$R(q) = lqr \tag{C.5}$$

Where l and r are coordinates of the unit 600-cell expressed as quaternions and q is the coordinate being operated upon, also expressed as a quaternion. Every element has an inverse, since $\tilde{l}R(q)\tilde{r} = \tilde{l}lqr\tilde{r} = q$.

Since there are 120 choices for each l and r, it is not unreasonable to assume there will be $120 \times 120 = 14400$ unique symmetry elements and our task is complete. Note, however, that $(-l)q(-r) = lqr$ and that every vertex in the 600-cell has an inverse point: for every vertex $(a\ b\ c\ d)$ there is a corresponding vertex $(-a\ -b\ -c\ -d)$. Apparently we are double counting the symmetry operations. For instance note that both $l = r = 1 + 0i + 0j + 0k$ and $l = r = -1 + 0i + 0j + 0k$ are suitable as identity operations. Therefore this procedure generates only 7200 unique operations, and the quaternions form a 2:1 mapping onto the rotation group.[157,158]

The remaining 7200 operations are generated by combining the existing rotations with an inversion operation:

$$\tilde{R}(q) = l\tilde{q}r \tag{C.6}$$

Now that we have enumerated all the symmetry elements, we convert them to more familiar rotation matrices. One such representation[†] is presented here:[157]

$$R(q) = lqr \Rightarrow \begin{pmatrix} l_1 & -l_2 & -l_3 & -l_4 \\ l_2 & l_1 & -l_4 & l_3 \\ l_3 & l_4 & l_1 & -l_2 \\ l_4 & -l_3 & l_2 & l_1 \end{pmatrix} \begin{pmatrix} r_1 & -r_2 & -r_3 & -r_4 \\ r_2 & r_1 & r_4 & -r_3 \\ r_3 & -r_4 & r_1 & r_2 \\ r_4 & r_3 & -r_2 & r_1 \end{pmatrix} \begin{pmatrix} q_1 \\ q_2 \\ q_3 \\ q_4 \end{pmatrix} \tag{C.7}$$

[†]This is a 2:1 homomorphism[157] from the quaternions to a 4D matrix rotation group: $\mathfrak{Q} \times \mathfrak{Q} \xrightarrow{2:1} \mathfrak{R}_4$.

The l and r quaternions on the left-hand side of the arrow become the 4×4 matrices **l** and **r** on the right side. The arbitrary quaternion q becomes a column vector $\vec{q}$. The signs of some elements of the **r** matrix are different from its **l** counterpart: this is because the r quaternion is right-multiplied on q while the l quaternion operates from the left.

Since quaternion algebra is associative—specifically, since $(lq)r = l(qr)$—the matrices **l** and **r** in Equation C.7 commute. Another feature of this representation is that the quaternion conjugate corresponds to the transpose of the matrix ($\tilde{r} \rightarrow \mathbf{r}^T$), and $\tilde{r}r \rightarrow \mathbf{r}^T\mathbf{r} = \mathbf{I}$, the identity matrix.

Finally, we need a matrix representation for the inversion operation $\tilde{q}$. Unsurprisingly, this will be a matrix which sends $\vec{q}$ to $-\vec{q}$, which is $-\mathbf{I}$; a matrix with -1 on all diagonal positions and 0 elsewhere.

Thus we have generated matrices for all 14400 symmetry elements. It is a group: every element has an inverse element and the set contains the identity. That there is also closure under multiplication will become evident when we work out the group structure in the next section, but for proof using quaternions see Conway.[158]

C.2.1 A Note on 4D rotations

Consider the familiar 2D rotation matrix for a rotation in a plane about an angle θ:

$$\mathbf{R_{2D}}(\theta) = \begin{pmatrix} \cos\theta & -\sin\theta \\ \sin\theta & \cos\theta \end{pmatrix} \tag{C.8}$$

Some properties of $\mathbf{R_{2D}}$ are generalizable to matrix rotations $\mathbf{R}$ of any dimension: $\mathbf{R}$ is orthogonal ($\mathbf{R}^{-1} = \mathbf{R}^{T}$) and length-preserving ($|\mathbf{R}| = 1$). In particular, these properties hold in three dimensional rotations:

$$\mathbf{R_{3D}}(\theta) = \begin{pmatrix} \cos\theta & -\sin\theta & 0 \\ \sin\theta & \cos\theta & 0 \\ 0 & 0 & 1 \end{pmatrix} \tag{C.9}$$

Unlike $\mathbf{R_{2D}}$, $\mathbf{R_{3D}}$ is not a unique representation of a rotation about θ in three dimensions. In this case, $\mathbf{R_{3D}}$ is a rotation of θ about the z-axis. However, any 3D rotation about θ is only a change of basis away from the representation for $\mathbf{R_{3D}}$ shown here: in other words, the coordinate system can always be chosen such that the axis of rotation lies in the z-direction.

In this respect, $\mathbf{R_{3D}}$ is conceptually similar to $\mathbf{R_{2D}}$. In fact, $\mathbf{R_{3D}}$ can be written as an embedding of $\mathbf{R_{2D}}$ along with a fixed axis:

$$\mathbf{R_{3D}}(\theta) = \left(\begin{array}{cc|c} & & 0 \\ \multicolumn{2}{c|}{\mathbf{R_{2D}}(\theta)} & 0 \\ \hline 0 & 0 & 1 \end{array}\right) \tag{C.10}$$

Again, this makes intuitive sense–a 3D rotation is nothing more than a 2D rotation with a fixed direction perpendicular direction (the axis of rotation). A 4D rotation, however, is in general not simply a 3D rotation with a fixed direction in four-space. Although rotations of the type

$$\mathbf{R_{4D}}(\theta) = \left(\begin{array}{ccc|c} & & & 0 \\ & \mathbf{R_{3D}}(\theta) & & 0 \\ & & & 0 \\ \hline 0 & 0 & 0 & 1 \end{array}\right) \tag{C.11}$$

can certainly be constructed, we must now allow for a new rotation of a type

$$\mathbf{R_{4D}}(\theta,\phi) = \left(\begin{array}{cc|cc} & & 0 & 0 \\ \multicolumn{2}{c|}{\mathbf{R_{2D}}(\theta)} & 0 & 0 \\ \hline 0 & 0 & & \\ 0 & 0 & \multicolumn{2}{c}{\mathbf{R_{2D}}(\phi)} \end{array}\right) = \begin{pmatrix} \cos\theta & -\sin\theta & 0 & 0 \\ \sin\theta & \cos\theta & 0 & 0 \\ 0 & 0 & \cos\phi & -\sin\phi \\ 0 & 0 & \sin\phi & \cos\phi \end{pmatrix} \tag{C.12}$$

This is a compound rotation that rotates in two orthogonal (hyper)planes by angles θ and ϕ, and the general form of 4D rotations. $\mathbf{R}_{4D}(\theta)$ from Equation C.11 is just a special case of Equation C.12 with $\phi = 0$. Clearly, this kind of rotation has no 2D or 3D analogue–there is no fixed axis: the axis of each part of the compound rotation lies in the rotating plane of the other rotation! Typically, the only fixed point is the origin. These three types of rotation are illustrated in Figure C.2.

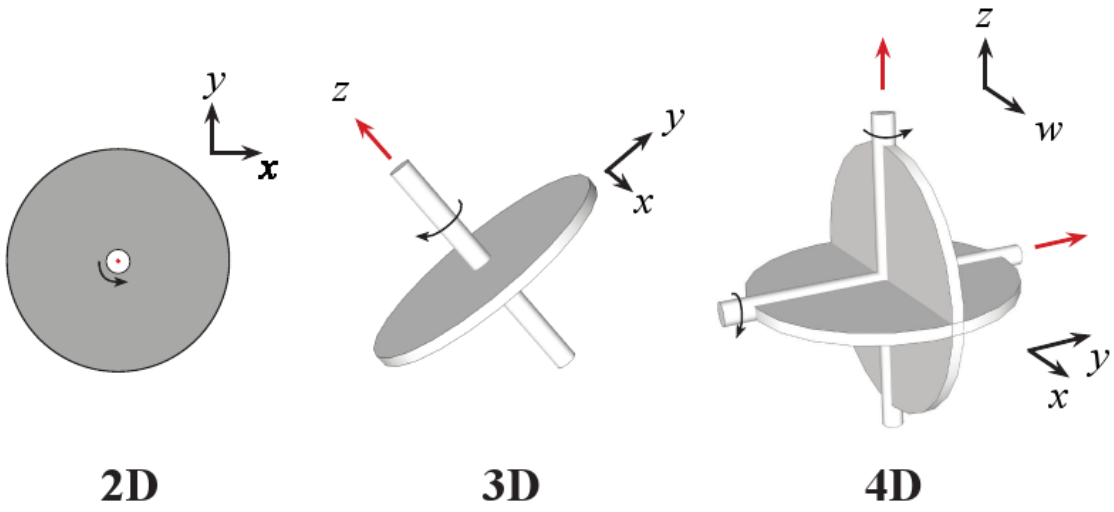

Figure C.2: Rotation in 2D, 3D, and 4D corresponding to Equations C.8, C.9, and C.12, respectively. The axes of rotation are in red. In the 4D rotation, the axes of rotation for each hyperplane lie in the orthogonal hyperplane.

The traditional chemical nomenclature for proper and improper rotational

symmetry elements–C_n and S_n–are not quite up to the task of describing compound rotations of this sort. For compound rotations we will use the notation C_nC_m; an n-fold and m-fold rotation in perpendicular planes.

The nature of the compound rotation will generally not be as obvious as in Equation C.12. Fortunately, rotation matrices $\mathbf{R}$ are diagonalizable and may be expressed as a decomposition of the eigenvalues and eigenvectors, via the usual relation:

$$\mathbf{R} = \mathbf{P}^{-1}\mathbf{\Lambda}\mathbf{P} \tag{C.13}$$

where the columns of $\mathbf{P}$ are the eigenvectors of $\mathbf{R}$, and $\mathbf{\Lambda}$ is a diagonal matrix with Λ_{ii} corresponding to the the eigenvector ith column of $\mathbf{P}$.

This decomposition makes the order of the rotation very easy to compute because the problem is reduced to taking powers of a diagonal matrix:

$$\mathbf{R}^n = \mathbf{P}^{-1}\mathbf{\Lambda}^n\mathbf{P} \tag{C.14}$$

The matrix $\mathbf{\Lambda}$, being nothing more than the rotation $\mathbf{R}$ in a particularly convenient basis, necessarily has the same determinant as $\mathbf{R}$. Specifically, the two 2D rotations now appear as 2×2 block diagonal matrices in $\mathbf{\Lambda}$:

$$\mathbf{\Lambda} = \left(\begin{array}{cc|cc} \lambda_1 & 0 & 0 & 0 \\ 0 & \lambda_2 & 0 & 0 \\ \hline 0 & 0 & \lambda_3 & 0 \\ 0 & 0 & 0 & \lambda_4 \end{array}\right) = \begin{pmatrix} \mathbf{\Lambda^{12}} & \mathbf{0} \\ \mathbf{0} & \mathbf{\Lambda^{34}} \end{pmatrix} \tag{C.15}$$

Each Λ_{12} and Λ_{34}, being a diagonalized 2×2 rotation matrix itself, has a determinant of 1 or -1. Although they may not always occur in the pattern shown in Equation C.15, there must always be at least two combinations of $\lambda_i\lambda_j = \pm 1$.

For example, the 10-fold symmetry operation

$$\begin{pmatrix} -\frac{1}{2\tau} & \frac{1}{2} & \frac{\tau}{2} & 0 \\ -\frac{1}{2} & -\frac{\tau}{2} & \frac{1}{2\tau} & 0 \\ -\frac{\tau}{2} & \frac{1}{2\tau} & -\frac{1}{2} & 0 \\ 0 & 0 & 0 & -1 \end{pmatrix}$$

has eigenvalues -1,-1, $-(-1)^{2/5}$, and $(-1)^{3/5}$. By inspection, the two orthogonal diagonalized 2×2 $\mathbf{\Lambda^{ab}}$ must be:

$$\mathbf{\Lambda^{12}} = \begin{pmatrix} -1 & 0 \\ 0 & -1 \end{pmatrix} \text{ and } \mathbf{\Lambda^{34}} = \begin{pmatrix} -(-1)^{2/5} & 0 \\ 0 & (-1)^{3/5} \end{pmatrix}$$

For this operation, $\mathbf{\Lambda^{12}}$ is of order 2 and has a determinant of 1. We could call this a C_2 or ε^* operation. $\mathbf{\Lambda^{34}}$ is of order 10 and also has a determinant of 1.

So is this operation $C_{10}\sigma_d$, or $C_{10}C_2$? We have for this operation two real eigenvalues, which implies the existence of two fixed axes of rotation or a fixed plane. Recall that a true compound rotation should have no fixed axes—hence this operation is called $C_{10}\varepsilon^*$.

In general, the order of the rotation C_nC_m is the least common multiple of n and m. For instance, the rotation $C_{10}\varepsilon^*$ is a tenfold operation: a 10-fold rotation in one plane simultaneous with a two-fold reflection in an orthogonal plane. We shorten double names (e.g. the identity is ε and not $\varepsilon\varepsilon$) and omit the identity element if we can do so without ambiguity.

C.3 Classes

A character table is a statement of all conjugacy classes and their characters under each representation. Having found the group elements and a suitable

way to manipulate them (as matrices), we turn to finding the conjugacy classes.

Let **a**, **b**, and **g** be members of our symmetry group[‡]. If there exists an element **g** such that

$$\mathbf{gag}^{-1} = \mathbf{b} \tag{C.16}$$

then **a** and **b** are said to be conjugate. If **a** and **b** are conjugate to one another, they are said to belong to the same conjugacy class along with all other elements they are conjugate to. An element can belong to one and only one conjugacy class, and therefore the classes partition the group. All members of a conjugacy class have the same order. The matrices belonging to a conjugacy class all share the same determinant, trace, and eigenvalues.

Partitioning the group into classes can be solved quickly with brute force. Starting with any element **a**, compute $\mathbf{gag}^{-1}$ for all **g**. From Equation C.16, all the resulting 14400 products are conjugate, so simply take the unique ones as a class. Repeat this procedure as needed with a remaining group element **b** until no elements remain.

The classes shown in Table C.1 are the proper rotations that have analogues in 3D. The table shows the number of elements in each class, along with the matrix trace and order of all the elements in the class. We also give an example operation and a name according to the scheme given above.

Looking at the examples, the names are fairly self-evident: in every rotational example, a 3×3 matrix is completely orthogonal to the remaining dimension.

[‡]Henceforth we will treat all elements as matrices, but theorems and relations apply to general groups unless otherwise stated.

Table C.1: Classes of proper rotations $|\mathbf{R}| = 1$ with at least one fixed axis ($\exists\lambda \in \Re$)

Elements	Tr	Order	Example	Name
1	4	1	$\begin{pmatrix} 1 & 0 & 0 & 0 \\ 0 & 1 & 0 & 0 \\ 0 & 0 & 1 & 0 \\ 0 & 0 & 0 & 1 \end{pmatrix}$	ε
1	-4	2	$\begin{pmatrix} -1 & 0 & 0 & 0 \\ 0 & -1 & 0 & 0 \\ 0 & 0 & -1 & 0 \\ 0 & 0 & 0 & -1 \end{pmatrix}$	ε^*
450	0	2	$\begin{pmatrix} 1 & 0 & 0 & 0 \\ 0 & 1 & 0 & 0 \\ 0 & 0 & -1 & 0 \\ 0 & 0 & 0 & -1 \end{pmatrix}$	$\varepsilon\varepsilon^*$
400	1	3	$\begin{pmatrix} 1 & 0 & 0 & 0 \\ 0 & 0 & 1 & 0 \\ 0 & 0 & 0 & 1 \\ 0 & 1 & 0 & 0 \end{pmatrix}$	C_3
144	$2-\tau$	5	$\begin{pmatrix} -\frac{1}{2\tau} & \frac{1}{2} & \frac{\tau}{2} & 0 \\ -\frac{1}{2} & -\frac{\tau}{2} & \frac{1}{2\tau} & 0 \\ \frac{\tau}{2} & -\frac{1}{2\tau} & \frac{1}{2} & 0 \\ 0 & 0 & 0 & 1 \end{pmatrix}$	C_5
144	$1+\tau$	5	$\begin{pmatrix} \frac{\tau}{2} & \frac{1}{2\tau} & \frac{1}{2} & 0 \\ \frac{1}{2\tau} & \frac{1}{2} & -\frac{\tau}{2} & 0 \\ -\frac{1}{2} & \frac{\tau}{2} & \frac{1}{2\tau} & 0 \\ 0 & 0 & 0 & 1 \end{pmatrix}$	C_5
400	-1	6	$\begin{pmatrix} 0 & 1 & 0 & 0 \\ 0 & 0 & 1 & 0 \\ -1 & 0 & 0 & 0 \\ 0 & 0 & 0 & -1 \end{pmatrix}$	$C_6\varepsilon^*$
144	$-\tau-1$	10	$\begin{pmatrix} -\frac{1}{2\tau} & \frac{1}{2} & \frac{\tau}{2} & 0 \\ -\frac{1}{2} & -\frac{\tau}{2} & \frac{1}{2\tau} & 0 \\ -\frac{\tau}{2} & \frac{1}{2\tau} & -\frac{1}{2} & 0 \\ 0 & 0 & 0 & -1 \end{pmatrix}$	$C_{10}\varepsilon^*$
144	$\tau-2$	10	$\begin{pmatrix} \frac{\tau}{2} & \frac{1}{2\tau} & \frac{1}{2} & 0 \\ -\frac{1}{2\tau} & -\frac{1}{2} & \frac{\tau}{2} & 0 \\ -\frac{1}{2} & \frac{\tau}{2} & \frac{1}{2\tau} & 0 \\ 0 & 0 & 0 & -1 \end{pmatrix}$	$C_{10}\varepsilon^*$

Table C.2 shows the improper rotations, and has some very important classes. In particular, it contains symmetry classes that are very visibly connected with geometric features of the 600-cell. The class $C_4\sigma$ is a four-fold rotation orthogonal to a reflection, similar to an S_4 operation in 3D. A 3D tetrahedron has 3 S_4 axes, and there are 600 tetrahedra in the 600-cell: $3 \times 600 = 1800$, the number of elements in this class.

Similarly, there are 1200 $C_3\sigma$ and $C_6\sigma$ operations in Table C.2–there are 1200 triangular faces in the 600-cell. The $C_5\sigma$ and $C_{10}\sigma$ operations correspond to the 720 edges found in the 600-cell.

Table C.2: Classes of improper rotations $|\mathbf{R}| = -1$ with at least one fixed axis ($\exists \lambda \in \Re$)

Elements	Tr	Order	Example	Name
60	2	2	$\begin{pmatrix} 1 & 0 & 0 & 0 \\ 0 & 1 & 0 & 0 \\ 0 & 0 & 1 & 0 \\ 0 & 0 & 0 & -1 \end{pmatrix}$	σ
60	-2	2	$\begin{pmatrix} 1 & 0 & 0 & 0 \\ 0 & -1 & 0 & 0 \\ 0 & 0 & -1 & 0 \\ 0 & 0 & 0 & -1 \end{pmatrix}$	$\sigma\varepsilon^*$
1800	0	4	$\begin{pmatrix} 0 & 1 & 0 & 0 \\ 1 & 0 & 0 & 0 \\ 0 & 0 & 0 & 1 \\ 0 & 0 & -1 & 0 \end{pmatrix}$	$C_4\sigma$
1200	-1	6	$\begin{pmatrix} 0 & 1 & 0 & 0 \\ 0 & 0 & 1 & 0 \\ 1 & 0 & 0 & 0 \\ 0 & 0 & 0 & -1 \end{pmatrix}$	$C_3\sigma$
1200	1	6	$\begin{pmatrix} 1 & 0 & 0 & 0 \\ 0 & 0 & 1 & 0 \\ 0 & 0 & 0 & 1 \\ 0 & -1 & 0 & 0 \end{pmatrix}$	$C_6\sigma$
720	$\tau - 1$	10	$\begin{pmatrix} \frac{\tau}{2} & \frac{1}{2\tau} & \frac{1}{2} & 0 \\ \frac{1}{2\tau} & \frac{1}{2} & -\frac{\tau}{2} & 0 \\ -\frac{1}{2} & \frac{\tau}{2} & \frac{1}{2\tau} & 0 \\ 0 & 0 & 0 & -1 \end{pmatrix}$	$C_5\sigma$
720	$-\tau$	10	$\begin{pmatrix} -\frac{1}{2\tau} & \frac{1}{2} & \frac{\tau}{2} & 0 \\ -\frac{1}{2} & -\frac{\tau}{2} & \frac{1}{2\tau} & 0 \\ \frac{\tau}{2} & -\frac{1}{2\tau} & \frac{1}{2} & 0 \\ 0 & 0 & 0 & -1 \end{pmatrix}$	$C_5\sigma$
720	$\tau - 1$	10	$\begin{pmatrix} -\frac{1}{2\tau} & \frac{1}{2} & \frac{\tau}{2} & 0 \\ -\frac{1}{2} & -\frac{\tau}{2} & \frac{1}{2\tau} & 0 \\ -\frac{\tau}{2} & \frac{1}{2\tau} & -\frac{1}{2} & 0 \\ 0 & 0 & 0 & 1 \end{pmatrix}$	$C_{10}\sigma$
720	τ	10	$\begin{pmatrix} \frac{\tau}{2} & \frac{1}{2\tau} & \frac{1}{2} & 0 \\ -\frac{1}{2\tau} & -\frac{1}{2} & \frac{\tau}{2} & 0 \\ -\frac{1}{2} & \frac{\tau}{2} & \frac{1}{2\tau} & 0 \\ 0 & 0 & 0 & 1 \end{pmatrix}$	$C_{10}\sigma$

Finally, in Table C.3, we tabulate the double rotations: those containing no real eigenvalues. While these classes are interesting in their own right, they are lost under projection to 3D and are not of particular interest to us for chemical applications.

Table C.3: Classes of proper rotations $|\mathbf{R}| = 1$ with no fixed axes ($\neg\exists\lambda \in \Re$)

Elements	Tr	Order	Example	Name
40	-2	3	$\begin{pmatrix} -\frac{1}{2} & \frac{\tau}{2} & \frac{1}{2\tau} & 0 \\ -\frac{\tau}{2} & -\frac{1}{2} & 0 & \frac{1}{2\tau} \\ -\frac{1}{2\tau} & 0 & -\frac{1}{2} & -\frac{\tau}{2} \\ 0 & -\frac{1}{2\tau} & \frac{\tau}{2} & -\frac{1}{2} \end{pmatrix}$	C_3C_3
60	0	4	$\begin{pmatrix} 0 & 1 & 0 & 0 \\ -1 & 0 & 0 & 0 \\ 0 & 0 & 0 & 1 \\ 0 & 0 & -1 & 0 \end{pmatrix}$	C_4C_4
288	-1	5	$\begin{pmatrix} 0 & \frac{1}{2\tau} & \frac{\tau}{2} & \frac{1}{2} \\ 0 & -\frac{1}{2} & -\frac{1}{2\tau} & \frac{\tau}{2} \\ 0 & \frac{\tau}{2} & -\frac{1}{2} & \frac{1}{2\tau} \\ -1 & 0 & 0 & 0 \end{pmatrix}$	C_5C_5
24	$2(\tau-1)$	5	$\begin{pmatrix} \frac{1}{2\tau} & \frac{\tau}{2} & 0 & \frac{1}{2} \\ -\frac{\tau}{2} & \frac{1}{2\tau} & \frac{1}{2} & 0 \\ 0 & -\frac{1}{2} & \frac{1}{2\tau} & \frac{\tau}{2} \\ -\frac{1}{2} & 0 & -\frac{\tau}{2} & \frac{1}{2\tau} \end{pmatrix}$	C_5C_5
24	-2τ	5	$\begin{pmatrix} -\frac{\tau}{2} & \frac{1}{2\tau} & \frac{1}{2} & 0 \\ -\frac{1}{2\tau} & -\frac{\tau}{2} & 0 & \frac{1}{2} \\ -\frac{1}{2} & 0 & -\frac{\tau}{2} & -\frac{1}{2\tau} \\ 0 & -\frac{1}{2} & \frac{1}{2\tau} & -\frac{\tau}{2} \end{pmatrix}$	C_5C_5
40	2	6	$\begin{pmatrix} \frac{1}{2} & \frac{\tau}{2} & \frac{1}{2\tau} & 0 \\ -\frac{\tau}{2} & \frac{1}{2} & 0 & \frac{1}{2\tau} \\ -\frac{1}{2\tau} & 0 & \frac{1}{2} & -\frac{\tau}{2} \\ 0 & -\frac{1}{2\tau} & \frac{\tau}{2} & \frac{1}{2} \end{pmatrix}$	C_6C_6
24	$2(1-\tau)$	10	$\begin{pmatrix} -\frac{1}{2\tau} & \frac{\tau}{2} & 0 & \frac{1}{2} \\ -\frac{\tau}{2} & -\frac{1}{2\tau} & \frac{1}{2} & 0 \\ 0 & -\frac{1}{2} & -\frac{1}{2\tau} & \frac{\tau}{2} \\ -\frac{1}{2} & 0 & -\frac{\tau}{2} & -\frac{1}{2\tau} \end{pmatrix}$	$C_{10}C_{10}$
24	2τ	10	$\begin{pmatrix} \frac{\tau}{2} & \frac{1}{2\tau} & \frac{1}{2} & 0 \\ -\frac{1}{2\tau} & \frac{\tau}{2} & 0 & \frac{1}{2} \\ -\frac{1}{2} & 0 & \frac{\tau}{2} & -\frac{1}{2\tau} \\ 0 & -\frac{1}{2} & \frac{1}{2\tau} & \frac{\tau}{2} \end{pmatrix}$	$C_{10}C_{10}$
288	1	10	$\begin{pmatrix} \frac{1}{2} & \frac{\tau}{2} & \frac{1}{2\tau} & 0 \\ -\frac{1}{2\tau} & \frac{1}{2} & -\frac{\tau}{2} & 0 \\ 0 & 0 & 0 & 1 \\ \frac{\tau}{2} & -\frac{1}{2\tau} & -\frac{1}{2} & 0 \end{pmatrix}$	$C_{10}C_{10}$
1200	0	12	$\begin{pmatrix} \frac{1}{2} & \frac{\tau}{2} & \frac{1}{2\tau} & 0 \\ \frac{1}{2\tau} & -\frac{1}{2} & \frac{\tau}{2} & 0 \\ 0 & 0 & 0 & 1 \\ -\frac{\tau}{2} & \frac{1}{2\tau} & \frac{1}{2} & 0 \end{pmatrix}$	$C_{12}C_{12}$
480	$1-\tau$	15	$\begin{pmatrix} -\frac{1}{2\tau} & \frac{\tau}{2} & 0 & \frac{1}{2} \\ \frac{1}{2} & -\frac{1}{2\tau} & 0 & \frac{\tau}{2} \\ \frac{\tau}{2} & \frac{1}{2} & 0 & -\frac{1}{2\tau} \\ 0 & 0 & -1 & 0 \end{pmatrix}$	$C_{15}C_{15}$
480	τ	15	$\begin{pmatrix} \frac{\tau}{2} & \frac{1}{2\tau} & \frac{1}{2} & 0 \\ 0 & 0 & 0 & 1 \\ -\frac{1}{2\tau} & -\frac{1}{2} & \frac{\tau}{2} & 0 \\ \frac{1}{2} & -\frac{\tau}{2} & -\frac{1}{2\tau} & 0 \end{pmatrix}$	$C_{15}C_{15}$
720	0	20	$\begin{pmatrix} \frac{\tau}{2} & \frac{1}{2\tau} & \frac{1}{2} & 0 \\ \frac{1}{2} & -\frac{\tau}{2} & -\frac{1}{2\tau} & 0 \\ 0 & 0 & 0 & 1 \\ -\frac{1}{2\tau} & -\frac{1}{2} & \frac{\tau}{2} & 0 \end{pmatrix}$	$C_{20}C_{20}$
720	0	20	$\begin{pmatrix} \frac{1}{2\tau} & \frac{\tau}{2} & 0 & \frac{1}{2} \\ -\frac{1}{2} & -\frac{1}{2\tau} & 0 & \frac{\tau}{2} \\ \frac{\tau}{2} & -\frac{1}{2} & 0 & \frac{1}{2\tau} \\ 0 & 0 & -1 & 0 \end{pmatrix}$	$C_{20}C_{20}$
480	$-\tau$	30	$\begin{pmatrix} -\frac{\tau}{2} & \frac{1}{2\tau} & \frac{1}{2} & 0 \\ 0 & 0 & 0 & 1 \\ -\frac{1}{2\tau} & \frac{1}{2} & -\frac{\tau}{2} & 0 \\ -\frac{1}{2} & -\frac{\tau}{2} & -\frac{1}{2\tau} & 0 \end{pmatrix}$	$C_{30}C_{30}$
480	$\tau-1$	30	$\begin{pmatrix} \frac{1}{2\tau} & \frac{\tau}{2} & 0 & \frac{1}{2} \\ \frac{1}{2} & \frac{1}{2\tau} & 0 & -\frac{\tau}{2} \\ \frac{\tau}{2} & -\frac{1}{2} & 0 & \frac{1}{2\tau} \\ 0 & 0 & 1 & 0 \end{pmatrix}$	$C_{30}C_{30}$

C.4 Representations

The representations and their characters for each conjugacy class may be computed once we have partitioned the group into classes. To illustrate the strategy, let's consider a much smaller group C_{3v}. The character table of C_{3v} is shown in Table C.4.

Recall the general property of character tables that the number of representations equals the number of classes. In the case of C_{3v}, there are three classes: the identity, three-fold rotations, and reflections. Therefore, there are three irreducible characters of the group C_{3v}: $\mathbf{A_1}$, $\mathbf{A_2}$, and $\mathbf{E}$. We will call the number of classes and irreducible representations r. In the case of C_{3v}, $r = 3$.

Some more notation: let us denote the classes Y_i (for conjugacy classes, and to avoid confusion with C_n rotations) and the irreducible characters χ^i. So we have $Y_1 = \varepsilon$, $Y_2 = 2C_3$, and $Y_3 = 3\sigma_v$ and $\chi^1 = \mathbf{A_1}$, $\chi^2 = \mathbf{A_2}$, and $\chi^3 = \mathbf{E}$. Furthermore, for the character of an operation from the class Y_j under the representation χ^i we use the symbol χ^i_j. For example, the character of a C_3 operation under the $\mathbf{E}$ representation is $\chi^3_2 = -1$. The character of a σ_v operation under the $\mathbf{A_1}$ representation is $\chi^1_3 = 1$.

Let h_i be the number of elements in the class Y_i: in Table C.4, the identity element class has one element so $h_1 = |Y_1| = 1$. Correspondingly, $h_2 = |Y_2| = 2$,

Table C.4: Character table for the symmetry group C_{3v}

	Y_1	Y_2	Y_3
	ε	$2C_3$	$3\sigma_v$
$\mathbf{A_1}$	1	1	1
$\mathbf{A_2}$	1	1	-1
$\mathbf{E}$	2	-1	0

the number of C_3 operations and $h_3 = |Y_3| = 3$, the number of σ_v operations.

Finally, recall that the first column of a character table—the characters of the identity under the various representations—give the dimensionality of those representations. These special characters we will denote d_i. In accordance with our above notation for characters under the ith representation, $d_i = \chi^i_1$.

We use the algorithm given in Holt,[159] p. 256. We will first describe the algorithm in general terms, then apply it to C_{3v}. We define a new quantity c_{jkl} as follows: pick an element g in the class Y_l. Then for all elements a in Y_j and b in Y_k, let the number of times $ab = g$ be c_{jkl}. If the c_{jkl} can be computed, we can use the following useful relation:[159]

$$\frac{h_j\chi^i_j}{d_i}\frac{h_k\chi^i_k}{d_i} = \sum_l^r c_{jkl}\frac{h_l\chi^i_l}{d_i}, \tag{C.17}$$

where the indices j,k, and l are from 1 to r. Let us construct r matrices M_j where the (k,l) entry is c_{jkl}. We can rewrite Equation C.17 then as:

$$\frac{h_j\chi^i_j}{d_i}\begin{pmatrix} \frac{h_1\chi^i_1}{d_i} \\ \frac{h_2\chi^i_2}{d_i} \\ \vdots \end{pmatrix} = \begin{pmatrix} c_{j11} & c_{j12} & \cdots \\ c_{j21} & c_{j22} & \cdots \\ \vdots & \vdots & \ddots \end{pmatrix}\begin{pmatrix} \frac{h_1\chi^i_1}{d_i} \\ \frac{h_2\chi^i_2}{d_i} \\ \vdots \end{pmatrix} \tag{C.18}$$

According to Equation C.18, for each i representation each of the matrices M_j has as an eigenvector $\left(\frac{h_1\chi^i_1}{d_i}\ \frac{h_2\chi^i_2}{d_i}\ \ldots\ \frac{h_r\chi^i_r}{d_i}\right)$. The problem is then reduced to finding the common eigenvectors of r matrices of size $r\times r$, from which the d_i are quickly computed.

Let us see how this works in practice, once again using the C_{3v} symmetry group. It is helpful to have the multiplication table computed (Table C.5) so that the c_{jkl} can be quickly computed. This becomes especially important as the group becomes large, since we want to avoid doing the same costly matrix operations over and over.

Table C.5: Multiplication table for C_{3v}

	ε	C_2	C_2^2	σ	σ'	σ''
ε	ε	C_2	C_2^2	σ	σ'	σ''
C_2	C_2	C_2^2	ε	σ''	σ	σ
C_2^2	C_2^2	ε	C_2	σ'	σ''	σ
σ	σ	σ'	σ''	ε	C_2	C_2^2
σ'	σ'	σ''	σ	C_2^2	ε	C_2
σ''	σ''	σ	σ'	C_2	C_2^2	ε

For example, c_{323}–the number of times the product of a σ reflection times a C_2 rotation becomes another σ reflection; say σ''. This can be read directly from Table C.5: the three rows corresponding to σ, σ', and σ'' meet the two columns corresponding to C_2 and C_2^2 to form six products, and σ'' appears twice. Note that we could have used σ or σ' as both also appear twice–hence our choice of representative does not matter, and $c_{323} = 2$.

Computing all the c_{3kl} in this fashion gives us M_3:

$$c_{3kl} \rightarrow M_3 = \begin{pmatrix} 0 & 0 & 1 \\ 0 & 0 & 2 \\ 3 & 3 & 0 \end{pmatrix}. \tag{C.19}$$

Similarly,

$$M_1 = \begin{pmatrix} 1 & 0 & 0 \\ 0 & 1 & 0 \\ 0 & 0 & 1 \end{pmatrix} \text{ and } M_2 = \begin{pmatrix} 0 & 1 & 0 \\ 2 & 1 & 0 \\ 0 & 0 & 2 \end{pmatrix}. \tag{C.20}$$

Since ε can only end up in its own class when multiplied by itself, it is no surprise that M_1 is the identity matrix. M_3 has the following eigenvectors:

$$\begin{aligned} \vec{v}_1 &= (1\ 2\ \bar{3}) \\ \vec{v}_2 &= (1\ 2\ 3) \\ \vec{v}_3 &= (1\ \bar{1}\ 0), \end{aligned}$$

with corresponding eigenvalues -3, 3, 0, respectively. Therefore, from Equation C.17, we have the following equalities:

$$\begin{pmatrix} \frac{h_1\chi_1^1}{d_1} & \frac{h_2\chi_2^1}{d_1} & \frac{h_3\chi_3^1}{d_1} \\ \frac{h_1\chi_1^2}{d_2} & \frac{h_2\chi_2^2}{d_2} & \frac{h_3\chi_3^2}{d_2} \\ \frac{h_1\chi_1^3}{d_3} & \frac{h_2\chi_2^3}{d_3} & \frac{h_3\chi_3^3}{d_3} \end{pmatrix} = \begin{pmatrix} 1 & 2 & -3 \\ 1 & 2 & 3 \\ 1 & -1 & 0 \end{pmatrix}. \tag{C.21}$$

And inserting the values for h_i: $h_1 = 1$, $h_2 = 2$, $h_3 = 3$ and solving for χ_j^i we have:

$$X = \begin{pmatrix} \chi_1^1 & \chi_2^1 & \chi_3^1 \\ \chi_1^2 & \chi_2^2 & \chi_3^2 \\ \chi_1^3 & \chi_2^3 & \chi_3^3 \end{pmatrix} = \begin{pmatrix} d_1 & 0 & 0 \\ 0 & d_2 & 0 \\ 0 & 0 & d_3 \end{pmatrix} \begin{pmatrix} 1 & 1 & -1 \\ 1 & 1 & 1 \\ 1 & -\frac{1}{2} & 0 \end{pmatrix}. \tag{C.22}$$

Thus solving the character table X up to the dimensions, d_i. For a group as small as C_{3v}, one could simply invoke the facts that the squares of the dimensionalities add up to the order of the group ($\sum_i^r d_i^2 = |G|$) and the rows of the character table are orthogonal. It is immediately apparent, then, that $d_1 = d_2 = 1$ and $d_3 = 2$. This reproduces the character table in Table C.4, although traditionally we would place the identical representation in the first row.

However, we should not rely on there being a unique sum of squares to determine d_i. To solve the problem generally, we turn to a special case of the Character Orthogonality Theorem, which states:

$$\sum_{g \in G} \chi^i(g) \chi^i(g)^* = |G|\,, \tag{C.23}$$

meaning that under a given irreducible representation χ^i the sum of the character of each group element g times its complex conjugate equals the order of the group, $|G|$. Since we have already partitioned the group into classes, and we know that every element of a class has the same character under a given representation, we can recast Equation C.23 in a more enlightening form:

$$\sum_j^r h_j \chi_j^i \chi_j^{i*} = |G|\,. \tag{C.24}$$

In this form, we may compute d_i directly. For example, consider χ^1_j in Equation C.22. We have

$$\begin{aligned}\chi^1_1 &= d_1 \\ \chi^1_2 &= d_1 \\ \chi^1_3 &= -d_1,\end{aligned}$$

so substituting into to Equation C.24 gives

$$d_1^2 + 2d_1^2 + 3d_1^2 = 6,$$

which means $d_1 = 1$, as expected.

A caveat: we were able to solve the character table of C_{3v} with just the eigenvectors of M_3 only because M_3 has no degenerate eigenvalues and hence no linearly dependent eigenvectors. If no single M_j supplies the required r independent eigenvectors, then we must somehow extract more eigenvalues from the remaining M.

Suppose when solving the character table of C_{3v} we had started with M_2 in Equation C.20 rather than M_3. M_2 has eigenvectors

$$\begin{aligned}\vec{v}_1 &= (0\,0\,1) \\ \vec{v}_2 &= (1\,2\,0) \\ \vec{v}_3 &= (1\,\bar{1}\,0),\end{aligned}$$

corresponding to eigenvalues 2, 2, and -1. In this case, we must find another M_j for which $\vec{v}_1$ and $\vec{v}_2$ do not share an eigenvalue, for instance in M_3. Note that the one eigenvector from M_2 that we can use–$(1\,\bar{1}\,0)$–is shared with M_3.

C.5 The Character Table

The character table for the symmetry group of the 600-cell is split over Tables C.6 – C.9. We use a slightly modified version of the traditional Mulliken scheme of naming irreducible representations, since **A**, **B**, **E**, **T**, **G**, **H**, etc. for irreducible representations of dimension 1, 1, 2, 3, 4, 5 respectively is impractical when irreducible representations of up to dimension 48 are present. A simplified notation is desired: rather than use a capital letter, we simply use the dimension as the symbol. We keep the subscripts *g* (*gerade*) and *u* (*ungerade*) to specify whether a representation is symmetric or antisymmetric with respect to inversion, respectively. $\mathbf{A_g}$ becomes 1_g, $\mathbf{H_u}$ becomes 5_u and so on.

As mentioned above (Section C.3), the improper rotations appear to correspond to familiar three-dimensional rotations. In addition to their appearance in the full character table, we include the irreducible representations of the improper rotations separately in Table C.10. For comparison, the character tables[160] for I_h, T_d, D_{3h}, and D_{5h} are provided in Tables C.11-C.14. This connection is merely suggestive: a rigorous investigation between the characters of representations of symmetry operations in the 4D and 3D group is not performed here.

Table C.6: Character table for the symmetry group of the 600-cell, columns 1-12. The top row indicates the order of elements in the corresponding class.

	1	2	2	2	2	3	3	4	4	5	5	5
	ε	ε^*	$60\sigma\varepsilon^*$	60σ	$450\varepsilon\varepsilon^*$	$400C_3$	$40C_3C_3$	$1800C_4\sigma$	$60C_4C_4$	$144C_5$	$144C_5$	$24C_5C_5$
1_g	1	1	1	1	1	1	1	1	1	1	1	1
1_g	1	1	-1	-1	1	1	1	-1	1	1	1	1
4_u	4	-4	-2	2	0	1	-2	0	0	$2-\tau$	$\tau+1$	$\frac{2}{\tau}$
4_u	4	-4	-2	2	0	1	-2	0	0	$\tau+1$	$2-\tau$	-2τ
4_u	4	-4	2	-2	0	1	-2	0	0	$2-\tau$	$\tau+1$	$\frac{2}{\tau}$
4_u	4	-4	2	-2	0	1	-2	0	0	$\tau+1$	$2-\tau$	-2τ
6_g	6	6	0	0	-2	0	3	0	2	2τ	$2-2\tau$	$\tau+3$
6_g	6	6	0	0	-2	0	3	0	2	$2-2\tau$	2τ	$4-\tau$
8_u	8	-8	0	0	0	2	-4	0	0	-2	-2	-2
8_g	8	8	0	0	0	2	5	0	4	-2	-2	3
9_g	9	9	-3	-3	1	0	0	1	-3	$\tau+1$	$2-\tau$	3τ
9_g	9	9	-3	-3	1	0	0	1	-3	$2-\tau$	$\tau+1$	$-\frac{3}{\tau}$
9_g	9	9	3	3	1	0	0	-1	-3	$\tau+1$	$2-\tau$	3τ
9_g	9	9	3	3	1	0	0	-1	-3	$2-\tau$	$\tau+1$	$-\frac{3}{\tau}$
10_g	10	10	0	0	2	-2	4	0	6	0	0	5
16_u	16	-16	-4	4	0	1	4	0	0	1	1	-4
16_u	16	-16	0	0	0	-2	-2	0	0	2τ	$2-2\tau$	$-4\tau-2$
16_u	16	-16	0	0	0	-2	-2	0	0	$2-2\tau$	2τ	$4\tau-6$
16_u	16	-16	4	-4	0	1	4	0	0	1	1	-4
16_g	16	16	-4	-4	0	1	4	0	0	1	1	-4
16_g	16	16	4	4	0	1	4	0	0	1	1	-4
18_g	18	18	0	0	2	0	0	0	-6	-2	-2	3
24_u	24	-24	0	0	0	0	-6	0	0	-2τ	$\frac{2}{\tau}$	$2-6\tau$
24_u	24	-24	0	0	0	0	-6	0	0	$\frac{2}{\tau}$	-2τ	$6\tau-4$
24_g	24	24	0	0	0	0	3	0	-4	-2τ	$\frac{2}{\tau}$	$4\tau-3$
24_g	24	24	0	0	0	0	3	0	-4	$\frac{2}{\tau}$	-2τ	$1-4\tau$
25_g	25	25	-5	-5	1	1	-5	-1	5	0	0	0
25_g	25	25	5	5	1	1	-5	1	5	0	0	0
30_g	30	30	0	0	-2	0	-3	0	-2	0	0	5τ
30_g	30	30	0	0	-2	0	-3	0	-2	0	0	$-\frac{5}{\tau}$
36_u	36	-36	-6	6	0	0	0	0	0	1	1	6
36_u	36	-36	6	-6	0	0	0	0	0	1	1	6
40_g	40	40	0	0	0	-2	1	0	4	0	0	-5
48_u	48	-48	0	0	0	0	6	0	0	-2	-2	-2

Table C.7: Character table for the symmetry group of the 600-cell, columns 13-20

	5 $24C_5C_5$	5 $288C_5C_5$	6 $1200C_6\sigma$	6 $1200C_6\sigma$	6 $400C_6\varepsilon^*$	6 $40C_6C_6$	10 $144C_{10}\varepsilon^*$	10 $144C_{10}\varepsilon^*$
1_g	1	1	1	1	1	1	1	1
1_g	1	1	-1	-1	1	1	1	1
4_u	-2τ	-1	-1	1	-1	2	$-\tau-1$	$\tau-2$
4_u	$\frac{2}{\tau}$	-1	-1	1	-1	2	$\tau-2$	$-\tau-1$
4_u	-2τ	-1	1	-1	-1	2	$-\tau-1$	$\tau-2$
4_u	$\frac{2}{\tau}$	-1	1	-1	-1	2	$\tau-2$	$-\tau-1$
6_g	$4-\tau$	1	0	0	0	3	$2-2\tau$	$2\,\tau$
6_g	$\tau+3$	1	0	0	0	3	2τ	$2-2\tau$
8_u	-2	3	0	0	-2	4	2	2
8_g	3	-2	0	0	2	5	-2	-2
9_g	$-\frac{3}{\tau}$	-1	0	0	0	0	$2-\tau$	$\tau+1$
9_g	3τ	-1	0	0	0	0	$\tau+1$	$2-\tau$
9_g	$-\frac{3}{\tau}$	-1	0	0	0	0	$2-\tau$	$\tau+1$
9_g	τ	-1	0	0	0	0	$\tau+1$	$2-\tau$
10_g	5	0	0	0	-2	4	0	0
16_u	-4	1	1	-1	-1	-4	-1	-1
16_u	$4\tau-6$	1	0	0	2	2	$\frac{2}{\tau}$	-2τ
16_u	$-4\tau-2$	1	0	0	2	2	-2τ	$\frac{2}{\tau}$
16_u	-4	1	-1	1	-1	-4	-1	-1
16_g	-4	1	-1	-1	1	4	1	1
16_g	-4	1	1	1	1	4	1	1
18_g	3	3	0	0	0	0	-2	-2
24_u	$6\tau-4$	-1	0	0	0	6	$2-2\tau$	2τ
24_u	$2-6\tau$	-1	0	0	0	6	2τ	$2-2\tau$
24_g	$1-4\tau$	-1	0	0	0	3	$\frac{2}{\tau}$	-2τ
24_g	$4\tau-3$	-1	0	0	0	3	-2τ	$\frac{2}{\tau}$
25_g	0	0	1	1	1	-5	0	0
25_g	0	0	-1	-1	1	-5	0	0
30_g	$-\frac{5}{\tau}$	0	0	0	0	-3	0	0
30_g	5τ	0	0	0	0	-3	0	0
36_u	6	1	0	0	0	0	-1	-1
36_u	6	1	0	0	0	0	-1	-1
40_g	-5	0	0	0	-2	1	0	0
48_u	-2	-2	0	0	0	-6	2	2

Table C.8: Character table for the symmetry group of the 600-cell, columns 21-28

	10 $24C_{10}C_{10}$	10 $24C_{10}C_{10}$	10 $288C_{10}C_{10}$	10 $720C_{10}\sigma$	10 $720C_{10}\sigma$	10 $720C_5\sigma$	10 $720C_5\sigma$	12 $1200C_{12}C_{12}$
1_g	1	1	1	1	1	1	1	1
1_g	1	1	1	-1	-1	-1	-1	1
4_u	$2-2\tau$	2τ	1	$1-\tau$	τ	$\frac{1}{\tau}$	$-\tau$	0
4_u	2τ	$2-2\tau$	1	τ	$1-\tau$	$-\tau$	$\frac{1}{\tau}$	0
4_u	$2-2\tau$	2τ	1	$\frac{1}{\tau}$	$-\tau$	$1-\tau$	τ	0
4_u	2τ	$2-2\tau$	1	$-\tau$	$\frac{1}{\tau}$	τ	$1-\tau$	0
6_g	$\tau+3$	$4-\tau$	1	0	0	0	0	-1
6_g	$4-\tau$	$\tau+3$	1	0	0	0	0	-1
8_u	2	2	-3	0	0	0	0	0
8_g	3	3	-2	0	0	0	0	1
9_g	3τ	$-\frac{3}{\tau}$	-1	$-\tau$	$\frac{1}{\tau}$	$-\tau$	$\frac{1}{\tau}$	0
9_g	$-\frac{3}{\tau}$	3τ	-1	$\frac{1}{\tau}$	$-\tau$	$\frac{1}{\tau}$	$-\tau$	0
9_g	3τ	$-\frac{3}{\tau}$	-1	τ	$1-\tau$	τ	$1-\tau$	0
9_g	$-\frac{3}{\tau}$	3τ	-1	$1-\tau$	τ	$1-\tau$	τ	0
10_g	5	5	0	0	0	0	0	0
16_u	4	4	-1	1	1	-1	-1	0
16_u	$4\tau+2$	$6-4\tau$	-1	0	0	0	0	0
16_u	$6-4\tau$	$4\tau+2$	-1	0	0	0	0	0
16_u	4	4	-1	-1	-1	1	1	0
16_g	-4	-4	1	1	1	1	1	0
16_g	-4	-4	1	-1	-1	-1	-1	0
18_g	3	3	3	0	0	0	0	0
24_u	$6\tau-2$	$4-6\tau$	1	0	0	0	0	0
24_u	$4-6\tau$	$6\tau-2$	1	0	0	0	0	0
24_g	$4\tau-3$	$1-4\tau$	-1	0	0	0	0	-1
24_g	$1-4\tau$	$4\tau-3$	-1	0	0	0	0	-1
25_g	0	0	0	0	0	0	0	-1
25_g	0	0	0	0	0	0	0	-1
30_g	5τ	$-\frac{5}{\tau}$	0	0	0	0	0	1
30_g	$-\frac{5}{\tau}$	5τ	0	0	0	0	0	1
36_u	-6	-6	-1	-1	-1	1	1	0
36_u	-6	-6	-1	1	1	-1	-1	0
40_g	-5	-5	0	0	0	0	0	1
48_u	2	2	2	0	0	0	0	0

Table C.9: Character table for the symmetry group of the 600-cell, columns 29-34

	15	15	20	20	30	30
	$480C_{15}C_{15}$	$480C_{15}C_{15}$	$720C_{20}C_{20}$	$720C_{20}C_{20}$	$480C_{30}C_{30}$	$480C_{30}C_{30}$
1_g	1	1	1	1	1	1
1_g	1	1	1	1	1	1
4_u	$1-\tau$	τ	0	0	$\frac{1}{\tau}$	$-\tau$
4_u	τ	$1-\tau$	0	0	$-\tau$	$\frac{1}{\tau}$
4_u	$1-\tau$	τ	0	0	$\frac{1}{\tau}$	$-\tau$
4_u	τ	$1-\tau$	0	0	$-\tau$	$\frac{1}{\tau}$
6_g	τ	$1-\tau$	$\frac{1}{\tau}$	$-\tau$	τ	$1-\tau$
6_g	$1-\tau$	τ	$-\tau$	$\frac{1}{\tau}$	$1-\tau$	τ
8_u	1	1	0	0	-1	-1
8_g	0	0	-1	-1	0	0
9_g	0	0	$-\tau$	$\frac{1}{\tau}$	0	0
9_g	0	0	$\frac{1}{\tau}$	$-\tau$	0	0
9_g	0	0	$-\tau$	$\frac{1}{\tau}$	0	0
9_g	0	0	$\frac{1}{\tau}$	$-\tau$	0	0
10_g	-1	-1	1	1	-1	-1
16_u	-1	-1	0	0	1	1
16_u	$1-\tau$	τ	0	0	$\frac{1}{\tau}$	$-\tau$
16_u	τ	$1-\tau$	0	0	$-\tau$	$\frac{1}{\tau}$
16_u	-1	-1	0	0	1	1
16_g	-1	-1	0	0	-1	-1
16_g	-1	-1	0	0	-1	-1
18_g	0	0	-1	-1	0	0
24_u	-1	-1	0	0	1	1
24_u	-1	-1	0	0	1	1
24_g	τ	$1-\tau$	1	1	τ	$1-\tau$
24_g	$1-\tau$	τ	1	1	$1-\tau$	τ
25_g	0	0	0	0	0	0
25_g	0	0	0	0	0	0
30_g	$-\tau$	$\frac{1}{\tau}$	τ	$1-\tau$	$-\tau$	$\frac{1}{\tau}$
30_g	$\frac{1}{\tau}$	$-\tau$	$1-\tau$	τ	$\frac{1}{\tau}$	$-\tau$
36_u	0	0	0	0	0	0
36_u	0	0	0	0	0	0
40_g	1	1	-1	-1	1	1
48_u	1	1	0	0	-1	-1

Table C.10: Partial character table for the symmetry group of the 600-cell for classes of improper rotations. Irreducible representations which are character 0 for every class are omitted.

	2	2	4	6	6	10	10	10	10
	$60\sigma\varepsilon^*$	60σ	$1800C_4\sigma$	$1200C_6\sigma$	$1200C_6\sigma$	$720C_{10}\sigma$	$720C_{10}\sigma$	$720C_5\sigma$	$720C_5\sigma$
1_g	1	1	1	1	1	1	1	1	1
1_g	−1	−1	−1	−1	−1	−1	−1	−1	−1
4_u	−2	2	0	−1	1	$1-\tau$	τ	$\frac{1}{\tau}$	$-\tau$
4_u	−2	2	0	−1	1	τ	$1-\tau$	$-\tau$	$\frac{1}{\tau}$
4_u	2	−2	0	1	−1	$\frac{1}{\tau}$	$-\tau$	$1-\tau$	τ
4_u	2	−2	0	1	−1	$-\tau$	$\frac{1}{\tau}$	τ	$1-\tau$
9_g	−3	−3	1	0	0	$-\tau$	$\frac{1}{\tau}$	$-\tau$	$\frac{1}{\tau}$
9_g	−3	−3	1	0	0	$\frac{1}{\tau}$	$-\tau$	$\frac{1}{\tau}$	$-\tau$
9_g	3	3	−1	0	0	τ	$1-\tau$	τ	$1-\tau$
9_g	3	3	−1	0	0	$1-\tau$	τ	$1-\tau$	τ
16_u	−4	4	0	1	−1	1	1	−1	−1
16_u	4	−4	0	−1	1	−1	−1	1	1
16_g	−4	−4	0	−1	−1	1	1	1	1
16_g	4	4	0	1	1	−1	−1	−1	−1
25_g	−5	−5	−1	1	1	0	0	0	0
25_g	5	5	1	−1	−1	0	0	0	0
36_u	−6	6	0	0	0	−1	−1	1	1
36_u	6	−6	0	0	0	1	1	−1	−1

I_h	ε	ε^*	15σ	$15C_2$	$20C_3$	$12C_5$	$12{C_5}^2$	$20S_6$	$12S_{10}$	$12{S_{10}}^3$
$\mathbf{A_g}$	1	−1	−1	1	1	1	1	−1	−1	−1
$\mathbf{A_g}$	1	1	1	1	1	1	1	1	1	1
$\mathbf{T_{1g}}$	3	3	−1	−1	0	$-\tau$	$1-\tau$	0	$1-\tau$	$-\tau$
$\mathbf{T_{2g}}$	3	3	−1	−1	0	$1-\tau$	$-\tau$	0	$-\tau$	$1-\tau$
$\mathbf{T_{1u}}$	3	−3	1	−1	0	$-\tau$	$1-\tau$	0	$\frac{1}{\tau}$	τ
$\mathbf{T_{2u}}$	3	−3	1	−1	0	$1-\tau$	$-\tau$	0	τ	$\frac{1}{\tau}$
$\mathbf{G_g}$	4	4	0	0	1	−1	−1	1	−1	−1
$\mathbf{G_u}$	4	−4	0	0	1	−1	−1	−1	1	1
$\mathbf{H_g}$	5	5	1	1	−1	0	0	−1	0	0
$\mathbf{H_u}$	5	−5	−1	1	−1	0	0	1	0	0

Table C.11: Character Table for the I_h group.

T_d	ε	$3C_2$	$6\sigma_d$	$8C_3$	$6S_4$
$\mathbf{A_1}$	1	1	1	1	1
$\mathbf{A_2}$	1	1	−1	1	−1
$\mathbf{E}$	2	2	0	−1	0
$\mathbf{T_1}$	3	−1	−1	0	1
$\mathbf{T_2}$	3	−1	1	0	−1

Table C.12: Character Table for the T_d group.

D_{3h}	ε	σ_h	$3\sigma_v$	$3C_2$	$2C_3$	$2S_3$
$\mathbf{A_1'}$	1	1	1	1	1	1
$\mathbf{A_2'}$	1	1	−1	−1	1	1
$\mathbf{A_1''}$	1	−1	−1	1	1	−1
$\mathbf{A_2''}$	1	−1	1	−1	1	−1
$\mathbf{E'}$	2	2	0	0	−1	−1
$\mathbf{E''}$	2	−2	0	0	−1	1

Table C.13: Character Table for the D_{3h} group.

D_{5h}	ε	σ_h	$5\sigma_v$	$5C_2'$	$2C_5$	$2S_5$	${2C_5}^2$	${2S_5}^3$
$\mathbf{A_1'}$	1	1	−1	−1	1	1	1	1
$\mathbf{A_1'}$	1	1	1	1	1	1	1	1
$\mathbf{A_1''}$	1	−1	1	−1	1	−1	1	−1
$\mathbf{A_1''}$	1	−1	−1	1	1	−1	1	−1
$\mathbf{E'}_1$	2	2	0	0	$-\frac{1}{\tau}$	$-\frac{1}{\tau}$	$-\tau$	$-\tau$
$\mathbf{E'}_2$	2	2	0	0	$-\tau$	$-\tau$	$-\frac{1}{\tau}$	$-\frac{1}{\tau}$
$\mathbf{E''}_1$	2	−2	0	0	$-\frac{1}{\tau}$	$\frac{1}{\tau}$	$-\tau$	τ
$\mathbf{E''}_2$	2	−2	0	0	$-\tau$	τ	$-\frac{1}{\tau}$	$\frac{1}{\tau}$

Table C.14: Character Table for the D_{5h} group.

C.6 Example Projection: the D_{3h} cluster

Central to Chapter 2 is the notion of projections of the 4D 600-cell vertices into 3D clusters. In this section, we will present the algorithm for the projection that creates the D_{3h} cluster. We know from our previous construction of the D_{3h} cluster that the projection should preserve a 3-fold rotation axis and one horizontal mirror plane, and contain 3 coplanar pseudo five-fold axes intersecting at 60° (the angle between the equivalent [100], [010] and [110] directions in hexagonal space groups). Therefore, we arbitrarily choose a triangular face from the 600-cell to form the basis of our projection. If we force the triangle to remain regular after the projection, the three-fold symmetry of the D_{3h} cluster is ensured. This triangle will become the three ITr sites, in the language of Chapter 2.

Enforcing the mirror plane is more subtle. In the 600-cell, every triangular face is shared between two tetrahedra, implying the existence of another pair of vertices equal distances above and below the plane of the triangle (which will become the IL sites after projection). Taken together, these five vertices (3 ITr + 2 IL) sit in the familiar trigonal bipyramidal ligand arrangement. To continue the analogy, the bond lengths of the axial atoms to a hypothetical central atom need to be equal to preserve the mirror plane. This geometrical arrangement is shown in Figure C.3.

Mathematically, we want to construct a projection matrix that sends the 4D equatorial sites of Figure C.3 (the equilateral triangle of gold spheres) to an equilateral triangle in 3D. Furthermore, we want to guarantee the vector connecting the two axial sites, (1 0 0 0) – $(\frac{1}{2}\ \frac{1}{2}\ \frac{1}{2}\ \frac{1}{2})$ = $(\frac{1}{2}\ \frac{\bar{1}}{2}\ \frac{\bar{1}}{2}\ \frac{\bar{1}}{2})$, remains perpendicular to the

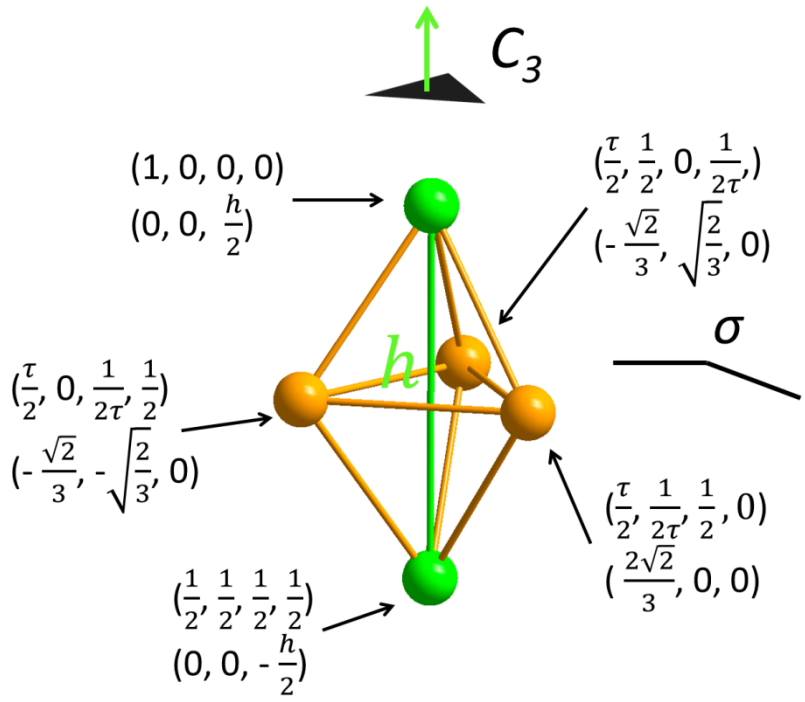

Figure C.3: Geometry of the trigonal bipyramid in 4D and 3D. τ is the Golden Ratio: $\tau = (1 + \sqrt{5})/2$. The three gold spheres represent the vertices of the preserved equilateral triangle (ITr), which is regular in 4D and in 3D and lie in the σ mirror plane of the D_{3h} cluster. These three points all lie in the mirror plane. The two green spheres are the axial vertices (IL), and specify the C_3 axis of the D_{3h} cluster. In the 600-cell, these points are positioned such that the two tetrahedra are regular. In 3D this need not be the case: mirror plane symmetry is preserved for any h, thus we are free to choose h in specifying our projection.

plane of the triangle after projection. Thus, we have the matrix equation:

$$\mathbf{M}\begin{pmatrix} \frac{1}{2} & \frac{\tau}{2} & \frac{\tau}{2} & \frac{\tau}{2} \\ -\frac{1}{2} & 0 & \frac{1}{2} & \frac{1}{2\tau} \\ -\frac{1}{2} & \frac{1}{2\tau} & 0 & \frac{1}{2} \\ -\frac{1}{2} & \frac{1}{2} & \frac{1}{2\tau} & 0 \end{pmatrix} = \begin{pmatrix} 0 & -\frac{\sqrt{2}}{3} & -\frac{\sqrt{2}}{3} & \frac{2\sqrt{2}}{3} \\ 0 & -\sqrt{\frac{2}{3}} & \sqrt{\frac{2}{3}} & 0 \\ h & 0 & 0 & 0 \end{pmatrix}$$

Where the 4D columns on the left map to the corresponding 3D columns on the

right. Solving for **M** gives the projection matrix:

$$\mathbf{M} = \begin{pmatrix} 0 & \frac{\sqrt{3-\sqrt{5}}}{3} & \frac{1}{3}\sqrt{5\left(3+\sqrt{5}\right)} & -\frac{1}{3}\sqrt{2}\left(2+\sqrt{5}\right) \\ 0 & \sqrt{\frac{7}{3}+\sqrt{5}} & \frac{-1-\sqrt{5}}{\sqrt{6}} & -\sqrt{\frac{2}{3}} \\ \frac{h}{2} & -\frac{h}{2} & -\frac{h}{2} & -\frac{h}{2} \end{pmatrix}$$

When projecting from 4D to 3D, the extra dimension is necessarily squeezed out. In the context of the D_{3h} cluster, this means geometrical motifs nearest to the center of the cluster will be more regular: the three equatorial sites in Figure C.3 form an equilateral triangle, and the variable h can be chosen so that the two axial sites form two perfect tetrahedra on either side of the mirror plane. As we project more sites, however, the newly formed tetrahedra of the D_{3h} cluster will become more and more distorted. This is no surprise, since the perfect tetrahedral packing in the 600-cell is not possible in 3D.

A quantitative measure of this trend is straightforward. If the sites nearest to the center of the D_{3h} cluster constitute "more perfect" tetrahedra, then logically the very center of the cluster must be the "most perfect" in terms of geometric regularity. Since the D_{3h} cluster is centered on the origin, we would like to know which 4D vectors project to (0 0 0). This family of 4D vectors is known as the kernel or null space of the projection matrix **M**, and turns out to be the vector (3 1 1 1) which we will call **k**. All vectors collinear to **k** also lie in the kernel.

The vector **k** has the following meaning: 4D vectors more parallel to **k** - that is, 4D vectors v for which $|\mathbf{k} \cdot \mathbf{v}|$ is large - project to points in the D_{3h} cluster near the origin which form regular or nearly regular tetrahedra. Vectors for which $|\mathbf{k} \cdot \mathbf{v}|$ is small lie farther out in the cluster, and form more distorted tetrahedra. Vectors for which $|\mathbf{k} \cdot \mathbf{v}| = 0$ lie farthest from the center and make up completely flattened tetrahedra.

The quantity $|\mathbf{k} \cdot \mathbf{v}|$ can be either positive or negative. In fact, two D_{3h} clusters may be formed from the all 120 $\mathbf{v}$ which correspond to the points in the 600-cell: one from all the points for which $|\mathbf{k} \cdot \mathbf{v}| > 0$ and one for which $|\mathbf{k} \cdot \mathbf{v}| < 0$. The points for which $|\mathbf{k} \cdot \mathbf{v}| = 0$ are shared between the two, and are said to lie on the equator of the projection. None of the projections in Chapter 2 include the equatorial points.

Finding projections for the other clusters follows a similar algorithm. The T_d cluster is particularly straight-forward: pick a tetrahedron in the 600-cell that corresponds with the IT sites of the projected structure, then solve for the projection matrix $\mathbf{M}$ as above. The D_{5h} cluster was constructed by noting that five tetrahedra meet at every edge in the 600-cell: one simply picks a vector corresponding to this edge plus three points on the pentagonal wheel formed by the tetrahedral packing and projects these to the IL and three corresponding IP sites. For the I_h cluster, recall that twenty tetrahedra meet at a vertex in the 600-cell: simply pick any four vertices (except the point where they meet) and project them directly to congruent sites on II–congruent meaning that, for example, if the vertices are neighbors in the 600-cell, the should remain neighbors in the projected cluster.

APPENDIX D

ADDITIONAL DIMENSIONS: NEW CRYSTALS FROM E_8

D.1 Introduction

Since the 600-cell is a point object, it is impossible to generate an extended structure in three dimensions using the projection methods described in Chapter 2.

However, as mentioned near the end of Chapter 3, the point-group of the 600-cell is isomorphic to a subgroup of the 8D lattice E_8. Projections of the E_8 lattice may then be used to generate 4D and 3D quasicrystals.[100] Of particular interest, however, are rational quasicrystalline approximants.

Previous work by Berger *et al* defines a projection scheme for generating quasicrystal approximants of T_d (*i.e.* $\bar{4}3m$) point symmetry.[104] Of the binary structures rationalized, on the order of 70-80% of the atomic sites were correctly placed: that is, the projected site was within 1 Å of the true crystallographic site. We will use their approach here.

Dshemuchadse *et al* recently published a comprehensive survey of face-centered cubic large (with cell parameters in the range 17.1833 Å $\leq a \leq$ 71.490 Å) intermetallic structures.[2] They categorized the structures first by space group, and then into more specific types characterized by cluster geometry and arrangment. Additionally, Bader charge analysis[161,162] was performed on every structure. This analysis in particular lets us see how much electron transfer occurs in a binary structure between the electronegative and electropositive element.

We restrict our analysis to binary structures with space-group symmetry

$F\bar{4}3m$, and use the projection scheme outlined in[104] which guarantees the structures projected from E_8 are of T_d symmetry.

D.2 Projected Structures

The E_8 lattice is the closest-packed lattice in eight dimensions,[163] with each lattice point having 240 nearest neighbors. The coordinates are simple to express: for any integers $n_{1\ldots8}$, the points

$$\begin{aligned}&(n_1\ n_2\ n_3\ n_4\ n_5\ n_6\ n_7\ n_8)\\ &(n_1\ n_2\ n_3\ n_4\ n_5\ n_6\ n_7\ n_8) \quad + \quad \left(\frac{1}{2}\ \frac{1}{2}\ \frac{1}{2}\ \frac{1}{2}\ \frac{1}{2}\ \frac{1}{2}\ \frac{1}{2}\ \frac{1}{2}\right)\end{aligned}$$

both belong to E_8 if the sum of n_i is even.

To distinguish between points in 3D after projection from E_8, we use the notion of projected distance. Projected distance is the shortest distance from the E_8 lattice point to the 3D subspace of the projection. Formally, for some 3×8 projection matrix $\mathbf{M}$ which sends the 8D vector $\mathbf{v}$ to the 3D vector $\vec{v}$—that is, $\mathbf{M}\mathbf{v} = \vec{v}$—the projected distance is defined:

$$d(\mathbf{v}) = \left\|\mathbf{v} - \text{proj}\ \mathbf{v}\right\|. \tag{D.1}$$

Here, proj $\mathbf{v}$ is the projection of $\mathbf{v}$ onto the 3D subspace defined by the three rows of $\mathbf{M}$ ($\mathbf{m}_1$, $\mathbf{m}_2$, and $\mathbf{m}_3$). Although projected distances correspond to a Euclidean distance, it is the distance between two 8D points and thus corresponds to a non-physical displacement. Furthermore, the E_8 lattice is not yet endowed with any physical dimension: therefore, projected distance is unitless.

We must be careful about language here: the projection function returns an 8D vector "most like" the original 8D vector, but lying in the subspace spanned

by the rows of $\mathbf{M}$. If $\mathbf{v}$ can be written as a linear combination of $\mathbf{m}_n$, then $\text{proj}\,\mathbf{v} = \mathbf{v}$ and $d(\mathbf{v}) = 0$. The projection function is *not* the projection from 8D to 3D: categorically, $\text{proj}\,\mathbf{v} \neq \mathbf{M}\mathbf{v}$! Instead:

$$\begin{aligned} \text{proj}\,\mathbf{v} &= \frac{\mathbf{m}_1 \cdot \mathbf{v}}{\|\mathbf{m}_1\|}\mathbf{m}_1 + \frac{\mathbf{m}_2 \cdot \mathbf{v}}{\|\mathbf{m}_2\|}\mathbf{m}_2 + \frac{\mathbf{m}_3 \cdot \mathbf{v}}{\|\mathbf{m}_3\|}\mathbf{m}_3 \qquad \text{(D.2)} \\ &= \mathbf{M}^\top \,\text{diag}\left(\frac{1}{\|\mathbf{m}_1\|}, \frac{1}{\|\mathbf{m}_2\|}, \frac{1}{\|\mathbf{m}_3\|}\right) \cdot \mathbf{M}\mathbf{v}, \qquad \text{(D.3)} \end{aligned}$$

where $\text{diag}\,(a_1, a_2 \ldots a_n)$ generates an $n \times n$ square matrix with $a_1 \ldots a_n$ on the diagonal entries and zero elsewhere.

The choice of $\mathbf{M}$ for cubic structures of T_d symmetry is discussed in Berger *et al.*[104] It is chosen so that two arbitrary symmetry equivalent tethrahedra in the E_8 lattice project into 3D and form the *IT* and *OT* sites (in keeping with the notation of Chapter 2). One such projection is:

$$\mathbf{M} = \begin{pmatrix} 0 & 0 & -2t & 0 & 1 & 1 & -1 & -1 \\ 0 & 0 & 0 & -2t & 1 & -1 & 1 & -1 \\ 0 & -2t & 0 & 0 & 1 & -1 & -1 & 1 \end{pmatrix} \qquad \text{(D.4)}$$

Here, t is a parameter governing the relative sizes of the *IT* and *OT* and the projected unit cell. Taking t as successive approximations of τ ($\frac{1}{1}, \frac{2}{1}, \frac{3}{2} \ldots \tau$), we can in principle generate increasingly complex approximants all the way up to the quasicrystal at $t = \tau$. In this chapter, however, we will restrict our analysis to $t = \frac{2}{1}$ structures.

Notice that in the rows of $\mathbf{M}$ in Equation D.4 — vectors which span the 3D subspace of projection — are all of equal magnitude. With this in mind, we can can simplify the expression for the projection given in Equation D.3 to $\text{proj}\,\mathbf{v} = (4 + 4t^2)^{-\frac{1}{2}}\mathbf{M}^\top\mathbf{M}\mathbf{v}$.

Fixing projected distances controls the point symmetry of the 3D crystal.

To ensure that our projections have at least T_d point symmetry, the projected distances of the IT and OT sites must be the same: that is, $d(\mathbf{v}_{IT}) = d(\mathbf{v}_{OT})$ for any $\mathbf{v}_{IT}$ and $\mathbf{v}_{OT}$ sites.[104] Since there are eight sites controlling the symmetry — four from the IT and four from the OT — this generates seven constraints on our projection: $d(\mathbf{v}_{IT_1}) = d(\mathbf{v}_{IT_2}) = d(\mathbf{v}_{IT_3}) = d(\mathbf{v}_{IT_4}) = d(\mathbf{v}_{OT_1}) = d(\mathbf{v}_{OT_2}) = d(\mathbf{v}_{OT_3}) = d(\mathbf{v}_{OT_4})$. As a consequence, we have some freedom of choice in deciding where the origin of the projection is in 8D space. Specifically, instead of generating 3D structures from $\mathbf{Mv}$, where $\mathbf{v}$ is an E_8 lattice points, we can include an origin shift $\mathbf{s}$ so that our projection scheme becomes

$$\vec{v} = \mathbf{M}(\mathbf{v} - \mathbf{s}). \tag{D.5}$$

Solving for $\mathbf{s}$ in Equation D.5 subject to the above constraints gives us the form of $\mathbf{s}$:

$$\mathbf{s} = (x_1\ 0\ 0\ 0\ x_2\ x_2\ x_2\ x_2), \tag{D.6}$$

where x_1 and x_2 are free parameters. Any search for structure matches must therefore independently vary x_1 and x_2 enough so that $\mathbf{s}$ at least reaches the next lattice points in E_8: this requires that $x_1 = 0 \ldots 2$ and $x_2 = 0 \ldots 1$.

D.3 Structure Search

A systematic search of projected structures from E_8 was carried out. Projected structures were compared to real structures to gauge the applicability of the projection procedure. We restricted our structure search to those binary structures tabulated in Dshemuchadse *et al*[2] which belong to space group $F\bar{4}3m$ and are fully-ordered or at most contain only partial vacancies and mixed sites. In the

Table D.1: Summary of Experimental Structures Matched. Adapted in Part from Dshemuchadse *et al*.[2]

Composition	a/Å	Pearson	Reference
$Li_{81.0}Pb_{19.0}$[2]	20.089	$cF420$	Goward *et al*[164]
$Zn_{82.7}Pt_{17.3}$	18.14	$cF400$	Thimmaiah *et al*[112]
$Zn_{80.0}Pt_{20.0}$	18.091	$cF408$	Thimmaiah *et al*[112]
$Cu_{78.6}Sn_{21.4}$	17.980	$cF412$	Booth *et al*[165]
$Na_{86.3}Tl_{13.7}$[2]	24.154	$cF408$	Samson & Hansen[166]
$Sc_{86.3}Os_{13.7}$[2]	20.771	$cF408$	Chabot *et al*[167]
$Mg_{86.3}Rh_{13.7}$[2]	20.148	$cF408$	Westin & Edshammar[168]
$Mg_{87.9}Ir_{12.1}$	20.1148	$cF396$	Bonhomme & Yvon[169]
$Zn_{78.4}Fe_{21.6}$	17.963	$cF408$	Koster & Schoone[19]

[2] Indicates a fully-ordered structure

case of mixed sites, the site is taken to be the majority element for purposes of matching the structure. The structures are tabulated in Table D.1.

The **s** vector was varied over x_1 and x_2 in steps of 0.01 with $0 \leq x_1 \leq 2.0$ and $0 \leq x_1 \leq 1.0$ using a purpose-built projection program. Comparing the projected structures to real structures was performed with custom scripts integrated with the Cerius[2] suite of programs.[115] An atomic site is considered to be matched it if lies within 1 Å of the true experimental site.

Still, there is some subjectivity in what determines a good match. Most importantly, the atomic sites should preferentially match projected sites with low projected distance. Additionally, there should be separation between the atomic species with respect to projected distance: the model is more useful if it can say something about the site colorings in addition to the atomic structure. However,

other criteria such as percentage of sites matched or average distances between theoretical and experimental sites could conceivably be used.

Fortunately, the "best" matches for all the structures tested—again, a subjective balance between total sites matched and separation of atomic species—all appeared near a single **s**-vector, with $x_1 = 0.71$ and $x_2 = 0.14$. The site matches for each structure are summarized in Tables D.2 and D.3: in each table, a column for the the projected distance, $d(\mathbf{v})$, is given alongside the fractional coordinates x, y, and z and site multiplicities of the *projected* coordinate. Every additional two columns correspond to the experimental structure labeled at the top: listed in each of these two columns are the experimental element type and the separation distance, in Å, between the true site and the theoretical projected site. Table D.2 corresponds to structures which are fully-ordered and Table D.3 corresponds to structures which may have mixed sites or partial vacancies.

In both cases, we place an upper limit on projected distances we will accept: 1.10. This is again arbitrary. If we allow points very distant from the center of the projection to be counted we can in principle match all the sites, but the model becomes much less convincing as there are large segments of unmatched sites: projected sites which find no corresponding atomic site. The limit is denoted by a horizontal line below 1.10 on Tables D.2 and D.3.

Table D.2: Fully-ordered structure matches

Projected Distance	x	y	z	M	$Li_{81.0}Pb_{19.0}$		$Sc_{86.3}Os_{13.7}$		$Mg_{86.3}Rh_{13.7}$		$Mg_{86.3}Ir_{13.7}$	
0.49	0.15	0.15	0.65	16	Pb	0.31	Os	0.70	Rh	0.58	Ir	0.60
0.52	0.10	0.10	0.40	16	Pb	0.56	Os	0.01	Rh	0.04	Ir	0.03
0.58	0.05	0.25	0.25	24	Pb	0.41	–	–	–	–	–	–
0.60	0.00	0.00	0.20	24	Pb	0.40	Os	0.86	Rh	0.74	–	–
0.84	0.10	0.40	0.60	16	Li	0.52	Sc	0.40	Mg	0.57	Ir	0.29
0.86	0.05	0.05	0.05	16	Li	0.20	Sc	0.31	Mg	0.15	–	–
0.87	0.20	0.20	0.20	16	Li	0.58	Sc	0.30	Mg	0.41	Mg	1.06
0.87	0.20	0.30	0.70	16	Li	0.12	Sc	0.25	Mg	0.08	Mg	0.08
0.90	0.00	0.00	0.30	24	Li	0.53	–	–	–	–	–	–
0.91	0.15	0.35	0.65	16	–	–	–	–	–	–	–	–
0.92	0.10	0.10	0.60	16	Li	0.90	–	–	–	–	–	–
0.98	0.05	0.05	0.25	48	Li	1.19	Sc	0.33	Mg	0.42	Mg	0.44
0.99	0.00	0.20	0.20	48	–	–	–	–	–	–	–	–
1.01	0.00	0.00	0.50	4	Li	0.00	–	–	–	–	–	–
1.02	0.05	0.15	0.55	48	–	–	–	–	–	–	–	–
1.04	0.10	0.20	0.30	48	–	–	Sc	0.32	Mg	0.25	Mg	0.21
1.05	0.10	0.10	0.30	48	–	–	–	–	–	–	–	–
1.06	0.15	0.25	0.55	96	–	–	–	–	–	–	–	–
1.08	0.00	0.10	0.30	96	–	–	–	–	–	–	–	–
1.10	0.20	0.20	0.70	16	–	–	–	–	–	–	–	–
1.10	0.15	0.15	0.55	48	Li	0.92	Sc	0.36	Mg	0.35	Mg	0.45
1.10	0.20	0.20	0.30	16	Li	1.05	–	–	–	–	–	–
1.11	0.05	0.15	0.35	48	–	–	–	–	–	–	–	–
1.12	0.10	0.10	0.20	48	–	–	–	–	–	–	–	–
1.14	0.05	0.45	0.55	16	–	–	–	–	–	–	–	–
1.14	0.05	0.05	0.55	16	–	–	–	–	–	–	–	–
1.14	0.10	0.10	0.10	16	–	–	–	–	–	–	–	–
1.18	0.15	0.15	0.35	16	–	–	–	–	–	–	–	–
1.19	0.00	0.20	0.30	48	–	–	–	–	–	–	–	–
1.21	0.00	0.10	0.10	48	–	–	–	–	–	–	–	–
1.23	0.20	0.30	0.60	48	–	–	–	–	–	–	–	–
1.23	0.05	0.25	0.55	48	–	–	–	–	–	–	–	–
1.27	0.00	0.10	0.20	96	–	–	–	–	–	–	–	–
1.27	0.05	0.05	0.15	48	–	–	–	–	–	–	–	–
1.27	0.05	0.35	0.55	48	–	–	–	–	–	–	–	–
1.29	0.20	0.20	0.60	48	–	–	–	–	–	–	–	–
1.30	0.15	0.15	0.15	16	–	–	–	–	–	–	–	–
1.30	0.05	0.15	0.25	96	–	–	–	–	–	–	–	–
1.30	0.10	0.20	0.60	48	–	–	–	–	–	–	–	–
1.31	0.25	0.25	0.25	4	–	–	–	–	–	–	Mg	0.00
1.32	0.00	0.00	0.00	4	–	–	–	–	–	–	–	–
1.33	0.25	0.25	0.55	24	Li	0.49	Sc	0.23	Mg	0.35	Mg	0.42
1.34	0.15	0.35	0.55	48	–	–	–	–	–	–	–	–
1.35	0.00	0.00	0.10	24	–	–	–	–	–	–	Mg	0.66
1.38	0.00	0.10	0.40	48	–	–	–	–	–	–	–	–
1.38	0.15	0.25	0.25	24	–	–	–	–	–	–	–	–
1.39	0.25	0.25	0.65	24	–	–	–	–	–	–	–	–
1.39	0.05	0.15	0.15	48	Li	0.61	Sc	0.45	Mg	0.43	Mg	0.55
1.40	0.10	0.30	0.60	48	Li	0.66	Sc	0.69	Mg	0.62	Mg	0.60
1.40	0.00	0.00	0.40	24	–	–	Sc	0.13	Mg	0.11	Mg	0.16

Table D.3: Structure matches which have mixed or deficient sites

Projected Distance	x	y	z	M	$Zn_{80.0}Pt_{20.0}$		$Zn_{82.7}Pt_{17.3}$		$Cu_{78.6}Sn_{21.4}$		$Na_{86.3}Tl_{13.7}$		$Zn_{78.4}Fe_{21.6}$	
0.49	0.15	0.15	0.65	16	Pt	0.30	Pt	0.35	Sn	0.35	Tl	0.73	Fe	0.57
0.52	0.10	0.10	0.40	16	Pt	0.50	Pt	0.44	Cu	0.51	Tl	0.06	Fe	0.04
0.58	0.05	0.25	0.25	24	Pt	0.37	Zn	0.38	Cu	0.42	–	–	–	–
0.60	0.00	0.00	0.20	24	Pt	0.36	Pt	0.36	Cu	0.47	Tl	0.85	Fe	0.69
0.84	0.10	0.40	0.60	16	Zn	0.41	Zn	0.41	Cu	0.49	Na	0.64	Fe	0.48
0.86	0.05	0.05	0.05	16	Zn	0.14	Zn	0.11	Cu	0.02	Na	0.23	Fe	0.08
0.87	0.20	0.20	0.20	16	Zn	0.55	Zn	0.46	Cu	1.04	Na	1.16	Zn	0.30
0.87	0.20	0.30	0.70	16	Zn	0.13	Zn	0.11	Cu	0.23	Na	0.11	Fe	0.04
0.90	0.00	0.00	0.30	24	Zn	0.39	Zn	0.45	Sn	0.34	–	–	–	–
0.91	0.15	0.35	0.65	16	–	–	–	–	–	–	–	–	–	–
0.92	0.10	0.10	0.60	16	–	–	–	–	–	–	–	–	–	–
0.98	0.05	0.05	0.25	48	Zn	1.08	Zn	1.15	–	–	Na	0.51	Zn	0.46
0.99	0.00	0.20	0.20	48	–	–	–	–	Sn	1.11	–	–	–	–
1.01	0.00	0.00	0.50	4	–	–	–	–	–	–	–	–	–	–
1.02	0.05	0.15	0.55	48	–	–	–	–	–	–	–	–	–	–
1.04	0.10	0.20	0.30	48	–	–	–	–	–	–	Na	0.25	Zn	0.22
1.05	0.10	0.10	0.30	48	Zn	1.05	–	–	Cu	0.41	–	–	–	–
1.06	0.15	0.25	0.55	96	–	–	–	–	–	–	–	–	–	–
1.08	0.00	0.10	0.30	96	–	–	–	–	–	–	–	–	–	–
1.10	0.20	0.20	0.70	16	–	–	–	–	–	–	–	–	–	–
1.10	0.15	0.15	0.55	48	Zn	0.75	Zn	0.65	Cu	0.70	Na	0.48	Zn	0.36
1.10	0.20	0.20	0.30	16	Zn	0.80	Zn	0.22	Cu	0.01	–	–	–	–
1.11	0.05	0.15	0.35	48	–	–	–	–	–	–	–	–	–	–
1.12	0.10	0.10	0.20	48	–	–	–	–	–	–	–	–	–	–
1.14	0.05	0.45	0.55	16	–	–	–	–	–	–	–	–	–	–
1.14	0.05	0.05	0.55	16	Zn	0.32	Zn	0.23	Cu	0.19	–	–	–	–
1.14	0.10	0.10	0.10	16	–	–	–	–	–	–	–	–	–	–
1.18	0.15	0.15	0.35	16	–	–	Zn	0.68	–	–	–	–	–	–
1.19	0.00	0.20	0.30	48	–	–	–	–	–	–	–	–	–	–
1.21	0.00	0.10	0.10	48	–	–	–	–	–	–	–	–	–	–
1.23	0.20	0.30	0.60	48	–	–	–	–	–	–	–	–	–	–
1.23	0.05	0.25	0.55	48	Zn	1.19	–	–	Cu	1.16	–	–	Zn	1.19
1.27	0.00	0.10	0.20	96	–	–	–	–	–	–	–	–	–	–
1.27	0.05	0.05	0.15	48	–	–	–	–	–	–	–	–	–	–
1.27	0.05	0.35	0.55	48	–	–	–	–	–	–	–	–	–	–
1.29	0.20	0.20	0.60	48	–	–	–	–	–	–	–	–	–	–
1.30	0.15	0.15	0.15	16	–	–	Pt	0.45	–	–	–	–	–	–
1.30	0.05	0.15	0.25	96	–	–	–	–	–	–	–	–	–	–
1.30	0.10	0.20	0.60	48	–	–	–	–	–	–	–	–	–	–
1.31	0.25	0.25	0.25	4	–	–	–	–	–	–	–	–	–	–
1.32	0.00	0.00	0.00	4	–	–	–	–	–	–	–	–	–	–
1.33	0.25	0.25	0.55	24	Zn	0.42	Zn	0.49	Cu	0.43	Na	0.44	Zn	0.27
1.34	0.15	0.35	0.55	48	–	–	–	–	–	–	–	–	–	–
1.35	0.00	0.00	0.10	24	–	–	–	–	–	–	–	–	–	–
1.38	0.00	0.10	0.40	48	–	–	–	–	–	–	–	–	–	–
1.38	0.15	0.25	0.25	24	–	–	–	–	–	–	–	–	–	–
1.39	0.25	0.25	0.65	24	–	–	–	–	–	–	–	–	–	–
1.39	0.05	0.15	0.15	48	Zn	0.48	Zn	0.50	–	–	Na	0.53	Zn	0.26
1.40	0.10	0.30	0.60	48	–	–	Zn	0.55	–	–	Na	0.85	–	–
1.40	0.00	0.00	0.40	24	–	–	–	–	–	–	Na	0.21	Zn	0.11

D.4 Projected Distance and Electron Transfer

In addition to tabulating and classifying numerous F-centered complex cubic intermetallic structures, Dshemuchadse *et al*[2] provide Bader charge analysis for all structures analyzed. With this technique, the limits of an individual atom is based on a calculated electron density: a plane is fixed perpendicular to a line between an atom and one of its nearest neighbors. The position of the plane is chosen as the minimum of electron density along this line. The set of all planes from all nearest neighbors then forms a bounding region over which the density can be integrated and the number of electrons for the atomic site may be computed.

Previous work notes a correlation between projected distance and atomic radius of the constituent atoms,[104] with larger atoms having the shortest projected distance. Other comparisons such as electronegativity difference or difference in atomic mass did not seem to correspond to projected distance. Since we have seen in the previous chapters that structure and electron count are intimately related, we think this may be worth as second look. Here, we will see if there is any correlation between sites which gain or lose electrons (by way of the Bader charge analysis) and projected distance.

Unfortunately, Dshemuchadse *et al* give only the range of electron transfer for each element in any given structure, rather than the electron transfer at each site. Their results, then, are largely rationalized by electronegativity: electrons are on average more likely to be near more electronegative sites. Notice also that in every one of our selected structures in Table D.1, the minority element is the more electronegative one (although Cu and Sn are very close).

As a starting point for our comparison, we first determine the difference in average projected distance for each element type. This is computed as a simple sum of the projected distance values for each *matched site* (weighted for their multiplicities) divided by the total number of sites. Unmatched sites are ignored. This average is taken for both element types in the binary, and the absolute value of the difference is taken. Again, we only consider matches up to a projected distance of 1.10. Figure D.1 shows the compounds arranged by increasing difference in average projected distance.

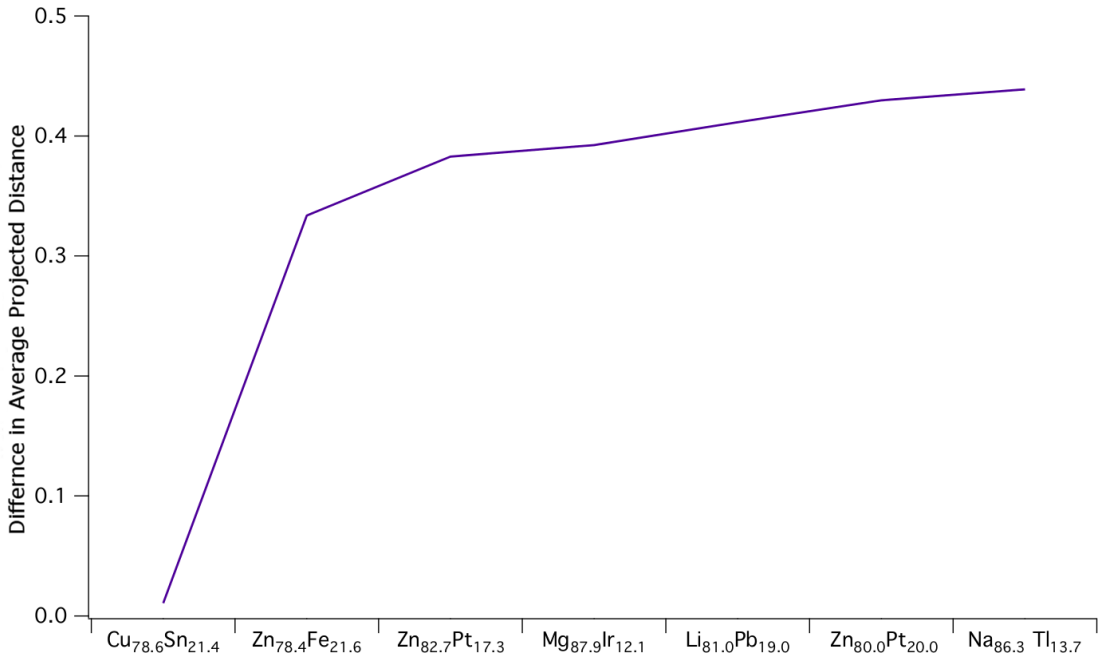

Figure D.1: Difference in average projected distances

Encouragingly, $Cu_{78.6}Sn_{21.4}$ sits on the left. In Figure D.2, we show the ranges of electron gain or loss for each element type. For instance, a Mg site in $Mg_{87.9}Ir_{12.1}$ may lose up to 1.4 electrons or gain as many as 0.8 electrons. Ir sites in the same structure gain between 5.7 and 6.8 electrons, according to the Bader charge analysis. The structures are arranged in the same order as in Fig-

ure D.1: increasing difference in average projected distance from left to right.*

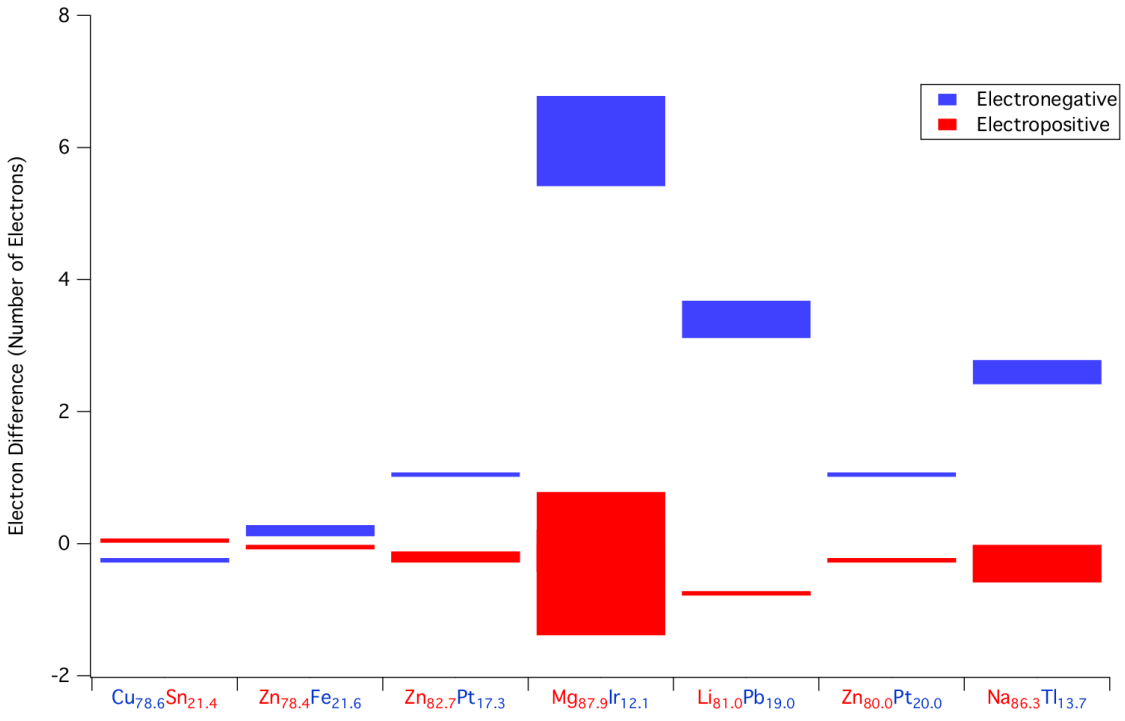

Figure D.2: Bader Charge Analysis of electron gain and loss. Results taken from the Supplemental Information of Dshemuchadse *et al*[2]

On the left we see $Cu_{78.6}Sn_{21.4}$ and $Zn_{78.4}Fe_{21.6}$ which have very little electron transfer according to the Bader charge analysis. Correspondingly, they have the lowest differences in average projected distance. The structures with the broadest ranges: $Mg_{87.9}Ir_{12.1}$, $Li_{81.0}Pb_{19.0}$, and $Na_{86.3}Tl_{13.7}$, all tend to the right side corresponding to large differences in average projected distance.

The two Pt-Zn structures reveal an important shortcoming in this kind of reasoning. Unsurprisingly, as seen in Figure D.2 Bader charge analysis pre-

*In both plots, $Sc_{86.3}Os_{13.7}$ and $Mg_{86.3}Rh_{13.7}$ are omitted since the projected sites matching the sites in those structures are identical to $Na_{86.3}Tl_{13.7}$ below the cutoff. Additionally, their ranges of electron transfer are similar.

dicts roughly the same amount of electron transfer both structures. Shouldn't these structures have nearly identical average projected distances? We can see that in Table D.3 that Zn replaces Pt at one site with low projected distance in $Zn_{82.7}Pt_{17.3}$, which is the primary cause of the lowering of the difference in average projected distance. Our model is not nearly precise enough to account for this subtlety though, and should still be treated as more heuristic than exact.

D.5 Conclusions

In Chapters 2 and 3, we showed the utility of a higher-dimensional approach to understanding not just in real space atomic clusters but also reciprocal-space clusters. The E_8 lattice is a natural way of extending the 4D 600-cell point object to an extended object—but at what cost?

Adding four spatial dimensions vitiates our spatial intuition, leaving us only with mathematical tools. Unlike the 600-cell, which can be imagined as a perfect tetrahedral packing that is almost-but-not-quite possible in 3D, the E_8 lattice is virtually opaque to such simple understanding.

Nevertheless, if we want to generate entire crystal structures rather than just atomic clusters, we will need an extended structure regardless of which dimension we choose to project from. It is already known that a 4D quasicrystal can be generated from the E_8 lattice.[100] This projected quasicrystal maintains the symmetry group of the 600-cell. For future studies, we propose taking *rational* approximants of this 4D quasicrystal to generate 3D crystal structures. In this way, we can generate extended structures with the right symmetry (or pseudo symmetry in 3D) without sacrificing our understanding of 4D geometry.

BIBLIOGRAPHY

[1] Eliot, G. *Middlemarch: a study of provincial life*, Harper's Library ed.; Harper & Bros.: New York, 1876.

[2] Dshemuchadse, J.; Jung, D. Y.; Steurer, W. *Acta Crystallographica Section B-Structural Science* **2011**, *67*, 269–292.

[3] Belin, C. H. E.; Belin, R. C. H. *Journal of Solid State Chemistry* **2000**, *151*, 85–95.

[4] Allio, C. Binäre, zinkreiche Phasen der Elemente Rhodium, Ruthenium und Osmium. Ph.D. thesis, Philipps-Universität-Marburg, 2010.

[5] Mott, N. F.; Jones, H. *The Theory of the Properties of Metals and Alloys*; Clarendon Press: Oxford, 1936.

[6] Massalski, T. B.; Okamoto, H. *Binary alloy phase diagrams*, 2nd ed.; ASM International: Materials Park, Ohio, 1990.

[7] Degtyareva, V. F.; Smirrnova, H. S. *Zeitschrift Fur Kristallographie* **2007**, *222*, 718–721.

[8] JP, 2012; `http://en.wikipedia.org/wiki/File:William_Rowan_Hamilton_Plaque_-_geograph.org.uk_-_347941.jpg`.

[9] Moult, J.; Fidelis, K.; Kryshtafovych, A.; Tramontano, A. *Proteins: Structure, Function, and Bioinformatics* **2011**, *79*, 1–5.

[10] Friauf, J. B. *J. Am. Chem. Soc.* **1927**, *49*, 3107–3114.

[11] Grime, G.; Morris-Jones, W. *Philosophical Magazine Series 7* **1929**, *7*, 1113–1134.

[12] Misch, L. *Metallwirtschaft, Metallwissenschaft, Metalltechnik* **1935**, *14*, 897–899.

[13] Bradley, A. J.; Gregory, C. H. *Philosophical Magazine* **1931**, *12*, 143–162.

[14] Bradley, A. J.; Thewlis, J. *Proceedings of the Royal Society of London Series A-Containing Papers of a Mathematical and Physical Character* **1926**, *112*, 678–692.

[15] Westgren, A.; Phragmén, G. *Phil. Mag.* **1925**, *311-341*.

[16] Yurko, G. A.; Barton, J. W.; Parr, J. G. *Acta Cryst.* **1959**, *12*, 909–911.

[17] Lonie, D. C.; Zurek, E. *Comp. Phys. Comm.* **2010**, *182*, 372387.

[18] Oganov, A. R.; Glass, C. W. *Journal of Chemical Physics* **2006**, *124*.

[19] Koster, A. S.; Schoone, J. C. *Acta. Crys. Sect. B* **1981**, *37*, 1905–1907.

[20] Lind, H.; Boström, M.; Petříček, V.; Lidin, S. *Acta. Cryst. Sect. B* **2003**, *59*, 720–729.

[21] Nover, G.; Schubert, K. *J. Less-Common Metals* **1980**, *75*, 51–63.

[22] Morton, A. J. *Phys. Status Solidi A* **1974**, *23*, 275–289.

[23] Morton, A. J. *Phys. Status Solidi A* **1975**, *31*, 661–674.

[24] Broddin, D.; Tendeloo, G. V.; Landuyt, J. V.; Amelinckx, S.; Portier, R.; Guymont, M.; Loiseau, A. *Phil. Mag. A: Phy. Cond. Mat.* **1986**, *54*, 395–419.

[25] Lewis, G. N. *J. Am. Chem. Soc.* **1916**, *38*, 762–785.

[26] Langmuir, I. *J. Am. Chem. Soc.* **1919**, *41*, 868–934.

[27] Langmuir, I. *Science* **1921**, *54*, 59–67.

[28] Hückel, E. Z. *Z. Phys.* **1931**, *72*, 204–286.

[29] Hückel, E. Z. *Z. Phys* **1931**, *72*, 310–337.

[30] Hückel, E. Z. *Z. Phys.* **1932**, *76*, 628–648.

[31] Wade, K. J. *J. Chem. Soc. D: Chem. Commun.* **1971**, *15*, 792–793.

[32] Mingos, D. M. P. *Nature Phys. Sci.* **1972**, *236*, 99–102.

[33] Jones, H. *Proc. R. Soc. A* **1934**, *144*, 225–234.

[34] Berger, R. F.; Lee, S.; Johnson, J.; Nebgen, B.; Sha, F.; Xu, J. Q. *Chemistry-a European Journal* **2008**, *14*, 3908–3930.

[35] Berger, R. F.; Walters, P. L.; Lee, S.; Hoffmann, R. *Chemical Reviews* **2011**, *111*, 4522–4545.

[36] Noran, T. *Voyager (4.0)*; 1999.

[37] Cie., S. . *Program Package for X-ray diffraction (2.75)*; 1996.

[38] Cie., S. . *X-SHAPE (2.01)-Crystal Optimization for Numerical Absorption Correction*; 2001.

[39] Cie., S. . *X-RED (1.02)-Data Reduction Program*; 2001.

[40] Sheldrick, G. *Acta Cryst.* **2008**, *A*, 112–122.

[41] Gwyer, G. C. *Z. Anorg. Chem.* **1908**, *57*, 113–153.

[42] Burkhardt, U.; Ellner, M.; Grin, Y.; Baumgartner, B. *Powder Diffr.* **1998**, *13*, 159–162.

[43] Ormeci, A.; Grin, Y. *Israel J. Chem.* **2011**, *51*, 13491354.

[44] Edshammar, L. *Acta Chem. Scand.* **1967**, *21*, 647–651.

[45] Müller, U. *Inorganic structural chemistry*, 2nd ed.; Wiley: Chichester, England ; Hoboken, NJ, 2007.

[46] Hume-Rothery, W. *The Metallic State*; Clarendon Press: Oxford, 1931.

[47] Hume-Rothery, W. *Electrons, Atoms, Metals, and Alloys*; Dover: New York, 1963.

[48] Vogel, S. C.; Stein, F.; Palm, M. *Appl. Phys. A* **2010**, *99*, 607–611.

[49] Hoffmann, R. *J. Am. Chem. Soc.* **1963**, *39*, 1397–1412.

[50] Burdett, J. *Chemical Bonding in Solids*; Oxford University Press: New York, 1995.

[51] Hoffmann, R. *Solids and Surfaces: A Chemist's View of Bonding in Extended Structures*; VCH: New York, 1988.

[52] Schmidt, J.; Lee, S.; Fredrickson, D. C.; Conrad, M.; Sun, J.; Harbrecht, B. *Chem. Eur. J.* **2007**, *13*, 1394–1410.

[53] Burdett, J.; Lee, S.; McLarnan, T. *J. Am. Chem. Soc.* **1985**, *107*, 3083–3089.

[54] Burdett, J.; Canadell, E.; Hughbanks, T. *J. Am. Chem. Soc.* **1986**, *108*, 3971–3976.

[55] Miller, G.; Lee, C. S. *Eur. J. Inorg. Chem* **2001**, *40*, 338–345.

[56] Fredrickson, D.; Lee, S.; Hoffmann, R. *Angew. Chem.* **2007**, *46*, 1958–1976.

[57] Berger, R.; Lee, S.; Hoffmann, R. *Chem. Eur. J.* **2007**, *13*, 7852–7863.

[58] Landrum, G.; Glassey, W. **YAeHMOP** is freely available at `http://sourceforge.net/projects/yaehmop/`.

[59] Kresse, G.; Hafner, J. *Phys. Rev. B* **1993**, *47*, 558.

[60] Kresse, G.; Hafner, J. *Phys. Rev. B* **1994**, *49*, 14251.

[61] Kresse, G.; Furthmüller, J. *Comput. Mat. Sci.* **1996**, *6*, 15.

[62] Kresse, G.; Furthmüller, J. *Phys. Rev. B* **1996**, *54*, 11169.

[63] Perdew, J. P.; Zunger, A. *Phys. Rev. B* **1981**, *23*, 5048.

[64] Kresse, G.; Hafner, J. *J. Phys.: Condens. Matter* **1994**, *6*, 8245.

[65] Vanderbilt, D. *Phys. Rev. B* **1990**, *41*, 7892.

[66] Gaston, N.; Paulus, B.; Wedig, U.; Jansen, M. *Phys Rev Lett* **2008**, *100*, 226404.

[67] Ramírez, R.; Böhm, M. *Intl. J. Quant. Chem.* **1986**,

[68] *CRC Handbook of Chemistry and Physics 92nd Edition*; CRC Press, 2011.

[69] Pauling, L. *The Nature of the Chemical Bond and the Structure of Molecules and Crystals; An Introduction to Modern Structural Chemistry*, 3rd ed.; The George Fisher Baker non-resident lectureship in chemistry at Cornell University; Cornell University Press: Ithaca, N.Y.,, 1960; p 644 p.

[70] Frank, F. C.; Kasper, J. S. *Acta Crystallographica* **1958**, *11*, 184–190.

[71] Pearson, W. B. *The Crystal Chemistry and Physics of Metals and Alloys*; Wiley series on the science and technology of materials; Wiley-Interscience: New York, 1972; pp xix, 806 p.

[72] Sikiric, M. D.; Delgado-Friedrichs, O.; Deza, M. *Acta Crystallographica Section A* **2010**, *66*, 602–615.

[73] Delgado-Friedrichs, O.; O'Keeffe, M. *Acta Crystallographica Section A* **2010**, *66*, 637–639.

[74] Frank, F. C.; Kasper, J. S. *Acta Crystallographica* **1959**, *12*, 483–499.

[75] Yarmolyuk, Y. P.; Kripyakevich, P. I. *Kristallografiya* **1974**, *19*, 539–545.

[76] Yarmolyuk, Y. P.; Kripyakevich, P. I. *Sov. Phys. Crystallogr.* **1974**, *19*, 334–337.

[77] Shoemaker, D. P.; Shoemaker, C. B. *Acta Crystallographica Section B-Structural Science* **1986**, *42*, 3–11.

[78] Laves, F.; Witte, H. *Metallwirtschaft, Metallwissenschaft, Metalltechnik* **1935**, *14*, 645–649.

[79] Amerioun, S.; Yokosawa, T.; Lidin, S.; Haussermann, U. *Inorganic Chemistry* **2004**, *43*, 4751–4760.

[80] Bergman, G.; Waugh, J. L. T.; Pauling, L. *Acta Crystallographica* **1957**, *10*, 254–259.

[81] Samson, S. *Acta Crystallographica* **1967**, *23*, 586–600.

[82] Feuerbacher, M. et al. *Zeitschrift Fur Kristallographie* **2007**, *222*, 259–288.

[83] Gourdon, O.; Izaola, Z.; Elcoro, L.; Petricek, V.; Miller, G. J. *Inorganic Chemistry* **2009**, *48*, 9715–9722.

[84] Weber, T.; Dshemuchadse, J.; Kobas, M.; Conrad, M.; Harbrecht, B.; Steurer, W. *Acta Crystallographica Section B-Structural Science* **2009**, *65*, 308–317.

[85] Conrad, M.; Harbrecht, B.; Weber, T.; Jung, D. Y.; Steurer, W. *Acta Crystallographica Section B-Structural Science* **2009**, *65*, 318–325.

[86] Haji-Akbari, A.; Engel, M.; Keys, A. S.; Zheng, X. Y.; Petschek, R. G.; Palffy-Muhoray, P.; Glotzer, S. C. *Nature* **2009**, *462*, 773–U91.

[87] Sadoc, J. F.; Mosseri, R. *Geometrical Frustration*; Cambridge University Press: Cambridge ; New York, 2006.

[88] Kriyakevich, P.; Gladyshevskii, E.; Cherkashin, E. *Doklady Akademii Nauk SSSR* **1952**, *80*, 253–256.

[89] Sulonen, M. *Acta Polytechnica Scandinavica, Chemical-metallurgic series* **1962**, *18*, 22.

[90] Brandon, J. K.; Brizard, R. Y.; Chieh, P. C.; McMillan, R. K.; Pearson, W. B. *Acta Crystallographica Section B* **1974**, *30*, 1412–1417.

[91] Rajasekharan, T.; Schubert, K. *Zeitschrift Für Metallkunde* **1982**, *73*, 262–264.

[92] Shechtman, D.; Blech, I.; Gratias, D.; Cahn, J. W. *Phys. Rev. Lett.* **1984**, *53*, 1951–1953.

[93] Lee, C. S.; Miller, G. J. *Journal of the American Chemical Society* **2000**, *122*, 4937–4947.

[94] Lin, Q. S.; Corbett, J. D. *Inorganic Chemistry* **2004**, *43*, 1912–1919.

[95] Steurer, W. *Zeitschrift Für Kristallographie* **2004**, *219*, 391–446.

[96] Gomez, C. P.; Lidin, S. *Chemistry-a European Journal* **2004**, *10*, 3279–3285.

[97] Duneau, M.; Katz, A. *Phys. Rev. Lett.* **1985**, *54*, 2688–2691.

[98] Elser, V.; Henley, C. L. *Phys. Rev. Lett.* **1985**, *55*, 2883–2886.

[99] Boudard, M.; Deboissieu, M.; Janot, C.; Heger, G.; Beeli, C.; Nissen, H. U.; Vincent, H.; Ibberson, R.; Audier, M.; Dubois, J. M. *Journal of Physics-Condensed Matter* **1992**, *4*, 10149–10168.

[100] Elser, V.; Sloane, N. J. A. *Journal of Physics A-Mathematical and General* **1987**, *20*, 6161–6167.

[101] Sadoc, J. F.; Mosseri, R. *Journal of Physics A-Mathematical and General* **1993**, *26*, 1789–1809.

[102] Kraposhin, V. S.; Talis, A. L.; Dubois, J. M. *Journal of Physics-Condensed Matter* **2002**, *14*, 8987–8996.

[103] Kraposhin, V. S. *Metal Science and Heat Treatment* **2005**, *47*, 351–358.

[104] Berger, R. F.; Lee, S.; Johnson, J.; Nebgen, B.; So, A. C. Y. *Chemistry-a European Journal* **2008**, *14*, 6627–6639.

[105] Mosseri, R.; Sadoc, J. P. *Journal De Physique* **1986**, *47*, 281–297.

[106] Mosseri, R.; Sadoc, J. F. *Journal De Physique* **1990**, *51*, C7257–C7264.

[107] Kleman, M.; Friedel, J. *Reviews of Modern Physics* **2008**, *80*, 61–115.

[108] Rivier, N. *Journal De Physique* **1982**, *43*, 91–95.

[109] Nelson, D. R. *Physical Review Letters* **1983**, *50*, 982–985.

[110] Coxeter, H. *Regular Polytopes*; Dover Publications: New York, 1973.

[111] Johansson, A.; Westman, S. *Acta Chemica Scandinavica* **1970**, *24*, 3471–3479.

[112] Thimmaiah, S.; Richter, K. W.; Lee, S.; Harbrecht, B. *Solid State Sciences* **2003**, *5*, 1309–1317.

[113] Shi, N. C.; Li, X. Z.; Ma, Z. S.; Kuo, K. H. *Acta Crystallographica Section B-Structural Science* **1994**, *50*, 22–30.

[114] Erassme, J.; Lueken, H. *Acta Crystallographica Section B-Structural Science* **1987**, *43*, 244–250.

[115] Cerius^2. 2005; Version 4.9.

[116] Samson, S. *Acta Chemica Scandinavica* **1949**, *3*, 835–843.

[117] Kaskel, S.; Corbett, J. D. *Inorganic Chemistry* **2000**, *39*, 3086–3091.

[118] Friauf, J. B. *Physical Review* **1927**, *29*, 0034–0040.

[119] Bradley, A.; Cheng, C. *Zeitschrift für Kristallographie, Kristallgeometrie, Kristallphysik, Kristallchemie* **1938**, *99*, 480–487.

[120] Brandon, J. K.; Brizard, R. Y.; Chieh, P. C.; Mcmillan, R. K.; Pearson, W. B. *Acta Crystallographica Section B-Structural Science* **1974**, *B 30*, 1412–1417.

[121] Beaudry, B. J.; Daane, A. H. *Transactions of the American Institute of Mining and Metallurgical Engineers* **1960**, *218*, 854–859.

[122] Nassau, K.; Cherry, L. V.; Wallace, W. E. *Journal of Physics and Chemistry of Solids* **1960**, *16*, 123–130.

[123] Dwight, A. E. *Journal of the Less-Common Metals* **1975**, *43*, 117–120.

[124] Dwight, A. E. *Transactions of the American Society for Metals* **1961**, *53*, 479–500.

[125] Sugiyama, K.; Kaji, N.; Hiraga, K.; Ishimasa, T. *Zeitschrift Für Kristallographie* **1998**, *213*, 90–95.

[126] Matsuo, Y.; Hiraga, K. *Philosophical Magazine Letters* **1994**, *70*, 155–161.

[127] Shoemaker, C. B.; Keszler, D. A.; Shoemaker, D. P. *Acta Crystallographica Section B-Structural Science* **1989**, *45*, 13–20.

[128] Steurer, W. *Philosophical Magazine* **2006**, *86*, 1105–1113.

[129] Steurer, W.; Deloudi, S. *Acta Crystallographica Section A* **2008**, *64*, 1–11.

[130] Shevchenko, V. Y.; Blatov, V. A.; Ilyushin, G. D. *Glass Physics and Chemistry* **2009**, *35*, 1–12.

[131] Shevchenko, V. Y.; Blatov, V. A.; Ilyushin, G. D. *Structural Chemistry* **2009**, *20*, 975–982.

[132] Blatov, V. A.; Ilyushin, G. D.; Proserpio, D. M. *Inorganic Chemistry* **2011**, *50*, 5714–5724.

[133] de Laissardière, G. T.; Nguyen-Manh, D.; Mayou, D. *Progress in Materials Science* **2005**, *50*, 679–788.

[134] Sutton, A. P.; Finnis, M. W.; Pettifor, D. G.; Ohta, Y. *Journal of Physics C-Solid State Physics* **1988**, *21*, 35–66, L8374 Times Cited:319 Cited References Count:75.

[135] Stacey, T. E.; Fredrickson, D. C. *Dalton Transactions* **2012**, *41*, 7801–7813.

[136] Ashcroft, N. W.; Mermin, N. D. *Solid state physics*; Holt: New York, 1976.

[137] Massalski, T. B.; Mizutani, U. *Progress in Materials Science* **1978**, *22*, 151–262.

[138] Sato, H.; Toth, R. S. *Physical Review Letters* **1962**, *8*, 239–241.

[139] Paxton, A. T.; Methfessel, M.; Pettifor, D. G. *Proceedings of the Royal Society of London Series a-Mathematical Physical and Engineering Sciences* **1997**, *453*, 1493–1514.

[140] Hoistad, L. M.; Lee, S. *Journal of the American Chemical Society* **1991**, *113*, 8216–8220.

[141] Mackay, A. L. *Acta Crystallographica* **1962**, *15*, 916.

[142] Takeuchi, T.; Mizutani, U. *Physical Review B* **1995**, *52*, 9300–9309.

[143] Mizutani, U.; Asahi, R.; Sato, H.; Noritake, T.; Takeuchi, T. *Journal of Physics-Condensed Matter* **2008**, *20*, 275228.

[144] Mizutani, U.; Kamiya, A.; Matsuda, T.; Kishi, K.; Takeuchi, S. *Journal of Physics-Condensed Matter* **1991**, *3*, 3711–3718.

[145] Poon, S. J. *Advances in Physics* **1992**, *41*, 303–363.

[146] Lin, Q. S.; Corbett, J. D. *Journal of the American Chemical Society* **2007**, *129*, 6789–6797.

[147] Takeuchi, T.; Sato, H.; Mizutani, U. *Journal of Alloys and Compounds* **2002**, *342*, 355–359.

[148] Mizutani, U.; Takeuchi, T.; Sato, H. *Progress in Materials Science* **2004**, *49*, 227–261.

[149] Asahi, R.; Sato, H.; Takeuchi, T.; Mizutani, U. *Physical Review B* **2005**, *71*, 165103.

[150] Mizutani, U. *Hume-Rothery Rules for Structurally Complex Alloy Phases*; CRC Press: Boca Raton, 2011.

[151] Gourdon, O.; Gout, D.; Williams, D. J.; Proffen, T.; Hobbs, S.; Miller, G. J. *Inorganic Chemistry* **2007**, *46*, 251–260.

[152] Moody, R. V.; Patera, J. *Journal of Physics A-Mathematical and General* **1993**, *26*, 2829–2853.

[153] Lundeen, S. The finite reflection group H_4. Ph.D. thesis, Idaho State University, 2007.

[154] Coxeter, H. letter to John T. Graves, dated October 17, 1843.

[155] Baez, J. *Bulletin of the American Mathematical Society* **2002**, *39*, 145–205.

[156] Oss, S. L. v. *Verhandelingen Natuurkunde, Eerste Sectie* **1899**, *7*, 1–18.

[157] Val, P. d. *Homographies, Quaternions, and Rotations*; Claredon Press: Oxford, 1964.

[158] Conway, J. H.; Smith, D. A. *On Quaternions and Octonions : their Geometry, Arithmetic, and Symmetry*; AK Peters: Natick, Mass., 2003.

[159] Holt, D. F.; Eick, B.; O'Brien, E. A. *Handbook of Computational Group Theory*; Discrete Mathematics and its Applications; Chapman and Hall/CRC: Boca Raton, 2005.

[160] Carter, R. L. *Molecular Symmetry and Group Theory*; J. Wiley: New York, 1998.

[161] Bader, R. F. W. *Atoms in Molecules : a Quantum Theory*; The International Series of Monographs on Chemistry; Clarendon Press: Oxford ; New York, 1990.

[162] Henkelman, G.; Arnaldsson, A.; Jonsson, H. *Computational Materials Science* **2006**, *36*, 354–360.

[163] Conway, J. H.; Sloane, N. J. A. *Sphere packings, lattices, and groups*, 3rd ed.; Springer: New York, 1999.

[164] Goward, G. R.; Taylor, N. J.; Souza, D. C. S.; Nazar, L. F. *Journal of Alloys and Compounds* **2001**, *329*, 82–91.

[165] Booth, M. H.; Brandon, J. K.; Brizard, R. Y.; Chieh, C.; Pearson, W. B. *Acta Crystallographica Section B-Structural Science* **1977**, *33*, 30–36.

[166] Samson, S.; Hansen, D. A. *Acta Crystallographica Section B-Structural Crystallography and Crystal Chemistry* **1972**, *B 28*, 930.

[167] Chabot, B.; Cenzual, K.; Parthe, E. *Acta Crystallographica Section B-Structural Science* **1980**, *36*, 2202–2205.

[168] Westin, L.; Edshamma.Le, *Acta Chemica Scandinavica* **1971**, *25*, 1480.

[169] Bonhomme, F.; Yvon, K. *Journal of Alloys and Compounds* **1995**, *227*, L1–L3.